The Lamb Shift in Muonic Hydrogen

Die Lamb-Verschiebung in myonischem Wasserstoff

Tobias Nebel

München im Mai 2010

The Lamb Shift in Muonic Hydrogen

Die Lamb-Verschiebung in myonischem Wasserstoff

Tobias Nebel

Dissertation
an der Fakultät für Physik
der Ludwig–Maximilians–Universität
München

vorgelegt von
Tobias Nebel
aus München

München, den 21. Mai 2010

1. Gutachter: Prof. Dr. Theodor W. Hänsch

2. Gutachter: Prof. Dr. Martin Faessler

Tag der mündlichen Prüfung: 25. Juni 2010

Meiner Familie.

Bild: Paul Scherrer Institut, Markus Fischer.

Zusammenfassung

Diese Arbeit beschäftigt sich mit der erstmaligen Messung der $2S - 2P$ Lamb-Verschiebung in myonischem Wasserstoff (μp). Wegen seines Potentials, den rms Protonenladungsradius $r_p = \sqrt{\langle r_r^2 \rangle}$ zu extrahieren, wird dieses Experiment bereits seit 40 Jahren diskutiert. Doch erst der Fortschritt auf dem Gebiet der Myonenstrahlen und der Lasertechnologie aus jüngster Zeit haben es nun realisierbar gemacht. In diesem Projekt, durchgeführt an der Protonenbeschleuniger-Anlage des Paul–Scherrer–Instituts in der Schweiz, wurde das exotische Analogon zur klassischen Lamb-Verschiebung im Wasserstoff mittels Laserspektroskopie untersucht.

Negativ geladene Myonen werden an einem speziell entwickelten Niederenergie-Myonenstrahl mit einer Rate von $330\,\mathrm{s}^{-1}$ hergestellt und in 1 hPa H_2 Gas gestoppt. Dort werden hoch angeregte μp Atome gebildet, wovon die meisten prompt (innerhalb von ~ 100 ns) in den Grundzustand kaskadieren. Nur ein Bruchteil von 1.1 % formt μp Atome im langlebigen $2S$ Zustand mit einer Lebensdauer von 1.0 μs. Ein aufwendiges Lasersystem triggert auf jedes einlaufende Myon und liefert Laserpulse mit 0.2 mJ Energie bei $\lambda \simeq 6\,\mu$m und einer Wiederholungsrate von $500\,\mathrm{s}^{-1}$. Der Laser beleuchtet die μp Atome 900 ns nach der prompten Myonenkaskade und treibt den $2S - 2P$ Übergang. Während der nachfolgenden Abregung in den $1S$ Grundzustand wird ein 1.9 keV K_α Röntgenphoton emittiert, welches von großflächigen Avalanche-Photodioden detektiert wird. Eine Resonanzlinie erhält man, wenn man die Laserfrequenz durchstimmt und aus den entsprechenden Zeitspektren die Anzahl der laserinduzierten K_α Photonen bestimmt.

Abbildung 1:
Summierte Zeitspektren auf und neben der Resonanz. *Zeitspektren der* K_α *Photonen, summiert für Laserfrequenzen auf Resonanz (oben) und neben der Resonanz (unten), in linearer und logarithmischer Skala. Die prompten* K_α *Ereignisse sind blau unterlegt. Das Laserzeitfenster 900 ns nach der prompten Kaskade ist rot markiert.*

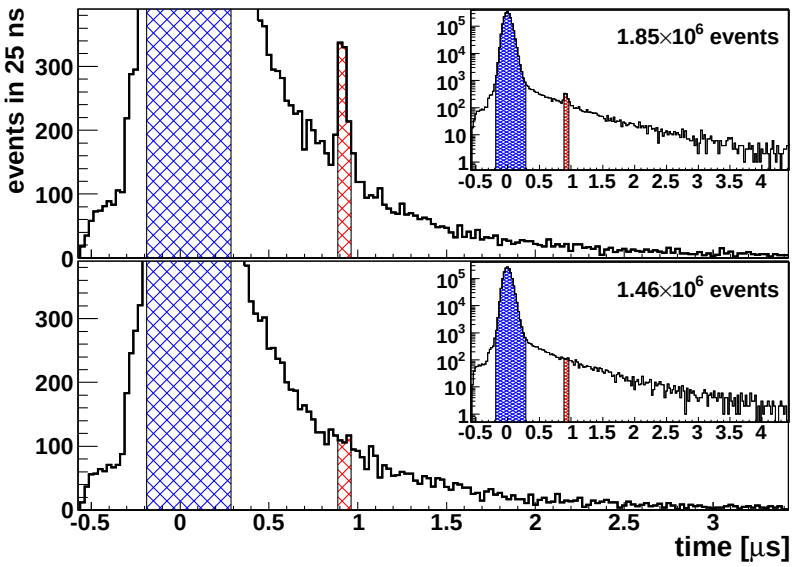

Für den gemessenen $\mu p(2S_{1/2}^{F=1} - 2P_{3/2}^{F=2})$ Übergang sind zwei solcher Zeitspektren in Figur 1 dargestellt. Diese sind einmal für Laserfrequenzen auf und einmal neben der Resonanz aufsummiert. Die laserinduzierten K_α Ereignisse heben sich klar vom exponentiell abfallendem Untergrund ab. Eine Resonanzlinie (Figur 2(a)) erhält man, indem man die Anzahl der laserinduzierten K_α Ereignisse (rot) auf die prompten Röntgenphotonen (blau) normiert (wodurch Messzeitunterschiede berücksichtigt werden) und gegen die Laserfrequenz aufträgt. Für die $2S_{1/2}^{F=1} - 2P_{3/2}^{F=2}$ Übergangsfrequenz in μp erhält man

$$\nu_{2S-2P} = 49\,881\,695\,(711)\,\mathrm{MHz} \tag{1}$$

mit einer relativen Unsicherheit von 1.4×10^{-5}.

Unter der Annahme korrekter QED Berechnungen der Lamb-Verschiebung in μp lässt sich ein neuer Wert für den rms Protonenladungsradius r_p angeben[1]:

$$r_p = 0.84192\,(65)\,\mathrm{fm} \tag{2}$$

Dieser Wert ist $5.0\,\sigma$ kleiner aber 10 mal präziser als der allgemein anerkannte CODATA-Wert $r_p = 0.8768\,(69)\,\mathrm{fm}$, welcher hauptsächlich von Wasserstoffdaten und QED-Rechnungen abhängt.

Verwendet man die genau gemessene $1S - 2S$ Übergangsfrequenz in Wasserstoff (relative Genauigkeit 1.4×10^{-14}) in Verbindung mit unserem neuen Wert für r_p, lässt sich ein neuer Wert für die Rydberg-Konstante R_∞ mit einer relativen Genauigkeit von 1.5×10^{-12} ermitteln:

$$R_\infty = 10\,973\,731.568\,161\,(16)\,\mathrm{m}^{-1} \tag{3}$$

Dies ist $-110\,\mathrm{kHz/c}$ oder $4.9\,\sigma$ vom CODATA-Wert entfernt, allerdings 4.6 mal genauer.

Der Ursprung dieser großen Diskrepanz ist bis jetzt noch nicht verstanden. Die Abweichung könnte durch fehlende QED Terme in Wasserstoff oder myonischem Wasserstoff, oder durch unentdeckte Fehler in einigen anderen Wasserstoffspektroskopie-Experimenten hervorgerufen sein. Am faszinierendsten wäre natürlich, wenn der Grund in Neuer Physik zu finden wäre.

Neben dem hier präsentierten $2S_{1/2}^{F=1} - 2P_{3/2}^{F=2}$ Übergang in μp wurden vier weitere Resonanzen in μp und in myonischem Deuterium (μd) untersucht, nämlich der $\mu p(2S_{1/2}^{F=0} - 2P_{3/2}^{F=1})$, der $\mu d(2S_{1/2}^{F=3/2} - 2P_{3/2}^{F=5/2})$, der $\mu d(2S_{1/2}^{F=1/2} - 2P_{3/2}^{F=3/2})$ und der $\mu d(2S_{1/2}^{F=1/2} - 2P_{3/2}^{F=1/2})$ Übergang. All diese Daten bedürfen noch einer rigorosen Analyse, sollen aber trotzdem in Figur 2(b)-(d) als vorläufige Ergebnisse präsentiert werden. Abgesehen von der erwähnten Verbesserung des Protonenladungsradius und der Rydberg-Konstanten wird man mit Hilfe dieser Daten in der Lage sein, die Genauigkeit des Deuteronladungsradius r_d um einen Faktor 20 zu verbessern, einen neuen Wert für den magnetischen Protonenradius (Zemach-Radius) mit einer relativen Genauigkeit von 3×10^{-2} zu liefern, einen experimentellen Wert für die Lamb-Verschiebung unabhängig vom (nicht genau bekannten) Zemach-Radius zu extrahieren und die Deuteron-Polarisierbarkeit zu bestimmen.

[1]Die hier präsentierten Ergebnisse sind etwas genauer als die in Ref. [1] vorgestellten und unterscheiden sich leicht von ihnen (z.B. $r_p = 0.84184\,(67)\,\mathrm{fm}$). Der Grund ist die hier vorgestellte verfeinerte Datenanalyse.

$\mu p(2S^{F=1}_{1/2} - 2P^{F=2}_{3/2})$

(a)

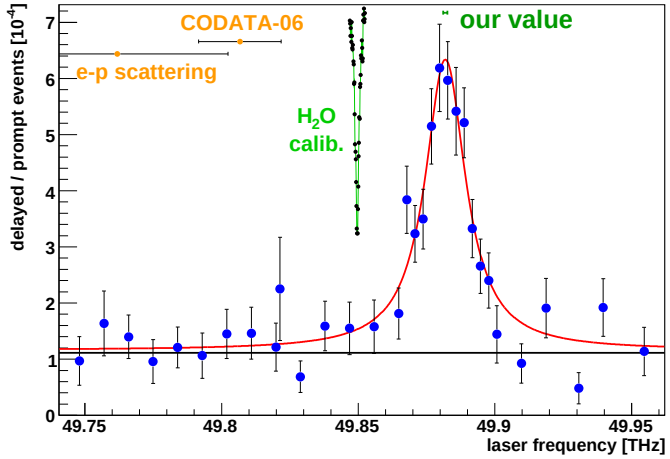

$\mu p(2S^{F=0}_{1/2} - 2P^{F=1}_{3/2})$

(b)

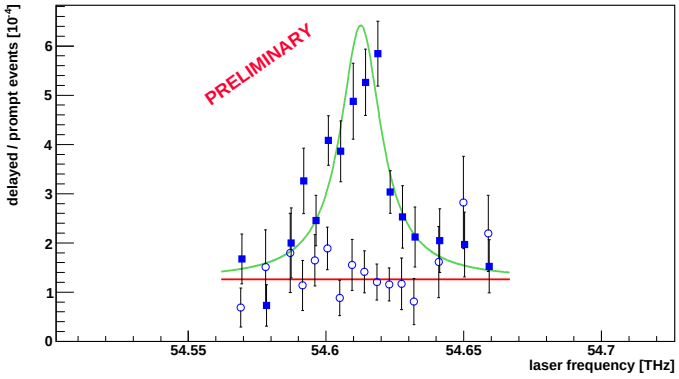

$\mu d(2S^{F=3/2}_{1/2} - 2P^{F=5/2}_{3/2})$

(c)

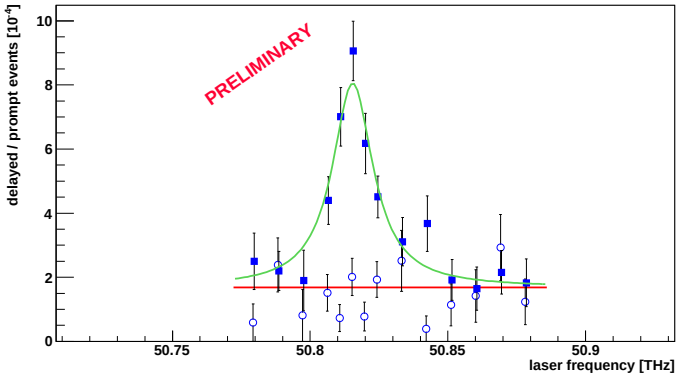

$\mu d(2S^{F=1/2}_{1/2} - 2P^{F=3/2}_{3/2})$

$\mu d(2S^{F=1/2}_{1/2} - 2P^{F=1/2}_{3/2})$

(d)

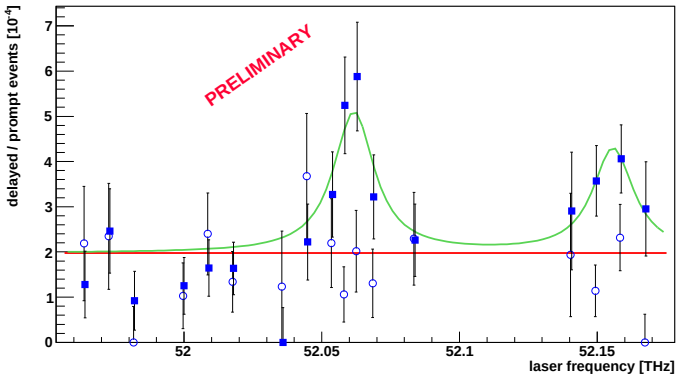

Abbildung 2: Beobachtete Resonanzen in μp und μd. *Die fünf während der 2009-Kampagne gemessenen Resonanzen sind gegen die Frequenz aufgetragen. Der Fokus dieser Arbeit liegt auf der Analyse und den Implikationen der Resonanz (a). Die Resonanzen (b)–(d) verstehen sich als vorläufige online Daten und bedürfen noch einer genauen Analyse und Studie der Systematiken. Deshalb sind deren Positionen nicht endgültig.*

Summary

The subject of this thesis is the first measurement of the $2S - 2P$ Lamb shift in muonic hydrogen (μp). Because of its potential to extract the rms proton charge radius $r_p = \sqrt{\langle r_r^2 \rangle}$, this experiment has already been under discussion for 40 years. Only recent progress in muon beams and laser technology made such a quest feasible. In this project, which has been performed at the proton-accelerator facility of the Paul–Scherrer–Institute in Switzerland, the exotic analogon to the classical Lamb shift in hydrogen has been examined by laser spectroscopy.

Negative muons are produced at a specially developed low-energy muon beam at a rate of $330\,\mathrm{s}^{-1}$ and are stopped in 1 hPa of H_2 gas. In the gas, highly excited μp atoms are formed, most of which promptly cascade to the ground state within ~ 100 ns. Only a fraction of 1.1 % forms μp atoms in the long-lived $2S$ state with a lifetime of 1.0 μs. An elaborate laser system triggered on every incoming muon delivers 0.2 mJ laser pulses at $\lambda \simeq 6\,\mu$m with $500\,\mathrm{s}^{-1}$ repetition rate. The laser illuminates the μp atoms 900 ns after the prompt muon cascade inducing the $2S - 2P$ transition when on resonance. A 1.9 keV K_α X-ray is emitted in the subsequent deexcitation to the $1S$ ground state and is recorded by large area avalanche photodiodes. A resonance line is obtained by scanning the laser frequency and recording the number of laser induced K_α X-rays in the respective time spectra.

For the measured $\mu p(2S^{F=1}_{1/2} - 2P^{F=2}_{3/2})$ transition, two such time spectra accumulated for laser frequencies on and off resonance are shown in Figure 3. The laser induced K_α events are clearly distinguishable from the exponential background. By normalizing the number of

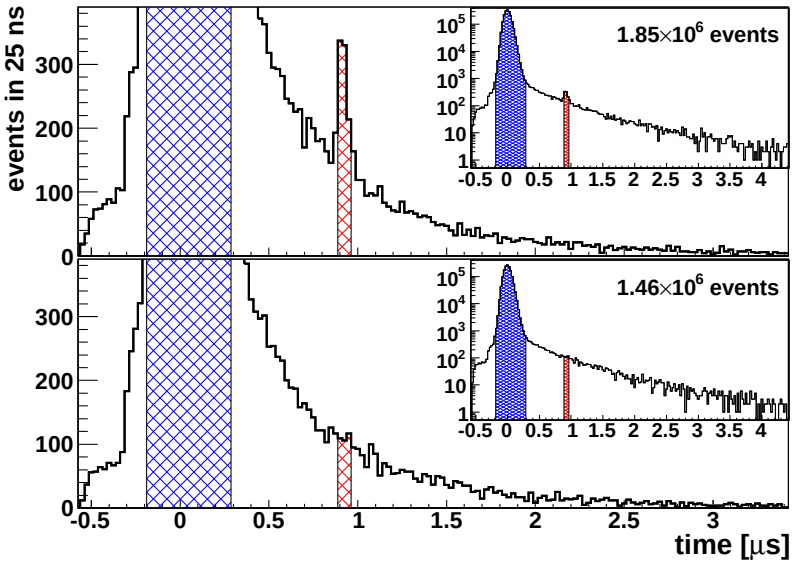

Figure 3: Accumulated time spectra on and off resonance. *Summed X-ray time spectra recorded on resonance (top) and off resonance (bottom) shown in linear and logarithmic scale. The contribution of the prompt X-rays is marked in blue. The laser time window 900 ns after the prompt cascade is indicated in red.*

laser induced K_α events (red) collected for each laser frequency to the number of prompt K_α X-rays (blue) to account for the varying measurement time, the resonance (Figure 4(a)) can be plotted and the transition frequency can be extracted. For the $2S_{1/2}^{F=1} - 2P_{3/2}^{F=2}$ transition in μp, it is given by

$$\nu_{2S-2P} = 49\,881\,695\,(711)\,\mathrm{MHz} \tag{4}$$

with a relative accurcy of 1.4×10^{-5}.

Assuming the correctness of the bound-state QED calculations of the Lamb shift in μp, a new value for the rms proton charge radius r_p can be derived[2]:

$$r_p = 0.84192\,(65)\,\mathrm{fm} \tag{5}$$

This value is $5.0\,\sigma$ smaller, but 10 time more precise than the commonly accepted CODATA value $r_p = 0.8768\,(69)$ fm, which is mostly dependent on hydrogen data and QED calculations.

Using the precisely measured $1S-2S$ transition frequency in hydrogen (relative accuracy of 1.4 parts in 10^{14}) and combining it with our new value of r_p, a new value for the Rydberg constant R_∞ can be derived with a relative accuracy of 1.5 parts in 10^{12}:

$$R_\infty = 10\,973\,731.568\,161\,(16)\,\mathrm{m}^{-1} \tag{6}$$

This is $-110\,\mathrm{kHz/c}$ or $4.9\,\sigma$ away from the CODATA value, but 4.6 times more precise.

The origin of this large discrepancy is yet to be unraveled. It might arise from missing QED terms both in hydrogen or muonic hydrogen, undiscovered errors in some hydrogen spectroscopy experiments, or most intriguingly, be attributed to New Physics.

Beside the $2S_{1/2}^{F=1} - 2P_{3/2}^{F=2}$ transition in μp reported here, four other resonances have been examined in μp and in muonic deuterium (μd), namely the $\mu p(2S_{1/2}^{F=0} - 2P_{3/2}^{F=1})$, the $\mu d(2S_{1/2}^{F=3/2} - 2P_{3/2}^{F=5/2})$, the $\mu d(2S_{1/2}^{F=1/2} - 2P_{3/2}^{F=3/2})$, and the $\mu d(2S_{1/2}^{F=1/2} - 2P_{3/2}^{F=1/2})$ transitions. They still have to be analyzed rigorously, but their preliminary data are presented in Figure 4(b)-(d). Apart from the mentioned improvements on the proton charge radius and the Rydberg constant, one will be able to increase the accuracy of the deuteron charge radius r_d by a factor of 20, provide a new value for the proton magnetic (Zemach) radius (with 3×10^{-2} relative accuracy), extract an experimental value for the Lamb shift independent of the (not well known) Zemach radius, and determine the deuteron polarizability.

[2]The results presented here are slightly more accurate and deviate marginally from the values published in Ref. [1] (f.ex. $r_p = 0.84184\,(67)$ fm) because of the refined data analysis of this thesis.

$\mu p(2S^{F=1}_{1/2} - 2P^{F=2}_{3/2})$

(a)

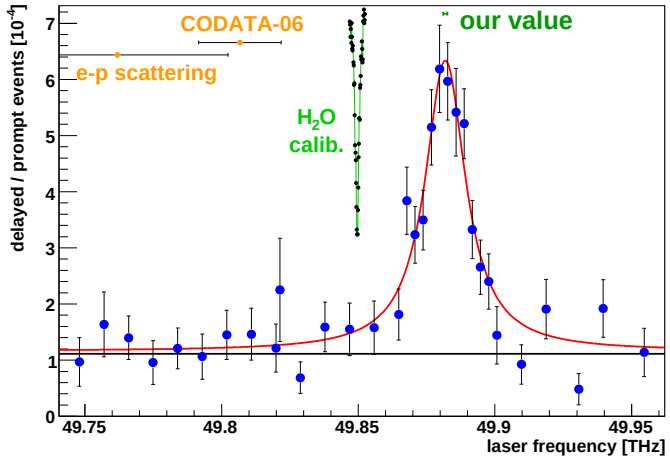

$\mu p(2S^{F=0}_{1/2} - 2P^{F=1}_{3/2})$

(b)

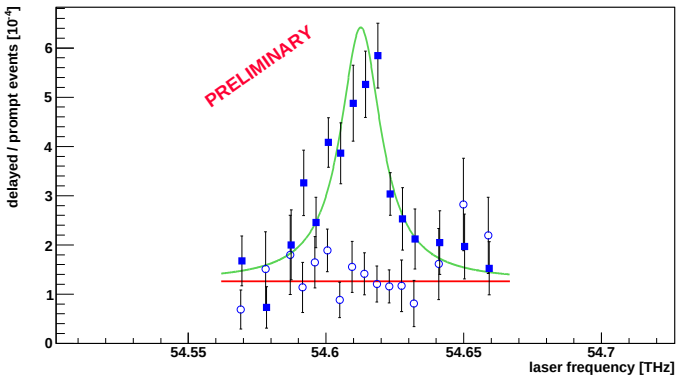

$\mu d(2S^{F=3/2}_{1/2} - 2P^{F=5/2}_{3/2})$

(c)

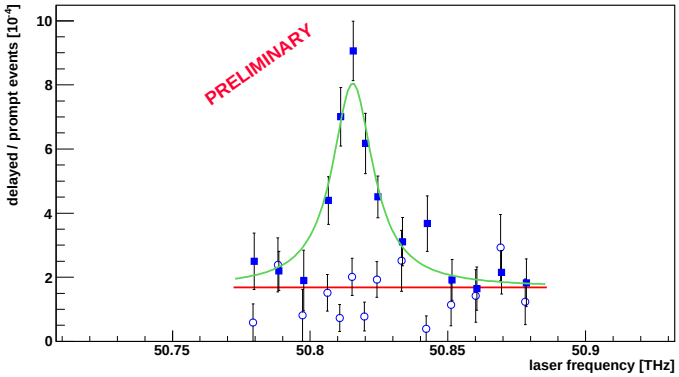

$\mu d(2S^{F=1/2}_{1/2} - 2P^{F=3/2}_{3/2})$

$\mu d(2S^{F=1/2}_{1/2} - 2P^{F=1/2}_{3/2})$

(d)

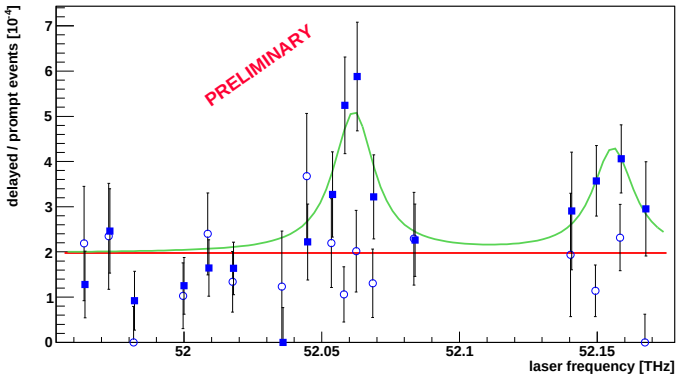

Figure 4: Observed resonances in μp and μd. *The five transitions measured in the 2009-campaign are plotted versus the frequency. The focus of this thesis lies on the analysis and implications of resonance (a). The resonances (b)–(d) represent preliminary online data and are still subject to a rigorous analysis and studies of the systematics. Therefore, their positions are not yet final.*

Contents

List of Figures

List of Tables

Chapter 1

The 2S – 2P Lamb Shift in Muonic Hydrogen

1.1 Introduction

Physics in the 20^{th} century has often been an interplay between the prediction of new phenomena on the theoretical side and their experimental verification in the laboratory. Over the years, and due to the exploding numerical possibilities and, of course, due to the steadily refined experimental ideas and the ever improving equipment, this quest of comparing nature to formulas has reached a level of precision never encountered before.

Within this pursuit, simple atomic systems, mostly a compound of one negatively and one positively charged particle, have served as vastly successful probes of the basic aspects of the laws of physics. It was the extensive investigation of the hydrogen atom in the early part of the 20th century that led to the birth of modern quantum mechanics when Heisenberg reinterpreted the classical picture of kinematics and mechanics in a quantum theoretical way in 1925. Three years later in 1928, Dirac unified the concepts of relativity and quantum mechanics [2]. The discovery of the Lamb shift in atomic hydrogen [3] in 1947 motivated the description of physical processes via quantum field theories.

Since then, many hydrogen-like systems have been considered both experimentally and theoretically, providing a fertile soil for refining our abstract portraiture of Nature's laws: by comparing experimental data to theoretical calculations, predictions can be verified leading to a steadily solidifying fundament of the entire field of physics.

A vivid example for this development is the confirmation of quantum electrodynamics (QED) of bound systems. Prominent QED-tests are manifold, among them the investigations on exotic systems such as muonium [4] or positronium [5] and the g-factor measurements in hydrogen-like oxygen [6] or carbon [7]. The most accurate test-instrument, however, is the absolute frequency measurement of (laser induced) transitions in simple atomic systems. Here, the Doppler-free two-photon spectroscopy

of atomic hydrogen [8,9] serves as the most prosperous instance of the confirmation of fundamental physics.

The $1S-2S$ transition frequency was measured with a spectacular relative uncertainty of $1.4 \cdot 10^{-14}$ [10]. However, the agreement of bound-state QED and experiment was limited to a precision level of a few parts per million. This stems from the fact that a central constant employed in the theoretical QED-calculations, the root mean square (rms) proton charge radius r_p, is independently only known to a 2 % accuracy [11]. To overcome this limitation in testing bound-state QED, our experiment intends to provide a 20 times more accurate independent value for r_p by measuring the $2S-2P$ Lamb shift in muonic hydrogen (μp).

In this thesis, the experiment to measure the Lamb shift in μp at a proton accelerator facility and the method to extract the $2S-2P$ resonance line position is described. For more than forty years, this measurement has been considered one of the fundamental experiments in atomic spectroscopy, but only recent progress in muon beams and laser technology made such an experiment feasible. Here, I report on the first successful measurement of the μp Lamb shift which was performed by our collaboration. The implementations of and the conclusions drawn from the obtained results will also be discussed. The energy difference between the $2S^{F=1}_{1/2}$ and $2P^{F=2}_{3/2}$ states of μp atoms has been determined by means of pulsed laser spectroscopy at wavelengths around 6.01 μm. This transition is chosen because it gives the largest signal of all six allowed optical 2S-2P transitions. All transitions are spectrally well separated and do not influence our measured resonance line. Data has also been taken (but not yet analysed) for another $2S-2P$ transition in μp and three other $2S-2P$ transitions in μd.

1.2 History of the Experiment

Following the measurements of the classical Lamb shift [3] in 1947 and of the magnetic moment of the electron in 1948 [12], bound state QED started developing. Looking for possible test grounds for this relatively new theory and triggered by the latest development in laser technology, Vernon Hughes (Yale University, USA), Val L. Teledgi (University of Chicago, USA), and Emilio Zavattini (CERN) started to consider the measurement of the $2S-2P$ energy difference in μp in the late 1960s [13] to test the vacuum polarization terms of QED.

A couple of years later, in 1969, the theoretician A. DiGiacomo (CERN) provided the first accurate QED-calculation of the $2S-2P$ energy difference in μp [14] at the instigation of Zavattini. Also, the principle of an experiment to measure this energy difference and the laser wavelength needed (6 μm) were discussed at that time.

In 1971, Vernon Hughes submitted a proposal to the NEVIS accelerator at Columbia University (USA) to measure the $2S$ lifetime in μp, in which the Lamb shift experiment was discussed. Although most of the processes involved in the $2S$ lifetime were qualitatively known, some crucial details about the long-lived $2S$ component were only

discovered by our group three decades later [15, 16]. Between 1976 and 1982, research continued at ETH Zürich and SIN (later PSI) in order to develop a suitable infra-red laser. It became clear in 1982 that the existence of the long-lived $2S$ state in μp could not be verified experimentally, and that, with the technology of that time, the required laser was not feasible. Furthermore, from 1980 on, hardly anybody still believed that QED could be violated on such a fundamental level. As a result, and after some major restructuring at SIN, the interest and the enthusiasm for the Lamb shift experiment in μp faded, until the aim of this experiment shifted from testing vacuum polarization terms towards the determination of the proton charge radius. This was motivated by the tremendous improvementt achieved in hydrogen spectroscopy (in particular the $1S-2S$ measurements), which called for a new independent and a more accurate value of the proton charge radius, required to compare their results to QED theory. In the 1990s, the μp Lamb shift experiment was brought back into the realm of possibility when Franz Kottmann, Leo Simons, and David Taqqu realized the first low-energy muon beamline.

A newly founded collaboration (consisting of $\sim$ 25 members of PSI, ETH, MPQ, LKB/Paris, Universidade de Coimbra/Portugal, Yale University, Princeton University, Université de Fribourg and others) successfully submitted a detailed proposal to PSI in 1998 to measure the Lamb shift in muonic hydrogen by means of laser spectroscopy. In 2002, a first engineering-run with the complete system working took place. The first data-taking run in 2003 was successful but did not yield a resonance line. An excimer-dye pumped laser system was employed which turned out to have a too low repetition rate and to be too slow. A new thin disk laser replacing the eximer-dye pump lasers was therefore developed at the University of Stuttgart by our colleagues A. Antognini and K. Schuhmann.

In the middle of the preparations for the next run, I joined the collaboration as a Ph.D. student in September 2005. The next beam time was unfortunately only scheduled for spring 2007, the entire laser system was transported to MPQ, and I got involved in the optimization of the Titanium:sapphire laser system and the infra-red laser system. Together with R. Pohl, I developed and tested new highly reflective mirror coatings for the target cavity, a crucial part of our experiment. Shortly before the run in 2007, our laser was united with the thin disk pumping laser at PSI. During the several months of beamtime, all hands were needed on deck and I was involved in most of the parts of the entire experiment especially during setup. The emphasis of my work during data-aquisition was put on operating the laser system, in particular the Titanium:sapphire subsystem. In the second half of my time as a Ph.D. student, starting after the 2007-run, I focussed on the analysis of the recorded data. For this, analysis techniques were refined, and tools and macros developed to learn about the properties and the behaviour of our data and, of course, to find a resonance line.

For the last and finally successful run during the summer of 2009, I was again involved in all aspects of the experiment, namely setup, testing, and improving of the

muon beam apparatus, the laser system, the detectors and their electronics, and the computer system. During the normal operation of this four-month-long beamtime, I concentrated on the data aquisition system and the online data analysis. After we had finally discovered the resonance lines reported here, I performed a rigorous data analysis which led to intriguing insights on the physics hidden in our data. This part of my work is presented in the Appendix of this thesis.

1.3 Muonic Hydrogen Energy Levels

In an elementary picture, the motion of an orbiting particle (in our case a negatively charged muon μ^-) in a simple hydrogen-like system (one orbiting particle bound to a simple nucleus, e.g. a proton) can be extracted from the well known Schrödinger equation of the hydrogen atom (see, e.g. Ref. [17]).

Looking a bit closer, one discovers that the relativistic energy $E = \sqrt{p^2c^2 + m^2c^4}$ of the orbiting muon (depending on its momentum and its spin) has to be considered. This leads to the formulation of the Dirac equation (e.g. Ref. [18]). Assuming an infinitely heavy nucleus with static Coulomb potential and charge Ze, one can retrieve an exact solution of the Dirac equation. The energy eigenvalues are given by [18, 19]:

$$E_{nj} = mc^2\, f(n,j)\,, \tag{1.1}$$

with

$$f(n,j) = \left[1 + \frac{(Z\alpha)^2}{\left(n - j - \frac{1}{2} + \sqrt{\left(j+\frac{1}{2}\right)^2 - (Z\alpha)^2}\right)^2}\right]^{-\frac{1}{2}} \tag{1.2}$$

Here, n is the principal quantum number, j is the sum of orbital and angular momentum of the muon, m is the muon mass, and α is the fine structure constant. For every level n, spin-orbit coupling introduces n different sublevels of the fine structure related to the different values of the angular momentum j. The function f can be expanded in $Z\alpha$ [20] so that

$$\begin{aligned} E_{nj} \simeq\; & mc^2 - mc^2\,\frac{(Z\alpha)^2}{2n^2} - mc^2\,\frac{(Z\alpha)^4}{2n^3}\left(\frac{1}{j+\frac{1}{2}} - \frac{3}{4n}\right) \\ & - mc^2\,\frac{(Z\alpha)^6}{8n^3}\left[\frac{1}{(j+\frac{1}{2})^3} + \frac{3}{n(j+\frac{1}{2})^2} + \frac{5}{2n^3} - \frac{6}{n^2(j+\frac{1}{2})}\right] + \ldots \end{aligned} \tag{1.3}$$

The first term in this expansion represents the relativistic mass energy. The second term describes the Bohr energy, i.e. the solution $E_n = -R_\infty\, hc\,\frac{Z^2}{n^2} = -mc^2\,\frac{(Z\alpha)^2}{2n^2}$ (R_∞ is the Rydberg constant) to the stationary Schrödinger equation of the hydrogen-like atom. Comparing alike terms of Equation (1.3) to those of the relativistic energy expansion

$$E = \sqrt{p^2c^2 + m^2c^4} \simeq mc^2 + \frac{p^2}{2m} - \frac{p^4}{8m^3} + \ldots\,, \tag{1.4}$$

reveals that the expansion in powers of $p^2/2m^2$ corresponds to an expansion in $(Z\alpha)^2$ so that relativistic corrections are given by terms proportional to even powers of $Z\alpha$.

Equation (1.3) does not yet consider the finite Mass M of the nucleus. This relativistic two-body problem can be expressed by the Bethe-Salpeter equation [21]. By truncating its sum over all interaction kernels and keeping only the kernel which describes the dominant binding energies between the two particles, one can construct an effective Dirac equation with an effective Dirac Hamiltonian H^{Dirac}:

$$H^{\mathrm{Dirac}} = \alpha \cdot (\mathbf{p} - e\mathbf{A}) + \beta m + V + \frac{\mathbf{p^2}}{2M}\,. \tag{1.5}$$

It is obtained by retaining only the kernel for the one-photon exchange between muon and nucleus [22]. In Equation (1.5), the term $\mathbf{p}^2/2M$ describes the kinetic energy of the nucleus. $(V, \mathbf{A})$ is the four-potential caused by the muon and the proton positions (with the Coulomb potential $V = -Z\alpha/r$ and the Breit potential $\mathbf{A}$). In this consideration, the proton is still considered to be spin-less.

Taking into account the most important corrections related to the finite mass M of the nucleus, Ref. [20] derives a general expression for the atomic energy levels:

$$\begin{aligned} E_{njl} = {} & mc^2 + Mc^2 + (f(n,j) - 1)\, m_r c^2 \\ & - (f(n,j) - 1)^2 \frac{m_r^2 c^2}{2(m+M)} + \frac{1 - \delta_{l0}}{(j + 1/2)(2l+1)} \frac{(Z\alpha)^4 m_r^3 c^2}{2n^3 M^2}\,. \end{aligned} \tag{1.6}$$

While the third term describes the Dirac energy of a static Coulomb source (corrected by the reduced mass $m_r = \frac{m\,M}{m+M}$), the last two terms relate to recoil corrections. Furthermore, the last term is responsible for a small breaking of the l degeneracy of the Dirac eigenstates.

1.4 The Lamb Shift in Muonic Hydrogen

In 1947, Lamb and Retherford [3] discovered that the energy levels of the same (n, j) quantum number are, in fact, not degenerate as the Dirac energies in Equation (1.6) would suggest. Initially, they measured the $2S_{1/2} - 2P_{1/2}$ energy difference in ordinary hydrogen to be 1000 MHz. Note that this energy difference cannot be attributed to the l dependence term in Eq. (1.6) (only 2 kHz in hydrogen).

This discrepancy initialized the development of QED. It became common to use the term *Lamb shift* for any deviation from the energies predicted by the Dirac equation partially corrected for the finite mass of the nucleus. The Lamb shift L_{njlF} can also be defined as the sum of all contributions to the energy levels beyond the first four terms in Equation (1.6) including the hyperfine splitting (HFS) E^{HFS}_{njlF}:

$$\begin{aligned} E^{\mathrm{total}}_{njlF} &= mc^2 + Mc^2 + (f(n,j) - 1)\, m_r c^2 \\ &- (f(n,j) - 1)^2 \frac{m_r^2 c^2}{2(m+M)} + L_{njlF}. \end{aligned} \tag{1.7}$$

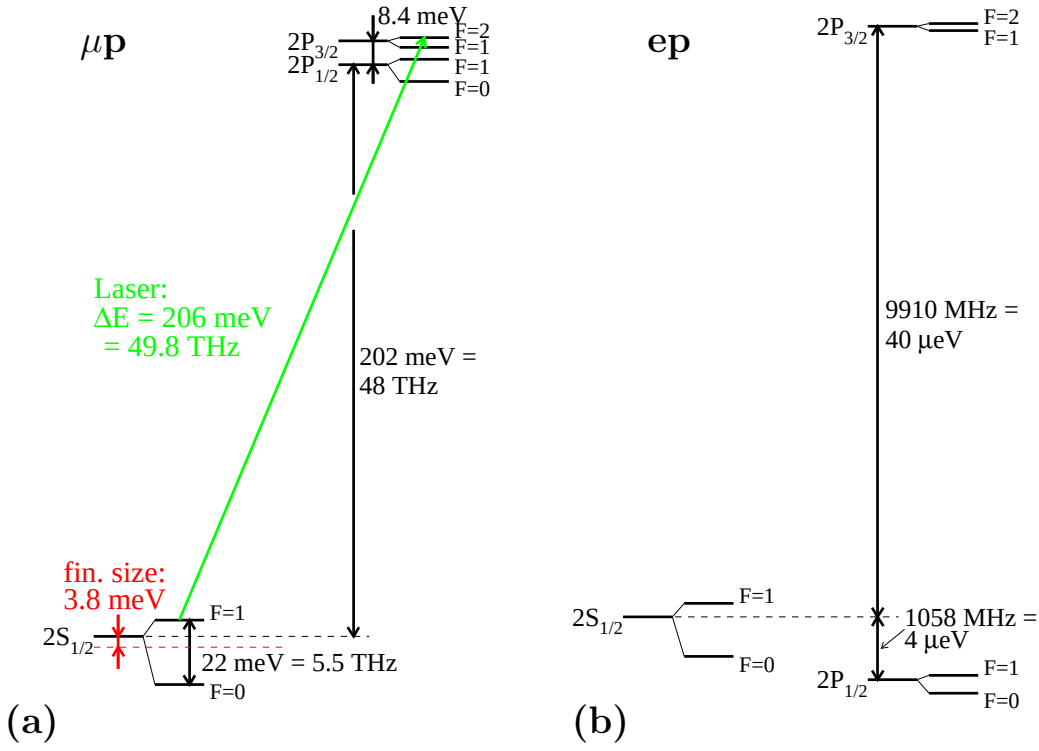

Figure 1.1: Level Scheme of Muonic and Electronic Hydrogen. ***(a)*** *The Lamb shift of muonic hydrogen is dominated by vacuum polarization which shifts the $2S_{1/2}$ level downwards. The finite size effect is as big as 2 %.* ***(b)*** *The level scheme for hydrogen shows that the Lamb shift is much smaller. Self energy effects dominate this level scheme and shift the $2S_{1/2}$ level upwards. Note the different scale of the two schemes.*

This equation describes the total binding energy of an atomic state characterized by the quantum numbers n, j, l, F (with the total angular momentum F). Usually, energy differences are measured so that the first two terms cancel out and only the remaining ones have to be considered.

1.5 The $\Delta E(2P_{3/2}^{F=2} - 2S_{1/2}^{F=1})$ Energy Difference

In the experiment reported here, the $\Delta E(2P_{3/2}^{F=2} - 2S_{1/2}^{F=1})$ Lamb Shift in μp (the exotic analogon to the classical Lamb shift [3]) has been measured. It is depicted in Figure 1.1(a). Note that the S levels are shifted downwards. Compared to the Lamb shift in ordinary hydrogen (Fig. 1.1(b)), it is four orders of magnitude larger. For clarity, the two level schemes are not drawn to scale. In contrast to electronic hydrogen (whose Lamb shift is dominated by self energy contributions) the largest contribution to the Lamb shift in μp stems from vacuum polarization (VP) effects. Corrections due to the finite size of the proton account to as much as 2 % making this transition predestined to deduce the proton charge radius from it.

The contributions to the Lamb shift $\Delta E^{\mathrm{LS}} \equiv \Delta E(2P_{1/2} - 2S_{1/2})$ in μp have been compiled and re-checked by P. Indelicato. A detailed treatment including all necessary references is given in Appendix A. Here, only the final equations and a summarizing compilation of all contributions to the Lamb shift are reproduced.

All contributions to ΔE^{LS} that are **independent** on the proton charge radius are presented in Table 1.2, whereas the contributions **depending** on the radius are listed in Table 1.3. For the $2S_{1/2} - 2P_{1/2}$ Lamb shift, we get according to Equation (A.1)

$$\Delta E^{\mathrm{LS}}/\mathrm{meV} = 206.0573\,(45) - 5.2262\,r_p^2/\mathrm{fm}^2 + 0.0347\,r_p^3/\mathrm{fm}^3\,, \tag{1.8}$$

where r_p is the mean spherical charge radius of the proton (cf. Section 1.6) given in fm. The uncertainty in the constant term is dominated by the proton polarizability contribution (# 25 in Table 1.2).

The origins of the splittings stemming from the fine structure (ΔE^{FS}), the $2S$ HFS ($\Delta E^{\mathrm{HFS}}_{2S}$), and the $2P_{3/2}$ HFS ($\Delta E^{\mathrm{HFS}}_{2P_{3/2}}$) are given in Appendix A and are quoted to be

$$\begin{aligned} \Delta E^{\mathrm{FS}} &= 8.352082\,\mathrm{meV}, \\ \Delta E^{\mathrm{HFS}}_{2S} &= 22.8148\,(78)\,\mathrm{meV}, \text{and} \\ \Delta E^{\mathrm{HFS}}_{2P_{3/2}} &= 3.392588\,\mathrm{meV}. \end{aligned} \tag{1.9}$$

Note that $\Delta E^{\mathrm{HFS}}_{2S}$ depends on the Zemach radius r_Z. It scatters widely and, therefore, contributes to as much as 0.0060 meV of above's uncertainty. Table 1.1 is a compilation of values for the Zemach radius. Here, we use $r_Z = 1.022\,\mathrm{fm}$ [23].

From this, the level energies $E_{2S^{F=1}_{1/2}}$ and $E_{2P^{F=2}_{3/2}}$ can be calculated according to Equation (A.5) so that, with r_p given in fm, the transition energy for the measured $2S^{F=1}_{1/2} - 2P^{F=2}_{3/2}$ transition in μp is evaluated to be

$$\Delta E(2P^{F=2}_{3/2} - 2S^{F=1}_{1/2})/\mathrm{meV} = 209.9779\,(49) - 5.2262\,r_p^2/\mathrm{fm}^2 + 0.0347\,r_p^3/\mathrm{fm}^3\,. \tag{1.10}$$

Method	**Reference**	**Zemach r_Z [fm]**	**Magnetic r_m [fm]**
Proton-electron scattering	[24]	1.0466	0.8309
Hydrogen HFS	[25]	1.045 ± 0.016	
Hydrogen, Proton-electron scattering	[26]	1.016 ± 0.016	
Proton-electron scattering	[27]	1.086 ± 0.012	
Proton-electron scattering (CMR)	[28]	1.072	0.854 ± 0.005
Proton-electron scattering (CMR)	[28]	1.076	$0.850\ ^{-\ 0.007}_{+\ 0.002}$
Hydrogen HFS	[29]	1.037 ± 0.016	

Table 1.1: Zemach Radius Values. *Different values for the Zemach radius r_Z obtained using proton electron scattering and the hydrogen HFS. The Zemach radius from Ref. [28] is obtained using the charge and magnetic radii (CMR), assuming different theorectical models [30].*

#	Contribution		Our selection		Pachucki [31–33]		Borie [34]	
		Ref.	Value	Unc.	Value	Unc.	Value	Unc.
1	NR One loop electron VP	[31, 32]			205.0074			
2	Relativistic correction (corrected)	[31–34]			0.0169			
3	Relativistic one loop VP	[34]	205.0282				205.0282	
4	NR two-loop electron VP	[14, 34]	1.5081		1.5079		1.5081	
5	Polarization insertion in two Coulomb lines	[31, 32, 34]	0.1509		0.1509		0.1510	
6	NR three-loop electron VP	[35]	0.00529					
7	Polarisation insertion in two and three Coulomb lines (corrected)	[35, 36]	0.00223					
8	Three-loop VP (total, uncorrected)				0.0076		0.00761	
9	Wichmann-Kroll	[34, 37, 38]	−0.00103				−0.00103	
10	Light by light electron loop contribution (Virtual Delbrück scattering)	[39]	0.00135	0.00135			0.00135	0.00015
11	Radiative photon and electron polarization in the Coulomb line $\alpha^2(Z\alpha)^4$	[31, 32]	−0.00500	0.0010	−0.006	0.001	−0.005	
12	Electron loop in the radiative photon of order $\alpha^2(Z\alpha)^4$	[40–42]	−0.00150					
13	Mixed electron and muon loops	[43]	0.00007				0.00007	
14	Hadronic polarization $\alpha(Z\alpha)^4 m_r$	[44–46]	0.01077	0.00038	0.0113	0.0003	0.011	0.002
15	Hadronic polarization $\alpha(Z\alpha)^5 m_r$	[45, 46]	0.000047					
16	Hadronic polarization in the radiative photon $\alpha^2(Z\alpha)^4 m_r$	[45, 46]	−0.000015					
17	Recoil contribution	[47]	0.05750		0.0575		0.0575	
18	Recoil finite size	[34]	0.01300	0.001			0.013	0.001
19	Recoil correction to VP	[34]	−0.00410				−0.0041	
20	Radiative corrections of order $\alpha^n(Z\alpha)^k m_r$	[19, 32]	−0.66770		−0.6677		−0.66788	
21	Muon Lamb shift 4th order	[34]	−0.00169				−0.00169	
22	Recoil corrections of order $\alpha(Z\alpha)^5 \frac{m}{M} m_r$	[19, 32, 34, 39]	−0.04497		−0.045		−0.04497	
23	Recoil of order α^6	[32]	0.00030		0.0003			
24	Radiative recoil corrections of order $\alpha(Z\alpha)^n \frac{m}{M} m_r$	[19, 31, 32]	−0.00960		−0.0099		−0.0096	
25	Nuclear structure correction of order $(Z\alpha)^5$ (Proton polarizability contribution)	[32, 34, 45, 48]	0.015	0.004	0.012	0.002	0.015	0.004
26	Polarization operator induced correction to nuclear polarizability $\alpha(Z\alpha)^5 m_r$	[46]	0.00019					
27	Radiative photon induced correction to nuclear polarizability $\alpha(Z\alpha)^5 m_r$	[46]	−0.00001					
	Sum		206.0573	0.0045	206.0432	0.0023	206.05856	0.0046

Table 1.2: Radius-Independent Contributions to the Lamb Shift. *All known radius-independent contributions to the Lamb shift in μp from different authors, and the one we selected. We follow the nomenclature of Eides et al. [19] Table 7.1. Item # 8 in Refs. [32, 34] is the sum of items # 6 and # 7, without the recent correction from Ref. [36]. The error of # 10 has been increased to 100 % to account for a remark in Ref. [19]. Values are in meV and the uncertainties have been added in quadrature. NR stands for non-relativistic, VP for vacuum polarization.*

Contribution	Ref.	Our Selection		Pachucki [32]	Borie [34]
Leading nuclear size contribution	[49]	−5.19745	$< r_p^2 >$	−5.1974	−5.1971
Radiative corrections to nuclear finite size effect	[32, 49]	−0.0275	$< r_p^2 >$	−0.0282	−0.0273
Nuclear size correction of order $(Z\alpha)^6 < r_p^2 >$	[31, 50–52]	−0.001243	$< r_p^2 >$		
Total $< r_p^2 >$ contribution		−5.22619	$< r_p^2 >$	−5.2256	−5.2244
Nuclear size correction of order $(Z\alpha)^5$	[31, 32]	0.0347	$< r_p^3 >$	0.0363	0.0347

Table 1.3: Radius-Dependent Contributions to the Lamb Shift. *All relevant radius-dependent contributions as summarized in Eides et al. [19], compared to Refs. [32, 34]. The values are given in meV and the proton charge radii in fm.*

1.6 The Proton Charge Radius $\mathbf{r_p}$

The proton is the simplest stable hadronic system and, as a basic constituent of matter, a profound knowledge of its properties is of fundamental interest [53–58]. One of its few accessible properties is its rms charge radius r_p, whose value is the result of quark interactions at low energy. The calculation of this parameter is one of the aims of lattice quantum chromodynamics [59].

One has to be careful which exact definition of the proton radius is applied [60]. In the Breit frame, the rms proton charge radius is defined by [61]

$$\langle r^2 \rangle_{\mathrm{ch}} = \int d\mathbf{r}\, r^2 \rho(\mathbf{r}). \tag{1.11}$$

Here, ρ is the 0^{th} component of the four-vector j^μ, as defined, f.ex., in Ref. [18]. The proton radius can also be described in terms of the Sachs charge and magnetic form factors G_E and G_M [62] or in terms of the not so common form factors $\widetilde{G}_E$ and $\widetilde{G}_M$ (see, e.g. [61]):

$$\begin{aligned} \langle r^2 \rangle_{\mathrm{ch}} &= -6\widetilde{G}'_E(0) \\ \langle r^2 \rangle_{\mathrm{E}} &= -6G'_E(0). \end{aligned} \tag{1.12}$$

The derivative in d/dQ^2 is represented by the prime. Note that $\langle r^2 \rangle_{\mathrm{E}}^{1/2}$ is often called the proton radius [63]. Both definitions are formally identical in the non-relativistic limit and are related through:

$$\langle r^2 \rangle_{\mathrm{ch}} = \langle r^2 \rangle_{\mathrm{E}} + \frac{3}{4M^2}. \tag{1.13}$$

The quantity $\langle r^2 \rangle_{DF} \equiv \frac{3}{4M^2}$ is known as the Darwin-Foldy term [18]. By convention, this term is usually considered to be a kinematic factor and is, therefore, not part of the proton structure.

The muonic hydrogen energy levels as described by Equation (1.6) contain a contribution for the S levels.

$$\frac{(Z\alpha)^4 m_r^3}{2n^3 M^2} \delta_{l0}\,. \tag{1.14}$$

This has to be compared to the leading nuclear size correction [49]:

$$\frac{2(Z\alpha)^4 m_r^3}{3n^3} \langle r^2 \rangle \delta_{l0}\,. \tag{1.15}$$

The term $\langle r^2 \rangle$ in Equation (1.15) corresponds to $\frac{3}{4M^2}$ in Equation (1.14). This implies that the Darwin-Foldy term is, by convention, attributed to the recoil correction and not to the finite size correction.

Therefore, the proton charge radius is defined consistently in electron scattering experiments as well as in QED considerations of the atomic system: both neglect the Darwin-Foldy term. Hence, r_p, which is used throughout this thesis, is defined to be

$$r_p^2 \equiv \langle r^2 \rangle_{\mathrm{E}} = \langle r^2 \rangle_{\mathrm{ch}} - \frac{3}{4M^2}\,. \tag{1.16}$$

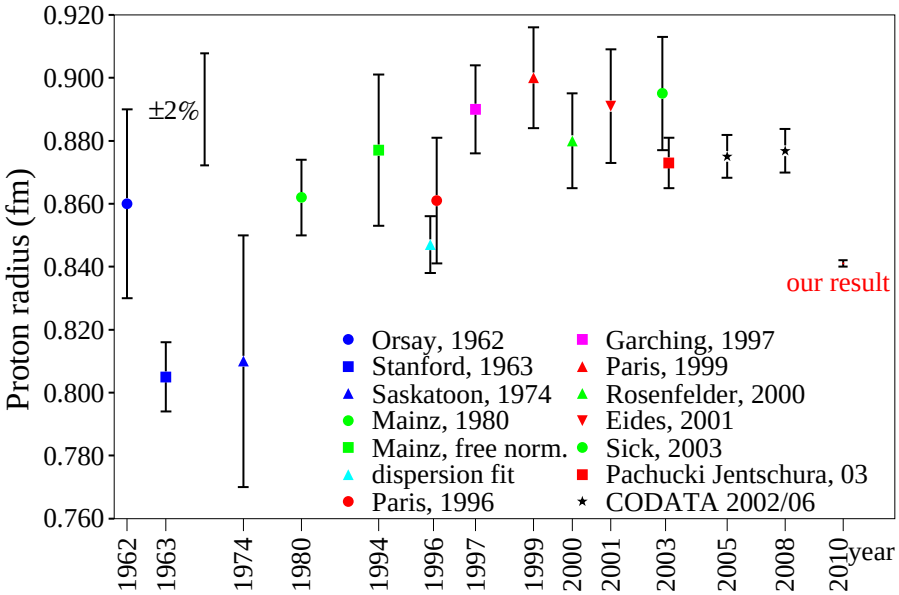

Figure 1.2: Temporal Development of the Proton Radius. *The temporal development of the proton radius over the 50 years is shown. Blue and green markers relate to data obtained from electron scattering [11, 63–69]. Values inferred from hydrogen experiments are represented by magenta and red markers [39, 70–74]. Black stars show the CODATA least squares adjustment. The result obtained from this project is indicated as well (cf. Sect. 4.5).*

The current knowledge of r_p is not very precise. It stems mainly from low energy electron scattering in hydrogen targets, a traditional method for obtaining nuclear radii. However, the experiments are rather difficult to perform and to analyze: the analysis converts the scattering cross section extrapolated to low momentum transfer into a value for r_p. As pointed out in Ref. [75], there are normalization problems causing the inconsistency of the results which have been published during the last 50 years [11, 63–69]. The values obtained from electron scattering range from 0.805 fm to 0.895 fm with a relative accuracy on the order of only 3 % (cf. Figure 1.2).

Another source of information on the proton charge radius stems from the finite size effect on the atomic binding energy in electronic hydrogen (ep) where it affects the Lamb shift on a level of 1.4×10^{-4}. The precisely measured Lamb shift (e.g. Refs. [8, 10, 70–72]) together with theorecital calculations of the QED contributions results in an accuracy of 1–2 %.

Global adjustments performed regularly by the Committee on Data for Science and Technology (CODATA) use all data concerning the fundamental constants available worldwide and perform a least square analysis to obain an accurate value for r_p. The CODATA 2006 adjustment [76] determines r_p with a relative accuracy of 7.8×10^{-3} to be:

$$r_p(\text{CODATA 2006}) = 0.8768\,(69)\,\text{fm}. \tag{1.17}$$

This value stems mostly from hydrogen and QED calculations. To test bound-state

QED in electronic hydrogen, an independent value of the r_p is required. The only available independent value is the one stemming from electron scattering, as discussed above. Hence, a further independent method to deduce r_p is mandatory. This motivates the μp Lamb shift spectroscopy experiment. It has provided another independent value for the proton radius with more than an order of magnitude higher precision (cf. Section 4.5). A temporal development of the value of the proton radius is shown in Figure 1.2.

1.7 The Rydberg Constant R_∞

Having determined a new value for the proton radius, we can also provide an updated value of the Rydberg Constant R_∞ using bound-state QED in electronic hydrogen. Following closely Ref. [77], this section explains briefly how this can be achieved.

In the simple Bohr model, the energy E_n of the hydrogen atomic levels only depends on the principal quantum number n:

$$E_n = -\frac{hcR_\infty}{n^2}\,. \tag{1.18}$$

The Rydberg constant R_∞ is a function of several fundamental constants and related to the fine structure constant α, the speed of light c, the Planck constant h, and the electron mass m_e through

$$R_\infty = \frac{\alpha^2 m_e c}{2h}. \tag{1.19}$$

In a more elaborate treatment, the hydrogen energy levels (similar to muonic hydrogen, cf. Equation (1.6)) can be expressed by the sum of three terms

$$E_{njl} = E_{nj}^{\mathrm{Dirac}} + E_n^{\mathrm{Recoil}} + L_{njl} \tag{1.20}$$

Both the Dirac energy E_{nj}^{Dirac} and the first relativistic recoil correction E_n^{Recoil} are exactly known functions of R_∞. The Lamb shift L_{njl} takes into account all known corrections including QED corrections, other relativistic corrections due to the recoil of the proton and effects of the proton charge distribution [19]. Equation (1.20) can thus be written as

$$E_{njl} = a_{nj} hcR_\infty + L_{njl} \tag{1.21}$$

where a_{nj} is an exactly known function of α and m_e/m_p. It is approximately given by the Bohr model (Eq. (1.18)) as $a_{nj} \simeq -1/n^2$. The $1S-2S$ frequency in ep can then be determined to be

$$\begin{aligned}\nu_{1S-2S} &= (a_{2,1/2} - a_{1,1/2})cR_\infty + (L_{2S_{1/2}} - L_{1S_{1/2}})/h \\ &\simeq \frac{3}{4}cR_\infty + (L_{2S_{1/2}} - L_{1S_{1/2}})/h\end{aligned} \tag{1.22}$$

The absolute experimental uncertainty of the centroid frequency ν_{1S-2S} is 34 Hz [10,76] but, up to now, the Lamb shift difference $L_{2S_{1/2}} - L_{1S_{1/2}}$ could only be calculated

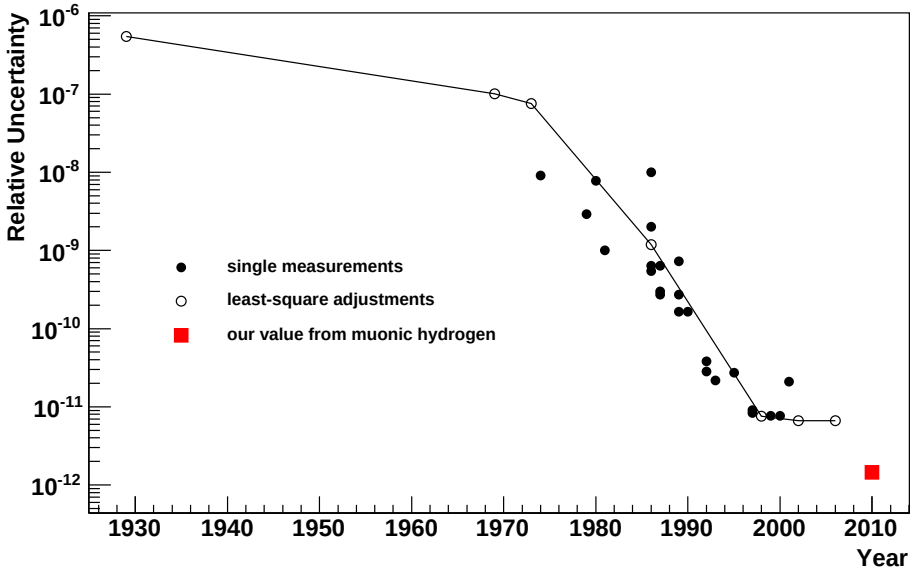

Figure 1.3: Relative Uncertainty of the Rydberg Constant. *This plot shows the temporal development of the fractional uncertainty of the Rydberg constant R_∞ over the past 80 years. Full circles stem from single measurements, empty circles represent least square adjustments. A new value for R_∞ with a relative uncertainty of 1.46×10^{-12} is obtained from our experiment.*

with an uncertainty of 44 kHz [77] because of the uncertainty of the proton radius r_p. Consequently, using just hydrogen $1S - 2S$, R_∞ could only be determined with a relative uncertainty of 1.8×10^{-11}. A more accurate value for R_∞ can be deduced from Equation (1.22) when one uses the new, more accurately determined value for r_p obtained from our experiment (cf. Section 4.5).

In addition to this simplified approach, the Rydberg constant can also be established through a least squares adjustment using all available hydrogen data with the values for α and m_e/m_p being given a priori [9]. Delivering the most accurate value, a global adjustment with the data concerning all fundamental constants performed by CODATA results in a relative uncertainty of 6.6×10^{-12} [76]:

$$R_\infty(\text{CODATA 2006}) = 10\,973\,731.568\,527\,(73)\,\text{m}^{-1} \tag{1.23}$$

Chapter 2

Experiment

In the experiment presented here, we have measured the energy difference between the $2S_{1/2}^{F=1} - 2P_{3/2}^{F=2}$ atomic levels in muonic hydrogen (μp), a two-body compound of a proton and a negatively charged muon [78]. During the 2009 beam-time, other transitions, namely the $2S_{1/2}^{F=0} - 2P_{3/2}^{F=1}$ in μp and the $2S_{1/2}^{F=3/2} - 2P_{3/2}^{F=5/2}$, the $2S_{1/2}^{F=1/2} - 2P_{3/2}^{F=3/2}$, and the $2S_{1/2}^{F=1/2} - 2P_{3/2}^{F=1/2}$ in μd were examined as well. However, this thesis will focus on the first resonance in μp. The resonance lines of the other transitions will only be mentioned briefly in Section 4.6 on the basis of the online analysis.

The Lamb shift experiment is conducted at the proton accelerator of the Paul Scherrer Institute (PSI) in Switzerland[1]. Here, a proton beam is accelerated to 2 mA at 590 MeV/c and collides with a 40 mm thick rotating-wheel (1 Hz) carbon target. Our experiment makes use of the secondary particles emitted through the πE5 port [79], a low momentum (10–120 MeV/c) pion and muon beam line looking at the target at an angle of 175 ° with respect to the proton beam. This is by far the most intense low-energy meson beam in the world.

Section 2.1 offers a brief overview of the principle of the experiment. After that, the apparatus will be covered: A specially designed muon beam line that captures, decelerates and processes the pions and muons in a cyclotron trap, a muon extraction channel, and a target solenoid have been developed for this experiment and are described in Section 2.2. While Section 2.3 presents the laser system employed to produce laser pulses to drive the atomic transition, Section 2.4 introduces the electronics and the data aquisition system needed to read out a large number of detectors and store the data in an appropriate manner.

2.1 Principle

The principle of the experiment is to stop low-energy muons in dilute hydrogen gas, form muonic hydrogen in the $2S$ state and, delayed with respect to the formation time of the muonic atom, drive the $2S - 2P$ atomic transition by means of an infra-red laser

[1] Paul Scherrer Institute, 5232 Villigen PSI, Switzerland, `http://www.psi.ch`

at 6 μm. The emission of 1.9 keV K_α X-rays during the instantaneous decay of the $2P$ state to the ground state serves as a signature for the induced transition.

Slow negative muons are decelerated in low-pressure (1.0 hPa) hydrogen (H_2) gas before they are captured and $\mu^- p$ atoms in highly excited states ($n \approx 14$) are formed [80–82]. At this principle quantum number, the overlap of muonic and electronic wave functions is maximal and n can be estimated from $n \approx \sqrt{m_r^{\mu p}/m_r^{ep}} \approx 14$, with $m_r^{\mu p}$ and m_r^{ep} being the reduced masses of the μp and the H atom. Through a series of different de-excitation processes (see, e.g. Refs. [80, 83]), most of the $\mu^- p$ atoms quickly cascade down to the $1S$ ground state, thereby emitting a *prompt* K-line X-ray. For 0.6 hPa, the cascade time has been determined to be $T_{cas}^{\mu p} = (37 \pm 5)$ ns [84].

At 1.0 hPa, only a fraction $\epsilon_{2S} = (2.76 \pm 0.17)\%$ of the μp atoms reaches the $2S$ state. This can be extracted from an interpolation from $2S$ population data taken from Refs. [85–87] (see also Fig. G.2 in Ref. [88]). In the absence of collisions, only two-photon transitions to the ground state could de-excite the μp atom. Since this rate is $1.5 \times 10^3\,s^{-1}$ [89] and therefore negligibly small compared to the muon decay rate of $4.6 \times 10^5\,s^{-1}$ (corresponding to the free muon lifetime $\tau_\mu = 2.197\,\mu$s), the $\mu p(2S)$ lifetime is primarily given by the muon lifetime.

In a gaseous environment, however, the behaviour of the $\mu p(2S)$ depends critically on its kinetic energy. Atoms with kinetic energies above the $2S-2P$ transition energy of 0.2 eV in the center-of-mass system (corresponding to 0.31 eV in the laboratory frame) can be collisionally quenched by undergoing a Stark transition to the $2P$ state followed by an immediate de-excitation to the ground state emitting a K_α X-ray:

$$\mu p(2S) + H_2 \rightarrow \mu p(2P) + H_2 \rightarrow \mu p(1S) + H_2 + K_\alpha. \tag{2.1}$$

This part of the $\mu p(2S)$ atoms being de-excited through inelastic collisions is termed *short-lived* component of the $2S$ state. During the 2003 run of this experiment, the short-lived $2S$ component was characterized for the first time. By recording the time-distribution of the K_α X-rays, the fraction of the short-lived component relative to all μp atoms as well as its lifetime could be determined experimentally, at a hydrogen gas pressure of 0.6 hPa [84]:

$$\epsilon_{2S}^{short} = 1.70^{+0.80}_{-0.56}\,\% \tag{2.2}$$

$$\tau_{2S}^{short} = 165^{+38}_{-29}\,\text{ns} \tag{2.3}$$

The probability of this quenching mechanism to occur is energy dependent and decreases with lower initial kinetic energy of the $\mu p(2S)$ atom.

The term *long-lived* component of the $2S$ state refers to μp atoms formed at kinetic energies below the above mentioned energy threshold or to those $\mu p(2S)$ atoms being able to avoid the inelastic quenching process (2.1) by losing enough kinetic energy during elastic collisions with the H_2-gas molecules before an inelastic collision could destroy the $2S$ state.

Two quenching channels affect the long-lived $\mu p(2S)$ atoms. During a collision with a H_2-molecule, the $2S$ state can be mixed with the $2P$ state allowing an electric dipole transition to the ground state with emission of a K_α photon:

$$\mu p(2S) + H_2 \rightarrow \mu p(\alpha\,|2S\rangle + \beta\,|2P\rangle) + H_2 \rightarrow \mu p(1S) + H_2 + K_\alpha. \tag{2.4}$$

This transition can only take place during the collision. Since the typical collision time is $T_{col} \sim 10^{-14}\,\mathrm{s}$ and much shorter than the radiative lifetime of the $2P$ state $\tau_{2P} \sim 10^{-11}\,\mathrm{s}$, the cross section $\sigma \sim 10^{-18}\,\mathrm{cm}^2$ [90] of this channel is suppressed by a factor of $T_{col}/\tau_{2P} \sim 10^{-3}$ compared to the cross section of the inelastic process (2.1).

The second quenching channel relevant for the $\mu p(2S)$ atoms is an non-radiative de-excitation mechanism to the $1S$ ground state: during the resonant formation of an excited muonic molecule followed by its auto-dissociation [91, 92],

$$\mu p(2S) + H_2 \rightarrow \{[(pp\mu)^+]^* pee\}^* \rightarrow \mu p(1S) + p + E_{kin} + \dots\,, \tag{2.5}$$

the $2S-1S$ transition energy (1.9 keV) is distributed among the μp atom and the proton as kinetic energy. With a cross section of $\sigma \sim 10^{-16}\,\mathrm{cm}^2$, it dominates over (2.4). It has a measured quenching rate of [16, 93]

$$\lambda_{2S}^{quench} = 5.1^{+2.4}_{-2.1} \times 10^5 \mathrm{s}^{-1} \cdot p\,[\mathrm{hPa}], \tag{2.6}$$

and a lifetime τ that is given by the rates of the resonant quenching channel (2.5) and of the muon decay λ_μ:

$$\tau_{2S}^{long} = (\lambda_{2S}^{quench} + \lambda_\mu)^{-1}. \tag{2.7}$$

Reference [94] suggests a non-molecular explanation for this quenching channel: the direct Coulomb $2S \rightarrow 1S$ de-excitation to the ground state.

For the experiment, a trade-off value for the H_2-gas pressure has to be found, where the lifetime of the long-lived $\mu p(2S)$ state is long enough to impose a feasible delay time on the laser system (cf. Sect. 2.3), to have a small enough muon stopping volume, and to have a high enough $\mu p(2S)$ population at the laser time. This is achieved at a pressure of 1 hPa at room temperature: here, $1.1 \pm 0.1\,\%$ of the total number of μp atoms form long-lived $\mu p(2S)$ with a lifetime $\tau_{2S}^{long} = 1.04^{+0.29}_{-0.21}\,\mu\mathrm{s}$ [16, 93].

Triggered by an incoming muon, a short laser pulse with a wavelength tunable around $\lambda \approx 6\,\mu\mathrm{m}$ (corresponding to the $2S - 2P$ energy difference) fills a mirror cavity surrounding the muon stop volume, about $0.9\,\mu\mathrm{s}$ after the muon stop and the cascade. When the laser is on resonance, μp atoms in the $2S$ state can be excited to the $2P$ state from where they decay to the $1S$ ground state instantaneously (lifetime $\tau_{2P} = 8.6\,\mathrm{ps}$). The emitted 1.9 keV K_α X-rays, which occur in time-coincidence with the laser pulse (termed *delayed* K_α X-rays), serve as a signal and are recorded at different laser wavelengths. A resonance curve is obtained by plotting the number of delayed X-rays (normalized to the prompt X-rays to account for beam-intensity fluctuations) versus the laser wavelength.

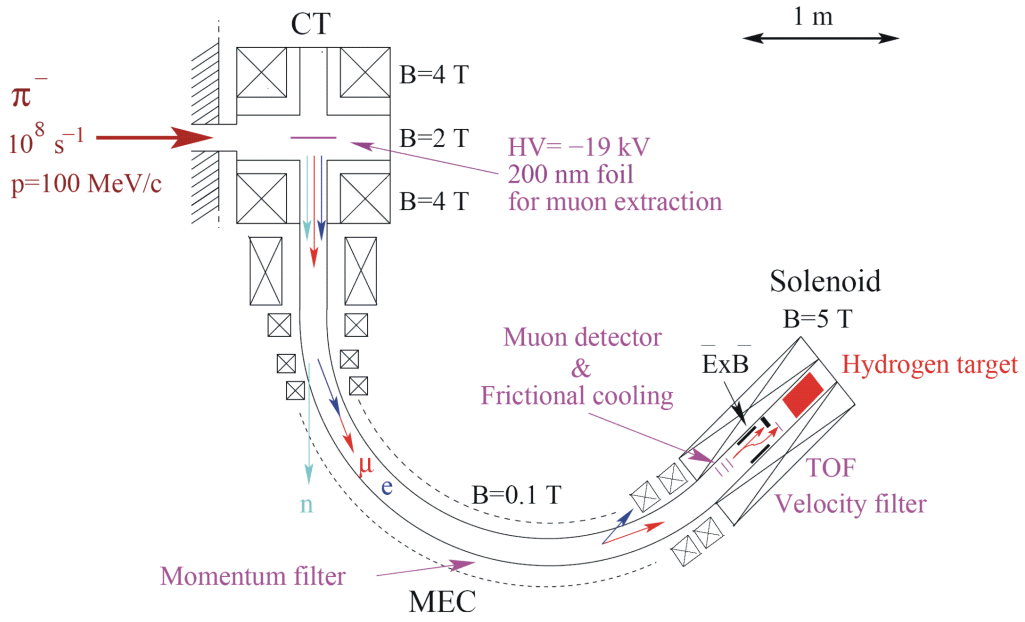

Figure 2.1: Low-Energy Muon Beam Line. *A schematic layout of the low-energy muon beam in the πE5 area at PSI. Shown are the cyclotron trap (CT), the muon extraction channel (MEC) and the target solenoid.*

2.2 Muon Beam

One key to the success of our experiment is the development of a novel low energy muon beam line at PSI. Since it is essential to stop the muons in hydrogen gas of very low gas pressures below 1 hPa (cf. Section 2.1), the muons with initial kinetic energies of several MeV have to be slowed down to energies below 3 keV. To efficiently decelerate muons within the muon lifetime of 2.2 μs and, at the same time, to reduce the background drastically is the aim of this newly developed low energy muon beam [95]. It consists of the cyclotron trap [96–98] acting as a magnetic bottle, a muon extraction channel guiding the low-energy muons and separating them from unwanted background, and a 5 Tesla superconducting solenoid housing the muon detectors and the hydrogen target. These three components of the beam line are described in the following. A schematic layout is shown in Figure 2.1.

2.2.1 Cyclotron Trap

With a momentum of 102 MeV/c, negatively charged pions ($10^8\,\mathrm{sec}^{-1}$) enter the cyclotron trap (CT) tangentially with a momentum spread of $\Delta p/p = \pm 6\,\%$ (FWHM). The purpose of the CT is to capture and decelerate these particles and produce low-energy muons which can be guided to a well-shielded experimental region. In such a manner, a high flux of secondary radiation, like neutrons or gamma rays, stemming

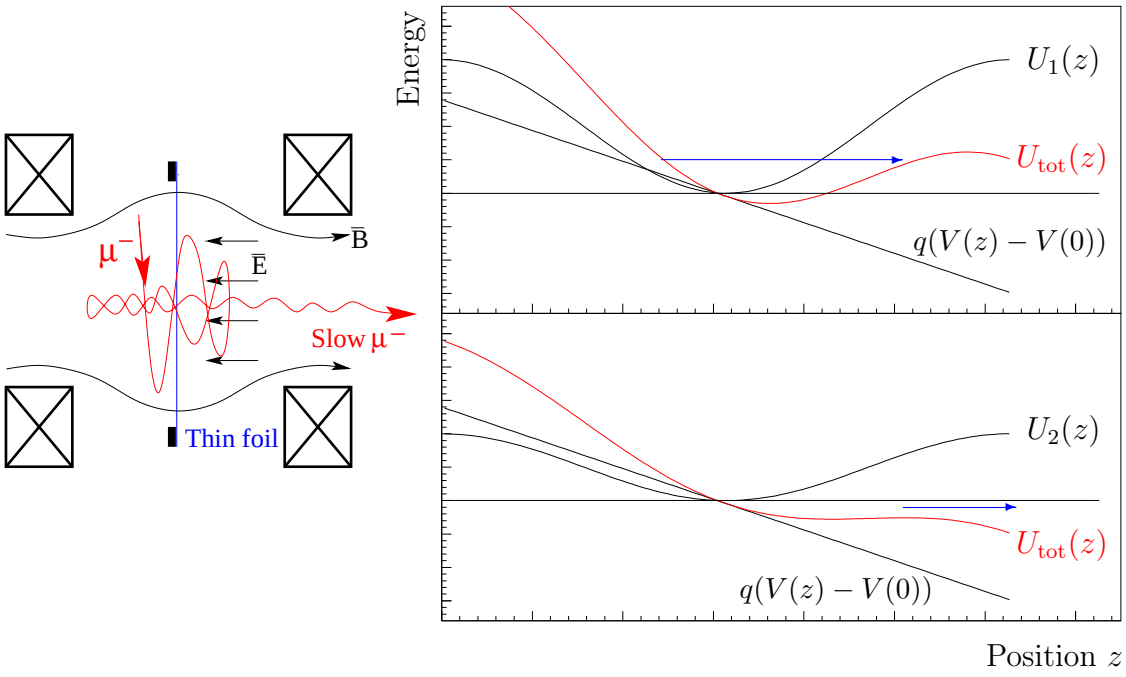

Figure 2.2: Schematic View of the Cyclotron Trap. ***(Left)*** *Cross section of the CT containing the extraction axis of the trap. The magnetic field creating a bottle-like pseudo potential is sketched in black, the trajectory of a decelerated muon projected onto the drawing plane in red. A thin metallized Formvar foil is mounted in the center plane of the CT and acts as a moderator for the muons. It is also kept on high voltage to supply an axial electric potential for extraction.* ***(Right)*** *Principle of the axial muon-extraction shown for two different transverse momenta. The pseudo-potential $U_{1/2}(z)$ is symmetric around the CT center. It scales with the ratio of the transverse to the longitudinal momentum and is distorted by the electric potential $q(V(z)-V(0))$ applied to the Formvar foil resulting in a total quasi-potential U_{tot}. Only when the muons have been slowed down considerably the magnetic pseudo-potential is small enough for the electric potential to accelerate the muons out of the — now weak — magnetic confinement of the CT.*

from pions hitting the CT-wall, can be avoided. The CT comprises of two superconducting ring coils 40 cm apart creating a magnetic field of 2 T in the central plane and 4 T in the center of the coils. A schematic is shown in Figure 2.2. Upon entering the CT, the pions pass a moderator ($5.4\,\mathrm{g/cm^2}$), the thickness of which is chosen such that they loose about half of their momentum and are left with 40 – 60 MeV/c, close to the optimum momentum to produce low-energy muons.

Having a lifetime of $2.6 \cdot 10^{-8}$ s, about 30 % of the moderated pions decay in flight into muons via their leptonic decay channel:

$$\pi^- \rightarrow \mu^- + \bar{\nu}_\mu. \tag{2.8}$$

The remaining 70 % are lost in the CT because they are either stopped in the moderator foil or they miss the moderator foil completely and hit the CT walls. A fraction of the muons has a suitable momentum vector to be captured by the magnetic pseudo

potential of the CT. The pseudo potential scales with the ratio of the transverse to the longitudinal momentum of the muons and is explained in Fig. 2.2. Muons produced at kinetic energies of a few MeV are radially and axially confined and are slowed down by multiple passes through a 160 nm thin Formvar foil (corresponding to 20 μg/cm^2) kept on negative high voltage (−18 kV) and mounted in the center plane of the CT. A 3 nm thin layer of nickel is sputtered onto the foil to make it conducting. When the muon is decelerated to kinetic energies of 10 – 50 keV, the electric potential dominates over the confining magnetic pseudo potential so that magnetic bottle is opened and the muons can leave the CT axially.

2.2.2 Muon Extraction Channel

Muons escaping the CT enter the muon extraction channel (MEC), a toroidal momentum filter (magnetic field $B = 0.15$ T) which favours particles with momenta around 2 MeV/c corresponding to muons with ~ 20 keV energy. It is constructed from 17 identical water-cooled ring coils mounted on a 130° segment of a circle with 1 m radius forming a toroidal magnetic field. Adiabatic magnetic field gradients help to keep the transmission of the MEC high. Between the 4 T of the CT and the 0.15 T of the MEC, this is achieved by inserting extra solenoids of 0.45 T and 0.25 T between the two devices (see Fig. 2.1). Since the 5 T target solenoid does not have an iron return yoke, its stray field can be used for this purpose and no such supplementary coil is required after the MEC.

In a particle accelerator environment, special care has to be taken to keep the background radiation in the measurement area at a tolerable level. Such radiation includes (among many others) neutrons stemming from pions hitting the apparatus walls, high-energy electrons from muon decay, and electrons with keV energies being expelled from the Formvar-foil in the CT. In the MEC, particles of mismatched momentum are absorbed by specially designed beam blocks. Charged particles with different momenta spiral around magnetic field lines with different radii of gyration thereby experiencing different vertical drifts in a toroidal magnetic field. Due to its toroidal geometry, a slight horizontal field gradient is present causing the momentum dependent deviation. Particles of wrong momentum can be eliminated by placing beam dumps and collimators at suitable vertical positions. In order to keep the trajectory of the 2 MeV/c muons in a horizontal plane, the 17 solenoids are tilted by $\sim 4°$ around their horizontal axes. To further minimize the background induced by neutrons produced in the CT (disturbing the delicate detectors in the target), a 1 m thick block of concrete is placed between the CT and the target solenoid.

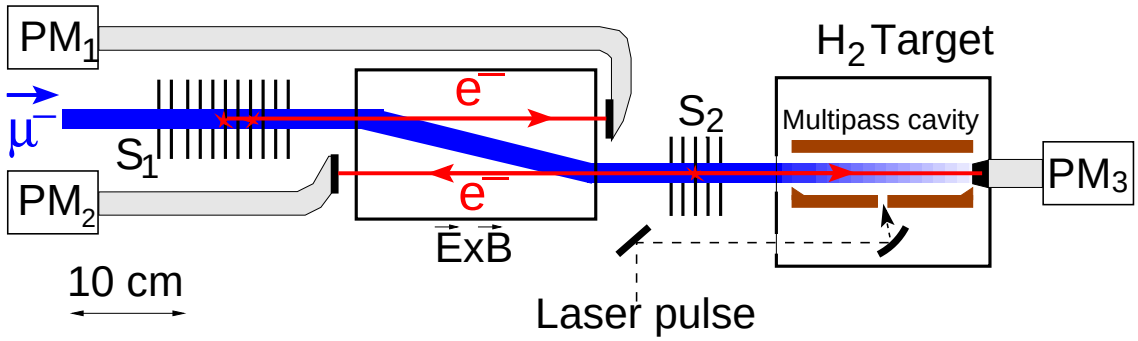

Figure 2.3: Schematic of the Target and Muon Detectors. *Muons entering from the left have to pass two stacks of carbon foils as well as an $\vec{E} \times \vec{B}$ velocity filter. Secondary electrons are detected in plastic scintillators monitored by photo multiplier tubes. They are explained in the text. The gas-target is filled with dilute H_2-gas and houses the target mirror cavity. Two arrays of LAAPDs are mounted on top and below the gas-volume (not shown).*

2.2.3 Target

In the MEC, the muons are guided some cm above the axis into the 20 cm bore hole of a 5 Tesla superconducting magnet of 1 m length. Inside this target solenoid, the muon beam is shifted onto the axis by the $\vec{E} \times \vec{B}$ filter (see below). It houses the entire target together with all relevant detectors as shown in Figure 2.3. The high magnetic field ensures minimal radial size of the muon beam thereby reducing the target volume to be illuminated by the laser.

Muon Detector

Upon entering the hydrogen target, the muons pass two muon detectors consisting of two stacks of ultra-thin carbon foils ($d = 4\,\mu g/cm^2$) and a velocity filter. The first stack S_1 consists of 5 carbon foils supported by stainless steel rings. These foils are connected through a resistive voltage-divider chain and kept at high voltage. Seven additional rings without foils in front and 3 after the foil-stack are necessary to achieve a smooth potential variation. The first and the last ring are electrically grounded, the first foil is kept at -12.5 kV. The muons first see a rising potential of -12.5 kV where they loose kinetic energy before passing the first foil. The muons loose about 2.5 keV of kinetic energy while passing through each of the five carbon foils and release secondary electrons. The electric potentials for the foils are chosen such that the energy loss is partly compensated before hitting the next carbon foil ($\Delta U = 1.8$ kV). In this way, the muons are frictionally cooled and compressed in phase space [99], and most importantly, slowed down.

Passing the carbon foils, the muons extract secondary electrons. In the stack potential, the emitted electrons are accelerated. In a 29 cm long $\vec{E} \times \vec{B}$ velocity filter

(capacitor plates 2 cm apart at +4.5 kV and −6 kV) the lighter and therefore much faster electrons are separated from the relatively slow muons: while the muons coming from the S_1 foil stack experience a shift of about 8 mm the electrons are not noticeably shifted. They hit a plastic scintillator and are detected via a long light-guide by a photo multiplier PM_1 ("S_1") in Fig. 2.3. After the $\vec{E} \times \vec{B}$ filter, the muons cross a second stack (S_2). The secondary electrons expelled from the two carbon foils installed in this stack are accelerated upstream (against the muon beam) and downstream and are detected in plastic scintillators connected to the photo multipliers PM_2 ("S_2-up") and PM_3 ("S_2-down"), respectively. The light yield of all three photo-multipliers is increased through further acceleration of the stack-electrons by applying a positive high voltage to the plastic scintillators.

To sum up, the muon detectors consisting of the two stacks S_1 and S_2 and the $\vec{E} \times \vec{B}$ velocity separator act as a non-destructive transmission detector for keV-muons, reduce the muon energy and frictionally cool the muon beam thereby reducing the phase space volume. They detect every muon separately and provide the trigger signal for the data aquisition system and the laser. Section 2.4.1 describes the detectors in more detail. Before entering the target through a 30 nm (4 μg/cm^2) thick Formvar window (F in Fig. 2.3), the muons have been decelerated to 3 – 6 keV in the above described manner.

Gas Target

Finally, the muons arrive in the gas target volume which is filled with 1.0 hPa of H_2-gas and, along the beam axis, has a length of 20 cm. The shape of the muon stop volume (5 × 12 × 194 mm) is a consequence of the energy spread and the stopping distribution of the muons in such low density hydrogen gas. The gas target is mounted inside the bore hole (diameter $d = 20$ cm) of the target solenoid and is surrounded by several detectors. Figure 2.4 shows two sectional schematic views of the gas target, its surrounding detectors, the mirror cavity, and the X-ray detectors: above and below the muon beam, two face-to-face rows of 10 large area avalanche photo-diodes (LAAPDs, 14×14 mm^2 active area) are mounted together with their pre-amplifiers and record the 1.9 keV K_α X-rays in a distance of 8 mm from the muon beam axis. The x-shaped detectors in the left sectional view are plastic scintillators (termed *electron paddles*) connected to photo multipliers and record the muon decay electrons spiralling in the 5 Tesla magnetic field.

Additional 1 μm thin Ag-coated polypropylen (PP) foils are installed in front of the LAAPDs to make the cavity light-tight for visible light and also to avoid unwanted background from μp atoms drifting into target walls. The hydrogen gas inside the gas volume is renewed continuously in order to keep it pure.

Muons enter the target and slow down in collisional processes with the hydrogen molecules before they are captured. Cascading down the energy levels, a fraction of the muons forms μp in the $2S$ state. The laser system (cf. Sect. 2.3) is triggered by

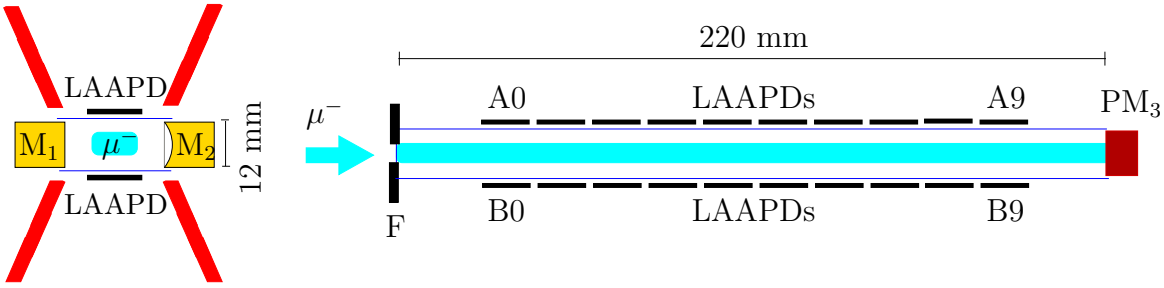

Figure 2.4: Sectional Views of the Gas Target and the Detectors. ***(Left)*** *A cross section through the target perpendicular to the muon beam direction. Schematically, the electron paddles (red), the LAAPDs, and the mirrors (yellow) are depicted. They are all arranged around the centered muon beam. For a picture of the entire assembly refer to Fig. 2.12.* ***(Right)*** *A sectional view along the muon beam shows the arrangement of the LAAPDs on top and below the muon beam (cyan). The gas volume is separated from the surrounding vacuum by Formvar foil (F) through which the muon beam has to enter. PM_3 is a plastic scintillator and photo multiplier assembly recording the muon detection electrons.*

an entering muon and sends out an infra-red laser pulse. This laser light is guided into the solenoid's bore hole parallel to the muon beam and gets deflected by an off-axis parabolic mirror and focussed through a small hole ($d = 0.63\,\mathrm{mm}$) in the center of one of the multi-pass cavity mirrors. The elongated muon stop volume is surrounded by two cylindrical high reflective mirrors which form a non-resonant multipass cavity. The multi-pass cavity encloses the muon stop volume, confines the injected laser light in all three dimensions and illuminates the muonic hydrogen atom formed somewhere inside the stopping volume. It provides a sufficiently homogenous irradiation of the interaction volume by the $6\,\mu\mathrm{m}$ laser light to drive the $2S - 2P$ transition effectively. The LAAPDs record the K_α photons which are emitted by the μp atoms when their $2P$ state decays into the $1S$ ground state immediately after the laser induced transition.

2.3 Laser System

The laser system employed for our experiment is introduced in this section [100]. Laser pulses at a wavelength between 5.48 – $6.04\,\mu\mathrm{m}$ are needed to drive the $2S - 2P$ transitions in μp and μd. This corresponds to a frequency of 49.6 – $54.6\,\mathrm{THz}$ resulting in a required tunability of $5\,\mathrm{THz}$. The measured bandwidth in the infra-red domain is $1.8\,\mathrm{GHz}$ which is small enough to be able to determine the resonance line position ($\Gamma_{2S-2P} = 18.6\,\mathrm{GHz}$ at FWHM) to $15\,\mathrm{ppm}$ or $0.7\,\mathrm{GHz}$. The energy per pulse is $\gtrsim 0.25\,\mathrm{mJ}$ after the Raman cell. A volume of $25 \times 7 \times 170\,\mathrm{mm}^3$ is to be filled by the laser light. The slightly different dimensions compared to the muon stop volume are a consequence of the μp atoms drifting and of the limited length of the cavity mirrors. The volume is illuminated with an laser fluence of $\sim 6\,\mathrm{mJ/cm}^2$, a sizeable fraction

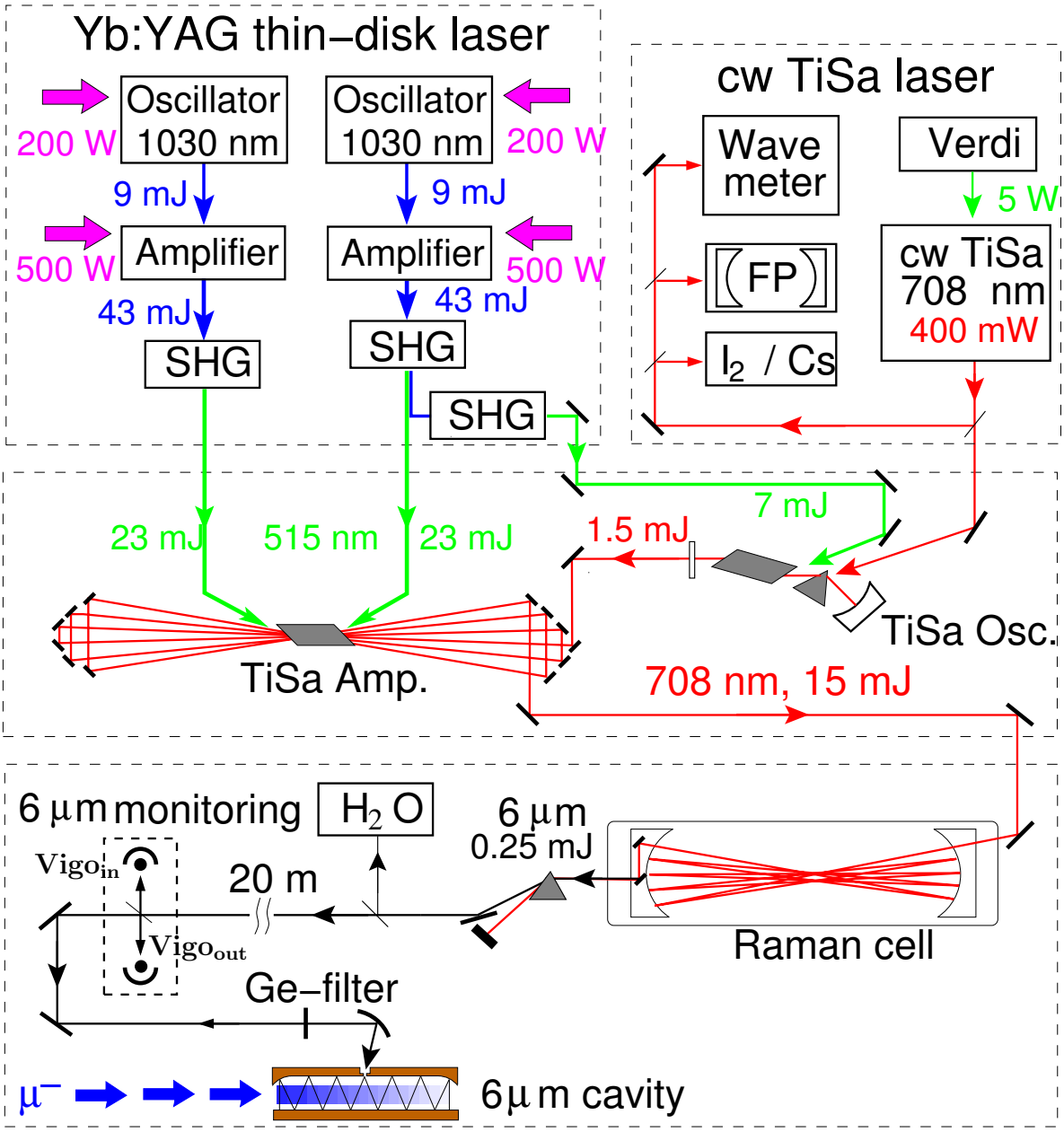

Figure 2.5: Schematic of the Laser System. *Infra-red laser pulses are obtained by sending strong 708 nm laser pulses through a H_2 filled Raman shifter. The red pulses are produced in a Ti:Sapph MOPA subsystem which is pumped by a frequency doubled thin disk laser unit and injection seeded by a wavelength controlled and tunable cw Ti:Sapph laser. The depicted abbreviated components are: Fabry-Pérot reference cavity (FP), iodine and cesium absorption cells (I_2/Cs), second harmonic generation (SHG), water absorption cell (H_2O), and fast infra-red photo diodes to monitor the light going into and leaking out of the target cavity ($Vigo_{\mathrm{in/out}}$).*

of the 16.6 mJ/cm^2 needed to saturate the $\mu p(2S^{F=1}_{1/2} - 2P^{F=2}_{3/2})$ transition [88]. The entire laser system is able to follow stochastic triggers stemming from muons entering the target at an average repetition rate of up to 500 s^{-1}. The time delay between the muon trigger and the pulse illuminating the target cavity has to be on the order of the μp(2S) lifetime which is 1 μs. This is the most stringent requirement to the laser necessitating the development of a cw pumped disk laser system (Section 2.3.1). All these specifications have to be fulfilled in a reliable manner over several months of beam time under accelerator conditions.

The laser system and its major components are sketched in Figure 2.5. Two ytterbium-YAG (Yb:YAG) thin disk laser units (Section 2.3.1) pump the entire pulsed laser system and provide 53 mJ of green laser pulses at 515 nm after second harmonic generation (SHG). Their pulses have a delay of only 400 ns relative to the muon trigger signal. They pump an injection seeded master oscillator power amplifier (MOPA) titanium sapphire (Ti:Sapph) laser system which delivers 15 mJ red pulses around $\lambda \approx 708$ nm.

At the output of the Ti:Sapph amplifier, the laser light enters an efficient and reliable 3rd-Stokes Raman shifter [101] (termed Raman cell, RC) operated at 15.5 bar of H_2 gas. Here, its wavelength is converted to the infra-red domain ($\lambda = 5.48 - 6.04\,\mu$m). The RC introduces a constant Raman shift ($\Delta\widetilde{\nu} = 3 \times 4155.2\,\mathrm{cm}^{-1}$) so that the frequency tuning of the cw Ti:Sapph laser translates directly into the infra-red. In such a way, the frequency control of the 6 μm laser can be performed directly in the much more convenient visible region. The frequency control of the Ti:Sapph oscillator is managed by seeding it with a single-mode continous wave (cw) Ti:Sapph laser. The absolute frequency calibration of the cw Ti:Sapph subsystem is achieved by a wavemeter and by iodine and cesium absorption cells. Water absorption spectroscopy is utilized to accurately calibrate the whole laser system directly in the infra-red domain (cf. Section 4.2.2).

After the RC, the infra-red laser light is guided through an evacuated beam line to avoid absorption in water and to bridge the distance to the target cavity. Two long mirrors to the left and right of the target volume form a nonresonant confinement cavity for the 6 μm light. The laser pulse enters the cavity through a small hole ($d = 0.63$ mm) in the center of one of the mirror substrates. The cavity confines the light with a lifetime of $\tau = 45\,(5)$ ns. Its mirror coating is treated in Appendix C. A small fraction of the light going into the target cavity (reflected from a CaF_2 window) and the light leaking out of the target cavity through the small entrance hole are monitored by fast infra-red photo diodes. This way, the energy information is available for every single laser pulse and information on the injection and confinement time of the pulse in the cavity can be extracted. A germanium (Ge) window seals the entire target cavity to avoid visible stray light.

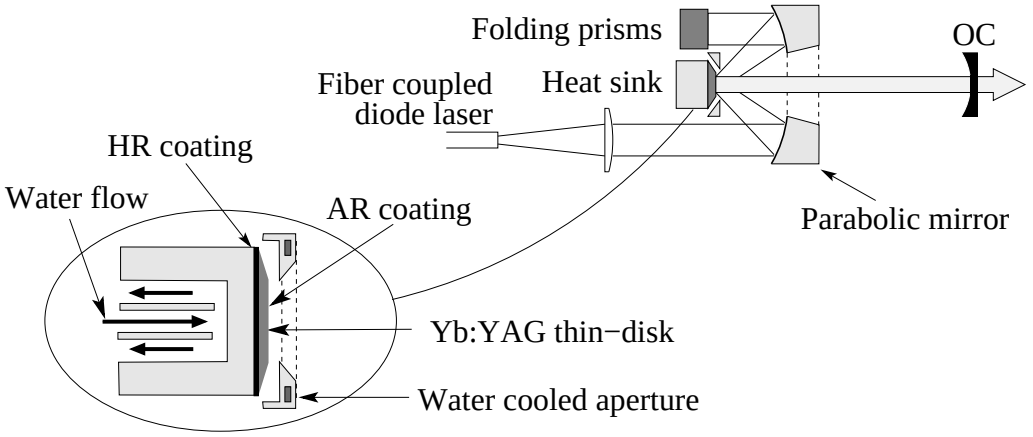

Figure 2.6: Principle of the Thin Disk Laser. *The laser crystal has the form of a thin disk (12 mm diameter, 200 µm thickness) and is soldered onto a water-cooled heat sink. The back side of the disk is HR coated for both the pump and the laser wavelength. The fiber coupled diode light is imaged onto the disk. The parabolic mirror and the folding prisms ensure a 12 pass pumping scheme. The fluorescence light exiting the beveled edges is absorbed by a water cooled apperture.*

2.3.1 Disk Laser

Two Yb:YAG thin disk laser units pump the entire laser system and provide a total of 86 mJ energy of the laser pulses at 1030 nm with a pulse duration of 35 ns. Yb:YAG as a gain medium has the advantage of a very small quantum defect (pumped by 940 nm InGaAs high power laser diodes), no up-conversion, no excited state absorption, high doping concentration, and, caused by all these advantages, a reduced waste heat production. In combination with the thin disk laser technology [102–104] it is possible to make use of many of these advantages. The necessity of a short delay between the electrical trigger and the laser output and the randomness of the trigger source (at a laser repetition rate of $500\,\mathrm{s}^{-1}$) called for the development of our thin disk laser pumping unit [105] which consists of a Q-switched master oscillator and a multipass power amplifier. The components will be briefly introduced in this section.

The concept of utilizing the gain medium in the form of a thin disk permits effective cooling (thus strong pumping is possible) and suffers only from small thermal lensing and depolarisation effects (from thermally induced stress birefringence). Yb:YAG as a gain medium has a long fluorescence lifetime ($\sim$ 1 ms [106]) and thus favours high energy storage per unit pump power but results in a large saturation fluence of $\sim 1\,\mathrm{J/cm^2}$. Drawbacks of Yb:YAG are its low gain and a relatively low damage threshold (a few $\mathrm{J/cm^2}$).

Principle

The principle setup of a thin disk laser head is explained in Figure 2.6. A thin (0.2 mm) Yb:YAG crystal disk with a diameter of 12 mm is soldered onto a copper heat sink which is efficiently cooled from behind by a constant water flow. The disk's back side is high reflectively (HR) coated for both the pump (940 nm) and the laser (1030 nm) wavelength. Its edges are beveled under an angle of $\alpha \simeq 10°$ to reduce amplified spontaneous emission (ASE) [105]. The cw pump laser light stems from a fiber coupled diode laser. For efficient absorption, the pump beam has to pass the thin disk in 12 double passes using a relay imaging system made from a parabolic mirror (focal length 32 mm), folding prisms acting as retro-reflectors, and the disk mirror itself. The laser cavity is made up from the disk (acting simultaneously as a mirror and as gain medium) and an output coupler (OC). This layout causes only a small phase distortion of the laser beam coming from thermally induced spherical and aspherical lens effects. Two oscillator-amplifier subunits have been developed (cf. Figure 2.5 top left) to conform to the experimental demands on the laser system.

Q-Switched Oscillator

The oscillator in each subunit is a Q-switched thin disk laser. It is operated in a cw-prelasing mode. Receiving a muon-trigger, its cavity is closed causing a fast intra-cavity pulse build-up. The circulating power is released when the cavity is opened completely, delivering 10 mJ pulses at 1030 nm with a measured beam-quality factor $M^2 \leq 1.1$ at a maximum repetition rate of up to 500 Hz and an internal delay of only 250 ns. Figure 2.7(a) illustrates the layout of the 1-m-long oscillator cavity. It includes the laser head, a telescope forming a laser spot size of $\omega \simeq 1$ mm on the disk, a Pockels-cell (PC) and a thin film polarizer (TFP). The gain medium is passed four times and a fixed $\lambda/4$ plate reduces interference between the two beams. Together with a second, adjustable $\lambda/4$ plate, the TFP acts as a polarization dependent output coupler. The PC (consisting of a BBO crystal[2] in a strong electric field) is used to alter the polarization inside the oscillator cavity on a fast time scale, thereby controlling its Q-switching dynamics. Figure 2.7(b) shows the electronic principle of the PC switching: prior to trigger with one cathode grounded, the other one is controlled by a feedback loop voltage $U_\epsilon \in [0, 400]$ V to stabilize the circulating power. Upon trigger, both cathodes are switched to high voltage (HV).

In order to have the shortest possible time delay between the electronical trigger and the pulse extraction, the oscillator cavity is kept in a cw-prelasing mode prior to trigger. It is continuously pumped by 200 W cw pump power at 940 nm and the oscillator is lasing close to threshold with the largest possible TFP transmission (output power ~ 1 W). In such a way, a large number of photons ($\sim 10^{11}$) is already circulating in the cavity when a trigger arrives. Upon trigger, the cavity is closed by applying

[2] beta barium borate (β-BaB_2O_4)

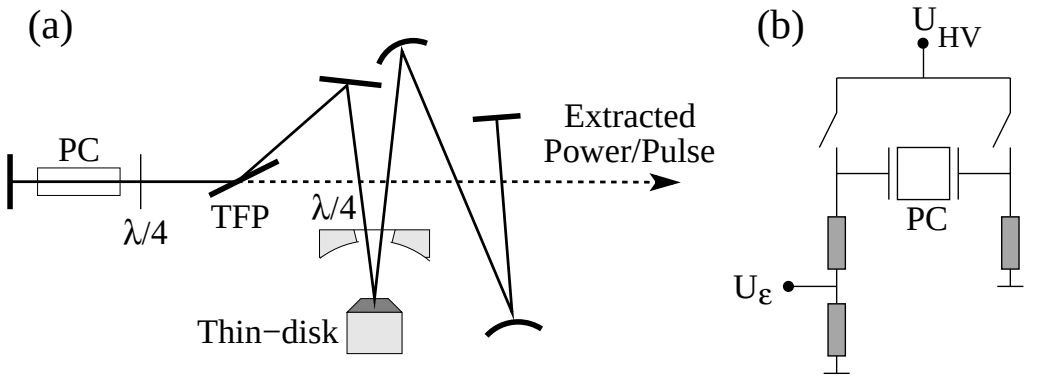

Figure 2.7: Q-Switched Disk Oscillator. ***(a)*** *The optical layout of the oscillator cavity is shown here. Applying a HV to the Pockels cell (PC) switches the polarization of the laser light inside the cavity. Depending on the direction of polarization, the thin film polarizer (TFP) closes the cavity completely or acts as an output coupler dumping the circulating power. The $\lambda/4$ plate close to the PC helps to set the polarization in the desired way. The one in front of the disk reduces interference of the two beams on the disk.* ***(b)*** *The principle electronics scheme to switch the PC. In prelasing mode, one PC cathode is kept at ground potential while the other one is controlled by a feedback voltage U_ϵ stabilizing the circulating laser power. To close and dump the cavity, one cathode after the other is switched to HV.*

a high voltage $U_{HV} \in [3, 4.5]\,\mathrm{kV}$ to one of the PC electrodes (switching time 30 ns) therby rotating the polarization of the light circulating inside the cavity. This way, the TFP becomes a high reflector resulting in a fast amplification of the circulating power and a fast pulse build-up. The cavity is dumped by raising the second PC cathode to HV reverting the previously introduced polarization shift and making the TFP transmissive again. Extracted pulses contain 5×10^{16} photons and have a pulse length of 35 ns (FWHM). Their energy scales with the cavity closure time and reaches up to 12 mJ. The procedure involving prelasing and fast cavity dumping shortens the time to reach the desired pulse energy significantly from 600 ns to 190 ns. After pulse extraction, ~ 1 ms of cw pumping is needed to reestablish stable baseline population inversion [105].

A gain of 1.25 per reflection at the disk mirror is measured. The total delay between trigger and optical output is the sum of cavity closure time (190 ns for 12 mJ pulses) and the switching time of the PC controller (60 ns) adding up to ~ 250 ns. The oscillator has been tested to give a stable output up to repetition rates of 850 Hz. The competition between higher order transversal modes and the fundamental eigenmode has to be suppressed by choosing a relatively large pump spot size ($\omega = 1.3$ mm) resulting in a stable mode of operation but in a comparably low pulse energy. Consequently, an oscillator-amplifier scheme has to be implemented in order to reach the required pulse energies.

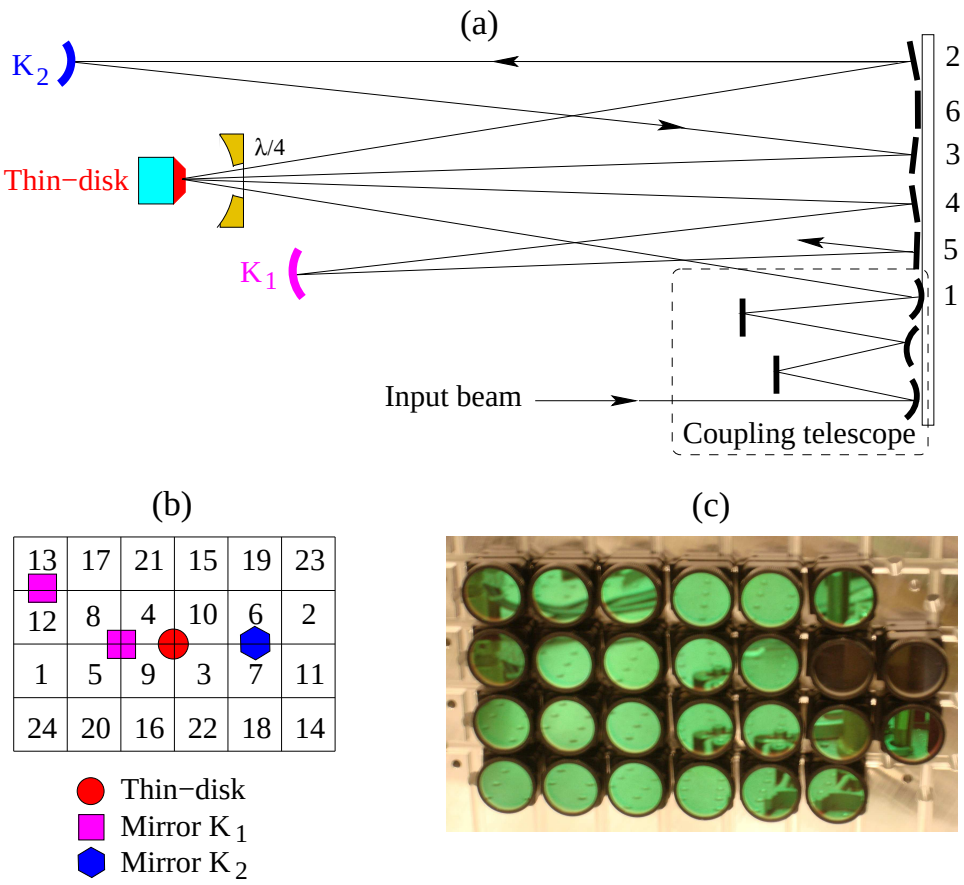

Figure 2.8: Multipass Thin Disk Amplifier. *The principle and beam routing of the 12-pass amplifier is illustrated here.* ***(a)*** *The optical path follows 1-disk-2-K_2-3-disk-4-K_1..., where K_1–K_2 defines the stable optical segment. The distance between the mirror array and the disk is 0.84 m.* ***(b)*** *The working principle of the mirror array clarifies how the 24 flat reflectors guide the beam for 12 passes. To proceed from one flat mirror to the next, the beam has to be reflected on one of the four mirror (2× K_1, K_2, and the disk) whose projections are depicted.* ***(c)*** *This photograph shows the mirror array consisting of compact mirror mounts for 25.4 mm optics.*

Multipass Amplifier

The multipass thin disk amplifier scheme is presented in Figure 2.8. It is made up of multiple instances of one intrinsically stable optical element composed by the disk and two curved mirrors $K_{1/2}$. By concatenating 12 such segments in series, a 12-pass amplifier is realized (Fig. 2.8(a)). An array of 24 mirros (depicted in Fig. 2.8(b)+(c)) is employed to independently align each segment and to concentrate the beam paths into a small volume. Compared to the classical 4-f propagation, the segmental design chosen here is insensitive to changing lens effects in the disk [105]. These lens effects vary from disk to disk and depend on running parameters such as pump beam intensity and size, and cooling water flow and temperature. The following elements have been chosen for a thin disk with vanishing focal power ($1/f = 0$) to compose one instance

of a stable segment: a concave mirror K_1 with $R_1 = 5000\,\text{mm}$ (at $z = 0\,\text{m}$), the disk at $z = 1.3\,\text{m}$, and a convex mirror K_2 ($R_2 = -2000\,\text{mm}$, $z = 3.8\,\text{m}$). In this configuration, the size of the laser eigenmode on the disk is independent of the disk's focal power. Only at the position of the convex mirror K_2 does the eigenmode size strongly depend on lens power variations of the disk. Since the damage threshold of the mirror coating is an order of magnitude higher than that of the disk's coating, this is acceptable.

One multipass amplifier unit achieves a total gain of 6.4 (1.17 per pass). The eigenmode size of the laser at the disk is $\omega \simeq 2\,\text{mm}$ with a pump spot size of $\omega = 2.3\,\text{mm}$ and a pump power density of $3.5\,\text{kW/cm}^2$. One system can deliver pulses of up to 48 mJ energy at a repetition rate of up to 850 Hz but, in order to retain some safety margin, has been operated with 43 mJ at up to 500 Hz. With an amplifier path length of $\sim 40\,\text{m}$, the time delay of the optical output after an electronic trigger is 400 ns. Further details on the mode shape in the amplifier, the influence of ASE on the laser properties, and the effective lifetime of Yb:YAG can be found in [105].

In our laser system, two of these disk laser oscillator-amplifier units are in use. The infra-red output of each unit is frequency doubled in two LBO crystals[3] in series (with a dichroic mirror between them to separate the 515 nm light from the 1030 nm) and is then utilized to pump the pulsed Ti:Sapph laser subsystem.

2.3.2 Laser System in the Visible

The laser system in the visible region consists of a cw Ti:Sapph ring laser seeding a pulsed Ti:Sapph oscillator, and a Ti:Sapph amplifier lasing at $\lambda \approx 708\,\text{nm}$. The entire system is described thoroughly in [88]. The pulsed Ti:Sapph laser is a concatenation of a 7 cm short, wavelength-selective master-oscillator cavity and a bow-tie configuration multi-pass power-amplifier emitting 6 ns short pulses with TEM_{00} transversal mode and pulse energies up to 15 mJ. By seeding the pulsed Ti:Sapph oscillator with a single-mode cw Ti:Sapph laser, its wavelength (and with it the wavelength of the entire laser system) is determined. The cw Ti:Sapph ring laser is pumped with a 5 W cw laser at 532 nm and locked to a transmission peak of an external reference Fabry-Pérot (FP) cavity (Sect. 4.2.1) with a linewidth of $\sim 5\,\text{MHz}$. The wavelength is controlled by several wavelength-selective intra-cavity elements. It is tunable from 690 – 750 nm which is limited by the spectral gain profile of Ti:Sapph crystal (centered around 780 nm) at the lower end and by the reflectivity of the intra-cavity mirrors at the upper end.

2.3.3 Laser System in the Infra-Red

The laser pulses stemming from the Ti:Sapph system are shifted into the mid infra-red by sequential Raman scattering in 15.5 bar of H_2 gas inside a multi-pass Raman cell [101] (RC). The conversion of 708 nm light to 6 μm is sketched in Figure 2.9.

[3] lithium triborate (LiB_3O_5)

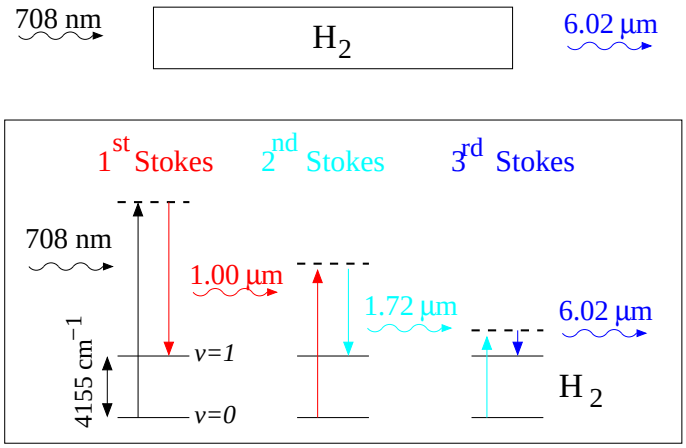

Figure 2.9: Sequential Raman Scattering. *A sequence of three Stokes shifts is needed to convert the photons from $\lambda = 708\,nm$ to $\lambda = 6.02\,\mu$m. With each Stokes conversion, a hydrogen molecule absorbs energy equivalent to $\widetilde{\nu} = 4155\,cm^{-1}$ thereby being excited from the ground to the first vibrational state. The virtual level (dashed line) is associated with the electronic excitations.*

Hydrogen has the largest Stokes shift of $\widetilde{\nu} = 4155.2\,\mathrm{cm}^{-1}$ so that a 708 nm photon with wavenumber $\widetilde{\nu} = 14128\,\mathrm{cm}^{-1}$ undergoing three sequential Stokes shifts looses $3 \times 4155\,\mathrm{cm}^{-1} = 12466\,\mathrm{cm}^{-1}$. The resulting wavenumber $\widetilde{\nu} = 1662\,\mathrm{cm}^{-1}$ corresponds to 6.02 μm.

In order to avoid water absorption inside the RC, the H_2 gas has to be continuously circulated through a liquid nitrogen trap to freeze out any water contaminating the gas. For the 2009 run, the circulation system has been renewed to increase the throughput and the cleaning efficiency. Other measures like cooling the entire RC to increase the Raman efficiency did not yield the desired effect because of mechanical misalignement due to the contraction of the RC. In 2009, a laser bandwidth of $\Gamma = 1750\,(250)$ MHz has been extracted from water absorption measurements (Sect. 4.2.3). This has to be compared to the 680 MHz observed during the beamtime in 2003 [88]. The discrepancy is attributed to the higher repetition rate ($200\,\mathrm{s}^{-1}$ compared to $50\,\mathrm{s}^{-1}$) and the larger input power in 2009 (15 mJ compared to 10 mJ) causing a broadening in the Raman process.

After the RC, the infra-red light is separated from all other Stokes components and the pump beam by passing a CaF_2 prism. Employing 3" copper optics with a Ge/ZnSe HR coating (reflectivity $R = 99.7\,\%$), the 6 μm laser beam is guided into the target through a 12 m long evacuated tube to avoid water absorption over such a long distance. Directly before the target, mode matching optics ensure the correct beam waist at the entrance hole of the target cavity ($\omega \simeq 0.1$ mm), and several detectors help to monitor the parameters of the laser pulses. Aside from the pulse energy and position of the beam entering and leaking out of the target cavity, several photo multiplier tubes make sure that no visible light is present at this location of the experiment.

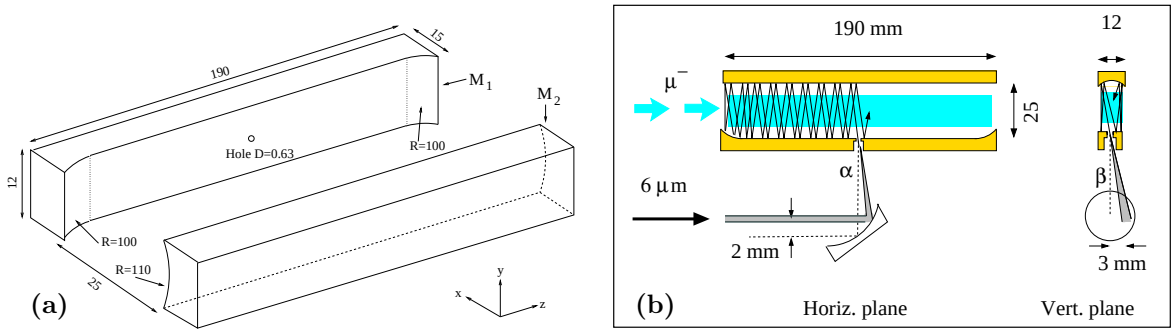

Figure 2.10: Target Cavity: Schematics and Principle. ***(a)*** *Schematics of the target cavity. A cylindrical and a flat mirror with cylindrical ears confine the laser light horizontally and vertically. An injection hole of 0.63 mm diameter is centered on the flat mirror. The dimensions are given in mm, the curvatures are exaggerated.* ***(b)*** *Principle of the target cavity. The mirrors are positioned to the left and right of xthe muon stop volume. With an injection angle deviating from 90°, the laser light washes out inside the cavity and is reflected ∼ 600 times illuminating the stop volume almost homogeneously. An off-axis paraboloid is used to focus the beam through the tiny entrance hole.*

2.3.4 Target Cavity

Upon entering the vacuum system of the muon beam apparatus, the laser light is sent to the target (see Figure 2.3). There, it is injected into the target cavity in order to illuminate the muon stop volume and to induce the μp transition. Figure 2.10 shows the schematics of the target cavity and demonstrates its principle. It is set up as an non-resonant multipass enhancement cavity consisting of two 190 mm long mirror but only 12 mm high substrates. One of them is designed as a cylindrical mirror (with a horizontal axis) achieving vertical confinement. Horizontal confinement is accomplished by cylindrical "ears" mounted at the ends of the flat mirror substrate such that the mirror surfaces merge continuously. By chosing the radius of curvature $R = 110\,\text{mm}$ of the cylindrical mirror not to be a multiple of the distance $d = 25\,\text{mm}$ between the mirrors, repeating laser spot patterns inside the cavity are avoided and the laser beam smears out. In such a way, the entire cavity volume is illuminated almost homogeneously. Simple geometrical optics shows that the radius of curvature of the ears either has to be $R = 2\,d$ or $R = 4\,d$ in order to retroreflect the beam at both ends of the cavity. $R = 4\,d = 100\,\text{mm}$ is chosen in our setup. This ensures an adiabatic return of the light at the ears, avoiding losses at the mirror ends.

The laser light is injected into the cavity by focussing it through the $D = 0.63\,\text{mm}$ entrance hole drilled into the center of the flat mirror (Figure 2.10(b)). An off-axis paraboloid (focal length $f = 50.8\,\text{mm}$) is used to achieve a beam waist of $\omega \simeq 0.1\,\text{mm}$ in the hole. Hitting the paraboloid off-center causes the beam being injected in an angle other than perpendicular (with horizontal angle α and vertical angle β) so that a volume can be illuminated. During the experiment, the values $\alpha = 40\,\text{mrad}$ and

$\beta = 65\,\text{mrad}$ are used. The height of the laser illuminated volume (designed to be 7 mm) is controlled by the angle β, i.e. by the vertical distance to the center at which the laser impinges on the paraboloid. With the focus of the paraboloid inside the hole, beam pointing instabilities only influence the size of the filled cavity volume but do not affect injection. Also, the cavity is fairly robust to misalignment of the mirrors with respect to each other. In the vertical dimension a misalignment of 10 mrad of the cylinder can be tolerated. Horizontally, a malpositioning of 0.5 mrad is accepted (0.1 mm for a $\sim 20\,\text{cm}$ long mirror substrate). An active stabilization is not required although it is aligned only once, put under vacuum, cooled significantly, and then left untouched for several weeks of operation.

An HR coating is needed to reach the required laser fluence inside the cavity. Dielectric coatings composed of Ge/ZnSe and Ge/ZnS from two different manufacturers have been tested in a cavity ringdown setup (cf. Appendix C). Finally, a Ge/ZnSe coating with a measured reflectivity $R = 99.89\,(1)\,\%$ has been achieved. Including losses from the entrance hole, from the seams between the ears and the flat substrate, and from other imperfections, this leads to a measured cavity confinement time of $\tau = 45\,(5)\,\text{ns}$ inside the target cavity.

2.4 Detectors and Electronics

2.4.1 Muon Detection

The muons entering the target are detected by a transmission detector as illustrated in Section 2.2.3 and serve as a trigger signal with a rate of $\sim 330\,\text{s}^{-1}$ detected and usable muons. With a maximum laser repetition rate of 500 Hz, this results in $\sim 200\,\text{s}^{-1}$ muon events with the laser being fired. It is desirable to trigger the data aquisition system and the laser only on muons that have the right kinetic energies to be stopped in the hydrogen gas and form muonic hydrogen.

Muons passing the carbon foils of the stacks S_1 and S_2 extract secondary electrons. For S_1, these electrons are separated from the muons by the $\vec{E} \times \vec{B}$ filter (cf. Fig. 2.3) and detected by a plastic scintillator mounted on a long Lucite light guide connected to photo multiplier PM_1 ("S_1"). While those electrons released from S_2 against the muon beam direction are also separated in the velocity filter and observed by PM_2 ("S_2-up") the electrons emitted downstream are detected by photo multiplier PM_3 positioned at the end of the target ("S_2-down"). In the 2009 run, a trigger signal is broadcast to the data aquisition system when the following coincidence is fulfilled:

$$S_1 \wedge (\,S_2\text{-up} \vee S_2\text{-down}\,) \tag{2.9}$$

This results in a very clean trigger signal: together with the correct timing of the three individual signals with respect to each other, this coincidence condition ensures that

the laser and the computers are only triggered by muons of the right kinetic energy and not by any kind of background.

The individual efficiencies are measured to be $\epsilon_{S1} = 80\,\%$, $\epsilon_{S2up} = 32\,\%$, and $\epsilon_{S2down} = 57\,\%$. The difference stems from the unequal number of carbon foils in the stacks as well as the fact that more electrons are emitted downstream than upstream. The combined effectiveness for S_2 is calculated to be $\epsilon_{S2} = \epsilon_{S2up} + (1 - \epsilon_{S2up}) \cdot \epsilon_{S2down} = 71\,\%$, while the overall effectiveness to detect a usable muon following the coincidence condition from Eq. (2.9) is the product of the two individual stack efficiencies $\epsilon_{S1 \wedge S2} = 57\,\%$. To ensure event-quality, the cases where a second muon has been detected by any of the three detectors are specially marked as such (cf. Section B.10). The effectiveness to detect second muons can be evaluated to be

$$\epsilon_{2nd} = \epsilon_{S1} + (1 - \epsilon_{S1}) \cdot \epsilon_{S2} = 94\,\%. \tag{2.10}$$

With $\sim$ 600 muons entering the target every second, a rate of $\sim$ 330 detected and usable muons per second is achieved. The time resolution of the muon detectors is 10 ns.

2.4.2 X-ray Detectors

After the laser has induced the $2S - 2P$ transition in a μp atom, the muon deexcites to the ground state immediately emitting a 1.9 keV X-ray. Twenty large-area avalanche photodiodes (LAAPD)[4] are mounted above and below the muon stop volume and record these $2P - 1S$ X-rays [107–110] in two face-to-face rows of 10 devices. They are mounted at a vertical distance of only 8 mm from the muon beam center to maximize the solid angle and detection efficiency. The LAAPDs are silicon photodiodes (p-n junctions) with a high reverse bias voltage applied to achieve high gain. Their large surface area of ($14 \times 14\,\mathrm{mm}^2$) and the small spacing maximizes the solid angle for the X-ray detection. The LAAPDs are cooled down to -30 ^{o}C employing an alcohol cooling circuit to achieve an optimal energy resolution and signal-to-noise ratio. At this temperature, the average energy resolution for the 1.9 keV X-rays is measured to be $\sim$ 30 % at FWHM. It is determined with 5.9 keV X-rays from a radioactive ^{55}Fe source and with 2.3 keV X-rays from a sulfur fluorescence [107]. The time resolution is around 35 ns, the typical dark current $\sim$ 10 nA. Depending on the individual LAAPDs, they are biased with a reverse high voltage of 1600 – 1690 V resulting in a gain of $\sim$ 200. This way, the amplitude of the 1.9 keV X-ray signal is sufficiently above the noise level and optimal energy resolution is ensured.

The LAAPD-signals are amplified by low-noise charge-sensitive integrating pre-amplifiers followed by linear amplifiers with a gain of 16 – 128. A picture of the LAAPDs and their pre-amplifiers is shown in Figure 2.11. The signal amplitude after the pre-amplifiers is about 2 mV. After the second amplification, the negative amplitude

[4]RMD Radiation Monitoring Devices Inc, Watertown, MA 02472, `http://www.rmdinc.com`

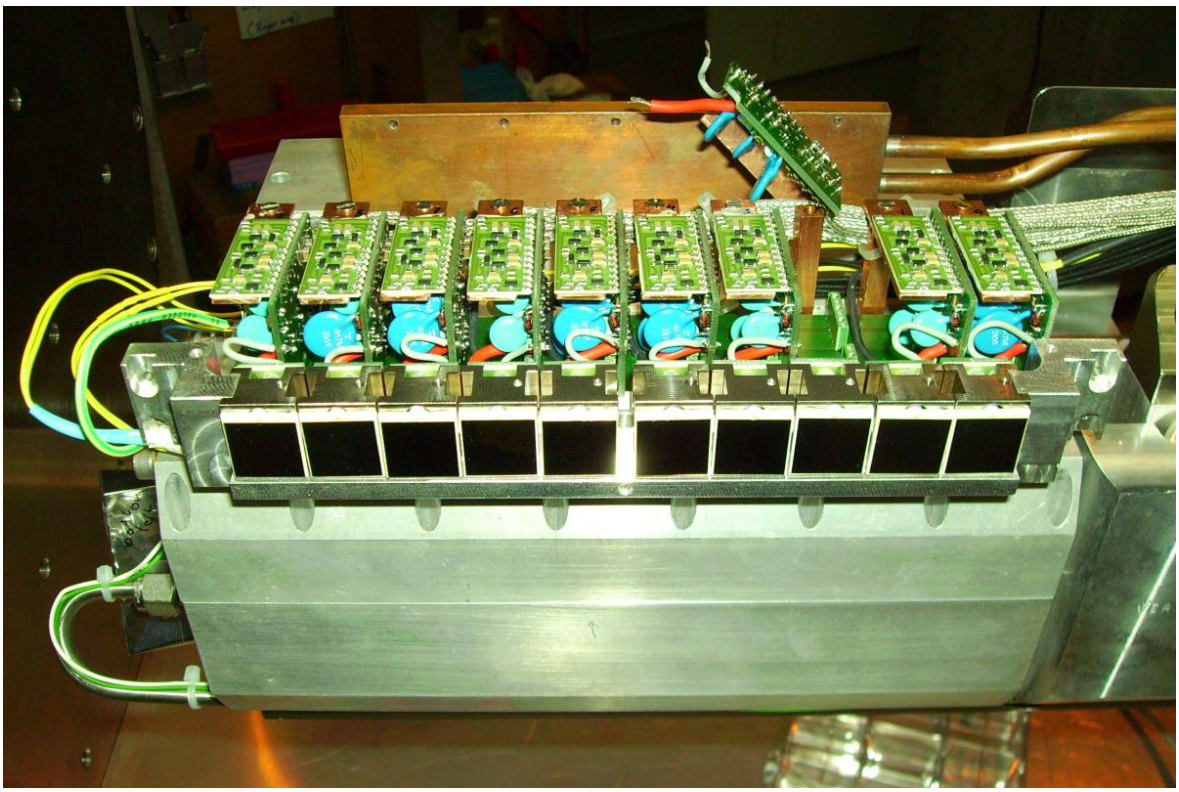

Figure 2.11: The LAAPDs and their Pre-Amplifiers. *A picture of the 10 A-side LAAPDs together with their pre-amplifiers. The LAAPDs are mounted on titanium blocks so that they can be efficiently cooled. The grounded copper shielding around the pre-amplifiers has been removed. Currently detached from the amplifiers' back side, the copper heat exchanger of the cooling circuit is visible in the back. In case of failure, the individual pre-amplifiers can be quickly replaced.*

signals are stored in 12 bit CAEN[5] wave form digitizers (WFDs). They store the data in ring buffers with a full signal height corresponding to 3752 bins (12 bit) at a length of 15 μs (4 ns per bin).

Together with their pre-amplifiers, their heat exchanger, and their compact mechanics, the LAAPDs are mounted on top and below the gas target (Sect. 2.2.3) inside the narrow bore hole (diameter 20 cm) of the target solenoid (cf. Figure 2.12). They have to be operated under vacuum in a 5 Tesla magnetic field, and they have to be insensitive to electro-magnetic and acoustic noise in the experimental hall.
The LAAPDs are labelled A0 – A9 (or sometimes 0 – 9) for the ones mounted above the target and B0 – B9 (or 10 – 19) for the ones mounted below. They are mounted in parallel to the muon beam where high numbers of the LAAPD labels are mounted further downstream (see also Figure 2.4).

[5]V1720 8 channel (250 MS/s ADC) WFDs by CAEN S.p.A., `http://www.caen.it/nuclear/`

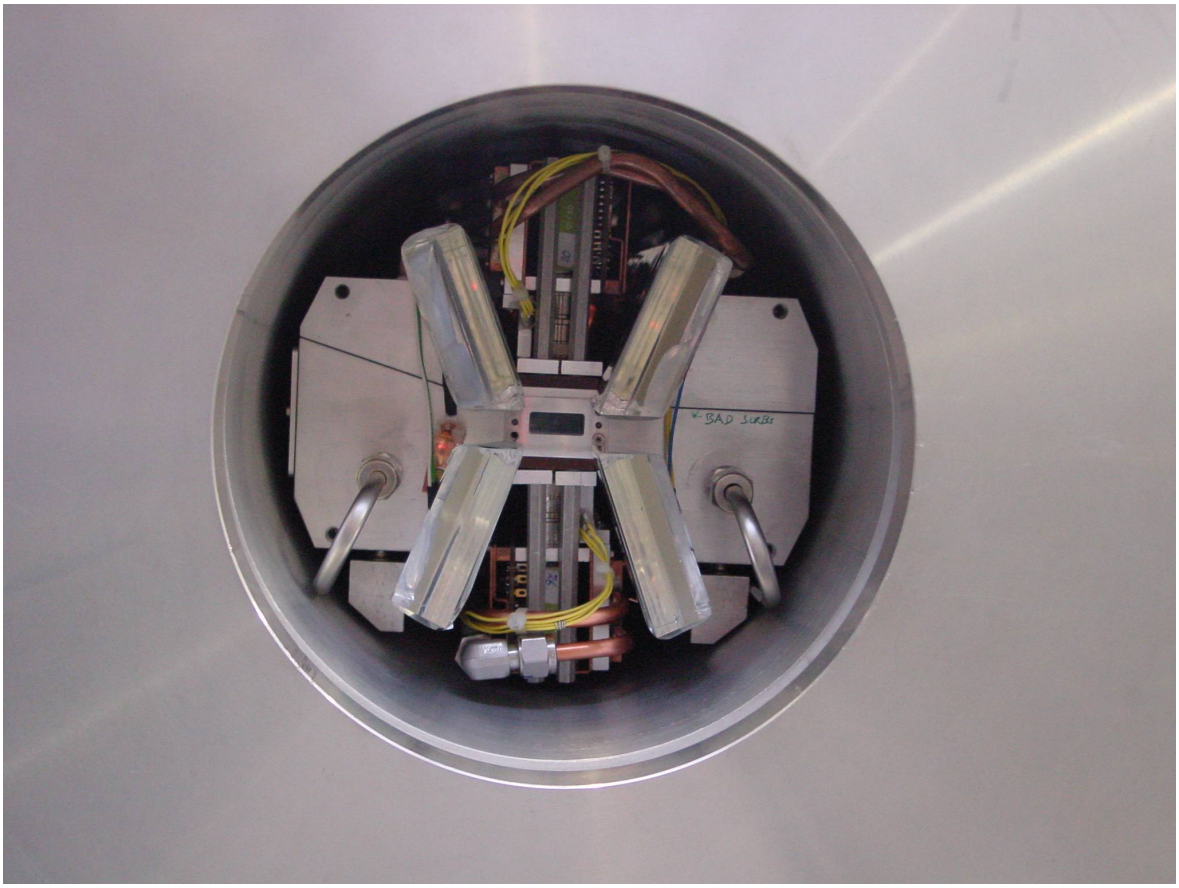

Figure 2.12: The Inside of the Target Solenoid. *A picture of the openened solenoid taken from downstream shows the target gas volume with gas inlet and outlet, the X-shaped plastic scintillators (electron paddles), and the LAAPD electronics with the pre-amplifiers (mounted vertically in the middle above and below the beam axis).*

2.4.3 Electron Detectors

The muon decay electrons are detected by four plastic scintillator plates. The left sectional view in Figure 2.4 shows a cross section of these scintillator plates in red arranged in the shape of an X. Electrons produced close to the muon beam axis spiral in the magnetic field of the target and hit the plastic scintillator plates (dimensions $250 \times 60 \times 5\,\mathrm{mm}^3$). They are connected to two photo multiplier (PM) tubes which read out the left (right) two plates, respectively. These electron detectors (also termed electron paddles) are denoted $\mathrm{E}^{left/right}$. A picture of the assembly is shown in Figure 2.12. The signal amplitude of the analog signals is processed by analog-to-digital convertors (ADCs) and stored by the data-aquisition system for the two detectors E^{left} and E^{right}. The analog signals are also sent to three discriminators each (termed low, medium, and high) which trigger on three different signal amplitudes. Time-to-digital converters (TDCs) record the timing information of the six different signals so that one is left with the timing information of the following electron detector signals: E^{left}_{hi}, E^{left}_{med}, E^{left}_{lo}, E^{right}_{hi}, E^{right}_{med}, and E^{right}_{lo}. For each of these six detector signals, a pipeline-TDC

(PTDC) is able to record more than one hit on the same detector so that multiple hits can be detected as well.

2.4.4 Laser Detectors

The entire laser system worked quite reliably during the run in 2009. Its performance is monitored by several detectors: the pulse energy of the disk laser's oscillators and amplifiers are recorded as well as the pulse energy of the pump laser light after the frequency doubling stages. Moreover, the energy of the pulsed Ti:Sapph part in the visible is logged shot-by-shot. The most important detectors of the laser system are, however, the Vigo-detectors[6] monitoring the laser light in the infra-red domain. Two fast mercury cadmium zinc telluride diodes ($Vigo_{\mathbf{in}}$ and $Vigo_{\mathbf{out}}$, see also Fig. 2.5) keep track of the 6μm light going into and out of the target cavity. They are used to calibrate the laser energy on a shot-by-shot basis. All of the above mentioned detectors are recorded and stored by the data aquisition system for every laser shot. Furthermore, a wavemeter tracked the wavelength of the visible laser pulses at the Ti:Sapph oscillator. Absolute frequency calibration is achieved by calibrated pyro-electrical detectors at the laser location and inside the beam area every few hours.

[6]Vigo System S.A., `http://www.vigo.com.pl`

Chapter 3

Data Analysis

With the experimental equipment described in Chapter 2, a measurement run with 8 weeks of setup time and a data aquisition time of 15 weeks was successfully completed in August 2009. During that time, we observed and measured 5 transitions in μp and in μd. After the 10-year-old history of this experiment (cf. Section 1.2), this was a relieving breakthrough and marked a tremendous success for the collaboration. Following the beamtime and the usual dismantling of the apparatus after a run, I started with a thorough and deliberate analysis of the recorded data of the first resonance in μp (the $2S_{1/2}^{F=1} - 2P_{3/2}^{F=2}$ transition).

This chapter gives a brief overview of this data analysis and summarize its results. For technical details on the analysing software, the methods used to analyze our data set and to extract the resonance line, the reader is referred to Appendix B. This appendix will also explain which cuts are applied to the data and how their optimum values for are deduced.

For each detected muon entering the target, the data aquisition (DAQ) system records all signals registered by the various detectors. Signals from the X-ray detectors (LAAPDs, Section 2.4.2), which are digitized by wave form digitizers (WFDs), are analyzed by the data analysis software. Together with the signals from the electron detectors (Section 2.4.3), they are combined into *events*. The events are then grouped into different classes, according to the number of recorded X-rays and electrons and their ordering. More than half of the $\sim 44 \times 10^6$ recorded events contain only electrons. Further 24 % of the events are made up of a single X-ray and a single electron. This includes the event class of interest to us: An X-ray of muonic origin followed by a muon-decay electron. Several cuts can be applied to the data belonging to the different event classes. Figure 3.1 shows the time spectra of certain event classes and points out the effect of some of the introduced cuts. The black trace is the time spectrum of all LAAPD detector hits recorded. The peak (visible in all the spectra) stems from the "prompt" muonic cascade when a muon stops in the H_2 target gas and forms a muonic hydrogen atom. During the cascade to the $1S$ ground state, K-line X-rays are emitted showing up in these spectra. Leaving the height of the prompt peak almost unchanged,

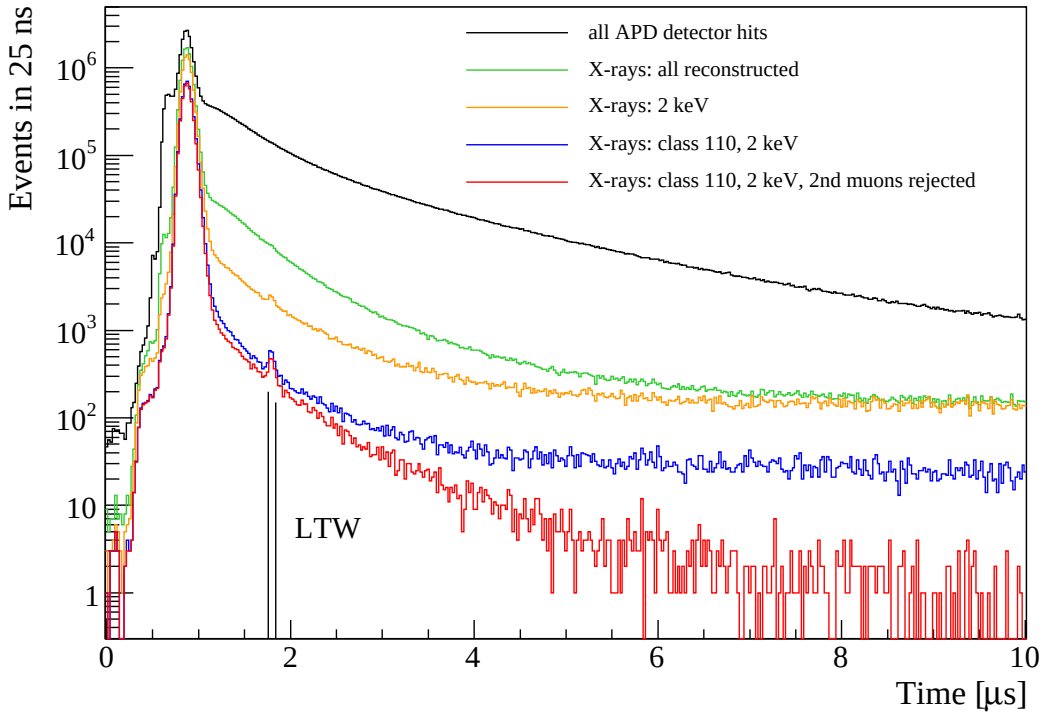

Figure 3.1: Time Spectra for different Event Classes. *The effect of the event classification and of the introduced cuts on the background at delayed times can be seen in the time spectra plotted here. The origin of the different spectra is explained in the text. The two vertical black lines indicate the laser time window (LTW) during which laser induced events are expected. The entire combination of cuts is required to reduce the delayed background level substantially and to reveal the laser-induced events in the LTW, the signal we are looking for.*

the number of events at times larger than 1 μs drops drastically when one looks at the time spectrum recorded for events containing at least one X-ray (green). Laser-induced events (i.e. K_α X-rays after the $2S - 2P$ transition has successfully been driven) can only occur when the laser pulse is illuminating the target volume. This is indicated in the figure by the laser time window (LTW). The entire procedure of data-analysis is necessary since, in the LTW, $\sim$ 1000 laser-induced events have to be distinguished from $\sim$ 5×10^5 background events. Already by looking at the X-ray events with X-ray energies of 2 keV (corresponding to K_α, orange histogram), an indication of a laser-induced peak above background is visible. One of the most important cuts is visualized through the transition of the orange to the blue histogram. Here, advantage is taken of the fact that a muon has a lifetime of $\tau_\mu = 2.2\,\mu$s and that it decays into an electron following

$$\mu^- \rightarrow e^- + \bar{\nu}_e + \nu_\mu. \tag{3.1}$$

The blue histogram represents only 2 keV X-rays with a delayed muon-decay electron detected. This event class is termed class 110 in App. B.7.2. The background here is already reduced such that a laser-induced peak is clearly visible. Finally, the red time spectrum introduces another cut and treats only those events which did not record a

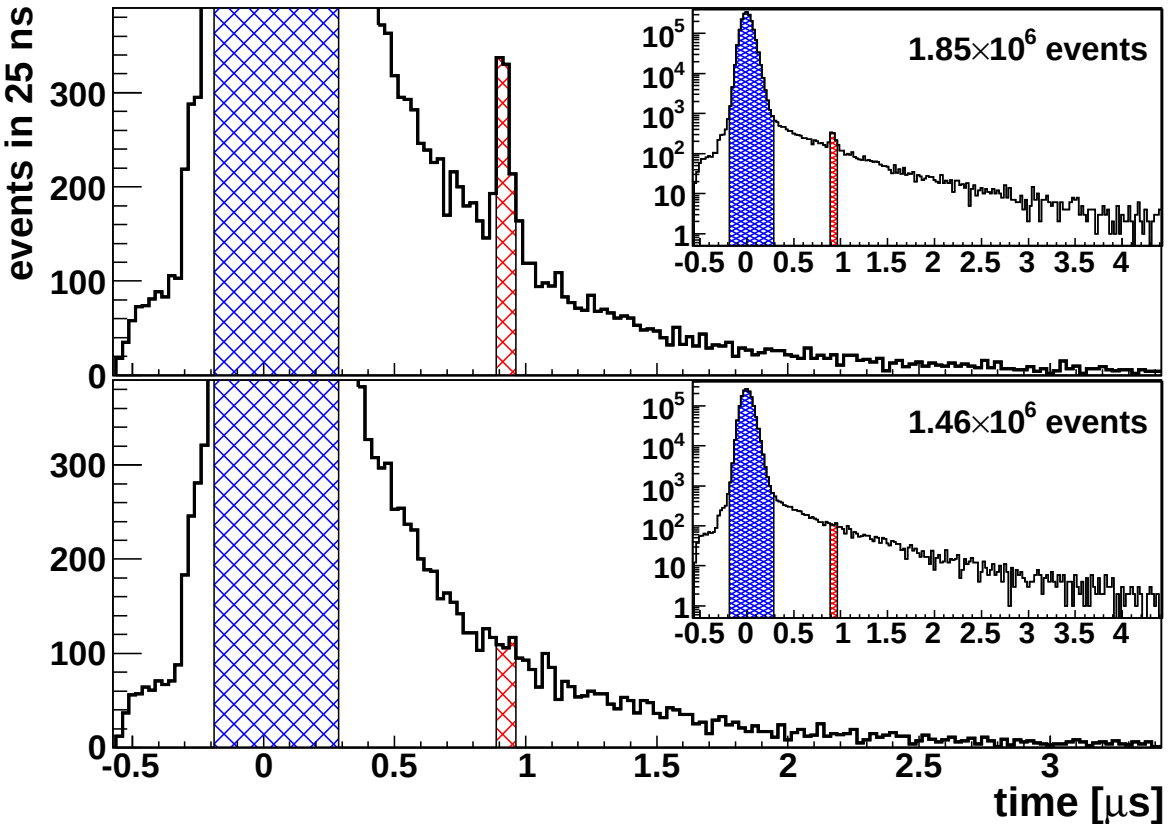

Figure 3.2: Accumulated Time Spectra on and off Resonance. *Summed X-ray time spectra recorded on resonance (top) and off resonance (bottom) shown in linear and logarithmic scale. The LTW $t \in [0.887, 0.962]\,\mu$s is indicated in red. The contribution of the prompt X-rays is marked in blue.*

second muon during a time window (*event gate*) related to the detection of the first muon (App. B.10).

In a last step, the events, which have been analyzed using the parameter-cuts introduced in Appendix B, are assigned to the laser frequency at which they have been recorded. In this way, a resonance line for the $\mu p(2S_{1/2}^{F=1} - 2P_{3/2}^{F=2})$ transition can be plotted versus the laser frequency. For this, the time information of the 2 keV X-rays with a delayed electron and without second muons present (i.e. class 110 events with 2 keV and 2^{nd} muon cuts, represented by the red histogram in Figure 3.1), are summed up into time specta, one for every laser frequency.

Figure 3.2 shows the time spectra of the mentioned X-ray class united into two groups, one on-resonance and one off-resonance. The on-resonance time spectrum is produced from events recorded ±17 GHz around the resonance peak, which has a natural linewidth of 18.6 GHz. Events from outside this range contribute to the time spectrum of the off-resonance data. In the plots, the prompt peak caused by the muonic cascade during μp formation is indicated in blue. For each laser frequency, it serves to normalize the data to the number of formed μp atoms. The 75 ns wide

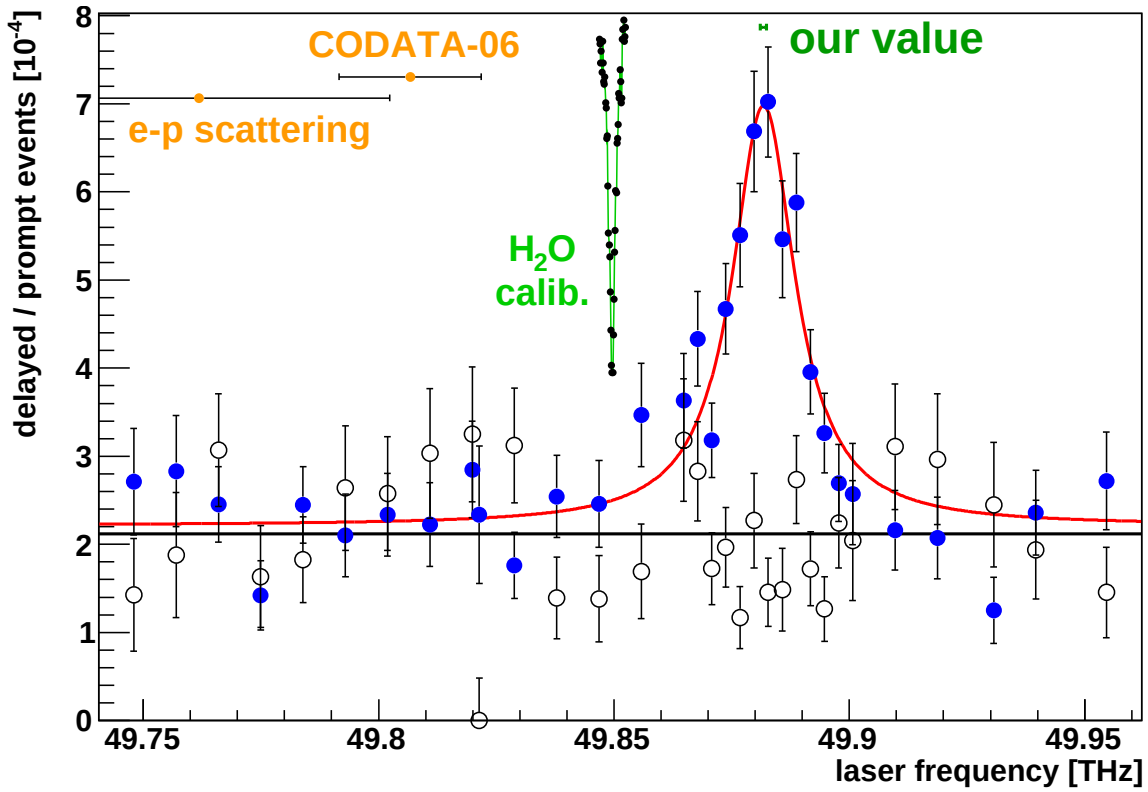

Figure 3.3: The Resonance as Obtained from this Data Analysis. *The* $2S^{F=1}_{1/2} - 2P^{F=2}_{3/2}$ *transition in* μp *is plotted versus the laser frequency (solid blue circles) obtained using generous parameter cuts introduced in Appendix B. The number of events in the LTW is normalized to the number of prompt events. The red fit is a Lorentzian profile on top of a flat fixed background. The empty circles represent data that have been recorded simultaneously under the same conditions. The only difference is that the correctly tuned laser has not been ready and could therefore not be fired. As expected, this data set does not show any indication of laser induced events. The predictions for the line position using the proton charge radius from CODATA [76] and from electron scattering [11, 111] as well as a water absorption line used for laser frequency calibration (Sect. 4.2.2) are indicated.*

LTW ($t \in [0.887, 0.962]\,\mu$s) is marked in red. It coincides with the LTW decuded from time calibration in App. B.5.2. Note the clear excess of events in the LTW of the on-resonance time spectrum.

The $2S - 2P$ resonance line is plotted in Figure 3.3. It is obtained by plotting the number of K_α events recorded in the LTW, normalized to the number of prompt events, as a function of the laser frequency. The fit to the data is a simple Lorentzian profile on top of a flat background. The data analysis with its rather wide parameter-cuts (which is explained in detail in Appendix B) is optimized such that the statistics and the position determination of the resonance line is maximized (which is accompanied by a degradation of the signal-to-background ratio). A more detailed treatment is given in Section 4.4 where this resonance is contrasted with the resonance obtained

from stringent cuts. With the wide cuts, we have in total measured 900 events in the resonance where 404 background events are expected. Three of the four parameters, namely the position of the Lorentzian, its amplitude, and its width are varied freely. Only the background amplitude is fixed to the value obtained from a fit to data recorded without laser (empty circles in Fig. 3.3). It agrees well with the extrapolated background amplitude in the LTW in the Laser_{on} data.

A centroid position of $49\,881\,700 \pm 670\,\text{MHz}$ and a width of $17.1 \pm 2.0\,\text{GHz}$ are extracted (cf. third item im Table 4.1). The uncertainties quoted are of statistical nature. The width is a bit smaller than the $19.0 - 20.5\,\text{GHz}$ expected in Section 4.3.7. A value of $\chi^2 = 32.2$ for 28 degrees of freedom (dof) or $\chi^2/dof = 1.15$ is associated with the fit. A fit of a flat line, assuming no resonance, would result in $\chi^2 = 251.9$ for 31 dof ($\chi^2/dof = 8.13$), making this line $15\,\sigma$ significant. For a final resonance including a more elaborate fit-model, the laser frequency calibration, and the systematics, refer to Section 4.4. The measurement time has varied between 3 and 13 hours per laser frequency. The data has been recorded at a rate of 8 events per hour in the LTW when on resonance. The background of $\sim 2\,\text{event/hour}$ originates mainly from falsely identified muon-decay electrons and from effects related to delayed muon transfer to the target walls.

Chapter 4

Calibration, Systematics, and Results

The resonance line for the $\mu p(2S^{F=1}_{1/2} - 2P^{F=2}_{3/2})$ transition as it is obtained from the analysis procedure of this thesis is presented in the previous chapter. A detailed description of the data-analysis that finds this resonance line can be found in Appendix B.

The first section of this chapter deals with the question whether a line-shape model is needed to fit the resonance properly (Section 4.1). It continues with the laser-frequency calibration (Sect. 4.2) in the visible and infra-red domain and with possible systematic effects (Sect. 4.3) influencing the position of the resonance line. As in the previous chapter, we focus on the $\mu p(2S^{F=1}_{1/2} - 2P^{F=2}_{3/2})$ transition, although many of the considerations are valid for the other recorded lines, as well. Section 4.3.6 summarizes all systematic and statistical uncertainties and gives a value for the expected linewidth. Finally, in Section 4.4, our obtained frequency of the first μp resonance is derived, and in Section 4.6, the other four transitions in μp and μd are introduced as preliminary results.

4.1 Laser Energy: Line-Shape Model

In order to account for laser pulse energy variations during the measurements, a model is developed to describe the intensity dependence of the resonance line-shape correctly [112]. During the 2009 data-taking period, the 6 μm laser pulse energy was recorded on a shot-by-shot basis with the help of several kinds of detectors. A fast calibrated pyro-electric detector (*Ophir*[1]) is used inside the laser hut to measure the pulse energy directly after the Raman cell in a humidity-free environment (see Sect. 2.3 for a description of the laser system). The laser energy is measured at a repetition rate of 250 Hz because this device cannot handle stochastic repetition rates. Another (slow) pyro-electrical detector (*Pyro*) monitors the laser energy in the muon beam area just outside the dry-nitrogen atmosphere before the target. Two fast mercury cadmium

[1] Ophir-Spiricon, LLC, `http://www.ophir-spiricon.com`

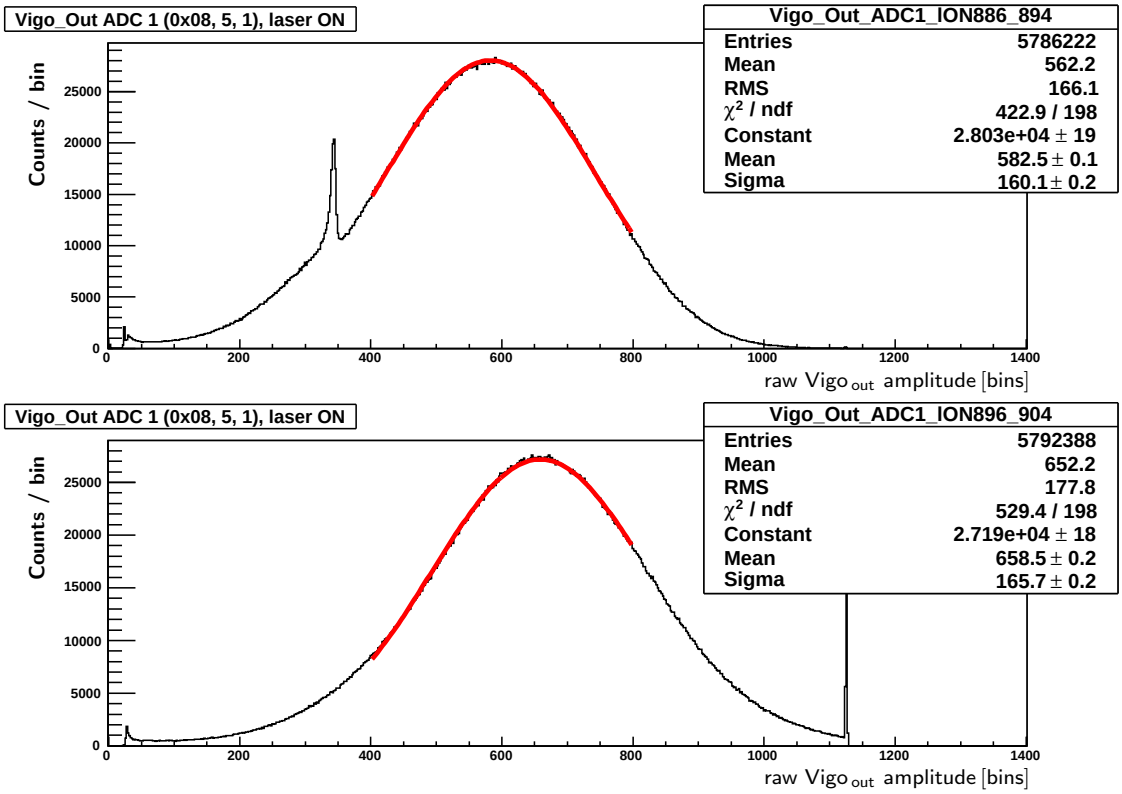

Figure 4.1: Uncalibrated Laser Energy Asymmetry. *The **uncalibrated** laser pulse energy observed in **Vigo$_{\mathbf{out}}$**. **(Top)** Summed up raw ADC values for all runs up to 13 GHz to the left of the center of the resonance (Fabry-Pérot (FP) fringes 886 – 894). The peak at raw amplitude $a \approx 350$ bins stems from a broken ADC-channel during some of the runs. **(Bottom)** The figure represents the runs up to 13 GHz to the right of the resonance's center (FP 896 – 904). Here, the ADC saturates at $a \approx 1120$ bins. The Gaussian fits to the distributions reveal a center position of $a_L = 583$ bins and $a_R = 659$ bins, respectively.*

zinc telluride diodes serve to monitor the light going into and out of the target cavity (*Vigo*$_{\mathbf{in}}$ and *Vigo*$_{\mathbf{out}}$, respectively). Since these diodes *Vigo*$_{\mathbf{in}}$ and *Vigo*$_{\mathbf{out}}$ only need a fraction of the used laser light, they are able to record the laser pulse energies for each event *while* the actual resonance-search takes place. For measurements with the pyro-electric detectors, on the other hand, the instruments have to be moved into the laser beam. This makes it necessary to insert exclusive short runs for laser energy measurements. Their aim is to obtain absolute energy calibration of the various laser detectors.

Introducing the problem

On resonce, the transition rate W_{ge} to drive muons from the initial (here label g for ground) to the excited state of the $\mu p(2S_{1/2}^{F=1} - 2P_{3/2}^{F=2})$ transition is given by Equation (E.23) in [88]:

$$W_{ge} = 8\,\pi \frac{\alpha}{\hbar} \cdot |\langle e|\epsilon \cdot \mathbf{r}|g\rangle|^2 \cdot \frac{I}{\Gamma}, \tag{4.1}$$

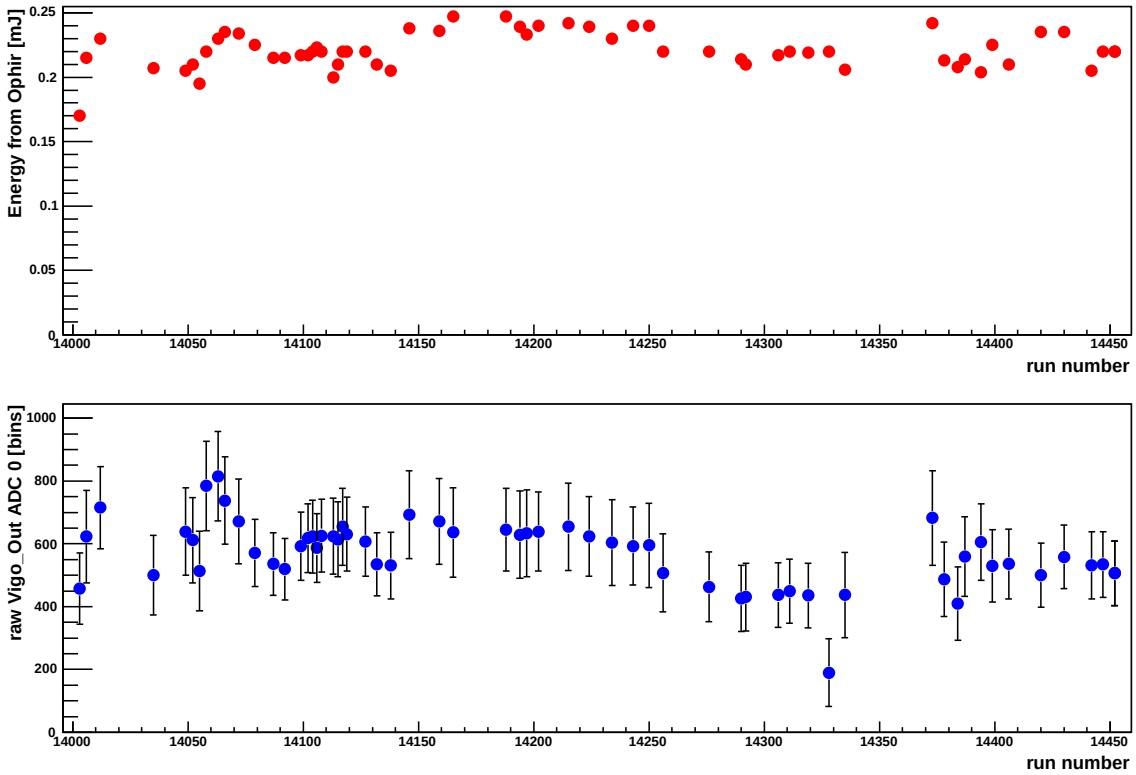

Figure 4.2: Calibration Data Available for *Vigo*$_{\mathbf{out}}$. *Neighbouring energy measurements of the two detectors* ***Ophir*** *and* ***Vigo*$_{\mathbf{out}}$** *are plotted here versus the run number. Runs which are directly followed or preceded by an* ***Ophir*** *calibration are considered. While the top plot shows the calibrated laser energy measurements (in mJ) performed with the* ***Ophir*** *detector, the bottom one charts the raw* ***Vigo*$_{\mathbf{out}}$** *ADC values. This plot is obtained from the center position of a Gaussian profile fitted to raw* ***Vigo*$_{\mathbf{out}}$** *ADC spectra as shown in Fig. 4.1. The error bars on this data set are the widths of the Gaussian fitted to the raw spectra. Both data sets coincide acceptably in their behaviour except around run #14328, where a fast drop in the laser energy occured.*

with the fine structure constant α, the transition matrix element $|\langle e|\epsilon \cdot \mathbf{r}|g\rangle|^2 = 5\, a_\mu^2$ (laser polarization ϵ, muon position operator $\mathbf{r}$), the natural line width of the resonance $\Gamma = 2\,\pi\,\Gamma_\nu = 117 \times 10^9\,\mathrm{s}^{-1}$, and the laser intensity I. The transition rate scales linearly with the laser intensity I which might cause a distortion of the resonance line if intensity variations occured during the campaign. A careful study of the laser energy calibration and the influence on the shape of the resonance line is, therefore, mandatory.

During the course of the run in 2009, a 13 % asymmetry in the **uncalibrated** laser energy was observed when comparing the left and right hand side of the resonance line. The information is given by the summed up raw *Vigo*$_{\mathbf{out}}$ ADC (analog-to-digital converter) spectra: Figure 4.1 shows Gaussian fits to the two summed up raw energy spectra for all events recorded between FP-fringe 886 – 894 (left side) and between 896 – 904 (right side). They are centered at a raw *Vigo*$_{\mathbf{out}}$ amplitude $\mathrm{a}_L = 583$ and

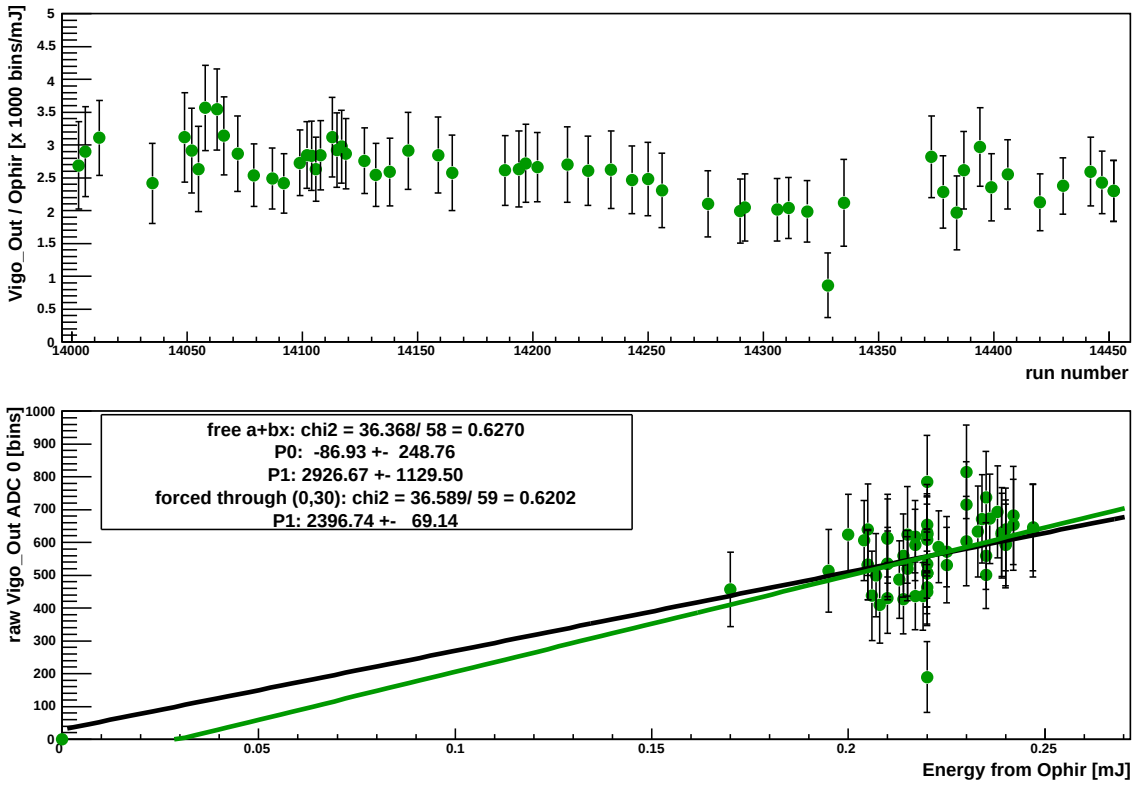

Figure 4.3: Correlation between *Vigo*$_{\mathbf{out}}$ and *Ophir*. ***(Top)*** *The ratio of* ***Vigo*$_{\mathbf{out}}$/*Ophir*** *in units of* [10^3 bins/mJ] *is plotted versus the run number.* ***(Bottom)*** *The scatter plot plots the raw* ***Vigo*$_{\mathbf{out}}$** *ADC value versus the laser energy measured with the* ***Ophir***. *It is given with a free linear fit (green line) and a linear fit forced through (0,30) with 30 being the known zero-point of the ADCs (black line). In both plots, the one prominent outlier belongs to run #14328, as explained in the text.*

$a_R = 659$, respectively. This asymmetry is treated in the following discussion.

According to investigations on a model Lorentzian resonance line on top of a flat background with one side of the Lorentzian being multiplied by a factor c, the shift of the fitted line center would be as large as 51 MHz/ΔE[%], resulting in a shift of 660 MHz for our apparent asymmetry of 13 %. Here, ΔE[%] is the left/right difference in laser energy given in percent.

Correlation between the laser detectors

In order to be able to calibrate the laser pulse energy adequately, a correlation between the laser detectors has to be established. For this, the relation of subsequent *Vigo*$_{\mathbf{out}}$ and *Ophir* measurements is examined in Figure 4.2. Figure 4.3 plots the correlation between the two as a ratio and in a scatter plot. A moderate correlation between the 6 μm energy measured with the *Ophir* in the laser hut at 250 Hz and with the *Vigo*$_{\mathbf{out}}$ detector at the exit of the target cavity can be identified. Except around run #14328 where the laser energy decreased on a fast time scale, the calibration

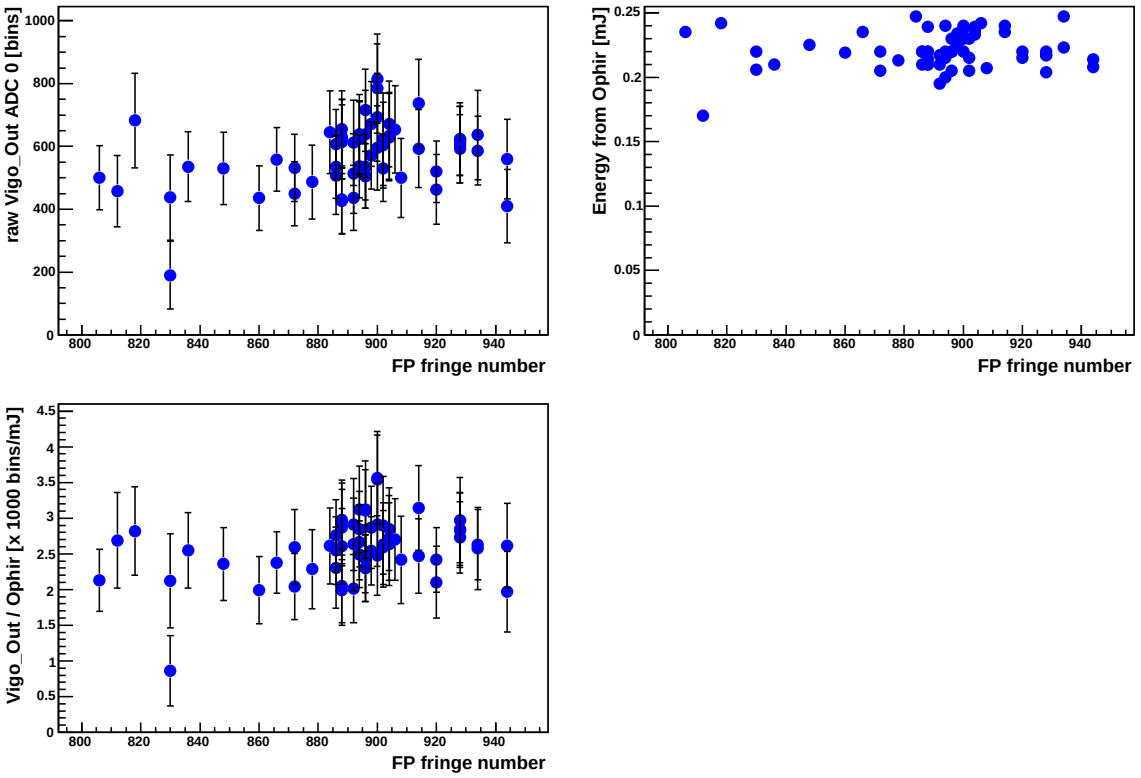

Figure 4.4: Frequency-Dependence of *Vigo*$_{\mathbf{out}}$ and *Ophir*. *The laser energy measurements from the raw* ***Vigo***$_{\mathbf{out}}$ *ADC and the calibrated* ***Ophir*** *detector are plotted versus the FP fringe number (equivalent to the laser frequency). Furthermore, their ratio (****Vigo***$_{\mathbf{out}}$***/Ophir****) is shown. Neither plot shows a systematic frequency-dependence of the laser energy.*

factor is only slowly-varying. This slow drift should most probably be attributed to long-term variations in the laser alignment between the laser hut and the beam area, or between the target cavity and *Vigo*$_{\mathbf{out}}$, or both.
To conclude, one can use the amplitude of *Vigo*$_{\mathbf{out}}$ to calibrate the laser pulse energy on a shot-by-shot basis using the nearest available *Ophir* calibration. The correlation for *Vigo*$_{\mathbf{in}}$ is slightly worse. Therefore, this detector serves as a backup calibration for cases where no information could be retrieved from *Vigo*$_{\mathbf{out}}$.

Asymmetry in the calibrated energy

The above mentioned method is used to calibrate the laser pulse energy of the first μp-resonance. The left/right asymmetry in the **calibrated** *Vigo*$_{\mathbf{out}}$ data is reduced significantly to only 4.6 %: the centroid of the fitted Gaussians are now found at $E_L = 0.212\,\mathrm{mJ}$ and $E_R = 0.222\,\mathrm{mJ}$, respectively.

The low asymmetry after the energy calibration shows that the strategy to search for and scan the resonance line during the beam time is appropriate: to average out possible systematic long-term drift in the experimental conditions (especially concerning the laser system), the laser frequency has been altered at short intervals of typically 3 hours

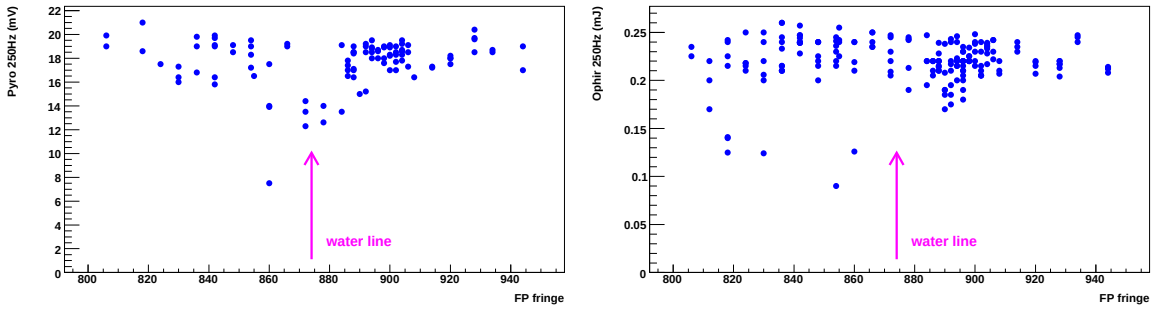

Figure 4.5: Influence of the Water Absorption on *Ophir*. ***Pyro*** *and* ***Ophir*** *data are plotted versus the FP fringe (equivalent to the laser frequency) to reveal a possible influence of a water-absorption line on the laser calibration quality. While for the* ***Pyro*** *detector (left), a dip at the location of the water line is fairly visible,* ***Ophir*** *does not exhibit such a dependency (right).*

over the entire scanning range. Nevertheless, the influence of the laser energy on the resonace line position will be studied more rigorously in the following sections.

Frequency-dependence of the 6 μm energy calibration

Experience gathered from earlier campaigns demand verification whether the 6 μm energy calibration is dependent on the laser frequency ν. In 2003, such a dependency could be observed in $Vigo_{\mathbf{in}}$ originating from an ethalon-effect in a CaF_2 beam splitter plate. The plano-parallel plates have been substituted by wedges suppressing this unwanted effect. In Figure 4.4, no frequency-dependence is visible in either the $Vigo_{\mathbf{out}}$ or the *Ophir* detector.

Furthermore, the independence of the *Ophir* data from water absorption effects has to be established. For this, Figure 4.5 compares the *Ophir* with the *Pyro* data. For a *Pyro* measurement, the laser light has to pass through ~ 10 cm of air. The *Pyro* data shows a slight dip at the location of a water absorption line. Since the *Ophir* detector is installed next to the laser beam inside a nitrogen-flushed housing, its data is free of any frequency dependent decline.

Energy line-shape model

The effect of the laser pulse energy on the resonance line is investigated more rigorously by introducing a line-shape model (LSM) accounting for laser energy induced systematic correlations. In order to do so, all recorded events are grouped into slices according to their calibrated laser energy. For every energy slice, the time spectra of the ($\mathbf{X}$+$\mathbf{e}^-_{delayed}$)-class (cf. Sect. B.7.2) with all applicable cuts are filled the usual way, and the number of "delayed/prompt" events are determined for every laser frequency. From this, a resonance-plot can be produced for every energy slice, as presented in Figure 4.6.

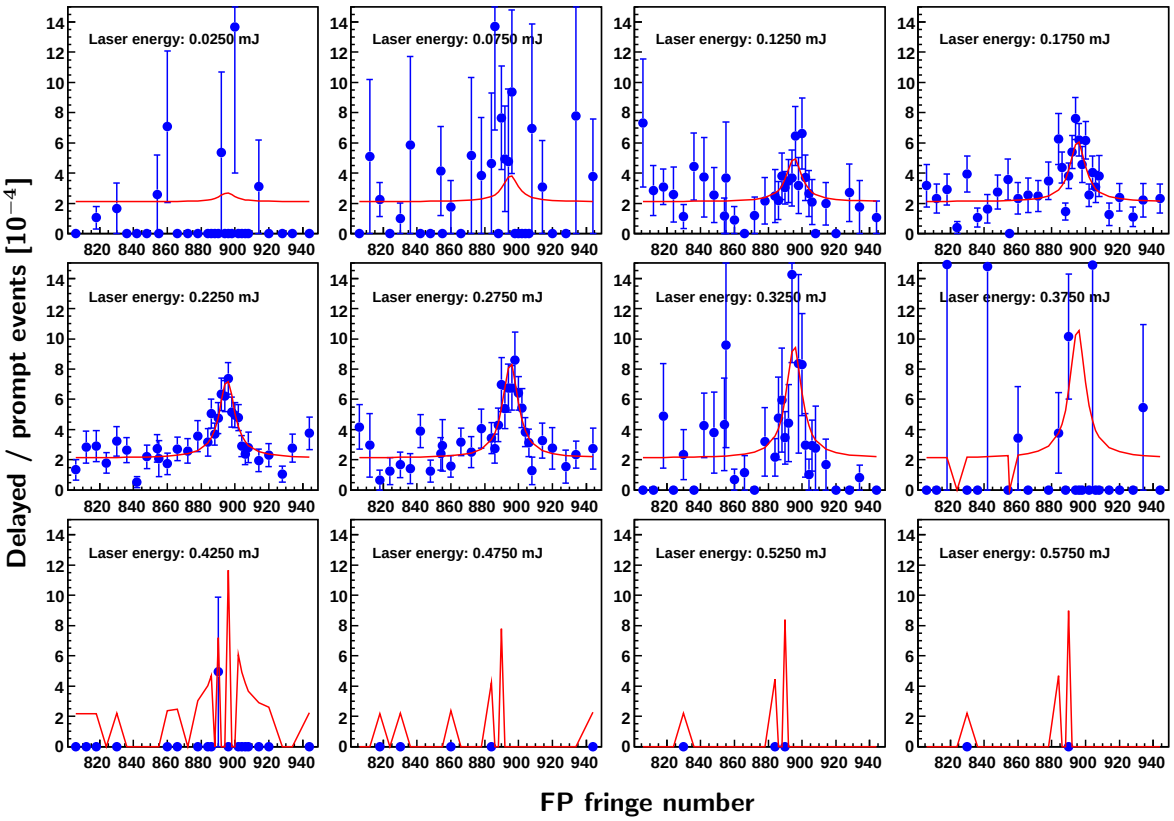

Figure 4.6: Energy Line-Shape Model Fit. *A correlated simultaneous fit of resonance data sets of several laser energy slices is shown here in red. For each energy slice, the number of delayed/prompt events is plotted versus the FP fringe number. The fitted resonance scales with the laser energy (given by the center of each energy slice) as is explained in the text. The error bars are purely statistical. A missing data point implies no available prompt events with this laser energy at the specific FP fringe. The red resonance line is only evaluated at existing data points and set to zero where no data is available. This explains the structure of the fit at higher laser energies where the statistics decreases.*

Finally, all resonance data are fitted simultaneously using an unsaturated Lorentzian profile of the form

$$f(\nu; BG,\, A,\, \gamma,\, \nu_0)_{fit} = BG + A \cdot I \cdot \frac{\gamma^2}{(\nu - \nu_0)^2 + \gamma^2}. \tag{4.2}$$

In this fit-function, the background amplitude BG, the resonance line's amplitude A, the half width at half maximum (HWHM) $\gamma = \frac{1}{2}\,\Gamma$, and the line position ν_0 are common fit parameters to all the resonance lines for the different laser intensities. The parameter I is set to the laser intensity for which the respective resonance data are obtained and ensures that the linear relation between the laser intensity and the transition rate is taken into account. In such a way, the different resonance lines are connected through the mentioned common parameters:

- a correlated amplitude of the resonance line that increases linearly with the laser energy,

Fit Procedure	**Center** [FP-fringes]	**Width** [FP-fringes]	**Background** [$\times 10^{-4} N_{prompt}$]	$\boldsymbol{\chi^2}$
Lorentz, free BG	895.35(44)	10.87 ± 1.45	2.21 ± 0.12	$31.6/28 = 1.13$
LSM, free BG	895.32(43)	10.54 ± 1.34	2.23 ± 0.12	$245.4/282 = 0.87$
Lorentz, fixed BG	895.33(45)	11.40 ± 1.34	2.12 ± 0.00	$32.2/28 = 1.15$
LSM, fixed BG	895.29(43)	11.08 ± 1.27	2.12 ± 0.00	$246.2/282 = 0.87$

Table 4.1: Comparison of the Fit Results. *Both the simple Loretzian fit and the line-shape model (LSM) fit are evaluated once with a freely varying background (BG) and once with the background amplitude fixed to the value extracted from the Laser$_{off}$-data. Width and center position are given in FP-fringes (equivalent to the laser frequency). A value of 282000 has to be added to the position value to get to the absolute FP-fringe number. All fits yield essentially the same center position. Although well inside the uncertainty, the widths for the free fit are slightly smaller.*

- an identical relative background amplitude, and
- an identical position and width of the fitted Lorentzian.

In such a way, the influence of the laser energy on the signal amplitude is taken into account. For every resonance line, the center of the energy slice is set to be the value for the laser energy.

A Poissonian maximum likelyhood fit is applied which, in contrast to a Gaussian χ^2-fit, can deal with low statistics data sets. It handles the probability correctly, for instance, to measure zero events when 3×10^{-4} are expected. Figure 4.6 displays an example of such a fit.

Center position: comparison of the fit methods

Finally, the newly developed line-shape model shall be compared with the ordinary Lorentzian fit. Both use a maximum likelihood minimization. The simple Lorentzian method treats all data independently of the associated laser pulse energy and fits an unsaturated Lorentzian to one set of resonance data.
The line-shape model fit makes use of the available laser pulse energy information and produces resonance data sets for each laser energy slice. For every run, it extracts the energy calibration from the detector *Vigo*$_{\mathbf{out}}$ ADC 0, or, if not yielding any information, from *Vigo*$_{\mathbf{out}}$ ADC 1, *Vigo*$_{\mathbf{in}}$ ADC 1, or *Vigo*$_{\mathbf{in}}$ ADC 0 (in this order, according to their quality). This way, the broken ADC-channels visible in Fig. 4.1 are taken care of.

Table 4.1 opposes the two fitting methods to each other. Both are once evaluated with the background varying freely and once with a background amplitude that is set

to the level extracted from the Laser_{off} data. All four center positions are almost identical. The fact that the background amplitude of the fixed fit is set to be slightly smaller than the one of the free fit is the reason that the width is larger. With a FSR of the FP of 1.5 GHz, the difference in the line positions is equivalent to 50 MHz, which is negligible compared to the statistical and systematic uncertainties (evaluated to be ~ 700 MHz in Section 4.4). The fact that the results of the simple Lorentzian fit and the LSM do not differ can be attributed to a randomized scan over the resonance during the beamtime: the laser-frequency has been changed frequently in a random way in order to average out laser intensity, as well as other fluctuations. Because the LSM represents the experimental conditions the best, its results are used for further analysis (with fixed background).

4.2 Laser-Frequency Calibration

To ensure correct frequency calibration of our laser system, the laser has to be calibrated in the visible as well as the infrared region. Before, during, and after the 2009 beamtime, spectroscopy has been performed repeatedly on rubidium, on iodine, and on cesium using the 708 nm light from the cw Ti:Sapph laser.
Several water absorption lines are utilized to calibrate the laser in the infrared domain. Introduced in the next two sections, both methods, in the visible and in the infrared region, are consistent with each other. With a statistical uncertainty of the $2S-2P$ resonance line of ~ 600 MHz (Sect. 4.4), the uncertainty of the laser frequency calibration should stay well below this value.

4.2.1 Calibration in the Visible

A Fabry-Pérot (FP) cavity serves as a frequency-marker to control the Ti:Sapph laser in the visible red by locking the cw-laser to one of its transmission peaks (see Sect. 2.3). The calibration of this FP and the verification of its long-term stability is described here.
The integral part of the FP cavity is a Zerodur spacer (L = 0.1 m) with optically contacted mirrors in a flat-concave configuration (R = 0.6 m). It is kept under vacuum and shielded from environmental fluctuations by being mounted into a thick-walled brass cylinder. The finesse of ~ 310 is given by the reflectivity of 99.5 % of the dielectric mirrors.

To first approximation, the frequency of the FP transmission peaks can be expressed by

$$\nu_N = N \cdot \text{FSR} + \Delta_F, \tag{4.3}$$

where the free spectral range $\text{FSR} = c/2L$, and Δ_F is the frequency shift due to the

Fresnel-dephasing ϕ_F introduced by the curvature of the mirror:

$$\Delta_F = \mathrm{FSR} \cdot \phi_F = \mathrm{FSR} \cdot \frac{1}{\pi} \arccos \sqrt{\left(1 - \frac{L}{R_1}\right)\left(1 - \frac{L}{R_2}\right)} = 201\,\mathrm{MHz} \tag{4.4}$$

Between 2003 and 2009, the FP cavity was calibrated in the range of $377 - 417\,\mathrm{THz}$ in Paris and at PSI. Three data-sets are available [113]:

- In 2003, the positions of the FP peaks were measured with respect to a two-photon transition and the D1 and the D2-lines in rubidium.
- The FP-fringes were also compared to 17 transition lines in iodine near 708 nm; two measurements performed in 2007, the rest in 2009.
- Five Doppler-free two-photon transitions in cesium served as a calibration reference near 707 nm, 719 nm, and 743 nm in 2009.

Rubidium

With the 2003 rubidium-spectroscopy data, a first estimate for the frequency calibration of the FP can be performed. This data has been obtained by measuring the frequency difference (beat) between two lasers, one locked to the FP and the other to a rubidium line measured by saturation absorption spectroscopy in a cell. The frequencies of three FP peaks at 794 nm, 780 nm, and 778 nm were measured to be

$$\begin{aligned}\nu_1 &= 377\,112\,236.8\,\mathrm{MHz}\\ \nu_2 &= 384\,227\,643.3\,\mathrm{MHz}\\ \nu_3 &= 385\,284\,770.3\,\mathrm{MHz}.\end{aligned}$$

From this, one can extract a first linear fit for the frequency of the N-th peak of the FP

$$\nu_N = N \cdot 1497.349619\,\mathrm{MHz} + 243.085\,\mathrm{MHz}, \tag{4.5}$$

which has a standard deviation $\sigma = 0.92\,\mathrm{MHz}$. The difference between the constant offset of 243.085 MHz and the calculated Fresnel shift (Eq. (4.4)) can be attributed to a frequency-dependent dephasing caused by the dielectric coatings of the cavity-mirrors. Light of higher frequency is reflected deeper in the coating resulting in a longer effective cavity length. This results compares with Eq. (4.3) so that a first estimate for the FSR = 1497.3496 MHz can be extraced.

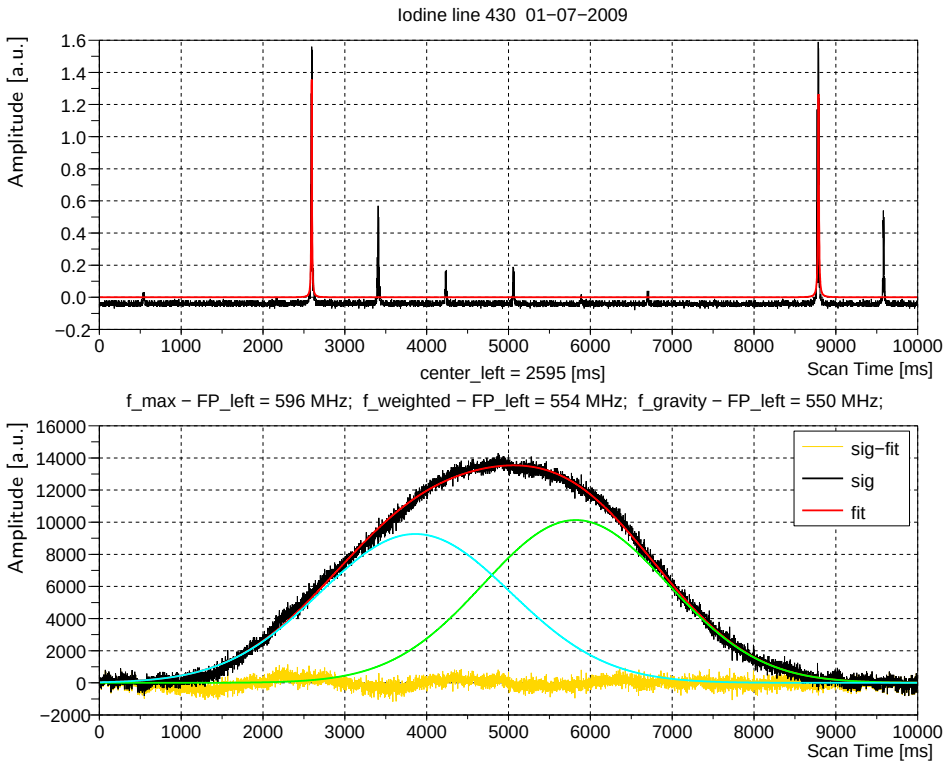

Figure 4.7: Example of an Iodine Absorption Spectrum. *The bottom plot shows one measurement of an absorption spectrum of the iodine line N° 430 versus the scan time which is proportional to the frequency. Since the line-shape stems from a convolution of overlapping, Doppler-broadened hyperfine lines, it is fitted phenomenologically with a sum of two Gaussians (green and cyan). The difference between the fit result (red) and the signal is drawn in yellow. A plot of the FP transmission spectrum is shown in the top figure. The FP is slightly misaligned to expose its higher-order transversal modes. The red function fits the principal transmission peaks omitting the higher order modes, and evaluates the center of the left peak to be at 2595 ms. With the help of the free spectral range of the FP (*FSR = 1497 *MHz) the relative position of the recorded peaks can be evaluated. For further analysis, the difference between the left FP peak and the fit-maximum of the iodine line* $f_{max} - FP_{left} = 596\,MHz$ *is used.*

Transition	Frequency from [116] [MHz]	FP-fringe number	Line Position to nearest FP-fringe [MHz]		Frequency of FP-fringe [MHz]	Diff. to Eq. (4.7) [MHz]
6S-10S (F=4)	424207800.3	283306	- 227.5	(17.3)	424208027.9	14.9
6S-10S (F=3)	424212270.9	283309	- 238.8	(21.1)	424212509.7	4.7
6S-9S (F=4)	403378771.1	269395	180.4	(12.6)	403378590.6	-3.4
6S-9S (F=3)	403383147.7	269398	63.4	(6.5)	403383084.4	-1.6
6S-8$D_{5/2}$ (F=4)	417052469.6	278527	235.5	(8.3)	417052234.1	-25.2

Table 4.2: Positions of Cesium Lines. *With the one-photon transition frequencies from Weber et.al. [116] (second column) for the stated two-photon transitions in cesium (obeying $\Delta F = 0$), and the fits according to Fig. 4.8, the frequencies of the nearest FP-fringes can be determined (fifth column). The uncertainties of the one-photon transition frequencies are stated in [116] to be 7.5 MHz. The relative line positions are an average of all available measurements at the respective transition. The last column states the difference of the obtained absolute FP-frequency to the final formula of Eq. (4.7).*

Iodine

Iodine absorption spectroscopy was performed in 2007 and 2009. In total, 76 spectra of 17 iodine lines are available. From the *"Atlas du spectre d'absorption de la molecule de l'iode entre 14000–15000 cm^{-1}"* [114], the measured lines between 14120 cm^{-1} – 14392 cm^{-1} are known to an accuracy of 180 MHz. The absorption spectra are recorded simultaneously with the transmission through the FP cavity, as shown in Fig. 4.7. They are fitted phenomenologically with a sum of two Gaussians, and the maximum of the fitted curves are used as results for the line positions. The absorption lines N^{o} 429 and N^{o} 430 were recorded 27 and 24 times, respectively, over a period of two years. From the 51 individual measurements, averages for the peak positions can be determined. Their relative positions to the nearest FP fringe are evaluated to $\Delta\nu_{429} = 701(31)$ MHz and $\Delta\nu_{430} = 565(26)$ MHz. The line positions do not exhibit any significant drift with respect to time nor any major scatter. From the 17 line positions, which were measured relative to FP fringes, one can extract the frequencies of those FP peaks. In order to do so, one has to take into account the mentioned uncertainties from the atlas and use a corrected frequency introduced in [115]:

$$\nu_{corr} = \nu_{atlas} \cdot (1 + 1.7 \times 10^{-7}) - 8.1 \times 10^{-3}\,(\mathrm{cm}^{-1}). \tag{4.6}$$

This correction stems from a refined model of the rovibrational levels of the I_2 molecule and a careful fit to all available data. For 14200 cm^{-1}, it corresponds to about −170 MHz. The accuracy of the line determination is refined to 30 MHz.

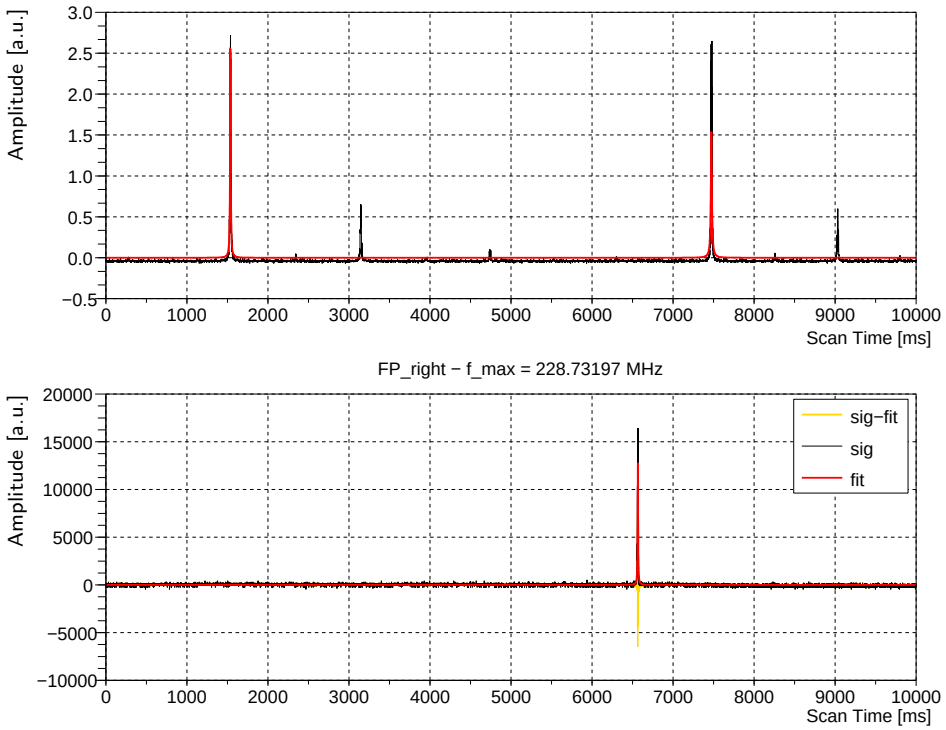

Figure 4.8: Example of a Cesium Two Photon Resonance. *The bottom plot shows a record of the $6S_{1/2} - 10S_{1/2}$ two-photon transition in cesium. It is much narrower than the iodine absorption spectra. A Gaussian is fitted to the data to determine the center of the transition. The relative position with respect to the nearest FP-fringe from the top plot is calculated from the difference of the two centers and accounts to $FP_{right} - f_{max} = 228.7\,MHz$. The exact amplitude structure of the FP modes beside the principal mode depends on the incoupling of the laser and differs slightly from the one in Fig. 4.7.*

Cesium

In October 2009, several Doppler-free two-photon transitions were observed in cesium, namely

- two hyperfine components (F = 3 and F = 4) of the $6\,S_{1/2} - 10\,S_{1/2}$ transition around 707 nm,
- two hyperfine components (F = 3 and F = 4) of the $6\,S_{1/2} - 9\,S_{1/2}$ transition near 743 nm, and
- the $6\,S_{1/2} - 8\,D_{5/2}$ transition near 719 nm starting from the F = 4 hyperfine level.

Here, the detection signal is obtained by collecting the decay-photons of the metastable upper states with a photo multiplier tube. An example of such a recording is shown in Fig. 4.8 and the results of the cesium measurements are collected in Tab. 4.2. The FP-fringe positions are obtained by comparing the fitted Cs-lines to the values obtained from Weber and Sansonetti [116], who cite an uncertainty of 7.5 MHz for

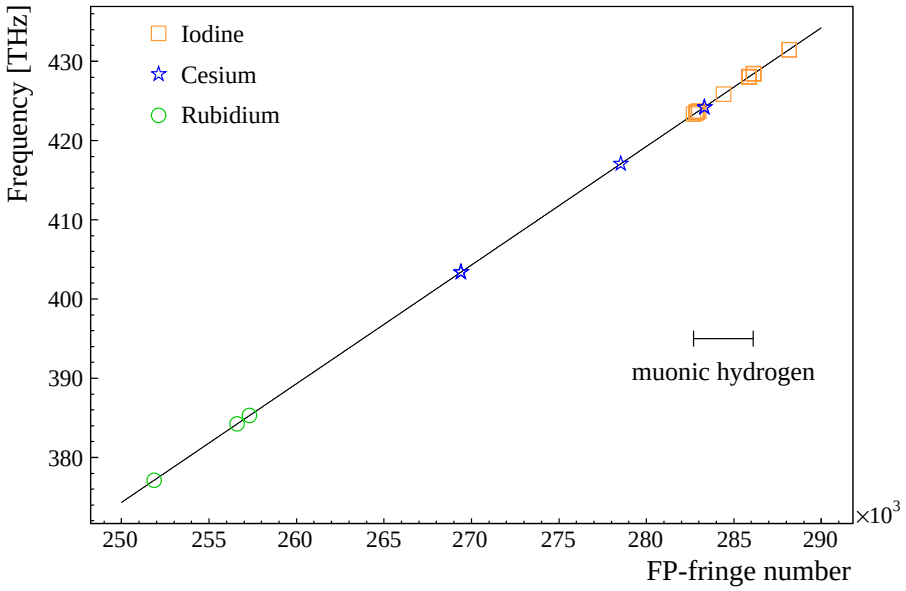

Figure 4.9: Frequency of the FP Fringes. *The frequency is plotted versus the FP-fringe number. The green circles originate from the rubidium-measurements, the blue stars from cesium. The 17 measurements in iodine (orange squares) are used for a cross-check of the quadratic fit from Equation (4.7) (black) applied to the more accurate data of rubidium and cesium. The frequency range of our measurements in μp and μd is indicated as well.*

their measurements. For each line, several recordings are made with a scatter of about 10–20 MHz. The results in columns 4 and 5 are based on an average of these recordings. Combining these two sources of uncertainty, the overall uncertainty of the relative line position to the nearest FP fringe (column 4) can be established to be better than 21 MHz.

Calibration of the Fabry-Perot Cavity

In Figure 4.9, all 25 different frequency measurements are plotted versus FP-peak number. The calibration of the FP versus frequency is extracted from the rubidium and cesium data. Using these for a quadratic fit, the frequency ν_N of the Nth FP-fringe is deduced to be

$$\nu_N = 1497.429740 \cdot N - 8972.487962 - 1.724901176059 \times 10^{-7} \cdot N^2 \text{ [in MHz]}, \quad (4.7)$$

with a standard deviation of 16.8 MHz. With the frequency-dependency stemming from the coating of the FP mirrors, the free spectral range FSR is then given by the derivative with respect to N:

$$\text{FSR} = 1497.429740 - 2 \cdot 1.724901176059 \times 10^{-7} \cdot N \text{ [in MHz]}. \quad (4.8)$$

The calibration can be tested by calculating the positions of the FP peaks close to the iodine lines and comparing them (including the corrections by Knöckel *et.al.* [115] from

N°	Position $\widetilde{\nu}$ [cm^{-1}]	Laser λ [μm]	Transition	Measurment Methods	#
1662	1662.80926	6.01	$\mu p(2S_{1/2}^{F=1} - 2P_{3/2}^{F=2})$	BN (cell), FP (air)	14
1654	1654.51675*	6.04	$\mu p(2S_{1/2}^{F=1} - 2P_{3/2}^{F=2})$	FP (air)	1
1822	1822.76062	5.48	$\mu p(2S_{1/2}^{F=0} - 2P_{3/2}^{F=1})$	PZT (air)	1
1695	1695.92896*	5.90	$\mu d(2S_{1/2}^{F=3/2} - 2P_{3/2}^{F=5/2})$	FP (air)	3
1739	1739.83872	5.75	$\mu d(2S_{1/2}^{F=1/2} - 2P_{3/2}^{F=3/2,1/2})$	PZT (air)	2

Table 4.3: Water Absorption Lines. *The five water lines used to calibrate the laser in the infra-red are introduced. The lines with their numbers and positions are taken from the HITRAN database [117]. The positions marked with an asterisk are already corrected for the air shift at atmospheric pressure. The approximate laser wavelengths are also given. Column 4 indicates the corresponding muonic transition. The measurement methods mentioned in column 5 are explained in the text. The number of measurements performed of each water line is given in the last column.*

Eq. (4.6)) to the measured ones. On average, the deviation between our measurements and the literature is -46.2 MHz (in acceptable agreement to the 30 MHz uncertainty from [115]).

In conclusion, the frequency of any FP-fringe can be accurately deduced with a typical uncertainty of 30 MHz. This is given by the standard deviation of the fit and the uncertainties on the Cs-lines. The error in the FSR can be estimated to be smaller than 3 kHz. This follows from opposing the iodine measurements with large FP-fringe number to the extrapolation to this FP-fringe number provided by Eq. (4.7). For the first resonance in μp, which is around FP N° 282895, the FSR can be quoted to be

$$\mathrm{FSR} = 1497.332\,(3)\,\mathrm{MHz}. \tag{4.9}$$

This value deviates slightly from the one arising from Equation (4.5) for rubidium. This difference can only partially be attributed to the different FP-fringe numbers. The FP was dismounted and reassembled again for a transport from Paris to PSI between 2003 and 2007. This might have caused small changes of the mechanical parameters. However, various calibration measurements in 2007 and 2009 show that there were no such changes during this period of time. In conclusion, the FP worked stably during the whole 2009 data aquisition period.

4.2.2 Water Calibration in the Infra-red

One-photon absorption spectroscopy in water is used to calibrate the laser system directly in the infra-red domain at 6 μm [118]. In total, 5 H_2O lines have been measured

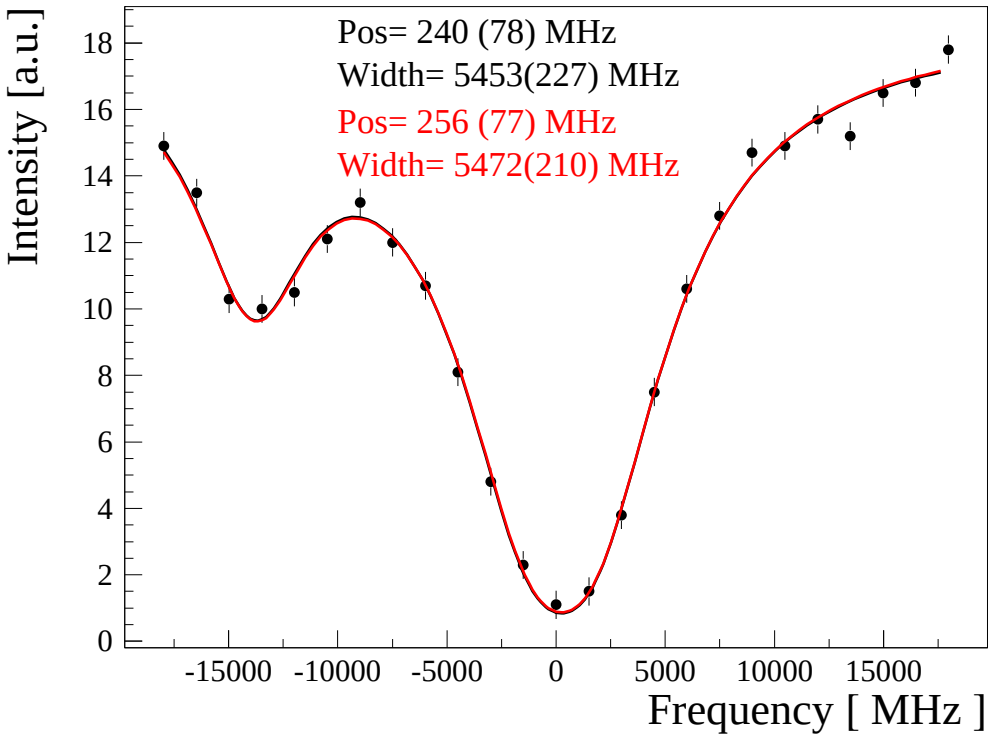

Figure 4.10: Absorption Spectrum of the Water Line 1695. *The absorption spectrum of the 1695 line measured in steps of 1.5 GHz. It was determined in air by the FP scan method. The small second peak is fitted with the position and amplitude as expected from HITRAN [117]. The relative position and amplitude are thus fixed parameters in the fit. The values given in black (red) are obtained from the fit with a tilted (flat) baseline, respectively. The reference FP is FP № 283537.*

during the campaign as summarized in Table 4.3. They are compiled by the HITRAN database [117]. The goal of HITRAN is to collect all available data and to have a theoretically self-consistent set of parameters while, at the same time, attempting to maximize the accuracy. Each of the used water lines have experimentally been measured (and not only reanalyzed) by at least two authors [119, 120]. The water lines are known to better than 2 MHz. For each measured muonic transition, at least one water line has been examined. Each muonic transition is within a $\lesssim 30$ GHz interval of a measured water calibration line, except for $(2S_{1/2}^{F=1/2} - 2P_{3/2}^{F=3/2,1/2})$, the second scan in μd, which is $\lesssim 100$ GHz apart.

The calibration measurements have been performed using three different methods:

- **Beat Note BN (cell):** A frequency offset lock between the cw Ti:Sapph laser and a diode laser is used:

$$\nu_{laser} = \nu_{diode} + \nu_{offset} \tag{4.10}$$

The diode lases at 708 nm and is referenced to the FP ($\nu_{diode} = \nu_{FPref}$). Tuning the offset frequency shifts the frequency of the laser system accordingly. This

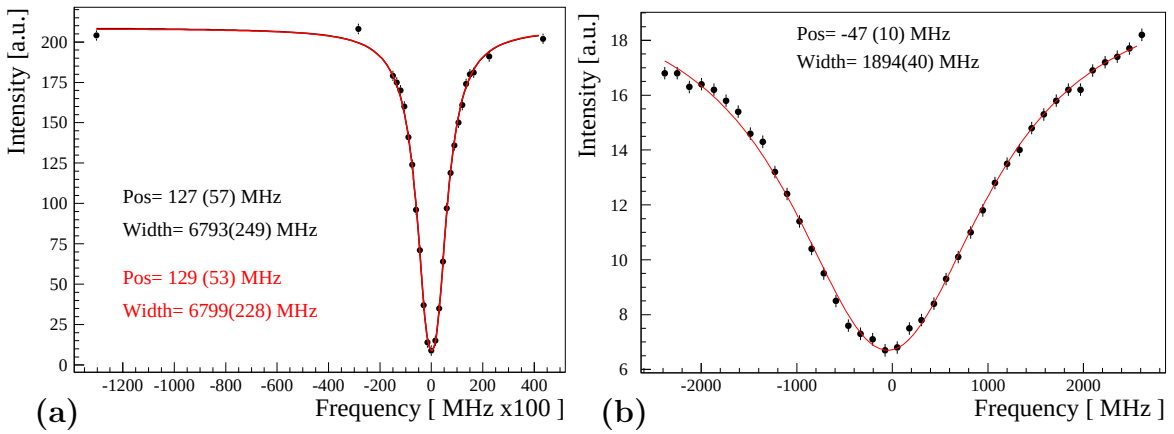

Figure 4.11: Absorption Spectra of the Water Line 1662. *Two examples of different measurements of the 1662 water line. Frequency $\nu = 0$ corresponds to FP-fringe №282874. Spectrum* ***(a)*** *is recorded in air and exhibits a clearly visible pressure broadening and air-shift. Both can be corrected for: according to the HITRAN database [117], the pressure broadening is 5.93 GHz, and the air-shift is 117 MHz. The fit results of the tilted (flat) baseline fit are given in black (red) in the plot. The scan of the laser frequency was performed in steps of the FSR of the FP, i.e. in steps of 1.5 GHz. The spectrum* ***(b)*** *was recorded in a water vapor cell with a few mbar of pure water. The beat note (BN) method was used to achieve the frequency scan.*

method is used only for water line №1662. A water vapor cell is employed with a water pressure in the mbar-range.

- **FP scan (air):** Here, the water line is simply scanned in air at atmospheric pressure. The distance travelled by the laser beam in air is ~ 10 cm. Since the air broadening for the water lines is ~ 6 GHz, the laser can be scanned in steps of 1.5 GHz. This is achieved by locking the laser to successive FP transmission peaks. This fast method can be applied to any of the water lines at any frequency.

- **PZT scan (air):** The frequency of the laser system is set by manually scanning the cw Ti:Sapph laser cavity length using a piezo-electric (PZT) active mirror. Similar to the FP scan, this method can be used for any water line at any pressure.

The recorded absorption spectra often show an asymmetric shape of the baseline. Its origin is not clearly understood but might stem from slow drifts in the laser power. In order to account for this behaviour when decucing the center position of the absorption lines, they are fitted with two models: a Lorentzian on top of a flat or a tilted baseline. Both agree well within their uncertainties. The error bars of the data points are set such that $\chi^2/dof = 1$. Figure 4.10 shows an absorption spectrum of water line №1695. It is recorded with the FP (air) method and displays a distinct double peak structure. Two examples of the 1662 water line are presented in Figure 4.11. While scan (a) is recorded in air and exhibits a ~ 6 GHz pressure broadening and an air shift of 117 MHz,

N°	**Position** $\widetilde{\nu}$ [cm^{-1}]	**Difference** $\nu_{H_2O} - \nu_{FP}$ [MHz]	**FP #**	**Frequency** ν_{FP} [MHz]	**Cross Check** $\Delta\nu_{FP}$ [MHz]
1662	1662.80926	−50	282874	49 849 817	(per def.) 0
1654	1654.51675*	−1739	282709	49 602 903	146
1822	1822.76062	−980	286077	54 645 968	183
1695	1695.92896*	180	283537	50 842 491	−60
1739	1739.83872	320	284416	52 158 732	22

Table 4.4: FP Frequencies From Water Absorption. *For each water line, the measured frequency difference between the absorption line and the reference FP-fringe is given. From this and the water line positions in column 2 (*: already corrected for the air shift), the absolute frequency of the FP-fringe can be deduced (column 5). The uncertainty on the tabulated water line positions translates to 2 MHz, the experimental uncertainty of the difference frequency determination (column 3) is 200 MHz. As explained in the text, the uncertainty of the absolute frequency value of the FP fringes is set to 300 MHz. A cross check can be performed by starting from FP N° 282874. The FSR of the FP (established in Sect. 4.2.1) can be used to bridge the gap to the next FP-fringe. The difference of this calculated value to the measured one is presented in the last column. It should be consistent with zero and scatters within the 200 MHz uncertainty stated in column 3.*

scan (b) is performed with a few mbar of water inside a vapor cell using the beat note (BN) technique.
Performing a weighted average on all 14 measurements of the water line N° 1662 one concludes for the frequency difference between the water line and the reference FP-fringe

$$\nu_{1662} - \nu_{FP282874} = (-50 \pm 200)\,\text{MHz}. \tag{4.11}$$

This result, together with those of the other water lines is summarized in Table 4.4: for each absorption line, the difference to a reference FP-fringe has been determined. The uncertainty on the difference frequency is 200 MHz for all water lines. From this, the absolute frequency values of the various reference fringes can be deduced. In the last column of the table, a consistency check is performed. Starting from FP N° 282874, the frequencies of the other fringes are calculated using the FSR of the FP (as determined in Sect. 4.2.1). The difference to the expected value is given here. Its statistical scattering indicates that the uncertainty of 200 MHz stated for $\nu_{H_2O} - \nu_{FP}$ in Eq. (4.11) is reasonable. The values show that the water lines have been identified correctly. It is worthwhile to mention that around the examined water lines, there are no other observable lines within at least 14 GHz. Moreover, the doublet of line 1695 is uniquely identified: within 45 GHz, no other sufficiently strong line exists with similar relative

intensities. The consistency check together with these mentioned facts make this water calibration of the laser in the infra-red domain a reliable tool.

In conclusion, the frequency of the laser system in the infra-red when locked to the FP-fringe N$^{\circ}$ 282874 is determined to

$$\boxed{\nu_{FP282874} = 49\,849\,817\,(300)\,\text{MHz}.} \tag{4.12}$$

Here, as for all reference fringes, the uncertainty has been enlarged from 200 MHz to 300 MHz to account for the following items:

- A systematic offset can be observed in the consistency check in the right most column of Table 4.4 (-80 MHz).
- The water lines are measured either with the *Pyro* detector directly after the Raman cell and after the absorption cell or with the *Vigo* and quadrant detectors after having travelled ~ 15 m inside the vacuum beam line into the target area (cf. Sect. 2.3.3). An average discrepancy of ($+250$ MHz) is observed between the *Pyro* and the target area measurements. This probably stems from a different propagation behaviour of higher order modes resulting in a pointing dependent frequency chirp of the laser.
- Another disagreement of $+40$ MHz between the *Pyro* and the target area detectors is found for the water lines which have been measured in air. The origin is unclear.
- Possible systematic shifts and broadening related to the repetition rate should also be covered by the assumed error of 300 MHz.

Comparing the 2009 data to the data obtained in the 2003-beamtime, a shift of $\sim$ 1 GHz is observed (when correcting for the H_2 gas pressure inside the Raman Cell). This can be explained by thermal processes in the Raman cell related to the different repetition rates at which the laser was operated (10 Hz compared to 250 Hz in 2009). The uncertainty related to the reference position of the water lines is below 2 MHz and therefore negligible.

4.2.3 Laser Bandwidth

The laser bandwidth can be extracted from the water calibration measurements, as well. The bandwidth is given mainly from the Raman process. Therefore, the laser bandwidth should resemble a Lorentzian. Nevertheless, its shape is not fully understood and is found to be between a Lorentzian and a Gaussian. This will have to be considered when determining the resonance line width in Section 4.3.7. From the best measurements performed with the *Pyro* detector on the water vapor cell, a weighted average for the laser bandwidth (at FWHM) can be deduced:

$$\Gamma_{Laser} = 1750\,(250)\,\text{MHz}. \tag{4.13}$$

4.3 Systematics

The systematic uncertainty of the $\mu p(2S^{F=1}_{1/2} - 2P^{F=2}_{3/2})$ resonance originates exclusively from the laser frequency calibration (as described in Sect. 4.2) which attributes to 350 MHz, about half of our statistical uncertainty of ~ 640 MHz. All other systematic effects which could possibly affect the resonance are treated in this section. The first part (Sect. 4.3.1) deals with the influence of the laser electric field on the resonance line (AC Stark effect). After Section 4.3.2 in which the DC Stark shift is estimated, the Zeeman effect (Sect. 4.3.3), the Doppler shift (Sect. 4.3.4), and the pressure shift (Sect. 4.3.5) are considered. Section 4.3.6 summarizes all uncertainties and concludes that the largest systematic uncertainty of 300 MHz stemming from the laser frequency calibration is still well below our statistical limit of 644 MHz.

4.3.1 AC Stark Effect

The AC Stark effect is related to the shift of atomic energy levels when the atom is subjected to a laser field. It is well known, that for one-photon transitions with infinite state lifetime, the AC Stark effect only results in a broadening of the resonance line [121]. In the case of the $2S - 2P$ transitions in muonic hydrogen, the AC Stark shift has to be reconsidered because of the lifetime of $\tau_{2P} = 8.5 \times 10^{-12}$ s of the $2P$ state.

Two-level atom with infinite state lifetime

In this picture, a simple two-level system with transition frequency ω_a under the influence of a monochromatic laser field (laser frequency ω_l) is inspected. The eigenfunctions of such a system are best described in terms of *dressed* states [17]. In order to solve the time dependent Schrödinger equation, one performs the rotating wave approximation (RWA), where one assumes that the laser is close to resonance, i.e. $\omega_l \gg \delta = \omega_l - \omega_a$ (δ is the detuning from the atomic resonance). The energy levels for the ground (g) and excited (e) state of the two-level system with the laser field present are shifted like

$$E_{g,e} = E^0_{g,e} + \frac{\hbar}{2}(-\delta \pm \Omega'). \tag{4.14}$$

$E^0_{g,e}$ are the energy levels of the bare states. $\Omega' = \sqrt{\Omega^2 + \delta^2}$ and Ω is the Rabi frequency. In the limit of a large laser detuning $\Omega \ll |\delta|$, the resulting energies are shifted by

$$\Delta E_g = \frac{\hbar\Omega^2}{4\delta}, \qquad \Delta E_e = -\frac{\hbar\Omega^2}{4\delta}, \tag{4.15}$$

leading to an AC Stark shift of $\delta_{AC} = \frac{\hbar\Omega^2}{2\delta}$.
In the other limit, the detuning is small compared to the Raby frequency ($\Omega \gg |\delta|$); the laser is close to resonance. In this case, the energy levels are shifted as

$$\Delta E_g = \mathrm{sgn}(\delta)\,\frac{\hbar\Omega}{2}, \qquad \Delta E_e = -\mathrm{sgn}(\delta)\,\frac{\hbar\Omega}{2}, \tag{4.16}$$

giving an AC Stark shift of $\delta_{AC} = \mathrm{sgn}(\delta)\,\hbar\Omega$. This means that the AC Stark shift changes its sign on resonance resulting in a net broadening of the resonance line.

The Rabi frequency expresses the strength of the coupling between the photon field and the atom. It is defined as

$$\Omega = \frac{-e|\mathbf{E}|}{\hbar} < e \mid r \mid g > \tag{4.17}$$

where $\mathbf{E}$ is the electric field, and $< e \mid r \mid g >$ is the transition matrix element. It is proportional to the square root of the laser intensity through

$$I = \frac{c\ \epsilon_0\ n}{2}|\mathbf{E}|^2. \tag{4.18}$$

Here, the laser intensity I is given in $\mathrm{W/m^2}$, the laser electric field in V/m. In the equation, $c = 3 \times 10^8\,\mathrm{m/s}$ is the speed of light, $\epsilon_0 = 8.85 \times 10^{-12}\,\mathrm{F/m}$ the dielectric constant, and n the refractive index of the medium.

At this point, we need to bear in mind the particularities of this experiment: the light (intensity) distribution inside the target cavity is only approximately homogeneous. Therefore, the assymetry resulting from the light shift variation has to be estimated.
Using Eq. (4.18), the laser electric field can be calculated for our purposes to be

$$|\mathbf{E}| = 2.75 \times 10^6\,\mathrm{V/m} \cdot \left(\frac{\mathcal{E}_{\mathrm{pulse}}/\mathrm{mJ}}{(A/\mathrm{cm^2})\ (\tau/\mathrm{ns})}\right)^{1/2}, \tag{4.19}$$

where $\mathcal{E}_{\mathrm{pulse}}$ is the laser pulse energy given in mJ, A the area of the beam in $\mathrm{cm^2}$ and τ its pulse length in ns. In our case, the lifetime of the $6\,\mu$m radiation is approximately 50 ns. Assuming a laser fluence of $16.5\,\mathrm{mJ/cm^2}$ (corresponding to the saturation fluence of the μp transition) and inserting fluence and lifetime into Eq. (4.19) yields $|\mathbf{E}| = 1.60 \times 10^4\,\mathrm{V/cm}$.
In the case of the $\mu p(2S^{F=1}_{1/2} - 2P^{F=2}_{3/2})$ transition, we have

$$|< e \mid r \mid g >|^2 = 5a_\mu^2, \tag{4.20}$$

with $a_\mu = 285 \times 10^{-15}\,\mathrm{m}$ being the muonic Bohr radius. Thus, the matrix element becomes $< e \mid r \mid g > = 637 \times 10^{-15}\,\mathrm{m}$. Inserting this value into Eq. (4.17) together with the obtained electric field and with $e/h = 2.42 \times 10^{14}\,\mathrm{A/J}$, leads to a Rabi frequency of $\Omega = 1529 \times 10^6\,\mathrm{rad/s}$. In the limit of small detuning, this results in an AC-Stark shift of the resonance frequency of maximally

$$\frac{|\delta_{AC}|}{h} \leq \frac{\Omega}{2\pi} = 250\,\mathrm{MHz}. \tag{4.21}$$

The intensity distribution of the laser light inside the target cavity has been simulated extensively [88]. According to this, the vertical distribution has a relative amplitude variation of 8/5 between the maximum and the minimum. With the square root dependence of the Rabi frequency on the laser intensity, this leads to a vertical asymmetry

of 26 % ($\hat{=}$ 66 MHz) in the AC Stark shift (using $\sqrt{8/5} = 1.26$). The horizontal asymmetry of the laser fluence along the muon beam depends on the losses induced by the reflections on the cavity mirrors: with a mirror reflectivity of $R = 99.9\%$ and ~ 100 reflections from the entrance hole to one of the ends, one obtains a total loss of 10 %. This yields to an AC Stark shift asymmetry of 5 % (i.e. 12.5 MHz).

Including the spontaneous decay

Following the argumentation by Shore [122], we generalize our considerations for a two-level system by including a spontaneous decay. In our case, this is given by the decay of the excited $2P$ state to the $1S$ ground state (lifetime $\tau_{2P} \sim 10^{-11}$ s). Redefining the zero point energies, the solution of the time dependent Schrödinger equation is reduced to a set of coupled equations describing the amplitudes in both states. In the RWA, which is well fulfilled in our case, we have

$$\frac{d}{dt}\begin{pmatrix} C_g \\ C_e \end{pmatrix} = \frac{i}{2}\begin{pmatrix} -(\omega_a - \omega_l) - i2\gamma_g & \Omega^* \\ \Omega & (\omega_a - \omega_l) - i2\gamma_e \end{pmatrix}\begin{pmatrix} C_g \\ C_e \end{pmatrix}. \tag{4.22}$$

Here, $\lambda_{g/e} = 2\,\gamma_{g/e}$ are the decay rates of the ground (excited) state. The behaviour is equivalent to the one of a damped harmonic oscillator. The complex eigenvalues of this expression are $E_\pm = \hbar W_\pm$ with

$$W_\pm = -\frac{i}{2}(\gamma_e + \gamma_g) \pm \frac{1}{2}\sqrt{\Omega^2 + [(\omega_a - \omega_l) + i\gamma_g - i\gamma_e]^2}. \tag{4.23}$$

In μp, the decay rate γ_g of the $2S$ state is negligible compared to Ω, and $\Omega \ll \gamma_e = 2\pi/2 * 18.6\,\text{GHz} \simeq 58 \times 10^9\,\text{rad/s}$. If we neglect the spontaneous decay, i.e. $\gamma_g = \gamma_e = 0$ we find that $W_\pm = \pm\frac{1}{2}\sqrt{\Omega^2 + (\omega_a - \omega_l)^2}$, which, apart from the different choice of the zero point energy, compares with Eq. (4.14). On resonance, we have $\omega_l = \omega_a$ and Eq. (4.23) reads

$$W_\pm \simeq -\frac{i}{2}\gamma_e \pm \frac{1}{2}\sqrt{\Omega^2 - \gamma_e^2}. \tag{4.24}$$

The entire argumentation shows that for a two-level system without spontaneous decay, the laser field causes the probabilities of the two states to oscillate without any loss in the oscillation amplitude. With the spontaneous deexcitation of one or two of the states, a damping term is introduced and causes the Rabi oscillation to fade out.
Because in our case $\Omega < \gamma_e$, the argument of the square root in Eq. (4.24) is negative resulting in purely imaginary eigenvalues. This implies that overdamping occurs and that the AC Stark shift is suppressed completely.

As a last step, we separate the real from the imaginary part of Eq. (4.23) by writing:

$$W_\pm = \pm\frac{1}{2}\,\widetilde{\Omega} - \frac{i}{2}\left[(\gamma_g + \gamma_e) \mp \Upsilon\right]. \tag{4.25}$$

To simplify the expression we have defined

$$X \equiv \Omega^2 + (\omega_a - \omega_l)^2 - (\gamma_g - \gamma_e)^2 \tag{4.26}$$

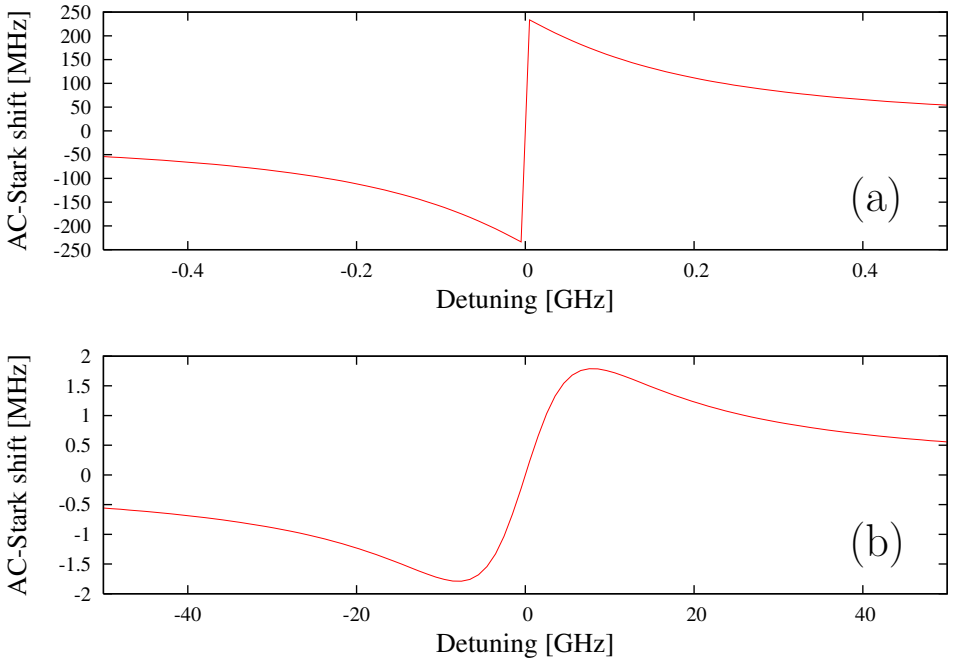

Figure 4.12: AC Stark Shift with and without Spontaneous Decay. *The real part* $\left(\widetilde{\Omega}\right)$ *of the exact energy eigenvalues (Eq. (4.25)) is plotted without any spontaneous decay (a) and with a damping term* γ_e *(b), which corresponds to the linewidth of 18.6 GHz of the* $2P$ *state. Note that the scale of the y-axis differs by a factor of* ~ 100.

$$\widetilde{\Omega} = \frac{1}{\sqrt{2}}\left[\sqrt{X^2 + 4(\gamma_g - \gamma_e)^2(\omega_a - \omega_l)^2} + X\right]^{1/2} \tag{4.27}$$

$$\Upsilon = \frac{1}{\sqrt{2}}\left[\sqrt{X^2 + 4(\gamma_g - \gamma_e)^2(\omega_a - \omega_l)^2} - X\right]^{1/2}. \tag{4.28}$$

The real part $(\widetilde{\Omega})$ describes the shift induced by the AC Stark effect. It is visualized versus the detuning δ in Figure 4.12 using realistic parameters. To make the AC Stark shift anti-symmetric around the origin, the eigenvalues of the unperturbed atom have been subtracted from $W_\pm$ in Eq. (4.25). The case without damping is represented in Fig. 4.12(a). For zero detuning, it recovers $|\delta_{AC}| = \Omega/2\pi = 250\,\text{MHz}$, the known result of Eq. (4.21). In Figure 4.12(b), the case of overdamping ($\gamma_e > \Omega$) is plotted as a function of the detuning. Here, the amplitude of the AC Stark shift is much less pronounced and vanishes completely for detuning $\delta = 0$. Conservatively, an uncertainty of 1 MHz is assumed.

Figure 4.13 displays the imaginary part Υ of the eigenvalues $W_\pm$ (again corrected for the eigenvalues of the unperturbed states). A broadening of less than 2 MHz (at HWHM) is observed on resonance. Compared to the natural linewidth of 18.6 GHz of the $2P$ state in muonic hydrogen, this is completely negligible.

Since we are not dealing with a pure two-level system, the non-resonant coupling to other hyperfine levels has to be estimated. For the $\mu p(2S^{F=1}_{1/2} - 2P^{F=2}_{3/2})$ transition,

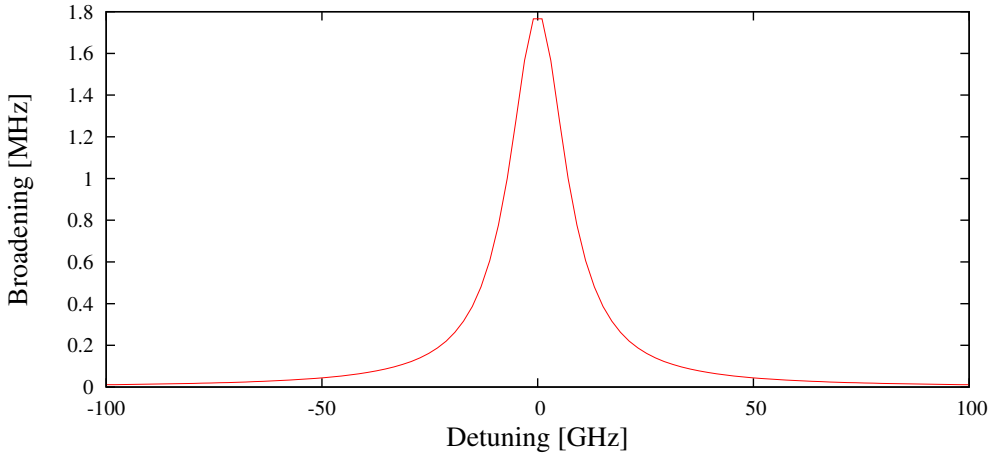

Figure 4.13: AC Stark Broadening with Spontaneous Decay. *The AC Stark broadening is plotted versus the delay δ as extracted from the imaginary part Υ (Eq. (4.28)). The damping term γ_e is chosen such that it matches the natural lifetime of the $2P$ state.*

the $2S_{1/2}^{F=1}$ state couples non-resonantly to the $2P_{3/2}^{F=1}$, the $2P_{1/2}^{F=1}$, and the $2P_{1/2}^{F=0}$ level with detunings of 785.36 GHz, 1880.71 GHz and 3770.85 GHz, respectively [123]. The energy shifts are given by $\Delta E_g = \frac{\hbar\Omega^2}{4\delta}$ (Eq. (4.15)). As these detunings are positive, the $2S_{1/2}^{F=1}$ level is shifted upwards. Assuming a conservative value of $\Omega = 1\,\text{GHz}$ for the Rabi frequency for the particular non-resonant transition [88], the shift is much smaller than 1 MHz and thus negligible. For the $2P_{3/2}^{F=2}$ state, the shift is negligible because this level is not coupled to the $2S_{1/2}^{F=0}$ level.

In summary, the instantaneous decay of the $2P$ state into the $1S$ ground state imposes an overdamping on the Rabi oscillations. This is seen when the AC Stark effect is considered including a damping term γ_e. This term leads to the fact that the AC Stark shift vanishes on resonance, and the broadening is $\sim 4\,\text{MHz}$ (FWHM) and, therefore, negligibly small.

4.3.2 DC Stark Shift

The DC Stark effect on the energy levels stems from static electric fields interacting with the atom. The main concern in our experiment is the electric field seen by the μp atom when moving in the 5 Tesla magnetic field of the target. In the following, this electric field component and its effect on the atomic energy levels are calculated.

Moving particle in a static magnetic field

Let z be the direction of the magnetic field inside the target solenoid and let the atom move along the x-axis. Then the Lorentz transformation for the electric and magnetic

field yields:

$$E'_x = E_x \tag{4.29}$$

$$E'_y = \frac{E_y - vB_z}{\sqrt{1-\beta^2}} \tag{4.30}$$

$$E'_z = \frac{E_z + vB_y}{\sqrt{1-\beta^2}} \tag{4.31}$$

where $\beta = v/c$. In our case $B_x = B_y = 0$ and $E_x = E_z = 0$ so that only E_y does not vanish:

$$E_y = \frac{\beta B_z}{\sqrt{1-\beta^2}} \tag{4.32}$$

For a velocity of $v = 4 \times 10^3\,\mathrm{m/s}$ (corresponding to 0.1 eV kinetic energy[2] for μp) $\beta = 1.3 \times 10^{-5}$. Thus, the electric field in Eq. (4.32) is $E_y = 2 \times 10^4\,\mathrm{V/m}$ for a 5 Tesla magnetic field. This is significantly larger than any stray field originating from the surface grounded LAAPDs or the electronics around the target.

Induced level shift

The energy levels of the μp $n = 2$ manifold are affected by the Stark effect. We consider the effect of an electric field on the four-level system with $n = 2$ in the $|nL_m\rangle$ notation (fine and hyperfine structure are neglected):

$$|2S_0\rangle, \quad |2P_1\rangle, \quad |2P_{-1}\rangle, \quad |2P_0\rangle\,. \tag{4.33}$$

The $|2P_m\rangle$ states are degenerate, and lie 0.2 eV above the $|2S_0\rangle$ state. The perturbation Hamiltonian for an electric field $\mathbf{E}$ in y-direction is:

$$\hat{H}_{pert} = e|\mathbf{E}|\,\hat{y} \tag{4.34}$$

where e is the electric charge and $\hat{y}$ the space operator in y-direction. The energy eigenvalues of the perturbed system are

$$E_\pm = \frac{1}{2}\left[(E_S + E_P) \pm \sqrt{(E_P - E_S)^2 + 4|H_{SP}|^2}\right] \quad \text{with} \tag{4.35}$$

$$H_{SP} = 3\,e\,a_\mu\,|\vec{E}|. \tag{4.36}$$

Here, E_S, E_P are the energy eigenvalues of the unperturbed $2S$ and $2P$ states, respectively, and $a_\mu = 4\,\pi\,\epsilon_0\hbar^2/m_\mu e^2$ is the Bohr radius for μp atoms. For a vanishing perturbation ($H_{pert} \to 0$), E_+ reduces to E_P and E_- to E_S.
The shift caused by the electric field is then given by

$$\begin{aligned}\delta_{DC} &= (E_+ - E_-) - (E_P - E_S) \\ &= \sqrt{(E_P - E_S)^2 + 4\,|H_{SP}|^2} - (E_P - E_S)\ .\end{aligned} \tag{4.37}$$

[2] A Monte Carlo simulation, which traces the slowing down of the μp atoms in the hydrogen gas, predicts that, in the laser time window, the average kinetic energy of the μp atoms is below 0.1 eV [124]. This considers energy dependent elastic and inelastic cross sections for $\mu p(2S) + H_2$ collisions calculated in [80].

Using the following numerical values:

$$H_{SP} = 3 \cdot 1.6 \times 10^{-19}\mathrm{C} \cdot 0.53 \times 10^{-10}\,\mathrm{m}/200 \cdot 2 \times 10^{4}\,\mathrm{V/m} \quad (4.38)$$

$$= 2.5 \times 10^{-27}\,\mathrm{J} = 1.6 \times 10^{-8}\,\mathrm{eV} \quad (4.39)$$

$$E_P - E_S = 0.2\,\mathrm{eV} \quad (4.40)$$

Since $H_{SP} \ll E_P - E_S$, we can perform an expansion of $\sqrt{1+x} = 1 + x/2 + \ldots$

$$\delta_{DC} = (E_P - E_S)\sqrt{1 + \frac{4\,|H_{SP}|^2}{(E_P - E_S)^2}} - (E_P - E_S) \quad (4.41)$$

$$\approx \frac{2\,|H_{SP}|^2}{(E_P - E_S)} = 2.6 \times 10^{-15}\,\mathrm{eV} \quad (4.42)$$

The DC Stark shift is 0.6 Hz and, therefore, together with the vanishing broadening, completely negligible.

4.3.3 Zeeman Shift

In our target, a 5 Tesla static magnetic field along the muon beam axis serves to keep the μ^- stopping volume small for reasons explained in Sect. 2.2. Here, the influence of this high magnetic field on the $2S - 2P$ transition frequency of the muonic atoms shall be discussed. A thorough treatment of the Zeeman effect in muonic hydrogen can already be found in [88]. Therefore, only a brief summary and the results are presented in this section.

The interaction between the muonic hydrogen atom and the external magnetic field $\mathbf{B}$ can be described according to Eq. (F.4) of [88]:

$$H_B = (g_L^\mu\,\mu_B^\mu\,\mathbf{L} + g_L^p\,\mu_B^p\,\mathbf{L} + g_S^\mu\,\mu_B^\mu\,\mathbf{S} + g_I\,\mu_B^p\,\mathbf{I}) \cdot \frac{\mathbf{B}}{\hbar} \quad (4.43)$$

$$= \left(g_L^\mu\,L_z + g_L^p\,\frac{\mu_B^p}{\mu_B^\mu}\,L_z + g_S^\mu\,S_z + g_I\,\frac{\mu_B^p}{\mu_B^\mu}\,I_z\right)\frac{\mu_B^\mu}{\hbar}B\,. \quad (4.44)$$

In this equation, g_L^μ, g_L^p, g_S^μ, and g_I are the muon orbital, the nuclear orbital, the muon spin and nuclear g-factors, respectively. $\mathbf{L}$ is the orbital momentum of the orbiting particle (the same as the one for the nucleus), $\mathbf{S}$ is the muon spin, and $\mathbf{I}$ the nuclear spin. The muon and proton magnetic moments are defined as $\mu_B^\mu = \frac{e\hbar}{2m_\mu c}$ and $\mu_B^p = \frac{e\hbar}{2Mc}$ with m_μ being the muon mass and M the proton mass. The values of these constants are summarized in Table 4.5, which shows that the magnetic moment of muonic hydrogen is suppressed by a factor of 1/207 compared to the one of electronic hydrogen because of the mass ratio of the electron to the muon.

Assuming weak magnetic fields (which is still valid for our magnetic field of 5 T) and using a pertubation approach, the energy levels split linearly according to Eq. (F.12) to lowest order to

$$\Delta E_B = g_F\,\mu_B^\mu\,m_F\,B. \quad (4.45)$$

Hydrogen	**Muonic Hydrogen**
$\mu_B^e = \frac{e\hbar}{2m_e c}$	$\mu_B^\mu = \frac{e\hbar}{2m_\mu c} \simeq \mu_B^e/207$
$\mu_B^p = \frac{e\hbar}{2Mc}$	μ_B^p
$g_L^e \simeq$ 1.00	$g_L^\mu \simeq$ 0.89
$g_L^p \simeq$ 0.00	$g_L^p \simeq$ 0.10
$g_S^e \simeq$ 2.00	$g_S^\mu \simeq$ 2.00
$g_I \simeq$ -5.58	$g_I \simeq$ -5.58

Table 4.5: Magnetic Properties of Hydrogen and Muonic Hydrogen. *A comparison of the magnetic properties between hydrogen and muonic hydrogen. The total magnetic moment of hydrogen results to be about 200 times larger than in muonic hydrogen. μ_B^e is the Bohr magneton, μ_B^μ and μ_B^p are the corresponding magnetic moments of the muon and the proton, with m_e being the electron mass and m_μ the muon mass. g_S stands for the g-factor of the orbiting particle, g_L for the corresponding orbital g-factor and g_I the proton spin g-factor. The superscripts indicate the particle: e for electron, μ for muon and p for proton.*

The hyperfine Lande g-factor can be calculated[3] from

$$g_F = g_J \frac{F(F+1) - I(I+1) + J(J+1)}{2F(F+1)} + g_I \frac{\mu_B^p}{\mu_B^\mu} \frac{F(F+1) + I(I+1) - J(J+1)}{2F(F+1)} \tag{4.46}$$

where

$$g_J = g_L \frac{J(J+1) - S(S+1) + L(L+1)}{2J(J+1)} + g_S \frac{J(J+1) + S(S+1) - L(L+1)}{2J(J+1)}. \tag{4.47}$$

The setup in our target is such that the laser light exciting the transitions is measured to be linearly polarized along the **B**-field axis (i.e. the atomic quantization axis). This leads to the constraint that only transitions with $\Delta m_F = 0$ can be driven. The Zeeman transition shift is calculated from the difference of the two involved level shifts (acc. to Eq. (4.45)). For linearly polarized light and evenly distributed sublevels ($m_F = -F, -F+1, \cdots, F-1, F$), the induced Zeeman shifts are of opposite sign and cancel out for $\pm m_F$ so that only a small broadening occurs.
Table 4.6 compiles the largest possible Zeeman level shifts and Zeeman transition shifts for linearly polarized light. Moreover, the maximum transition shifts are listed assuming 100 % circular polarized ($\sigma^\pm$) light. As mentioned, however, the laser light is linearly polarized. Adding a conservative admixture of 10 % of $\sigma^\pm$ light (possibly stemming from a slight birefringence of the vacuum windows the laser has to pass)

[3]Note that the g_F values stated in Eq. (F.13) of [88] are incorrect. The recalculated values can be found in Table 4.6

State	g_J	g_F	m_F	Level Shift (πP) [MHz]	Transition	Trans. Shift (πP) [MHz]	Max. Shift (σP) [MHz]
$\mu p\ (2S_{1/2}^{F=1})$	2.0	0.68	1	232			
$\mu p\ (2P_{3/2}^{F=2})$	1.26	0.79	1	268	$\mu p(2S_{1/2}^{F=1} - 2P_{3/2}^{F=2})$	36	$\pm$304
$\mu p\ (2S_{1/2}^{F=0})$	2.0	-	0	0			
$\mu p\ (2P_{3/2}^{F=1})$	1.26	1.73	0	0	$\mu p(2S_{1/2}^{F=0} - 2P_{3/2}^{F=1})$	0	$\pm$586
$\mu d\ (2S_{1/2}^{F=3/2})$	2.0	0.69	3/2	354			
$\mu d\ (2P_{3/2}^{F=5/2})$	1.29	0.79	3/2	405	$\mu d(2S_{1/2}^{F=3/2} - 2P_{3/2}^{F=5/2})$	50	$\pm$350
$\mu d\ (2S_{1/2}^{F=1/2})$	2.0	-0.6	1/2	-101			
$\mu d\ (2P_{3/2}^{F=3/2})$	1.29	0.96	1/2	163	$\mu d(2S_{1/2}^{F=1/2} - 2P_{3/2}^{F=3/2})$	265	$\pm$590
$\mu d\ (2P_{3/2}^{F=1/2})$	1.29	2.13	1/2	360	$\mu d(2S_{1/2}^{F=1/2} - 2P_{3/2}^{F=1/2})$	462	$\pm$260

Table 4.6: Zeeman Shifts for the μp and μd Transitions. *Summary of the Zeeman shifts in the 5 T magnetic field for both muonic hydrogen and deuterium. The fifth column gives the absolute Zeeman level shift for the largest possible m_F sublevel. Linear polarized (πP) light implying $\Delta m_F = 0$ is assumed. Since this shift is proportional to m_F it is automatically the largest level shift that can possibly be induced. The transition Zeeman shifts for linearly polarized light are given in the seventh column as the difference of the level shifts. However, if the population of the initial state is evenly distributed among the various $\pm m_F$ sublevels, the net Zeeman transition shift will be zero and only a broadening will occur on the order of $2 \times 36\,MHz \simeq 70\,MHz$. Postulating fully circular ($\sigma^{\pm}$) polarized light (σP), the last column calculates the theoretical maximum transition shift using $\Delta m_F = \pm 1$. With a conservative admixture of 10 % $\sigma^{\pm}$ polarized light (see text), the uncertainty of the Zeeman shift accounts to 30 MHz for the first μp transition.*

could results a shift of 30 MHz. Since this value is to be regarded an upper limit it is accounted for in the error budget as an uncertainty of 30 MHz.

A line broadening of the order of $2 \times 36\,\text{MHz} \simeq 70\,\text{MHz}$ is perceived for linearly polarized light and slightly more ($\simeq 100\,\text{MHz}$) for 10 % circular admixture.

4.3.4 Doppler Shift and Broadening

Since we are dealing with a one-photon transition, the first order Doppler effect has to be estimated. This section deals with the relativistic effect of a frequency shift caused by the high velocity of the muonic atoms. If the light and μp atoms propagate collinearly, the Doppler shift is given by

$$\frac{\omega}{\omega_a} = 1 \pm \frac{v}{c}. \tag{4.48}$$

An upper bound for the velocity v can be extracted from the lifetime of the short-

lived $2S$ component of the μp atoms. It is measured to be 100 ns at 1 hPa [84] and shows that a few hundred ns after the formation of the $2S$ state, the μp atoms have an average kinetic energy smaller than 0.31 eV, i.e. smaller than the threshold energy for radiative quenching. The kinetic energy of the μp atoms is therefore much below[4] 0.3 eV when the laser transition is induced $\sim 1\,\mu$s after the μp formation.

For a kinetic μp energy of 0.1 eV, the velocity is $v = 4 \times 10^3$ m/s, and this gives $v/c = 4 \times 10^3/3 \times 10^8 = 1.3 \times 10^{-5}$. The maximum Doppler shift assuming *collinearity* is thus of the order ± 13 ppm ($= 650$ MHz).

The reality, however, is different: since the muons undergo several large angle scattering processes before the μp formation, the directional correlation is lost. After muon capture, the $\mu p(2S)$ atom will keep being scattered elastically until the laser pulse arrives. We assume an upper limit of 10% for the angular correlation between the μp velocity and the muon beam direction. Moreover, the Doppler effect is reduced by a factor of 25 by the fact that the laser light has an average angle to the muon beam of $\pi/2 \pm \alpha$ with $\alpha < 40$ mrad being the injection angle of the laser beam into the target. Since the light is reflected ~ 100 times (with a mirror reflectivity of $R = 99.9\%$) before it changes direction at the cavity-ears ($+\alpha \longrightarrow -\alpha$), an asymmetry in the laser intensity of only 10 % is associated with the two beam directions $\pm\alpha$. Therefore, another reduction factor of 10 is introduced.

All in all, the Doppler shift is reduced by a factor of 2500 at least, resulting in a Doppler shift smaller than 200 kHz.

The Doppler broadening is caused by μp atoms with thermal energies exhibiting a Maxwell velocity distribution (with associated temperature T). The relative Doppler broadening (at FWHM) can be expressed by [125]:

$$\frac{\delta\nu}{\nu_a} = \frac{2}{c}\sqrt{\frac{2\,N_A\,k_B\,T\,\ln 2}{M}} = 7.16 \times 10^{-7}\sqrt{T/M}. \tag{4.49}$$

Here, ν_a is the atomic transition frequency, N_A is the Avogadro constant, k_B is the Boltzmann constant, and M is the molar mass. It is $M = 1$ for hydrogen and $M = 1.11$ for muonic hydrogen. T is the temperature of the muonic hydrogen gas and can be estimated the following way: With $E = 3/2\,k_B\,T$, the temperature associated with a kinetic energy of 0.1 eV is $T = 750$ K. The resulting Doppler broadening is 19.7 ppm, i.e. 1.0 GHz.

4.3.5 Collisional Effects

Outlined in Appendix F.3 in [88], the shift and the broadening due to collisions of the μp atom with the surrounding hydrogen gas are treated in the impact theory framework. This framework is well suitable for our experimental conditions, since it implies low gas densities and the time between collisions being large compared to the

[4] See footnote on page 67.

time duration of the collisions themselves. Expanding the electrostatic potential of the charge distribution of the hydrogen molecule in its multi-pole moments and integrating over all possible impact parameters yields values for the pressure shift and the pressure broadening (as derived in Eq. (F.37) in [88]):

$$\begin{aligned} \Delta\nu_{\text{shift}} &= 1.3\ \text{MHz} \times p/\text{hPa} \\ \Delta\nu_{\text{broadening}} &= 2.4\ \text{MHz} \times p/\text{hPa}. \end{aligned} \tag{4.50}$$

The experiment was performed at a target gas pressure of $p = 1\,\text{hPa}$. Therefore, the resulting collisional shift of $\Delta\nu_{\text{shift}} = 1.3\,\text{MHz}$ and the corresponding broadening of $\Delta\nu_{\text{broadening}} = 2.4\,\text{MHz}$ are irrelevant for the resonance lines in μp and in μd. Conservatively, both values get assigned uncertainties the same magnitude as the values themselves.

4.3.6 Uncertainty Budget: Grand Total

In this section, the various contributions to the uncertainties of the $\mu p(2S_{1/2}^{F=1} - 2P_{3/2}^{F=2})$ resonance line are summarized. Table 4.7 lists all the effects discussed in the previous sections.

Other possible effects are considered but do not impair the systematics. Molecular effects do not influence the transition frequency since the formed muonic molecules $pp\mu^+$ are known to deexcite quickly [126] and, therefore, do not contribute to the observed signal. Effects of a possible H_2O absorption are ruled out in Sect. 4.1, and non-resonant coupling to other states is discussed in Sect. 4.3.1.

Table 4.7 summarizes the systematic uncertainties to be 301 MHz compared to the 644 MHz statistical uncertainty. The line shape model is intrinsically included into the statistical contribution and therefore does not show up individually. With a transition frequency of 49.9 THz, this accounts to 12.9×10^{-6} (6.0×10^{-6}) relative statistical (systematic) uncertainty. The total absolute (relative) uncertainty assuming their sources to be independent is evaluated to be 711 MHz (14.2×10^{-6}). It turns out that we have therefore exceeded the original goal of 30 ppm of this experiment by a factor of 2.

4.3.7 Resonance Line Width Expected

The width of the resonance line is dominated by its natural linewith of 18.6 GHz [88]. With its contributions (listed in Table 4.7) being both Lorentzian and Gaussian, the resulting resonance line is strictly speaking a Voigt profile, a convolution of a Lorentzian (FWHM linewidth γ_L) and a Gaussian (FWHM linewidth f_G). The width f_V at half maximum of such a profile can be estimated to [127]

$$f_V \simeq 0.535\,\gamma_L + \sqrt{0.217 \cdot \gamma_L^2 + f_G^2}. \tag{4.51}$$

Effect	Shift [MHz]		Broadening (FWHM) [MHz]
	Value	Uncertainty	Value
Statistics	0	644	0
Calibration	0	300	0
AC Stark	0	< 1	4
DC Stark	0	$< 10^{-6}$	0
Zeeman	0	30	100
Doppler	0	< 0.1	1000
Collisional	0	1	2
Laser Bandwidth	-	-	1750
Grand Total (independ.)	0	$(644)_{stat}(301)_{syst}$	2073 – 2315

Table 4.7: Uncertainty Budget of the $\mu p(2S^{F=1}_{1/2} - 2P^{F=2}_{3/2})$ Resonance. *A summarizing table of all uncertainties discussed so far. The individual contributions have been addressed in the preceeding sections. The uncertainties of the Grand Total are added up quadratically assuming the independency of the multiple effects. The contribution of the listed effects to the line broadening is also given. The quoted range for the sum depends on whether the laser bandwidth is assumed to be Gaussian (lower bound) or Lorentzian (upper bound).*

All contributions summarized in Table 4.7 are of Lorentzian nature except the Doppler broadening (accounting for a Gaussian distribution) and the laser bandwith. The shape of the latter lies somewhere between a Lorentzian and a Gaussian (see Section 4.2.3). The width of the resonance line will, therefore, be found between the two extreme cases of the laser bandwith being purely Lorentzian or purely Gaussian.

In the case of a purely Gaussian laser bandwidth, the Gaussian contributions account to $f_G^{\text{Gauss}} = 2.0\,\text{GHz}$ (added quadratically), together with the Lorentzian contribution of $\gamma_L^{\text{Gauss}} = 18.7\,\text{GHz}$. This results in an expected linewidth for the Voigt profile of $f_V^{\text{Gauss}} = 19.0\,\text{GHz}$. Assuming a purely Lorentzian laser bandwidth, a linewidth for the Voigt profile of $f_V^{\text{Lorentz}} = 20.5\,\text{GHz}$ is calculated (with a Lorentzian (Gaussian) contribution of $\gamma_L^{\text{Lorentz}} = 20.5\,\text{GHz}$ ($f_G^{\text{Lorentz}} = 1\,\text{GHz}$)).

Hence, the experimentally observed resonance line width is expected to be

$$f_V = 19.75 \pm 0.75\,\text{GHz}. \tag{4.52}$$

Note that since $f_G \ll \gamma_L$ is fulfilled, the difference between the Voigt and the Lorentz profile is negligibly small. This justifies the use of a simple Lorentzian fitting function for the data analysis.

4.4 The $\mu p(2S_{1/2}^{F=1} - 2P_{3/2}^{F=2})$ Resonance

The fit of the resonance data of the $\mu p(2S_{1/2}^{F=1} - 2P_{3/2}^{F=2})$ line using the line-shape model explained in Sect. 4.1 and the rather wide cuts developed in Appendix B yields to a determination of the centroid position (in units of FSR of the FP) of

$$\text{Position} = 282895.292\,(430)\,\text{FSR} \tag{4.53}$$

and a purely Lorentzian width (at FWHM) of

$$\text{Width} \quad = 11.1\,(1.3)\,\text{FSR}. \tag{4.54}$$

In order to assign the correct frequency to the centroid position, one has to extrapolate from the closest FP-fringe at which the laser has been calibrated using a water line (as done in Section 4.2.2). According to Eq. (4.12), this is FP-fringe N$^{\underline{o}}$ 282874 with $\nu_{FP282874} = 49\,849\,817\,(300)$ MHz. According to Equation (4.9), the FSR of the FP cavity in the frequency range of this resonance is FSR = 1497.332 (3) MHz. The stated uncertainty for this value is completely irrelevant to the systematics budget. Note that the uncertainty of 300 MHz is already included in the error budget of the previous section.

This leads to a determination of the peak position of

$$\begin{aligned} \nu_{2S-2P} &= \nu_{FP} + \Delta\text{FP} \cdot \text{FSR} \\ &= 49849817.0\,\text{MHz} + 21.29 \cdot 1497.33\,\text{MHz} \\ &= 49881695.2\,\text{MHz}. \end{aligned} \tag{4.55}$$

Including the systematic and statistical uncertainties, one retrieves the following result for the $\mu p(2S_{1/2}^{F=1} - 2P_{3/2}^{F=2})$ transition

$$\boxed{\nu_{2S-2P} = 49\,881\,695\,(644)_{stat}(301)_{syst}\,\text{MHz},} \tag{4.56}$$

with the first uncertainty being the statistical and the second the systematic one. Adding the two uncertainties quadratically results in a total absolute uncertainty of 711 MHz which translates into a relative uncertainty of 1.4×10^{-5}.

The fitted width (at FWHM) of this resonance line can be calculated using Eq. (4.54) and the FSR of Eq. (4.9) to be

$$\boxed{\Gamma_{2S-2P} = 16.59 \pm 1.90\,\text{GHz},} \tag{4.57}$$

which turns out to be $1.5\,\sigma$ smaller than the expected width in Equation (4.52). The reason for this discrepancy is not fully understood but might be due to a slight overestimation of the background.

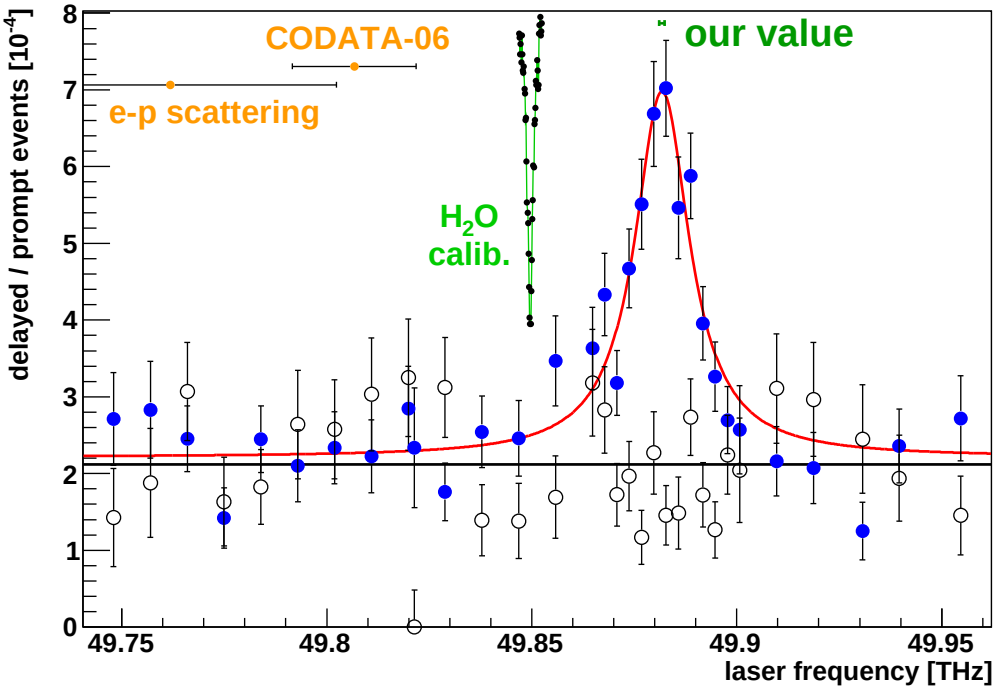

Figure 4.14: The μp$(2S^{F=1}_{1/2} - 2P^{F=2}_{3/2})$ Resonance: Wide Cuts. *The first transition in μp is plotted versus the laser frequency (solid blue circles). In it, the number of laser induced events is normalized to the number of prompt events. To improve statistics, the parameter cuts are chosen rather generously. This reduces the S/B ratio to* 3.3. *The empty circles represent Laser$_{off}$ data that have been recorded simultaneously (see text for more details).*

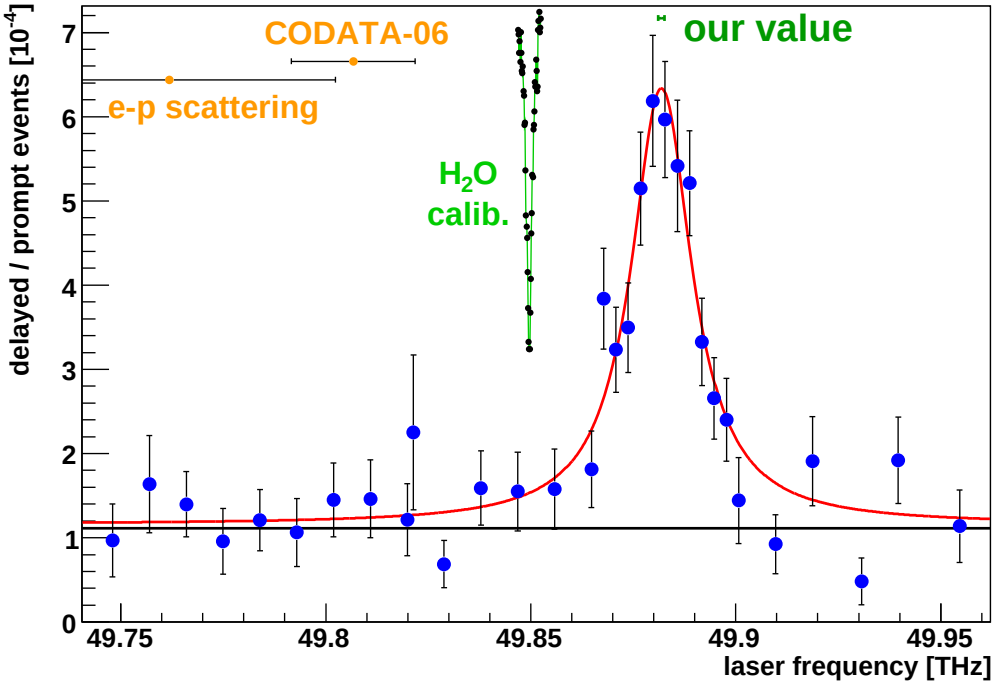

Figure 4.15: The μp$(2S^{F=1}_{1/2} - 2P^{F=2}_{3/2})$ Resonance: Strict Cuts. *This resonance line is produced from the same μp data as the one in Fig. 4.14. In contrast to the data analysis presented in the previous chapter, this resonance is based on stricter parameter cuts used during the online analysis. It contains less statistics but exhibits a S/B ratio of 5.7.*

The resonance which leads to the results stated here is presented in Figure 4.14. It is produced with rather wide parameter cuts as described in Appendix B. This leads to an increase in the statistics by $\sim 25\,\%$ and, therefore, to an improvement in the centroid determination. However, it deteriorates the signal-to-background (S/B) ratio. In the LTW, 900 events have been recorded with the wide cuts where 404 background events are expected (leading to 496 laser-induced events). The data is produced by normalizing the number of events in the LTW to the number of prompt events. The Laser$_{off}$ data is also presented (empty circles). It has been recorded simultaneously with the Laser$_{on}$ data, with the difference being that the laser could not be fired for these data. The background amplitude used as a fixed parameter in the fit is taken from the average of these data (solid black line). The plot also shows one representative absorption spectrum of the water line N$^{\underline{o}}$ 1662 which is used to calibrate FP-fringe N$^{\underline{o}}$ 282874. Moreover, it indicates the predictions for the line position using the proton radius from CODATA [76] and from electron scattering data [11, 111].

For comparison, the resonance line for the same μp transition obtained with much stricter parameter cuts is shown in Figure 4.15. It is published in Ref. [1] as $\nu_{2S-2P} = 49\,881\,880\,(760)$ MHz. The uncertainty of this value is 7 % larger than the one of this thesis. This is due to the different statistical uncertainties (700 MHz compared to 644 MHz) stemming from the two mentioned approaches to the analysis of the data. In Figure 4.15, the signal-to-background ratio is $S/B = 5.7$ (compared to $S/B = 3.3$ from above), but the statistics is worse (550 events on resonance compared to 900 events in Fig. 4.14). With these parameter cuts, only 155 background events are expected in the LTW so that 395 laser-induced events are obtained (101 less than with the wide-cut resonance from Fig. 4.14).

4.5 New Values for the Proton Radius and the Rydberg Constant

From the analysis of the $\mu p(2S_{1/2}^{F=1} - 2P_{3/2}^{F=2})$ resonance presented in this thesis, one can finally derive a new value for the proton radius r_p and for the Rydberg constant R_∞.

Proton Charge Radius $\mathbf{r_p}$

The frequency for the $2S_{1/2}^{F=1} - 2P_{3/2}^{F=2}$ transition given in Equation (4.56) corresponds to an energy of

$$\Delta E_{2S-2P} = 206.2941\,(29)\,\text{meV}, \tag{4.58}$$

with the uncertainty coming from the 711 MHz experimental uncertainty in the transition frequency. From Equation (1.10) describing all known QED contributions to the $2S_{1/2}^{F=1} - 2P_{3/2}^{F=2}$ energy difference, one obtains for r_p

$$\boxed{r_p = 0.84192\,(34)\,(56)\,\text{fm}.} \tag{4.59}$$

Here, the first quoted uncertainty is of experimental nature including the statistical and systematic parts. The second uncertainty stems from the theoretical uncertainty given in Equation (1.10). All in all, this results in $r_p = 0.84192\,(65)\,\text{fm}$ differing only marginally within its uncertainty from the value quoted in Ref. [1]. The relative uncertainty of 7.8×10^{-4} is a 26-fold improvement over the accuracy of the electron scattering value ($r_p = 0.895\,(18)\,\text{fm}$) [11] and a 10-fold improvement over the CODATA 2006 accuracy ($r_p = 0.8768\,(69)\,\text{fm}$) [76]. Our value is $5.0\,\sigma$ ($3.1\,\sigma$) smaller than the CODATA (electron scattering) value. The origin of this large discrepancy is unclear.

An additional term as large as 0.31 meV would be needed in Equation (1.10) to match our r_p value to the CODATA one if one takes the QED-calculations in μp for granted. This equates to 65 times the uncertainty claimed in Eq. (1.10).

The discrepancy could also arise from wrong measurements in hydrogen (H): the determination of r_p by CODATA can be regarded, in a simplified way, as an adjustment of the input parameters r_p and R_∞ to match the calculated QED to the measured transitions in H. These are the $1S - 2S$ [8, 10] and the $2S - nl$ transitions with $nl = 2P, 4, 6, 8S/D, 12D$ transitions in *ep*. However, since the $1S - 2S$ transition frequency has been measured with a relative accuracy of 1.4×10^{-14} (absolute 34 Hz [8, 10, 76]), an error of $\sim$ 1700 times the stated uncertainty would have to be introduced. Looking at the measurements of $2S - 8D$ [9, 72] and of $2S_{1/2} - 2P_{1/2}$ [128] in H, the stated experimental accuracy could, in principle, make these measurements subject to unknown systematic effects. Nevertheless, all hydrogen measurements point into the same direction and suggest a larger proton radius.

Rydberg Constant R_∞

Following the argumentation in Section 1.7, one can extract a new value for the Rydberg constant R_∞. Assuming the correctness of the Lamb shift calculations in μp (Section 1.5) and in ordinary hydrogen, we use the precise measurement of the $1S - 2S$ transition in hydrogen [8, 10], the H($1S$) and H($2S$) Lamb shifts newly calculated with our value for r_p, and the most recent value of the fine structure constant ($1/\alpha = 137.035\,999\,084$ [129]) and obtain

$$\boxed{R_\infty = 10\,973\,731.568\,161\,(16)\,\mathrm{m}^{-1}.} \tag{4.60}$$

This value is $-110\,\mathrm{kHz/c}$ or $4.9\,\sigma$ away from the CODATA value (Equation (1.23)), but with a relative accuracy of 1.5×10^{-12}, it is 4.6 times more precise.

4.6 Other μp and μd Resonances

In addition to the focus of this thesis, the $\mu p(2S^{F=1}_{1/2} - 2P^{F=2}_{3/2})$ resonance, three other resonances in μp and μd were measured and one more line in μd were observed in the 2009 beam time. The careful analysis of these four lines has yet to be performed. Therefore, all reported data here is **preliminary** and subject to change. Nevertheless, they are presented here.

Table 4.8 lists all the resonances measured together with the **statistical** accuracy of the position determination of the preliminary online analysis. Systematic studies are yet to be performed. Figure 4.16 presents the resonance lines apart from the first transition in μp. All lines are plotted versus the laser frequency and are scaled along the frequency axis such that the resonance widths match and the scanning regions can be compared. Note that all data in this section is preliminary and subject to be changed by a refined analysis.

Starting from both μp transitions, several scenarios can be considered. First of all, two values for the proton charge radius r_p can be calculated using the theoretically known energy differences of the two transitions. Moreover, a value for the $2S_{1/2} - 2P_{1/2}$ Lamb shift independent of the $2S$ HFS and the Zemach radius r_Z can be extracted if one *adds* both μp transitions in a correctly weighted manner and considers the $2P$ fine and hyperfine structure to be well known [130] (cf. Equation (A.5)). The *difference* of the two μp transition frequencies sheds light on the $2S$ HFS: with the HFS of the $2P_{3/2}$ state being calculated accurately [130], the frequency difference is simply equivalent to the $2S^{F=0}_{1/2} - 2S^{F=1}_{1/2}$ transition frequency. Since the Zemach radius r_Z [131] describes the first order nuclear structure correction to the HFS, a new value for r_Z can be deduced from this with about 3 % relative accuracy.

In μd, a major puzzle needs to be solved: neither the absolute line positions nor the relative positions of the lines among each other seem to be correct. It has to be

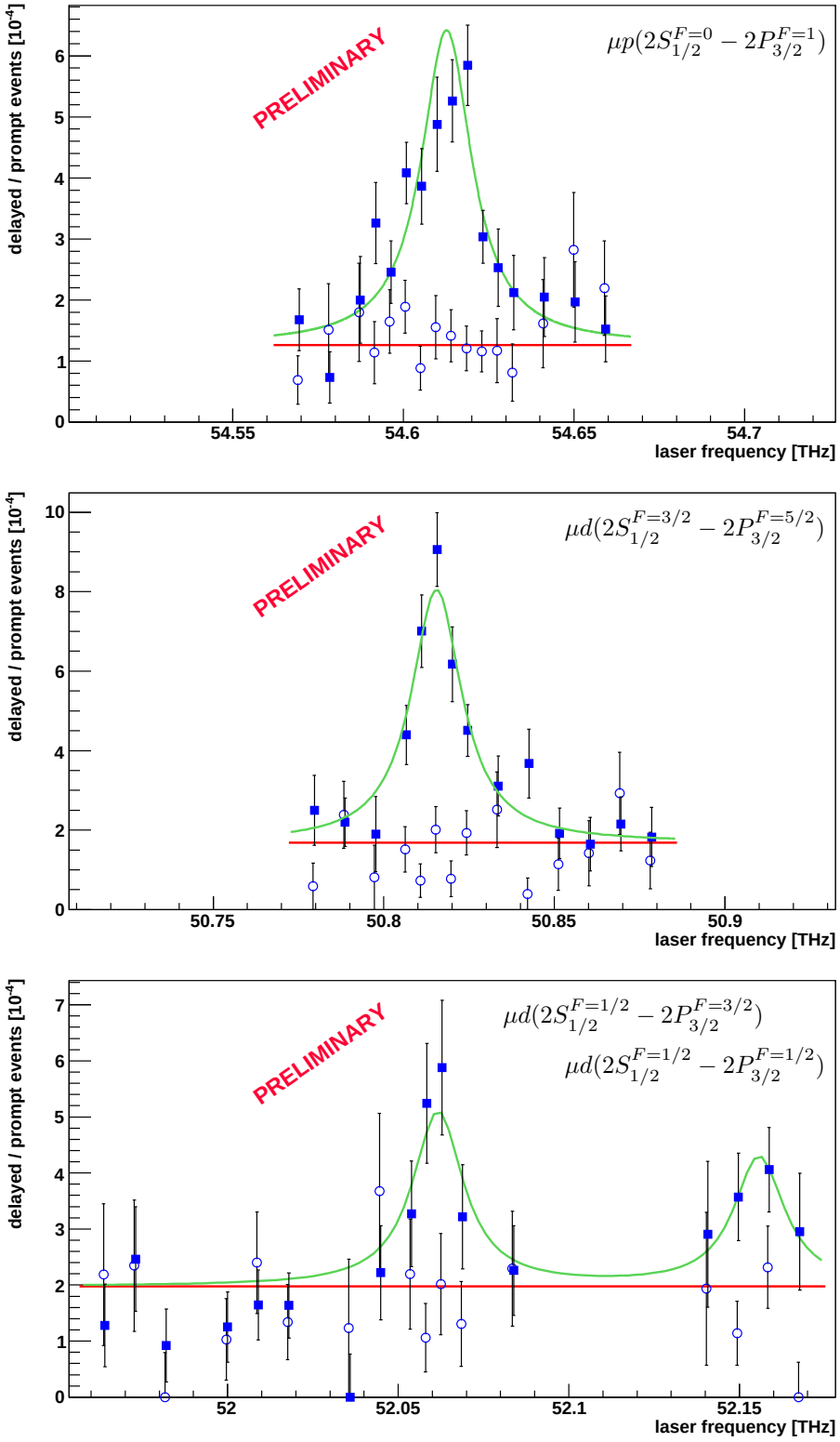

Figure 4.16: The Other Resonances in μp and μd. *The other four transitions measured in the 2009 campaign are plotted versus the laser frequency. Since all resonances possess the same linewidth, they are scaled so that their widths agree. The empty circles represent $Laser_{off}$ data that have been recorded simultaneously.*

Muonic Transition	Position [GHz]	Status	Rel. Uncertainty
$\mu p(2S^{F=1}_{1/2} - 2P^{F=2}_{3/2})$	49881.70 (71)	final	15 ppm
$\mu p(2S^{F=0}_{1/2} - 2P^{F=1}_{3/2})$	*54612.6 (1.2)*	statistical only	22 ppm
$\mu d(2S^{F=3/2}_{1/2} - 2P^{F=5/2}_{3/2})$	*50815.4 (1.0)*	statistical only	20 ppm
$\mu d(2S^{F=1/2}_{1/2} - 2P^{F=3/2}_{3/2})$	*52061.7 (2.2)*	statistical only	42 ppm
$\mu d(2S^{F=1/2}_{1/2} - 2P^{F=1/2}_{3/2})$	*52155.7 (3.5)*	statistical only	67 ppm

Table 4.8: The μp and μd Transitions. *All $2S-2P$ transitions in muonic hydrogen and deuterium examined during the 2009 campaign. Apart from the first transition in μp all values presented here are* ***preliminary*** *and the stated uncertainties are purely statistical. The last two transitions in μd appear together in the bottom plot in Fig. 4.16.*

mentioned that the theory of the Lamb shift in μd lacks redundancy. So far, only the paper of Borie [132] is available.

As in μp, the deuteron charge radius r_d can be extracted from the Lamb Shift measurements in μd. Apart from the vacuum polarization effects, the largest contributions to the μd Lamb shift are the finite nuclear size corrections and the nuclear polarizability corrections [132]. Based on correct QED calculations, on reliable values for the fine and hyperfine structure, and on a theoretical value for the nuclear polarizability [48, 133, 134], one can determine r_d from every μd transition individually.

On the other hand, one can also derive a prediction for the deuteron charge radius using hydrogen $1S-2S$ spectroscopy. In order to do so, the value for r_p deduced from our μp measurements needs to be inserted into the difference of the charge radii $r_d^2 - r_p^2$ obtained from the isotope shift in electronic hydrogen and deuterium [135, 136]. This leads to a prediction for r_d which can then be compared to the values for r_d obtained from our μd measurements.

The argumentation could also be turned around: one could verify the nuclear polarizability contribution to the μd Lamb shift. By supplying the predictive value for r_d to the μd Lamb shift, and assuming that the other QED terms are correct, the nuclear polarizability term is left as the only relevant free parameter. In such a way the nuclear polarizability calculations [48, 133, 134] could be tested.

However, there seem to be inconsistencies between the results of the online data and theoretical calculations. This has yet to be examined carefully. Hence, in order to resolve the puzzles raised by muonic deuterium, the data has to be analysed rigorously and the theory behind the Lamb shift has to be revised carefully.

4.7 Conclusions

Proposed 40 years ago, this experiment resolves a provocative quest of deducing the proton charge radius through a measurement of the Lamb shift in muonic hydrogen. It opens the way to test QED to an unprecedented level, delivers more accurate values for several physical (fundamental) constants, and will hopefully trigger new theoretical ideas to overcome the discrepancy between our observed value of the proton radius and the ones commonly accepted up to now.

Newly available experimental data will also support this pursuit. This is the reason, why the collaborators having measured μp and μd intend to continue the experimental work: in early 2010, the collaboration (now baptized **CREMA**-collaboration[5]) has successfully submitted a proposal to an external review committee at the Paul–Scherrer–Institute in Switzerland to measure the Lamb shift in muonic helium ions ($\mu^4\mathrm{He}^+$ and $\mu^3\mathrm{He}^+$). The aim is to determine the alpha-particle and helion rms charge radius. In addition, the fine and hyperfine structure components will be revealed, and the Zemach or magnetic moment distribution radius will be determined.

The contribution of the finite size effect to the Lamb shift ($2S-2P$ energy difference) in $\mu\mathrm{He}^+$ is as high as 20 %. Therefore a measurement of the transition frequencies with a moderate (for laser spectroscopy) precision of 50 ppm (corresponding to 1/20 of the line width) will lead to a determination of the nuclear rms charge radii with a relative accuracy of 3×10^{-4} (equivalent to 0.0005 fm). The limiting factor for the extraction of the radii from the Lamb shift measurements is given by the uncertainty of the nuclear polarizability contribution.

Combined with an ongoing experiment at MPQ aiming to measure the $1S - 2S$ transition frequency in He^+ [137], the Lamb shift measurement in $\mu\mathrm{He}^+$ will lead to a sensitive test of problematic and challenging bound-state QED terms. This measurement will also help to clarify the discrepancy found in our μp experiment. Additionally, a precise knowledge of the absolute nuclear radii of the He isotopes and the hyperfine splitting of $\mu^3\mathrm{He}^+$ provide a relevant test of few-nucleon theories.

[5] **C**harge **R**adius **E**xperiments using **M**uonic **A**toms

Appendix A

2S – 2P Splitting in Muonic Hydrogen

All the relevant contributions to the $2S^{F=1}_{1/2} - 2P^{F=2}_{3/2}$ transition have been compiled, revised, and double-checked by P. Indelicato. This Appendix is a reproduction of supplementary online material provided for our publication in Nature (Ref. [1]). It explains, how Equation (1.10) is derived.

The relation between the transition energy that we measured and the proton root mean square charge radius r_p requires detailed calculation of relativistic, QED and recoil corrections to the energies of the $2S$ and $2P$ levels, some of which are charge-radius dependent. As the proton has a magnetic moment, the hyperfine structure correction for each level has to be taken into account, as well as QED corrections to the hyperfine structure.

The main calculations directly applicable to muonic hydrogen can be found in the work of Pachucki [31–33] and Borie [34, 138]. Detailed description of existing terms can be found in the review and book of Eides, Grotch and Shelyuto [19, 39]. The fine structure splitting between the $2P_{1/2}$ and $2P_{3/2}$ levels is given in Refs. [34, 130]. Some hyperfine corrections can be found in the same references, but more precise calculations have been performed for the $2S$ and $2P$ states by Martynenko [130, 139].

Here we describe how we arrive at the equation that was used to extract the proton charge radius from the measurement. The task is not easy, as different authors use different terminology for identical terms. Moreover, the dependence on the proton radius is not always explicitly given for all terms.

The main uncertainties originate from the proton polarizability, and from different values of the Zemach radius. The Zemach radius describes the first order nuclear structure correction to the hyperfine splitting, given by the finite charge and magnetic moment distribution in the proton [131].

We started from Table I in Ref. [34] as it provides the exact Dirac contribution for the main vacuum polarization contribution to the Lamb shift. All listed contributions were checked against the other references provided above whenever possible. Summing

up the corrections given in the main table, we noticed that the equation provided in Ref. [34] does not exactly correspond to the values given in the table. Since these papers were published, a mistake in Ref. [35] was found and corrected in [36]. We then added a few small extra terms provided in [19]. Terms that are obtained by a formula depending only on fundamental constants have been recalculated with more significant digits. We also recalculated some of the radius-dependent part from the formulas provided in [19], to have consistent numerical accuracy whenever possible.

The list of all contributions, and the final values are presented in Table A.1 for the radius-independent part of the $2S_{1/2} - 2P_{1/2}$ Lamb shift, and in Table A.2 for the radius-dependent part. Note that there is a term called "Nuclear size correction of order $(Z\alpha)^6$" in Table 7.1 of Ref. [19], and "Finite size of order α^6" in Table I of Ref. [32], which is not included in Ref. [34]. In Ref. [32], it is provided as a proton radius independent term -0.0009 meV for $r_p = 0.862$ fm, but it actually contains both a r_p^2 and a r_p^4 contribution to the $2S_{1/2} - 2P_{1/2}$ splitting [19]. We include the r_p^2 dependent part in Tab. A.2, but we neglect the term $0.000043\, r_p^4 = 2.5 \cdot 10^{-5}$ meV, because it is irrelevant at our level of accuracy.

From these contributions we obtain the $2S_{1/2} - 2P_{1/2}$ Lamb shift

$$\Delta E^{\mathrm{LS}}/\mathrm{meV} = 206.0573(45) - 5.2262\, r_p^2 + 0.0347\, r_p^3\,, \tag{A.1}$$

where $r_p = \sqrt{< r_p^2 >}$ is the root mean square charge radius of the proton in fm. The uncertainties in Table A.1 have been added in quadrature to obtain the total uncertainty of 0.0045 meV. This value is dominated by the proton polarizability contribution of Borie [34] (#25 in our Table A.1), who took into account the scatter of the polarizability terms by several authors for her quoted uncertainty.

The $2S$ hyperfine structure depends on the Zemach radius r_Z. Here we follow Ref. [139], who uses $r_Z = 1.022$ fm (see Eq. (7) of Ref. [23]) and adopt

$$\Delta E_{2S}^{\mathrm{HFS}} = 22.8148\,(78)\ \mathrm{meV}. \tag{A.2}$$

Of above's total uncertainty of 0.0078 meV, 0.0060 meV are due to the scatter of various determinations of the Zemach radius.

The fine structure is given by [130]

$$\Delta E^{\mathrm{FS}} = 8.352082\ \mathrm{meV}, \tag{A.3}$$

which compares well with Borie's value 8.352 meV.

Finally, the $2P_{3/2}$ hyperfine structure is given by [130]

$$\Delta E_{2P_{3/2}}^{\mathrm{HFS}} = 3.392588\ \mathrm{meV}. \tag{A.4}$$

The $2P_{3/2}^{F=2}$ level shift with respect to the unperturbed $2P_{1/2}$ level is $\Delta E^{\mathrm{FS}} + \frac{3}{8}\Delta E_{2P_{3/2}}^{\mathrm{HFS}} = 9.6243$ meV. For comparison, Borie's value is 9.624 meV.

The level energies are thus:

$$\begin{aligned} E_{2S^{F=1}_{1/2}} =& \frac{1}{4}\Delta E^{\mathrm{HFS}}_{2S} = 5.7037\,(20)\ \mathrm{meV}, \\ E_{2P^{F=2}_{3/2}}/\mathrm{meV} =& \Delta E^{\mathrm{LS}} + \Delta E^{\mathrm{FS}} + \frac{3}{8}\Delta E^{\mathrm{HFS}}_{2P_{3/2}} \\ =& 215.6816\,(45) - 5.2262\,r_p^2 + 0.0347\,r_p^3\,. \end{aligned} \tag{A.5}$$

This leads to the transition energy for the measured $2S^{F=1}_{1/2}$ – $2P^{F=2}_{3/2}$ transition in muonic hydrogen:

$$\Delta E(2P^{F=2}_{3/2} - 2S^{F=1}_{1/2})/\mathrm{meV} = 209.9779\,(49) - 5.2262\,r_p^2 + 0.0347\,r_p^3\,, \tag{A.6}$$

where the uncertainty of the constant term is the quadratic sum of the uncertainty of the Lamb shift [Eq.(A.1)] and 1/4 of the 2S hyperfine structure [Eq.(A.2)]. Note that the r_p^3 term is for a "dipole" model of the proton form factor [34].

#	Contribution		Our selection		Pachucki [31–33]		Borie [34]	
		Ref.	Value	Unc.	Value	Unc.	Value	Unc.
1	NR One loop electron VP	[31, 32]			205.0074			
2	Relativistic correction (corrected)	[31–34]			0.0169			
3	Relativistic one loop VP	[34]	205.0282				205.0282	
4	NR two-loop electron VP	[14, 34]	1.5081		1.5079		1.5081	
5	Polarization insertion in two Coulomb lines	[31, 32, 34]	0.1509		0.1509		0.1510	
6	NR three-loop electron VP	[35]	0.00529					
7	Polarisation insertion in two and three Coulomb lines (corrected)	[35, 36]	0.00223					
8	Three-loop VP (total, uncorrected)				0.0076		0.00761	
9	Wichmann-Kroll	[34, 37, 38]	−0.00103				−0.00103	
10	Light by light electron loop contribution (Virtual Delbrück scattering)	[39]	0.00135	0.00135			0.00135	0.00015
11	Radiative photon and electron polarization in the Coulomb line $\alpha^2(Z\alpha)^4$	[31, 32]	−0.00500	0.0010	−0.006	0.001	−0.005	
12	Electron loop in the radiative photon of order $\alpha^2(Z\alpha)^4$	[40–42]	−0.00150					
13	Mixed electron and muon loops	[43]	0.00007				0.00007	
14	Hadronic polarization $\alpha(Z\alpha)^4 m_r$	[44–46]	0.01077	0.00038	0.0113	0.0003	0.011	0.002
15	Hadronic polarization $\alpha(Z\alpha)^5 m_r$	[45, 46]	0.000047					
16	Hadronic polarization in the radiative photon $\alpha^2(Z\alpha)^4 m_r$	[45, 46]	−0.000015					
17	Recoil contribution	[47]	0.05750		0.0575		0.0575	
18	Recoil finite size	[34]	0.01300	0.001			0.013	0.001
19	Recoil correction to VP	[34]	−0.00410				−0.0041	
20	Radiative corrections of order $\alpha^n(Z\alpha)^k m_r$	[19, 32]	−0.66770		−0.6677		−0.66788	
21	Muon Lamb shift 4th order	[34]	−0.00169				−0.00169	
22	Recoil corrections of order $\alpha(Z\alpha)^5 \frac{m}{M} m_r$	[19, 32, 34, 39]	−0.04497		−0.045		−0.04497	
23	Recoil of order α^6	[32]	0.00030		0.0003			
24	Radiative recoil corrections of order $\alpha(Z\alpha)^n \frac{m}{M} m_r$	[19, 31, 32]	−0.00960		−0.0099		−0.0096	
25	Nuclear structure correction of order $(Z\alpha)^5$ (Proton polarizability contribution)	[32, 34, 45, 48]	0.015	0.004	0.012	0.002	0.015	0.004
26	Polarization operator induced correction to nuclear polarizability $\alpha(Z\alpha)^5 m_r$	[46]	0.00019					
27	Radiative photon induced correction to nuclear polarizability $\alpha(Z\alpha)^5 m_r$	[46]	−0.00001					
	Sum		206.0573	0.0045	206.0432	0.0023	206.05856	0.0046

Table A.1: Radius-Independent Contributions to the Lamb Shift. *All known radius-independent contributions to the Lamb shift in μp from different authors, and the one we selected. We follow the nomenclature of Eides et al. [19] Table 7.1. Item # 8 in Refs. [32, 34] is the sum of items # 6 and # 7, without the recent correction from Ref. [36]. The error of # 10 has been increased to 100 % to account for a remark in Ref. [19]. Values are in meV and the uncertainties have been added in quadrature. NR stands for non-relativistic, VP for vacuum polarization.*

Contribution	Ref.	Our Selection		Pachucki [32]	Borie [34]
Leading nuclear size contribution	[49]	−5.19745	$< r_p^2 >$	−5.1974	−5.1971
Radiative corrections to nuclear finite size effect	[32, 49]	−0.0275	$< r_p^2 >$	−0.0282	−0.0273
Nuclear size correction of order $(Z\alpha)^6 < r_p^2 >$	[31, 50–52]	−0.001243	$< r_p^2 >$		
Total $< r_p^2 >$ contribution		−5.22619	$< r_p^2 >$	−5.2256	−5.2244
Nuclear size correction of order $(Z\alpha)^5$	[31, 32]	0.0347	$< r_p^3 >$	0.0363	0.0347

Table A.2: Radius-Dependent Contributions to the Lamb Shift. *All relevant radius-dependent contributions as summarized in Eides et al. [19], compared to Refs. [32, 34]. The values are given in meV and the proton charge radii in fm.*

Appendix B

Method of the Data-Analysis

In this Appendix, a step-by-step compendium shall guide through the data-analysis performed after the beam-time in 2009. It is intended to be a handbook to alleviate the future analysis of newly taken data and the re-analysis of the data presented here. Section B.1 describes the concepts of the wave-form analysis. The subsequent Sections B.2 – B.4 are concerned with details on the analysis of the raw wave form digitizer (WFD) spectra. With correctly tuned Analyzer parameters, one can approach the time calibration of the various detectors (Section B.5) and the energy calibration of the large area avalanche photo diodes (LAAPDs, cf. Sect. B.6). The event construction is introduced in Section B.7. In Section B.8 and Section B.9, procedures are explained how to properly set the delayed electron cut and the energy cut, respectively.
The last Section B.11 presents the resonance obtained with all the parameters and cuts developed in this chapter.

B.1 Principle of the Wave-Form Analysis

After a hit by an X-ray or an electron, the reverse-biased LAAPDs send out a current pulse which is converted to a negative voltage step in the pre-amplifiers. This signal is digitized by 12 bit WFDs as explained in Section 2.4.2. The amplitude of the pulse recorded is directly proportional to the energy deposited in the APD. 3752-bin traces (with 4 ns per bin corresponding to a total trace length of 15 μs) are read out by a front-end computer, processed by the data-analysis software (in the following referred to as the *Analyzer*), and plotted by its display module. More details of the Analyzer and its routines can be found in [140].

All signals recorded by all detectors after a muon entered the target and triggered the data-aquisition system are combined into one *event*. An event can be composed of multiple hits in multiple or single LAAPDs and electron detectors. The hits in LAAPDs recorded by the WFDs are referred to as *pulses*.

Figure B.1 displays an example of such an event processed by the Analyzer. Guided by this figure, a brief introduction to the wave form analysis is given in this paragraph

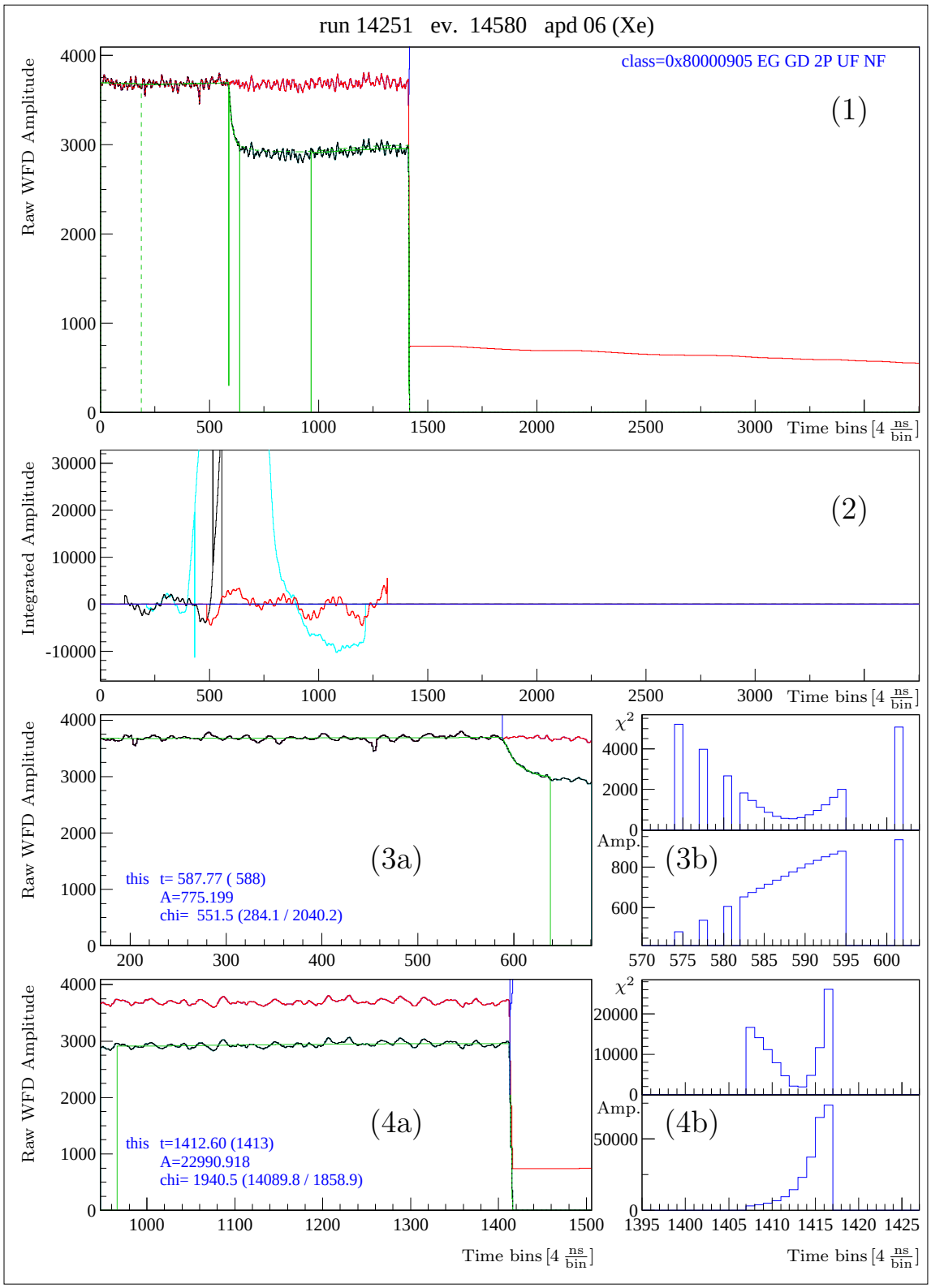

Figure B.1: WFD Signal and First Analysis. *This display is grouped in four elements: Panel (1) shows the wave-form recorded by one LAAPD as original (black) and after subtraction of the first pulse (red). Panel (2) illustrates the output of the ringing finder (cyan) and the edge finder for the first (second) pulse in black (red). The analysis of the fitting-routine is reproduced in the remaining elements (3) and (4): the fitted pulse (green) is shown together with the output of the fit (3a+4a), the χ^2-parabolas, and the corresponding fitted amplitudes (blue) (3b+4b). The x-axis of all panels is given in time bins $[4\,\frac{ns}{bin}]$. The y-axis is the 12 bit ADC value. Further details can be found in the text.*

with references to further details in the following sections. Figure B.1 contains two subsequent pulses recorded by one single LAAPD (A6): one X-ray followed by a saturating electron. Panel (1) of Fig. B.1 includes the original raw WFD-trace (black) and the trace after subtraction of the first successfully fitted pulse (red). Elementary for a successful fitting procedure are the standard responses of the LAAPDs, the so-called *Standard Wave Forms (SWFs)* introduced in Section B.2. In an initial procedure, the raw traces are checked for ringing present in the signals. The output of the ringing finder is plotted in cyan in Panel (2). If no ringing was detected in this trace, an edge finder (black output in the same panel) looks for the first indication of an edge (cf. Sect. B.3). The time bin in which an edge was discovered is passed as a starting value to the FitWave-routine (Sect. B.4) which fits a standard response function to the raw data. The fitted pulse (green) together with part of the raw wave-form (black) is shown in Panel (3a). After a successful fit, the results for the time bin, the fitted amplitude, and the χ^2 of the pulse are printed in blue into the same frame. The fitted pulse is subtracted from the black raw data generating the red wave-form. Moreover, the parabola of χ^2-minimization of the fitting procedure and the corresponding pulse-amplitude are outlined in Panel (3b) on the right.

Having completed the first pulse, the fitting routine starts from the beginning: now examining the wave-form (red) with the first pulse subtracted (1), the edge finder looks for the next edge (red edge finder output in Panel (2)). Here, it discovers a saturating raw amplitude (bin content equal to zero). Such pulses are treated by the Analyzer sub-routine FitElec (Sect. B.4.5). The result of this fit and the associated χ^2-parabola and amplitude-function are plotted in the two Panels (4a) and (4b) at the bottom of Fig. B.1.

Additionally, the Analyzer assigns certain classes to each event and each pulse printed in blue in Panel (1). The first flag is a classification for the complete event, deduced from the classifications of all WFD-spectra. For the showcase from Figure B.1, it reads **EG**, "event good". The remaining flags are dedicated to the specific WFD-trace: the analysis of this WFD-trace succeded (**GD**, "good"), and two pulses were fitted (**2P**). Since the trace contains underflow bins (**UF**) from saturating pulses, not the full WFD-trace was read out by the computer (**NF**, "not full").

B.2 Standard Wave Forms

The routine FitWave uses standard pulses to fit the WFD-traces. These standard pulses (termed *Standard Wave Forms (SWFs)*) describe the average responses of the individual LAAPDs (and their pre-amplifiers) to 2 keV X-rays and have to be established prior to data-analysis. For every LAAPD, these SWFs are developed from 150 hand-picked nice prompt 2 keV pulses: a spline is simultaneously fitted to all pulses to determine the standard response function. Since the standard responses depend on the properties and environmental conditions of the LAAPDs and their amplifiers, the SWFs are

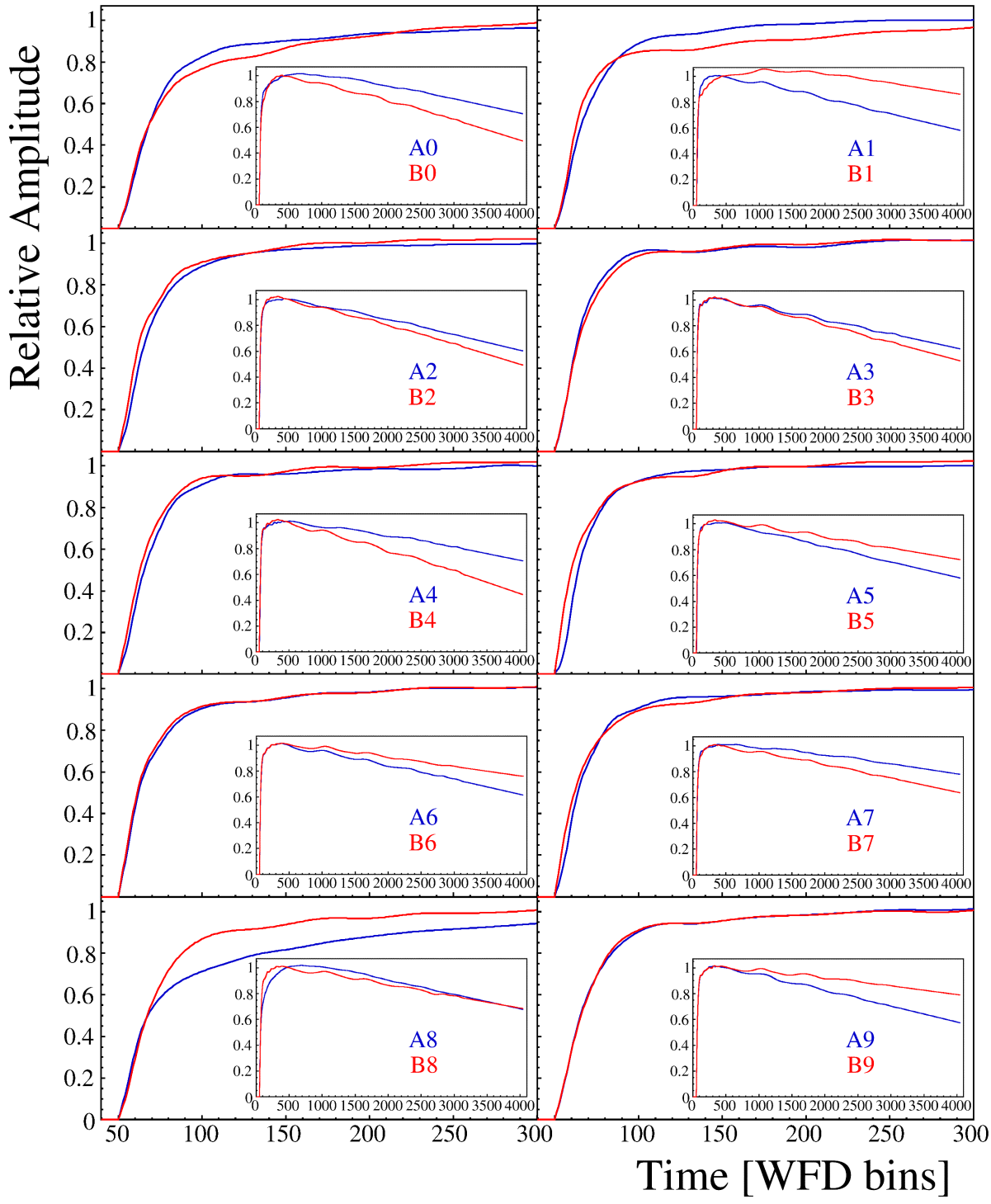

Figure B.2: The Standard Wave Forms for all LAAPDs. *For all 20 LAAPDs, a zoom into the interesting first 300 WFD time bins (4 ns/bin) of the SWFs is shown. The A-side LAAPDs are always shown in blue, the B-side LAAPDs in red. The inlays contain the complete SWFs of 4096 time bins length (corresponding to a trace of 16 µs) as they are used for the data analysis. Note that the SWFs are by convention positive and have to be inverted in order to be comparable to the wave form from Figure B.1 with its falling edge pulses.*

renewed when LAAPD-parameters change during the campaign.

For the fit, several parameters can be tuned. In order to speed up the procedure of producing SWFs, only the important early region of the pulse is fitted in the initial step. The length of this region *len_early* (starting with the beginning of the *pulse*) can be altered and is set to 400 time bins by default. The interpolation points (*pts_early*) in this region are not set equidistantly but such that fast-changing parts of the pulses are covered by more spline points. A typical value for *pts_early* is 20. In the late region (after *len_early*, fitted in a second step), where no fast changes occur, the number of interpolation points is set by their distance *dist_late* to each other (default 120 time bins). The parameter *tbin0* adjusts the correction to the Analyzer's *tbin* (i.e. the time bin which the fitting routine returns as the start bin of the pulse) for the first SWF guess. This parameter needs to be tuned in order to obtain a pulse with a well defined beginning of the rising edge.

Figure B.2 magnifies the essential first 300 WFD time bins (4 ns/bin) of the SWFs of all 20 LAAPDs. Note that the SWFs have to be inverted in order to be compared to Figure B.1. Their amplitudes are normalized to unity. Except A8, all LAAPDs behave similarly. Until the signal reaches 60 %, they exhibit a rise time of about 80 ns. The inlays in Fig. B.2 show the complete SWFs as they are used by the Analyzer. These standard pulses are fitted and then subtracted from the original WFD-traces.

B.3 Edge Finder

The edge finder is a tool to get a first hint of where the pulses are located. The common element of the edge finder is the cusp analysis incorporated into the Analyzer. For every bin i of the WFD-trace, it calculates $V_i^{edge} = S_i^{before} - S_i^{after}$, where S_i^{before} and S_i^{after} are the sums of the n bins before and after bin i, respectively. It then looks for a (local) maximum in V^{edge} indicating a step in the WFD-data. The value of V^{edge} at the maximum is proportional to the integral of this edge.

Figure B.3 clarifies the principle of the cusp analysis. The signal gets convoluted with the weighting function. The output, i.e. the difference of the two sums is maximum close to a location of an edge. For the edge finder it is favourable to choose a small number of bins (parameter *nbins*) to be summed up in order to be sensitive to fast features of the signal.

Similarly to the edge finder, a ringing finder is deployed in an initial step to check the wave-form for ringing events. Ringing events occur when high energetic particles hit one of the LAAPDs and cause neighbouring LAAPDs and their pre-amplifiers to oscillate. A ringing edge is detected when the ringing finder output stays above or below a certain threshold for a specified number of bins. If more than 5 positive edges or more than 2 negative edges are recognized, a WFD-trace is classified as ringing (**RG**), and the entire event is not analyzed any further.

Since the data read-out is triggered by separate integrating amplifiers with their

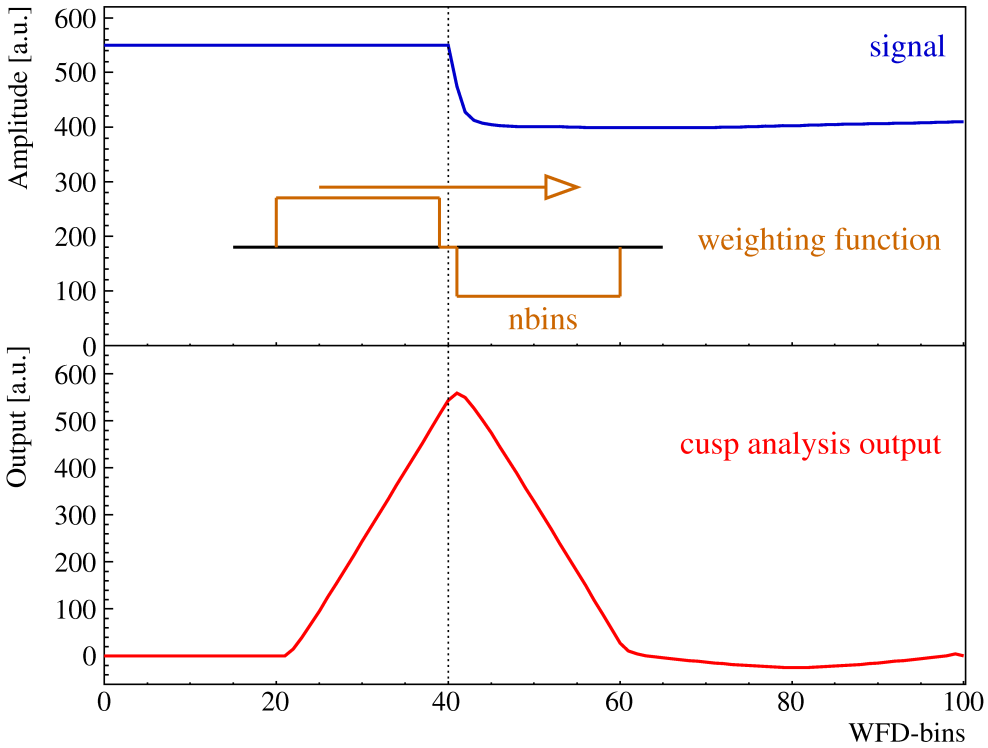

Figure B.3: Cusp Analysis of the Ringing Finder and Edge Finder. *The blue signal gets convoluted with the weighting function, which evaluates the difference of the* ***nbins*** *bins summed up before and after bin* ***i****. For a standard pulse, the maximum of the output (red) is close to the location of the edge. The value at the maximum is proportional to the integral of the edge found in the signal.*

own discriminators, only pulses above a certain amplitude threshold triggering these amplifiers will show up in the Analyzer as digitized traces. To find even the smallest pulses, the edge finder parameters have to be optimized.

B.3.1 Parameter *thr_pos*

In order to distinguish the smallest pulses from noise, the parameter *thr_pos*, i.e. the positive threshold above which the edge finder declares to have found an edge, has to be set to its optimum value. The unit of *thr_pos* is the raw WFD amplitude which is recorded as a voltage output from a detector and is a direct measure for the pulse energy.

Therefore, the analysis of a particular run (# 14251) is performed multiple times with varying *thr_pos*. The plots in Figure B.4 help to determine the correct value of *thr_pos*: Plot (a) shows the mean number of edges per pulse found by the edge finder analysis. A steep increase towards lower *thr_pos*-values suggests that, here, the edge finder triggers in noise and too many falsely identified edges are recorded. The number of WFD-traces without any edges declared by the edge finder is laid out in the Plot (b). At very small threshold-values, the edge finder triggers in noise (and small time markers

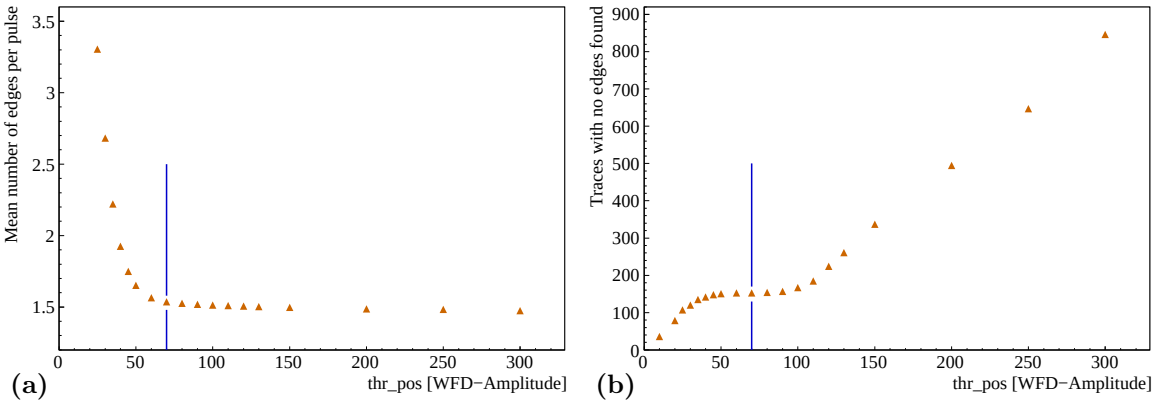

Figure B.4: Investigations on the Edge Finder Threshold *thr_pos*. ***(a)*** *The mean number of edges found per pulse by the WFD-analysis for a range of* ***thr_pos****-values is plotted in this panel. An increase to lower values of* ***thr_pos*** *is visible.* ***(b)*** *This plot shows the number of traces without any edge found as a function of* ***thr_pos****. The data for (a) and (b) stem from one run (# 14251). The LAAPD A5 shown here is a typical representative; the other LAAPDs behave similarly. A cutoff-value of 70 was chosen for all photo-diodes (blue vertical line). Below this threshold, the edge finder triggers in noise.*

added to the signal called fiducials), declaring almost everything as an edge. Only in the constant region is the threshold above the noise. In this regime, no real edges are present yet. At the transition to the linear slope, the hardware discriminator becomes visible: here, *thr_pos* is still below the amplitude at which the hardware discriminator starts flagging a pulse to be found. At higher *thr_pos*-values, the linear rise indicates that the threshold is chosen too large and small pulses are not discovered by the edge finder any longer.

Most of the wave forms recorded from the LAAPDs contain one or two pulses. Decreasing the threshold *thr_pos* to lower values will cause the edge finder detecting more and more edges originating from noise. In Fig. B.4(a), this behaviour starts to show below $thr\_pos = 70$. Fig. B.4(b) reveals (as explained above) that below $thr\_pos = 50$, the edge finder triggers in noise. For $50 < thr\_pos < 100$, the threshold is above noise but still below the hardware discriminator threshold. Therefore, edges with small amplitude are not yet discarded (this only starts to be the case for $thr\_pos > 100$). Together, both plots lead to the conclusion that a value of $thr\_pos = 70$ is optimal. The analysis of the other LAAPDs reveals similiar results so that this value is set globally.

B.4 FitWave

Once the edge finder has found an edge in the WFD-trace, it is handled by the Analyzer's fitting-routine **FitWave**. It attempts to do a two-parameter fit of the time *tbin* of the pulse and of its amplitude. For each trial position of *tbin*, the fit-routine determines a local baseline $p_0 + p_1 \cdot bin$ from the 400 bins before *tbin* accounting for

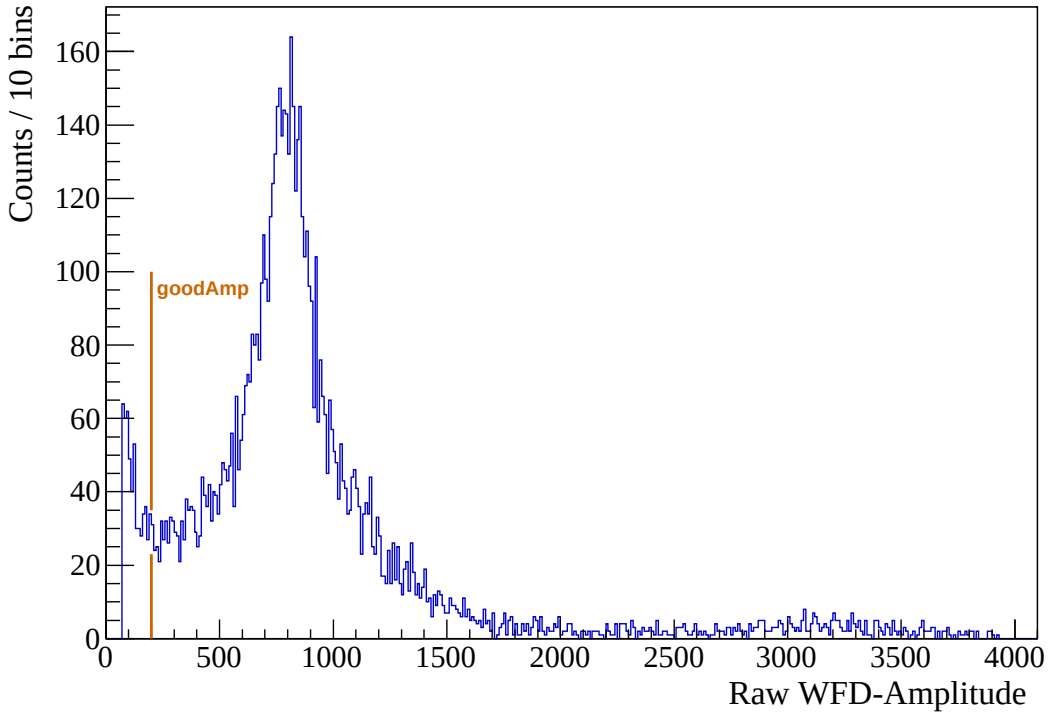

Figure B.5: Raw WFD Amplitude Spectrum: Setting Parameter *goodAmp*. *The raw amplitude spectrum of LAAPD A5 in run #14251. The fitted amplitude of all pulses recorded during this run is histogrammed. The raw WFD-amplitude is a measure for the energy of the recorded pulses. The peak belongs to the prompt* K_α *events. The tail at low amplitudes stems from falsely fitted pulses and from noise. The threshold* ***goodAmp*** *is introduced to discard events with low amplitudes in the noise-tail.*

possible drifts not caused by the signal itself. The signal after *tbin* is fitted to the baseline plus a standard response function (Standard Wave Form (SWF), cf. Sect. B.2). In doing so, it uses the information gathered by the edge finder: the fit starts at the bin *ebin*, the position of an edge found by the edge finder. For a perfect step function, this position would coincide with the location of the edge. The number of bins of the WFD-trace used to match it to the SWF (called *nTotal*) has to be kept as small as possible to ensure sufficient double pulse resolution (see Section B.4.4).

The upper plot in Figure B.1(3b) illustrates the numerical strategy of the fit-routine: at the start, the χ^2 of the fit is evaluated at every 9^{th} bin to find a minimum in the χ^2-parabola. Approaching the minimum, every 3^{rd} bin is evaluated until at the end, the fit's χ^2 is computed for every bin in the vicinity of the minimum. The fit has to fulfill an additional condition: at time bins far away from the actual location of the pulse, the fit with a very low amplitude returns in general a slightly lower χ^2-value than a proper fit of the pulse. Therefore, the fit-routine always has to stay above a certain amplitude and is forced to abort and continue into the opposite direction, if the fitted amplitude has fallen below the low-amplitude threshold *thrAmp* (see Section B.4.2).

Above a certain amplitude (*goodAmp*, Section B.4.1), the fit has found a significant

amplitude. Once FitWave has found a minimum in the χ^2-parabola accompanied by a high enough pulse-amplitude, it stores the time bin at which the pulse occurred (*tbin*), together with the amplitude and the χ^2-values.

B.4.1 Fit-Parameter *goodAmp*

The raw amplitude assigned to every pulse successfully fitted by FitWave is plotted for one LAAPD in Figure B.5, the raw WFD spectrum. The noise-floor and cases where the fit failed and fitted a lower amplitude show up as low-energy peak in this spectrum. The spectrum is cleansed by introducing the fit-parameter *goodAmp*. If the fitted amplitude stays below this threshold, the event is discarded and not processed any further. The spectrum in Fig. B.5 suggests to set $goodAmp = 200$, a value which is chosen globally since all LAAPDs perform similarly regarding this aspect.

B.4.2 Fit-Parameter *thrAmp*

During the fitting-procedure that finds the starting bin *tbin* of the pulse, the direction in which the next time bin is chosen depends on the slope of the χ^2-landscape. Usually, the fit continues downhill towards lower χ^2-values until a minimum is discoverd. The challenge for this routine is that the true minimum is only a local minimum with better global ones both left and right. Ideally, the fit with a baseline plus signal at the correct *tbin* should result in a reduced χ^2 of 1.0. However, far away from the pulse, in the background-region, a reduced χ^2 of 1.0 would already be obtained by only fitting a baseline. Since the real fit is performed using a baseline plus a signal, a fit far away from the location of the pulse should result in the reduced χ^2 becoming smaller than 1.0, where the fitted amplitude would be exceptionally small. Hence, in addition to looking at the χ^2-minimization, the fitted amplitude also has to be considered. Here, the parameter *goodAmp* ensures that pulses with too small amplitude are discarded (introduced in Sect. B.4.1).

The threshold *thrAmp* is the value for the fitted amplitude of a pulse where the fitter is urged to turn around and walk up the χ^2-slope until it finds the next local minimum in χ^2. Chosen too big, the true χ^2-minimum might not be found, and pulses with amplitudes below *goodAmp* that would normally be discarded can be shuffled to higher amplitudes. Good measures to determine adequate values for *thrAmp* are the mean raw amplitude of the low-energy part of the spectrum (below raw amplitude 600, but above *goodAmp*) and the number of entries in this raw amplitude spectrum evaluated for different *thrAmp*, laid out in Figure B.6. Here, the mean raw amplitude (for pulses with raw amplitude 200–600) decreases when *thrAmp* gets too big, indicating that low-energy pulses are fitted with a higher amplitude than they should be. This is confirmed by the simultaneous increase of number of entries in the entire spectrum.

The analysis of all LAAPDs reveals that, since they show equal behaviour, this parameter can be globally set to $thrAmp = 100$, which is half of *goodAmp*.

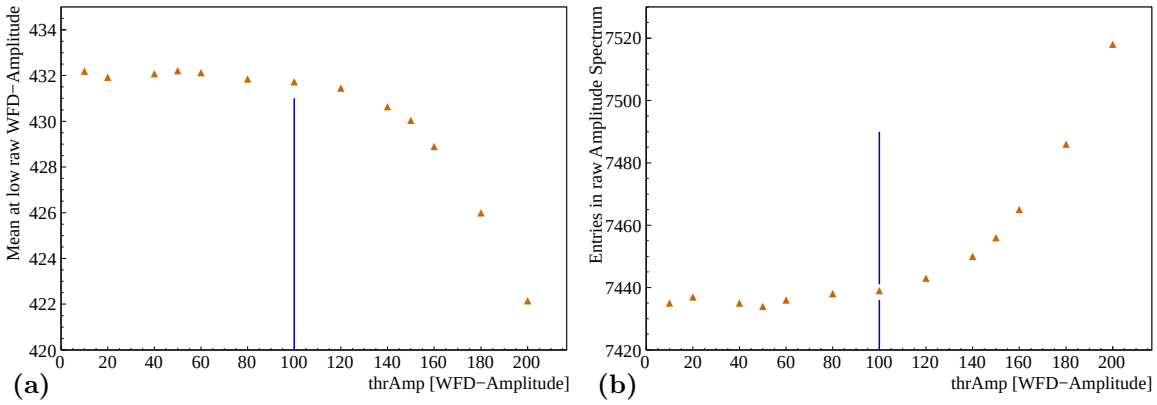

Figure B.6: Setting Parameter *thrAmp*. ***(a)*** *Plotted versus* ***thrAmp****, this panel shows the mean raw amplitude for pulses with raw amplitudes between 200 (****goodAmp****) and 600.* ***(b)*** *The number of entries of the entire raw amplitude spectrum for different* ***thrAmp*** *is shown in this plot. The blue vertical lines indicate the choice of* ***thrAmp****.* ***thrAmp*** *is a threshold for the raw WFD-amplitude. It is therefore directly related to the pulse energy recorded in the LAAPD. The data is based on LAAPD A5 in run #14251.*

B.4.3 Fit-Parameter *nrise*

Since the SWFs, the standard response of the LAAPDs to hits by X-rays, do not resemble an ideal step function, the edge finder's *ebin* will be different to the time bin where the pulse actually starts and FitWave would find it (*tbin*). The value of *ebin* is used by FitWave as a starting value for the χ^2-scan. The closer to the real *tbin* the fit can start, the closer it will be to the desired (local) minimum of the χ^2-parabola. It turns out that *ebin* differs systematically from *tbin* by the constant *nrise*. By correcting the start value of the fit $tbin^{\text{init}} = ebin - nrise$, the robustness of the fit can be improved. In such a way, faulty fit results, where the fitting-routine runs into a wrong minimum, can be avoided. The value *nrise* depends on the width of the edge finder window (*nbins*). In our case the best value of *nrise* is going to be -77. The orange amplitude spectrum in the inlay of Figure B.7 shows such a behaviour: with all other parameters set correctly, this spectrum was obtained by setting $nrise = -40$. Comparing it to the proper spectrum ($nrise = -77$, blue), one observes that many pulses in this 2 keV peak are not fitted properly. They are, instead, fitted with a very low amplitude and do not show up in this spectrum since they do not meet the *goodAmp*-criterion.

It turns out that the parameter *nrise* is fairly constant and only depends on the LAAPD. The accuracy of the fit is improved by eliminating this offset once and setting *nrise* to its proper values for all 20 LAAPDs. Therefore, the Analyzer fills a histogram recording $ebin - tbin$ for every pulse analyzed. The mean value for $ebin - tbin$ for every LAAPD is computed a single time and stored as *nrise* in a control-file. In all subsequent analysis, the fitting-routine FitWave starts to fit at $tbin = ebin - nrise$.

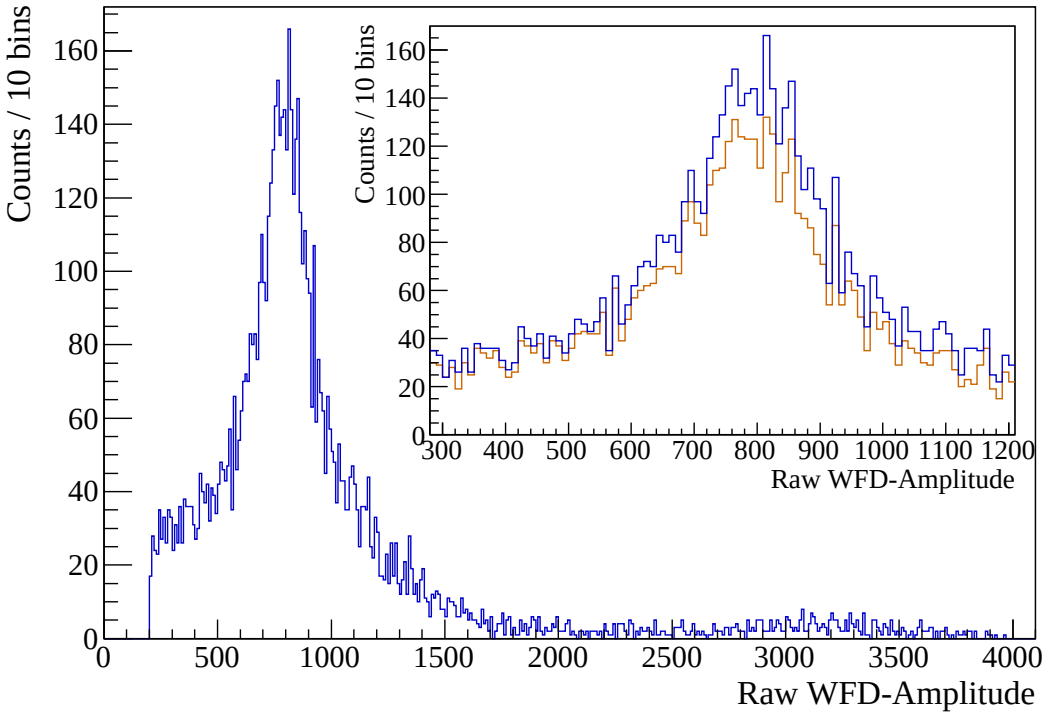

Figure B.7: Raw WFD Amplitude Spectrum after Adjusting Parameters. *This spectrum shows the raw WFD-amplitude all pulses recorded by LAAPD A5 in run #14251 after the parameters have been set to the correct values. In this case these are* ***thr_pos = 70***, ***goodAmp = 200***, ***thrAmp = 100***, *and* ***nrise = -77***. *The blue spectrum in the inlay is a close-up of the same data. The orange spectrum was obtained by setting* ***nrise = -40*** *to a wrong value to show the misbehaviour of the fit.*

B.4.4 Fit-Parameter *nTotal*

During data analysis, the pulses are analyzed the following way: the standard response function (SWF) is fitted to the signal to obtain the amplitude and time of the respective pulse. The number of time bins of the pulse being used to match it to the SWF is called *nTotal*. Obviously, the accuracy of the fit and, therefore, the accuracy for the amplitude benefits from a large *nTotal*, i.e. from a large fitted region. The trade-off for the gain in energy resolution is an impairment in resolving double pulses: with a non-negligible probability of 5 %, the decay electron of the muon decay will be recorded in the same LAAPD as the K_α X-ray. To detect and correctly classify these events a good double-pulse resolution is thus essential.

The optimal value for *nTotal* is, therefore, the minimum number of time bins for which the resolution is best. It is determined at the beginning of the data-analysis. For this, several high-statistics runs are re-analyzed with different *nTotal*-values, and the raw amplitude spectra, i.e. the histograms containing the pulse-amplitudes computed by FitWave (cf. Fig. B.7), are considered. Since most of the X-rays detected by the LAAPDs stem from the transitions in the muonic cascade, a sharp peak corresponding

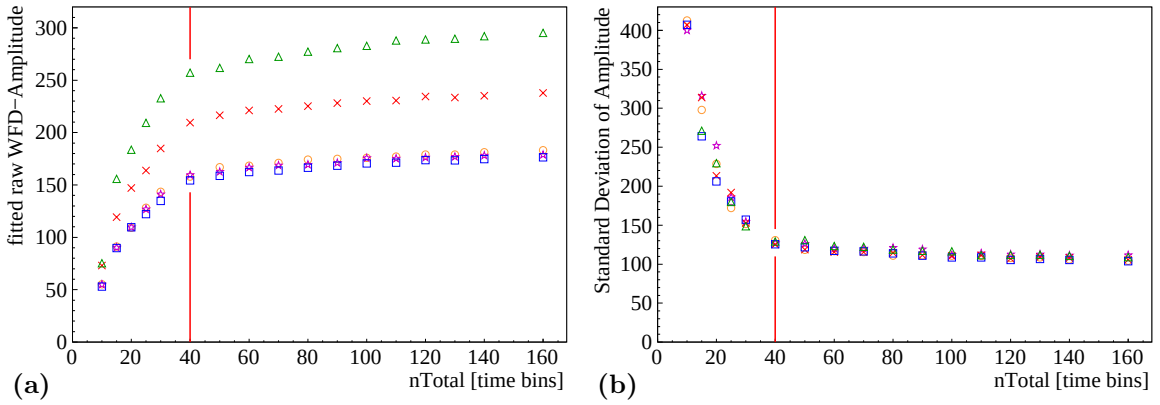

Figure B.8: Setting Fit-Parameter *nTotal*. *The two plots show the amplitude (a) and the standard deviation (b) of a simple Gaussian fitted to raw amplitude spectra of LAAPD A5 that were obtained with different values for* ***nTotal****. The different markers represent five different high-stastics runs throughout the campaign. Both plots indicate that at low* ***nTotal*** *the number of bins to match the WFD-trace with the SWF is too small for FitWave to work properly. They propose a value of* ***nTotal = 40*** *bins.*

to the 1.9 keV energy of the K_α-line is expected together with less pronounced features of the other Lyman-transitions (K_β and K_{rest}). The peaks of the raw amplitude spectra are fitted by a simple Gaussian function. The goal is to minimize the spread and maximize the amplitude of these peaks. According to this criterion, Figure B.8 reveals the optimum value for *nTotal* by plotting the amplitude and the standard deviation of the simple fit-functions versus the length of the fit-region (*nTotal*). This figure indicates that the fitting-routine FitWave needs a certain number of bins for the fits to work properly. Beyond the threshold drawn as a red vertical line, one does not gain much more energy resolution by increasing *nTotal*. Hence, this analysis implies a threshold of $nTotal = 40$ bins (equal to 160 ns).

Nevertheless, this value has to be reconsidered: high-frequency noise (several tens of MHz, corresponding to a period of ~ 15 WFD-bins) was observed on all LAAPDs during the 2009 beam-time. This can cause the fitting routing of the X-ray pulses to fail. An example of such a WFD-trace is shown in Figure B.9(a). Using a value for *nTotal* larger than the temporal spacing of two subsequent pulses, the fit (shown in green) of the first pulse (black trace) fails since the fit-region given by *nTotal* extends over the length of the first and into the region of the second pulse. With *nTotal* too small (on the order of the period of the high frequency noise), the noise ripples would dominate in the data-set to be fitted, which results in several small-amplitude pulses fitted into one physical pulse (not shown). To quantify this behaviour, one looks at the number of multiple pulses seen in *one* LAAPD, which have an energy $E < 1.3$ keV and a time difference less than 300 WFD-bins. The graph in Fig. B.9(b) shows that for $nTotal > 70$ bins the noise is less dominant. This value is used for further analysis of all LAAPDs. It corresponds to a minimum detectable double pulse separation of 280 ns.

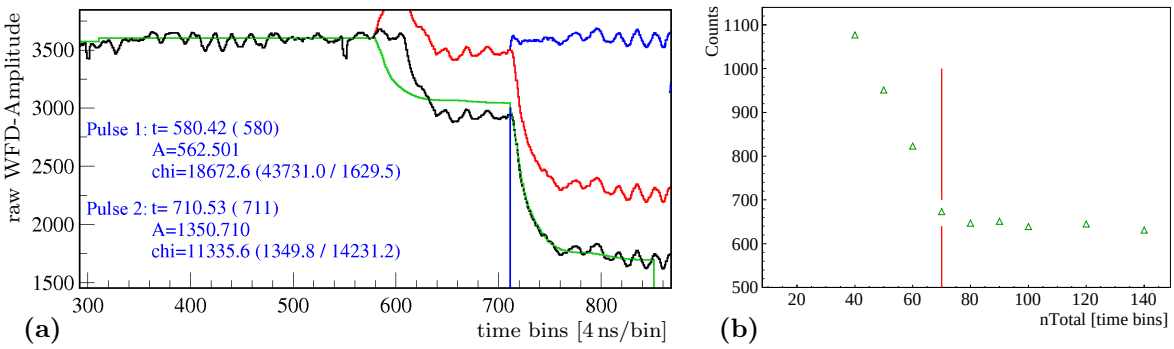

Figure B.9: Bad Fits with Wrong *nTotal*. ***(a)*** *A badly fitted WFD-Trace with high-frequency noise. The black trace is the original wave form with a double pulse structure (red after the subtraction of the first pulse, blue after subtraction of the second). The fit of the first pulse is shown in green.* ***nTotal*** *has to be set such that several oscillation periods of the noise component are covered ensuring a proper fit of the steep pulses. On the other hand, with* ***nTotal*** *chosen larger than the distance of the two subsequent pulses, the first of two pulses will be fitted incorrectly (shown).* ***(b)*** *The number of low-energy ($E < 1.3\,keV$) pulses that occured in one LAAPD with a time difference smaller than 300 bins is plotted versus* ***nTotal****. The data is based on run # 13777. The graph shows that for small* ***nTotal*** *an excess of small-energy pulses (with a small time difference to another pulse) is fitted. This is due to the increasing influence of the noise ripples when* ***nTotal*** *decreases. The plot suggests to set* ***nTotal*** *= 70 bins.*

After the fine tuning of all the fit parameters of the wave form analysis, which is presented in the previous sections, X-rays of energies down to 0.6 keV are detected and analysed adequately.

B.4.5 FitElec

The Analyzer sub-routine **FitElec** is responsible to fit saturated WFD-traces (i.e. those containing bins with content zero). These are caused by μ-decay electrons depositing several tens of keV of energy in the LAAPDs. FitElec's strategy is straightforward: for the bin one below the first saturated bin, fit the baseline and the SWF and evaluate the corresponding χ^2. Then, move bin per bin to earlier times and perform the fit computing the χ^2 until the minimum is found (compare also Fig. B.1-(4b)). FitElec, as well as FitWave, stores the fitted time bin *tbin*, the corresponding amplitude, and the χ^2-values. Being a robust routine, it usually does not need fine-tuned parameters.

B.5 Time Calibration

All gathered information only becomes valuable when the detectors are correctly calibrated in the time domain. Most importantly, the timing between LAAPDs detecting

the muonic X-rays and the electron paddles, which cover the muon-decay electrons, has to be known accurately. The employed calibration procedure for the LAAPDs as well as for the electron paddles and the muon detectors is described in the following section. The time calibration of the laser relative to the detected muons is reported in Section B.5.2. Since the laser time window in which the laser illuminates the target cavity and can drive the $\mu p(2S-2P)$ transition has a length of 75 ns, a timing accuracy well below 50 ns is desirable.

The calibration procedure makes use of the fact that the muon decays into an electron. The strong magnetic field inside the target forces some muon-decay electrons to spiral through two or more detectors and create physical coincidences. With energies of the decay electrons of up to 50 MeV (equivalent to an electron velocity $v_e \simeq c$), these coincidences happen instantaneously compared to our needed timing accuracy. Such coincidences between the E^{left} and the E^{right} detectors, between the LAAPDs and $\mathrm{E}^{left/right}$, and between the muon detectors and $\mathrm{E}^{left/right}$ can be used to calibrate these detectors relative to each other.

B.5.1 Timing of the Various Detectors

Due to different detector properties and different cable-lengths, the run-time for a signal from a detector-hit until it is digitized by the computer differs for every detector. Hence, the timing information is only useful when the individual detectors have been calibrated in the time domain with respect to each other. The relative timing between the electron detectors, the muon detectors, and the LAAPDs is defined with respect to the high-TDC (time-to-digital converter) of the left electron detector (E^{left}_{hi}, cf. Section 2.4.3).

Electron Paddles

In order to calibrate the electron paddles E^{left} and E^{right} with respect to each other, one employs coincidences from electrons that spiral in the strong magnetic field of the target thereby hitting both electron paddles. From this, a time difference spectrum of the two hits can be created, and the offset can be corrected. A simple Gaussian fitted to the spectrum's peak reveals a full width at half maximum (FWHM) of 20 ns suggesting that the timing accuracy among the electron paddles is known to 20 ns.

LAAPDs

Taking into account the rotational direction of the negatively charged electrons inside the target's magnetic field, the time calibration of the LAAPDs looks at electrons which deposit energy in both the X-ray detectors and the electron paddles: for the LAAPDs located above the target (A-side), the time difference with respect to E^{left} is considered. The bottom set (B-side) is inspected versus the E^{right} detector. Any offsets

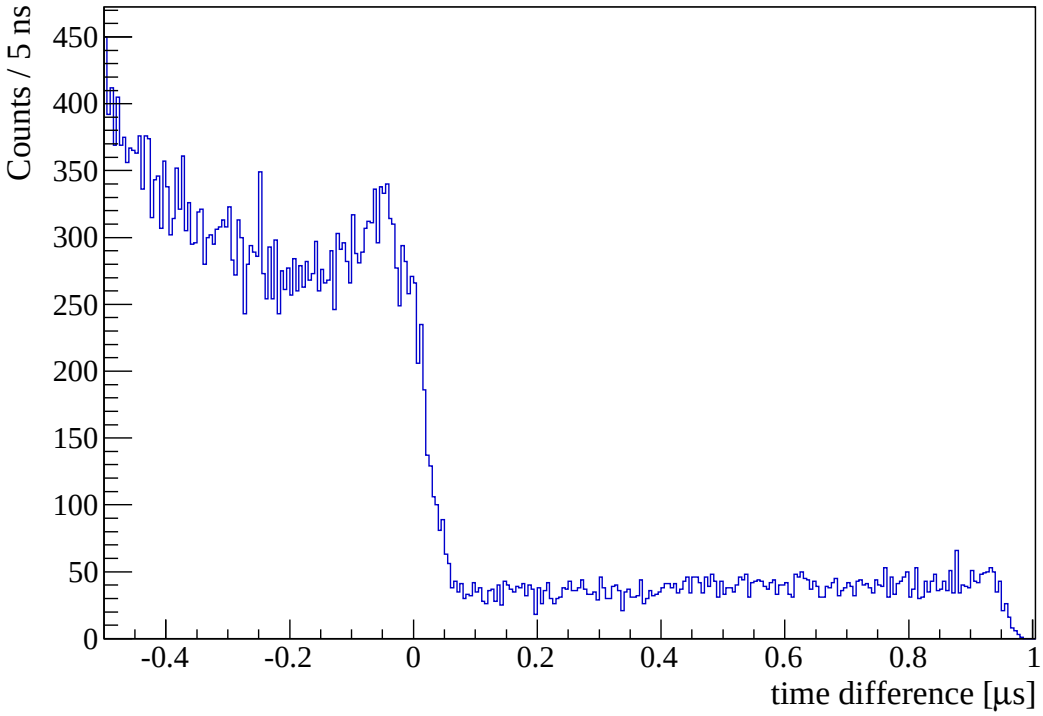

Figure B.10: Time Difference Spectrum of S1 and E^{left}. *The timing difference of two signals detected in the low-detectors of S1 and E^{left} is plotted in this histogram. A muon is detected in S1 and stopped in the target where it decays into an electron. This electron spirals in the target's magnetic field and is observed by E^{left}. The time difference spectrum indicates the commencement of the decay-signals at $\Delta t = t_{S1} - t_{E^{left}} = 0$ and towards more negative times. The noise floor at positive times stems from uncorrelated background, for instance from second (non-detected) muons entering the target. The data is from run # 14328.*

are adjusted and used for further analysis. The coincidence-spectra of the 20 LAAPDs with regard to their respective electron detector $E^{left/right}$ reveal a timing accuracy of 20 – 25 ns taken from the FWHM of a Gaussian fitted to the peak in the spectra.

Muon Detectors

In a third step, the calibration of the muon detectors S1, $S2^{up}$, and $S2^{down}$ with respect to the electron paddle E^{left} can be performed by looking at the arrival time of the decay electrons of those muons that have been detected by the respective muon detectors.

Figure B.10 shows a time difference spectrum of muons detected by S1 and their decay electrons recorded by the low-discriminator E^{left}_{lo} (introduced in Sect. 2.4.3). The decay signals start to appear at $\Delta t = t_{S1} - t_{E^{left}} = 0$ continuing toward more negative time difference values. This onset at $\Delta t = 0$ of the muon-decay electrons showing up in E^{left} can be set as physical coincidence. The time difference between a muon detected and the muon-decay electron (which have kinetic energies in the MeV range) showing up in E^{left} is negligible at the level of accuracy needed for our time calibration. The

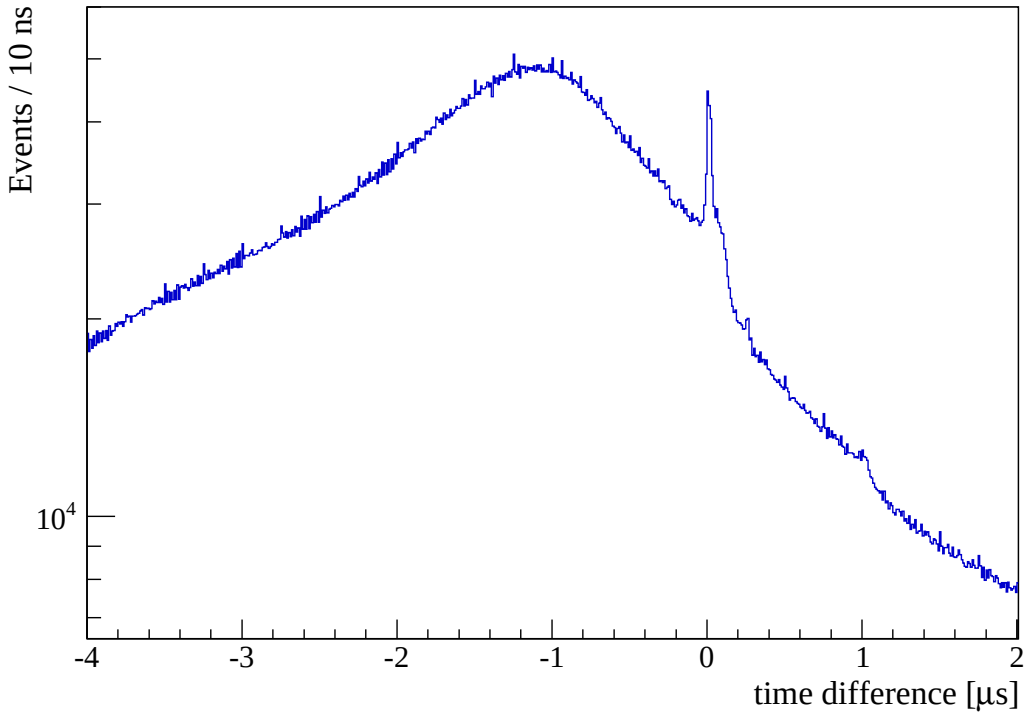

Figure B.11: Time Difference Spectrum of S2$^{\mathbf{down}}$ and E$^{\mathbf{left}}$. *The timing difference of two signals detected in the PTDC of $S2^{down}$ and in the low-detector of E^{left} is plotted in this histogram. In order to be less sensitive to stack-electrons which are detected in $S2^{down}$, the first hit in the PTDC is omitted and only time differences with the other PTDC-hits are shown. Electrons seen by both detectors simultaneously are responsible for the peak at $\Delta t = t_{S2^{down}} - t_{E^{left}} = 0$: a muon decay electron spirals in the target's magnetic field hitting both detectors $S2^{down}$ and E^{left}. This marker serves as time-reference to calibrate the muon detectors with respect to the electron paddles $E^{left/right}$. A marker position different from $\Delta t = 0$ would require a correction.*

fall time in this kind of spectrum is $\sim 50\,\mathrm{ns}$ giving an indication of the accuracy of this time calibration.

For the case of S2^{down} (the muon detector located directly after the target) this procedure can be verified by observing the signals from electrons spiraling through both S2^{down} and E^{left}. S2^{down} usually detects keV stack-electrons (i.e. the electrons emitted during the muon passage through stack S2), which, because of their low kinetic energy, have only a very small radius of gyration ($\sim 1\,\mathrm{mm}$) inside the high magnetic field and are not able to hit E^{left}. On the other hand, muon decay electrons possess much higher kinetic energies in the MeV range and, therefore, a much higher gyration radius. In such a way, they can hit both S2^{down} (on the muon beam axis) and the electron paddles E$^{left/right}$ ($\sim 3\,\mathrm{cm}$ away) producing coincidences which are shown in Figure B.11. Since the low energy stack-electrons (which almost always precede the muon decay electrons) would mask these decay electron coincidences, one looks at the time difference spectrum of the E_{lo}^{left}-TDC and the $\mathrm{S2}_{lo}^{down}$-PTDC (pipeline TDC, a TDC

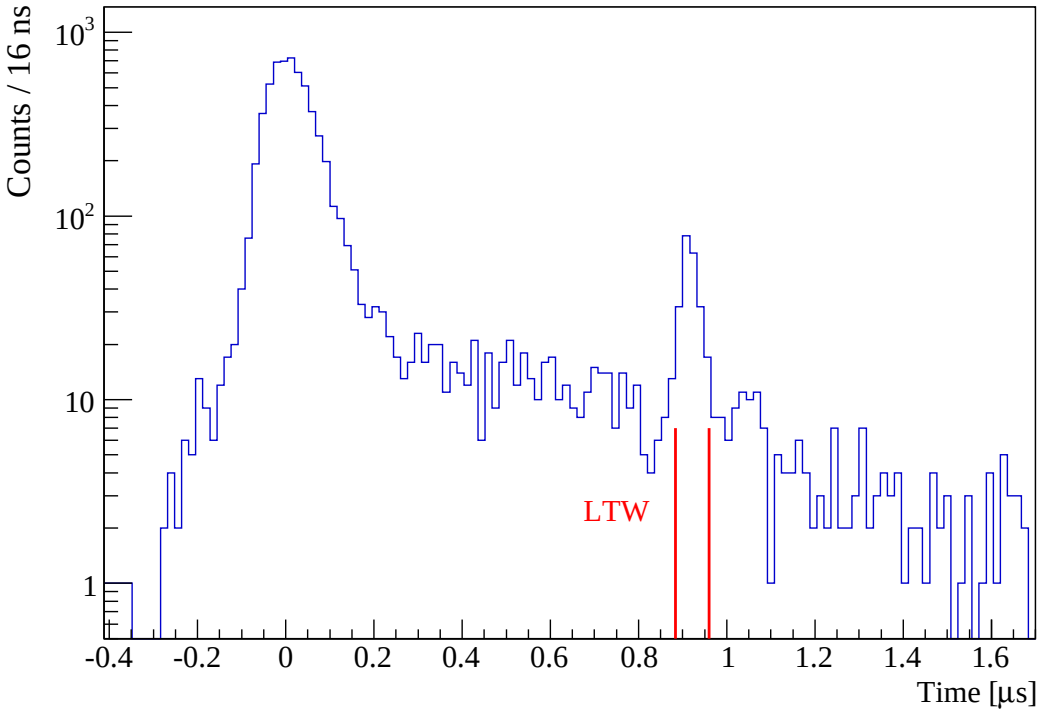

Figure B.12: Raw Time Spectrum LAAPD B5 Showing Visible Light. *The time retrieved from fitting pulses recorded in LAAPD B5 is plotted in this histogram for run # 13777. The peak appearing ∼ 900 ns after the prompt peak (stemming from the muonic cascade) is probably related to plasma production. Here, the laser is focussed into the 0.6 mm entrance hole in one of the target mirrors, thereby hitting the hole's rim and ablating debris from the substrate surface. This peak is not present in laser-off data (i.e. recorded data in which the laser has not been shot).*

which is able to record multiple hits) omitting the first hit in the PTDC. Figure B.11 shows such a spectrum. In it, the peak visible at $\Delta t = 0$ stems from μ-decay electrons. Any offset of this peak away from $\Delta t = 0$ would have to be included into the time calibration.

The muon detector $S2^{up}$ can be easily calibrated relative to $S2^{down}$. Typical FWHM values of the coincidences among the sub-detectors (low-TDC, medium-TDC, high-TDC and PTDCs, cf. Sect. 2.4.1) in the different detector-groups (E^{left}, E^{right}, S1, $S2^{up}$, and $S2^{down}$) are below 10 ns (well below the accuracy goal of $\sim$ 50 ns).

B.5.2 Relative Time Calibration of the Laser

Muons detected by the muon detectors (S1, $S2^{up}$, and $S2^{down}$) serve as a trigger for the entire laser system (cf. Sect. 2.3). With every muon trigger, the laser is fired and directed into the target cavity where the laser pulse illuminates the hydrogen gas volume. The arrival time of the laser pulse in the target cavity is an important piece of information necessary for the data-analysis: only when the laser is illuminating the tar-

get cavity, we will be able to drive the $\mu p(2S-2P)$ transition and detect laser-induced K_αX-rays. The time during which the cavity is illuminated (laser time window, LTW) is related to the lifetime of the mirror cavity. With the effective reflectivity of the cavity mirrors (cf. Appendix C) the lifetime can be determined to be 45 (5) ns. It can also be extracted from the time spectra belonging to the resonance line (cf. Figure B.19), where the laser-induced events are clearly visible. From this, the LTW is set to 75 ns.

During several runs of the 2009-campaign, visible light has been detected by some of the LAAPDs. Most likely, this originates from a plasma produced inside the gas target when the laser is focussed into the 0.6 mm entrance hole of the target cavity (Sect. 2.2.3). The emitted light is detected in the LAAPDs (especially in A4-5/B4-5, the ones closest to the entrance hole) and fitted by the fitting routine returning a time *tbin* (cf. Sect. B.4). Figure B.12 plots these times retrieved by fitting the pulses recorded in LAAPD B5 for one light-run (# 13777). While the prominent peak at $t = 0$ ns stems from the prompt muonic cascade, the smaller peak is attributed to laser ablation of debris material in the focus of the infrared laser inside the substrate hole. The time difference of the peaks' centroids (evaluated by simple Gaussian fits) is determined to be 914 ns. Because the LAAPDs have a finite time resolution of around 35 ns which becomes worse for smaller photon energies, the center of the light peak is not the actual start of the laser-induced events. As can be seen with the logarithmic scale in Figure B.12, the laser induced events begin to show up significantly about 25 – 30 ns before the center of the peak. Therefore, the LTW is set to $t \in [887; 962]$ ns using a width of 75 ns of the LTW as mentioned above. At the end of the data analysis, this can be cross checked and refined with the help of the time spectra of the K_αX-rays (cf. Figure B.19).

For normal data-taking, a photo-multiplier tube is monitoring the visible light produced inside the target cavity to avoid this effect. Furthermore, thin polypropylene-foils coated with a thin silver-layer are mounted in front of the LAAPDs to shield them from the visible light. This way, no such events could fake muonic X-rays in the LAAPDs.

B.6 Energy Calibration of the LAAPDs

The majority of the X-rays detected in the LAAPDs originates from the K_α-transition in the prompt muonic cascade. Therefore, the raw amplitude spectra of every single LAAPD comprise a distinct peak, the position of which depends on the gain of the LAAPDs and their amplifiers. The gain is contingent on the bias high voltage applied to the LAAPDs as well as on other parameters like temperature, components in use, etc.. This requires an LAAPD energy calibration which is performed on a run-by-run basis. The energy calibration has to be performed once per run and relies on a simple Gaussian fit to the peaks in the amplitude spectra and on a conversion table for every LAAPD over the entire campaign.

B.7 Event Construction

Every detected muon opens an event gate (*EVG*) during which signals from the detectors are accepted. With proper time and energy calibrations, these signals are interpreted by the Analyzer: for every event, hits in the electron detectors E^{left} and E^{right} are considered and pulses in the LAAPDs are fitted. The event construction of the Analyzer then looks for coincident detector-hits using Δt_{same}, a time window established beforehand (Sect. B.7.1). In a final step, all the detector-hits are classified into X-rays and electrons and grouped into different event classes (Sect. B.7.2). The rationale behind the classification is: X-rays can only show up in one LAAPD. Hits in the electron detectors E^{left} and E^{right} must be electrons. All signals with coinciding hits in multiple detectors (within Δt_{same}, see below) are considered to be electrons, as well.

B.7.1 Analyzer Parameter Δt_{same}

Every detector hit in the LAAPDs and the electron paddles (termed *happening*) gets assigned its time-stamp. The happenings are classified into groups of *unique times*. This is done by finding coincidences among the individual happenings which occured within a given time interval Δt_{same}. This parameter defines how similar in time two happenings have to be in order to be considered to have happened simultanously.

Figure B.13 shows a time difference spectrum of the happenings in each event of the entire campaign. It indicates a prominent peak with a steep exponential decay originating from physical coincidences caused by single particles. The almost flat component towards larger times results mainly from electron-signals. This plot suggests to set $\Delta t_{same} = 70 - 100\,\text{ns}$.

It is worthwhile to mention that time spectra of events composed of 2 keV X-rays followed by a delayed electron (with the 2^{nd}-muon cut applied) are rather insensitive to the choice of Δt_{same} because of the very effective 2^{nd}-muon cut (cf. Sect. B.10). Nevertheless, they show a peculiarity when increasing Δt_{same}: although the number of events at prompt times increases as expected (more low-energy signals in the electron-paddles and the LAAPDs can be grouped into one *unique time* to make up delayed electrons), the number of entries in the background region around the laser-time window decreases. Most of these background events are falsely identified 3 keV X-rays from muonic silver. A larger Δt_{same} causes more of these clean X-ray signals to be grouped together with other happenings into one *unique time* thereby falling out of the $\mathbf{X}+\mathbf{e}^-_{delayed}$ class (explained in the following section) and mimicking an electron event instead. This justifies to choose the lower bound $\Delta t_{same} = 70$ of the range mentioned above as a threshold for this parameter.

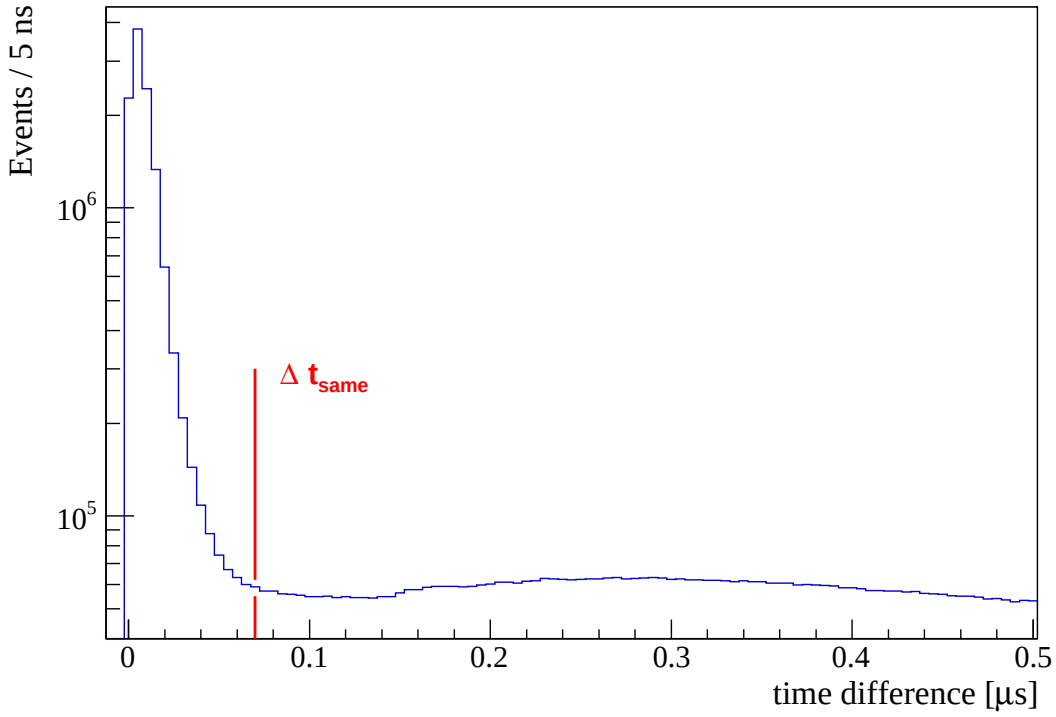

Figure B.13: Time Difference Spectrum of all Happenings. *For every laser event, the time difference of the happenings (i.e. detector clicks) occured in all detectors during this event is plotted. The strong peak at low Δt is produced by coincidences of single particles hitting several detectors. For the first μp resonance, 3.0×10^7 happenings have been recorded.*

B.7.2 Event Classification

The Analyzer groups all signals into electrons and X-rays, depending whether they are produced by allowed *electron detectors* or *X-ray detectors*. Signals are defined to stem from *electron detectors* if they are recorded in one of the electron paddles E^{left} and E^{right}. High-energetic detector hits in the LAAPDs or those in coincidence with another signal can also contribute to this class. In the latter case, where the electron produces signals in more than one detector, the electron signal is termed to have a *multiplicity* $M > 1$. Signals recorded from LAAPDs with a *multiplicity* $M = 1$ and with an energy below the electron threshold are associated with X-rays.

Every event read out after a muon trigger is then classified into different event classes according to the number and order of the X-rays and electrons. The event classes and their contributions to the $2S_{1/2}^{F=1} - 2P_{3/2}^{F=2}$ data set are broken down in Table B.1. Class 110 ($\mathbf{X}$+$\mathbf{e}^-_{delayed}$) originates from muonic X-rays and the muon-decay electron appearing at delayed times (cf. Sect. B.8) and is the one of interest for this experiment. As much as 19 % of all recorded events stem from a muonic X-ray followed by a correctly timed muon-decay electron.

Classifying the events into the different classes is essential for the success of the data analysis as can be seen in Figure B.14. Shown in logarithmic scale, it clarifies the

Event Class	Description	Contribution	
		absolute [$\times 10^6$]	relative [%]
01	$\mathbf{e^-}$	20.435	46.2
02	$\mathbf{2\,e^-}$	4.442	10.0
03	$\mathbf{3\,e^-}$	0.327	0.7
10	$\mathbf{X}$	6.815	15.4
11	$\mathbf{X + e^-}$	(sum) 10.502	23.7
110	$\mathbf{X + e^-_{delayed}}$	8.404	19.0
111	$\mathbf{X + e^-_{early}}$	0.081	0.2
112	$\mathbf{X + e^-_{late}}$	1.657	3.7
113	$\mathbf{e^- + X}$	0.361	0.8
12	$\mathbf{X + 2\,e^-}$	(sum) 1.381	3.1
120	$\mathbf{X + e^-_{delayed} + e^-}$	0.886	2.0
121	$\mathbf{X + e^-_{early} + e^-}$	0.033	0.1
122	$\mathbf{X + e^-_{late} + e^-}$	0.203	0.5
123	$\mathbf{e^- + X + e^-}$	0.247	0.6
124	$\mathbf{e^- + e^- + X}$	0.012	0.0
20	$\mathbf{2X}$	0.201	0.5
21	$\mathbf{2X + e^-}$	(sum) 0.129	0.3
210	$\mathbf{X + X + e^-}$	0.105	0.2
211	$\mathbf{X + e^- + X}$	0.015	0.0
212	$\mathbf{e^- + X + X}$	0.010	0.0
Total number of histogrammed events		44.231	100.0
Total number of processed events		45.370	
Total number of DAQ-triggers		46.355	
Total number of detected muons		312.372	

Table B.1: Event Classes and their Contributions. *Every event is categorized into an event class according to the number and order of X-rays and electrons. The different classes and subclasses are listed here together with their contribution to the complete data relating to the $2S^{F=1}_{1/2} - 2P^{F=2}_{3/2}$ resonance ($Laser_{on}$ and $Laser_{off}$ data are considered). The total number of processed events differs from the histogrammed events by those not belonging to one of the mentioned classes. The excess in data aquisition (DAQ) triggers stems from false triggers like ringing or cross-talk. The number of usable detected muons is presented as reference. The term $\mathbf{e^-_{delayed}}$ refers to electrons detected within the delayed electron time window (which is detector dependent, see Sect. B.8). Early (late) electrons appear before (after) this window. This data stems from 24 measurement days and is analysed with $\Delta t_{same} = 70\,ns$.*

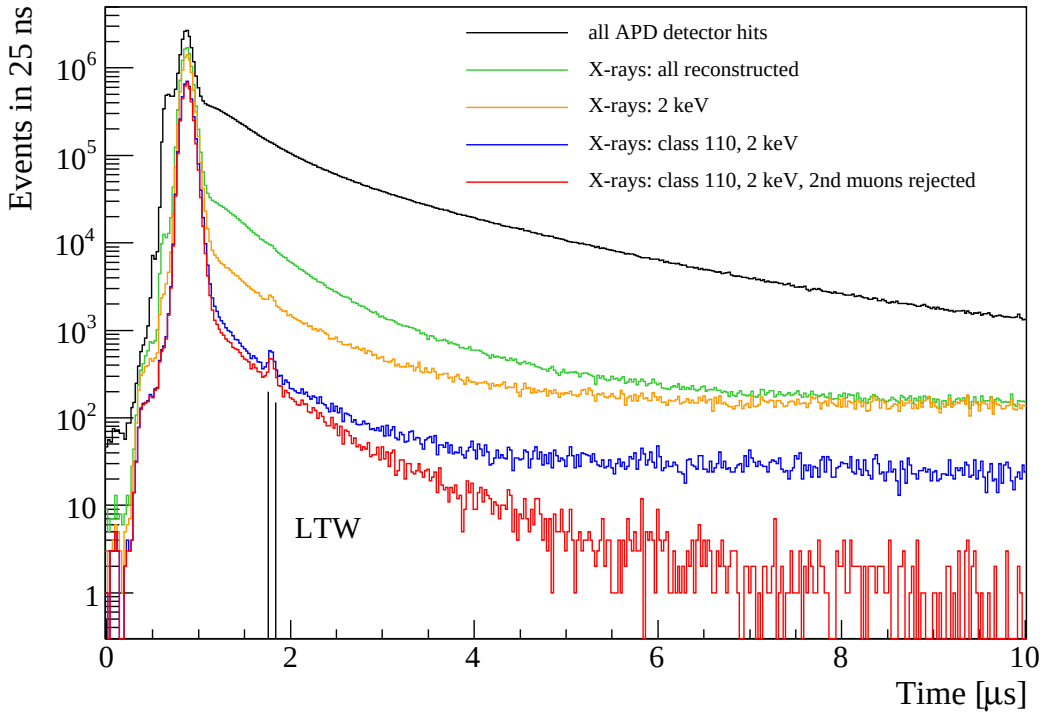

Figure B.14: Time Spectra for Different Event Classes. *The effect of the event classification on the background at delayed times can be seen in the time spectra plotted here. While all LAAPD-hits contribute to the top black spectrum, only those events with at least one X-ray present make up the green one. The orange plot imposes the 2 keV cut on all recorded X-rays. Additionally, the blue plot introduces the delayed electron cut. This spectrum is made up from class 110 X-rays with the 2 keV cut applied. Finally, the red time spectrum at the bottom shows the event class 110 ($\boldsymbol{X}$+$\boldsymbol{e}^-_{delayed}$) appended by the 2 keV energy cut (cf. Sect. B.9) and the 2^{nd}-muon cut (Sect. B.10). The two vertical black lines indicate the laser time window (LTW) during which laser induced events are expected. The entire combination of stringent cuts is required to reduce the delayed background level substantially and to reveal the laser-induced events in the LTW, the signal we are looking for.*

influence of the event classification on the background amplitude. The laser time window (LTW) is indicated. Starting from all LAAPD hits (black), more and more cuts are introduced and their influence on the background level can be observed nicely: considering only event classes with X-rays present (classes 10, 11, 12, 20, and 21) already reduces the delayed background by an order of magnitude but does not yet reveal the laser-induced events (green). The orange plot with the 2 keV cut imposed on all X-rays already shows a faint indication of laser-induced events. When looking at X-rays of the class 110 ($\mathbf{X}$+$\mathbf{e}^-_{delayed}$) with the 2 keV energy cut applied (blue plot) and the same data (red spectrum) with the additional constraint of the 2^{nd}-muon cut (Sect. B.10), a distinct feature starts to arise in the LTW. Only when stringent constraints have been imposed on the X-ray and the electron properties, the background is reduced adequately to reveal the laser-induced events in the LTW of the $\mathbf{X}$+$\mathbf{e}^-_{delayed}$ class.

B.8 Delayed Electron Window

Most of the recorded events stem from muon decay and contain an electron. Nevertheless, some electrons detected in the LAAPDs cause background at 2 keV. An effective way to reduce this background drastically is to allow only events containing a delayed electron. An X-ray of muonic origin is followed by an electron when the muon decays according to

$$\mu^- \rightarrow e^- + \bar{\nu}_e + \nu_\mu \tag{B.1}$$

with a lifetime of $\tau_\mu = 2.2\,\mu$s. Considering only the $\mathbf{X}$+$\mathbf{e}^-_{delayed}$ event class (see previous section) helps to reduce the background in the laser time window to an acceptable level (cf. Fig. B.14).

The hits in the electron paddles and the LAAPDs are recorded by TDCs with differently leveled discriminators (termed *low, medium,* and *high*, cf. Sect. 2.4). According to how many detectors report a signal during the same *unique time* (Sect. B.7.1), the electron signals are grouped in events of certain *multiplicity*. The electron detector **Paddle_hi_M1**, for instance, covers all electrons that are detected by one of the electron paddles, trigger the *high*-discriminator and do not cause any signal in one of the other allowed electron detectors. Electron events registered by **APD_hi_M2** are seen in the LAAPDs having enough energy to trigger the *high*-discriminator. They have *multiplicity* $M = 2$ since simultaneously, another signal is seen by a further electron detector. These detector-types accumulate statistics differently each having a characteristic effectiveness.

The aim is to develop detector-type dependent boundaries for the $\mathrm{e}^-_{delayed}$-window (pronounced [del–ˈi:]), the allowed window for the time difference $t_e - t_x$ between the muonic X-ray and the delayed decay electron. Choosing the right minimum value for $t_e - t_x$ excludes fast decaying background components from muonic silver. Similarly, the correct maximally allowed time difference $t_e - t_x$ prevents identifying accidental coincidences from an evenly distributed background. Doing this for all detector-types ensures the greatest possible statistics without compromising the signal-to-background level.

To find out the background level that can be most tolerated, one considers the resonance obtained for the $2S - 2P$ transition and examines the background-dependence of the fitted position and the position uncertainty of the resonance-curve. For this, the laser time window in the ($\mathbf{X}$+$\mathbf{e}^-_{delayed}$)-class time spectrum (similar to the red spectrum in Fig. B.14) is widened successively to accumulate an increasing number of background events while keeping the number of laser induced signal events constant. Figure B.15 shows the fitted resonance positions and its position uncertainties obtained by this procedure. While the blue stars represent the fit with the background amplitude varying freely, for the red triangles the background was held constant at a value determined from the Laser_{off} data. The data are plotted versus the fitted background normalized to 75 ns (the final width of the laser time window) and to the number of events in the

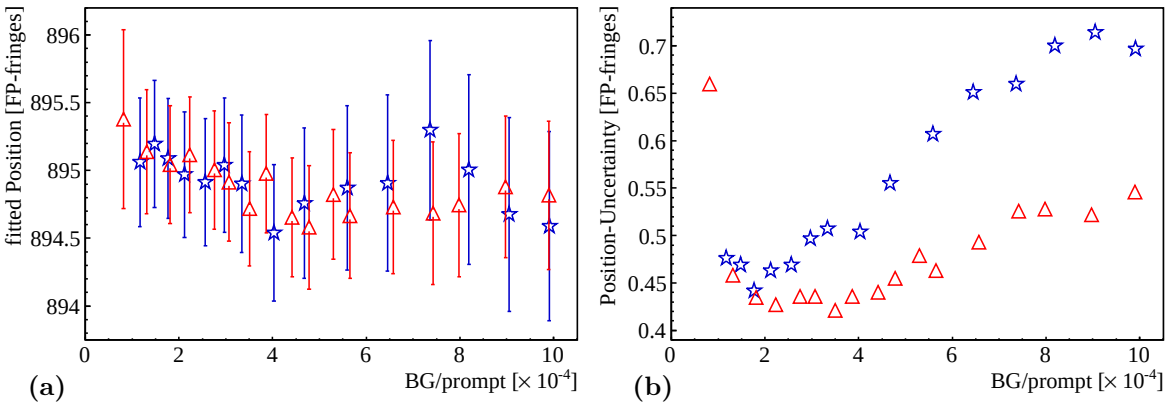

Figure B.15: Background Dependence of the Resonance Position and its Uncertainty. *The fitted position* ***(a)*** *and the position uncertainty* ***(b)*** *of the resonance curve of the* $2S - 2P$ *transition are plotted versus the normalized background level at laser times. These data are obtained by varying the width of the laser time window in the time spectra of the 110-class, therefore varying the background contribution while keeping the number of signal events approximately constant. The accumulated background is normalized to the number of prompt events. The blue stars are produced with a freely fitted background. The red triangles stem from a fit where the background in the laser time window is taken from* $Laser_{off}$ *data and set to be constant. For both methods, plot* ***(a)*** *shows a roughly constant resonance position for any background level. The position uncertainty is acceptable up to a background amplitude of* $\sim 3 \times 10^{-4}$*, as can be extracted from plot* ***(b)****.*

prompt peak. The plots reveal that for any background level the positions of the peak remain approximately constant (Fig. B.15(a)) and below a background level of 3×10^{-4} the position uncertainty is smallest (Fig. B.15(b)). From this it can be seen that even a considerable background level of 3×10^{-4} should not deteriorate the statistical significance of the data. Henceforth, we can increase the statistics by relaxing the cuts on the $e^-_{delayed}$-window and also on the X-ray energy (cf. Section B.9) until a background level of 3×10^{-4} is reached.

This finding is used to determine the upper and lower bounds of the $e^-_{delayed}$-windows for the time difference $t_e - t_x$ of every available electron detector-type. Figure B.16 introduces the characteristics of four instructive examples. The two plots show the number of prompt events (normalized to 1 μs) and the background events (normalized to the prompt events and the width of the laser time window of 75 ns) for varying slices of the time difference $t_e - t_x$ of the muonic X-ray and its decay electron. The left plot reveals the contribution of each single $e^-_{delayed}$-slice of every detector to the total background level. It is produced by taking the number of background and prompt events from the time spectra filled with events from the respective $e^-_{delayed}$-slices. Looking first at the high-statistics detectors, such as **Paddle_hi_M1**, one starts in the minimum of the left plot and, proceeding towards smaller time differences, evaluates the ratio of the sum of the background events to the sum of the prompt events. The time value

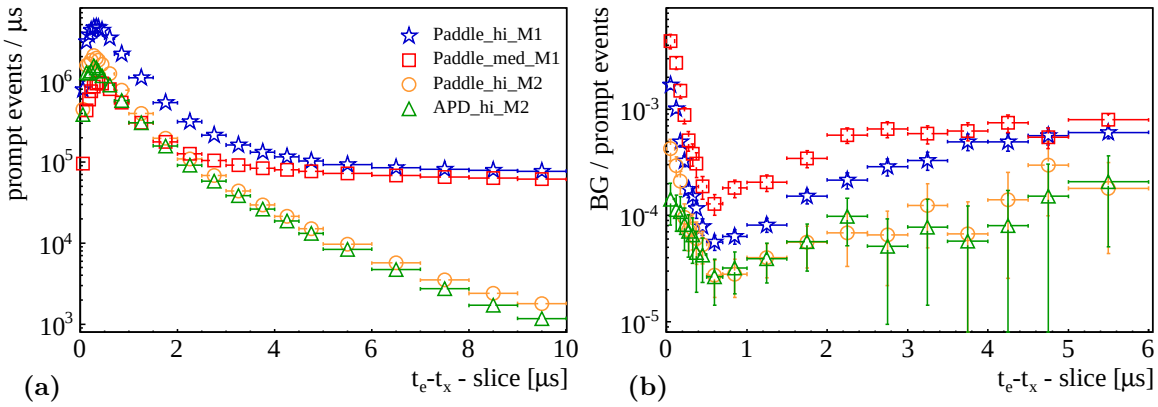

Figure B.16: Influence of the $e^-_{delayed}$-Slices on the Background. *Of all available electron detectors, four representatives are presented for a study of their behaviour.* ***(a)*** *The plot shows the contributions of each $e^-_{delayed}$-slices to the number of prompt events (normalized to 1 µs). Although* ***Paddle_hi_M1*** *contributes most to the statistics, it collects only accidental flat background for $t_e - t_x > 4\,\mu$s. Only detector-types with* ***multiplicity*** *$M = 2$ do not see any accidentals up to 10 µs and can therefore have a long $e^-_{delayed}$-window.* ***(b)*** *The background level normalized to the number of prompt events and to the width of the laser time window (75 ns) is plotted as a function of the $(t_e - t_x)$-slice. The plot shows, for instance, that detectors with $M = 2$ are less affected by background allowing for a much wider $e^-_{delayed}$-window.*

where this ratio meets the upper limit of 3×10^{-4} of the background level established earlier is set as lower boundary for the $e^-_{delayed}$-window of **Paddle_hi_M1**. Repeating this procedure into the other direction continuing from the graph's minimum uncovers the upper edge of this $e^-_{delayed}$-window. This recipe can be applied to all other electron detectors in order to establish the individual $e^-_{delayed}$-window bounds.

With the help of Figure B.16, differences in the detetectors' behaviour can be observed. In Fig. B.16(a), **Paddle_med_M1** (red squares) is much more sensitve to flat accidental background at large time differences than, for instance, **Paddle_hi_M2** which has multiplicity $M = 2$. Therefore, the dip in the plot of Fig. B.16(b) is much narrower and levels out much earlier. This plot shows how much the individual $e^-_{delayed}$-slices contribute to the background. On the other hand, those electrons with *multiplicity* $M = 2$ are very immune to accidental background as can be seen in the right plot. Hence, the $e^-_{delayed}$-windows for these electrons are chosen to be much wider.

The $t_e - t_x$ time difference spectra shown in Figure B.17 reveal that an upper bound of 6 µs should be selected for the $e^-_{delayed}$-windows. This is the time where the red histogram (produced with X-rays from within the LTW) hits the flat background of those X-rays before (green) and after (blue) the LTW. Note the logarithmic scale. The histograms are produced from the $(\mathbf{X}+\mathbf{e}^-_{delayed})$-class for X-rays recorded by **Paddle_med_M1** before, in, and after the LTW. The exponentially decaying feature of the LTW-data originates from laser-induced transitions in μp and can be distinguished from the accidental background up to 6 µs.

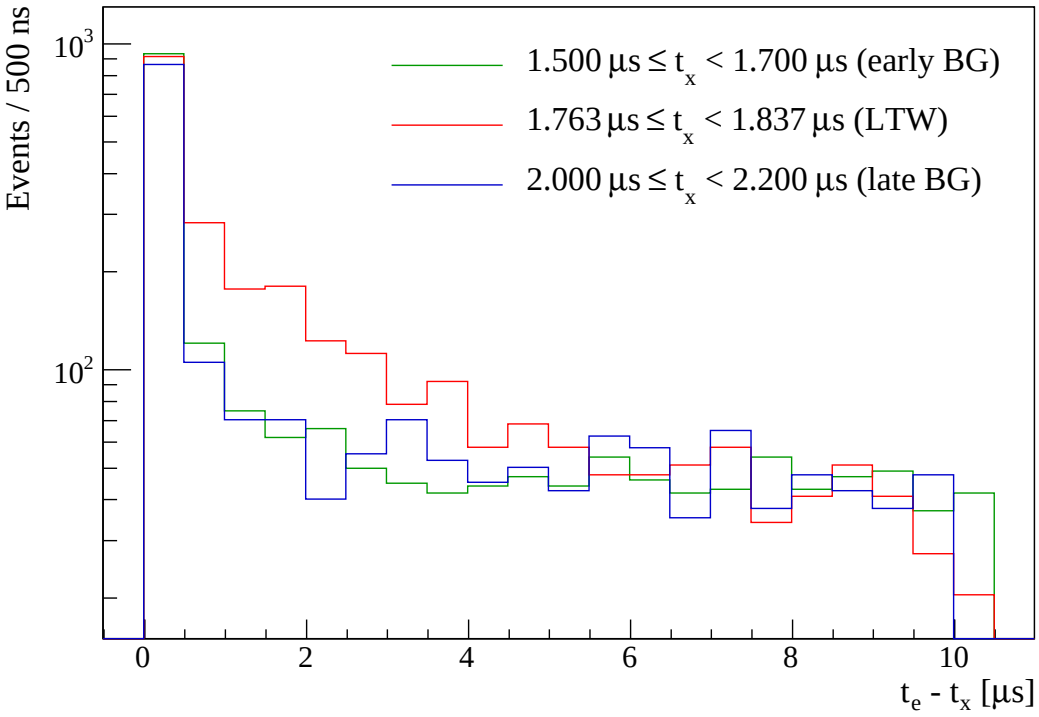

Figure B.17: Time Difference Spectra for Different X-ray Times. *This histogram shows the $t_e - t_x$ time difference for X-rays recorded before (green), in (red), and after (blue) the laser time window. The corresponding electron of the ($\boldsymbol{X}$+$\boldsymbol{e^-_{delayed}}$)-class is recorded by the **Paddle_hi_M1**-detector. While X-rays recorded both before and after the laser time only have accidentally correlated electrons, X-rays in the laser time window (LTW) stem from laser-induced μp transitions and exhibit an exponential decay up to $t_e - t_x = 6\,\mu$s. The data for $t_e - t_x > 9\,\mu$s cannot be taken into consideration since, here, the influence of the end of the $e^-_{delayed}$-window is visible and causes the recorded events to decrease. The three data sets are normalized such that their integrals in the region from 6 – 9 μs agree.*

The entire procedure is a good tool to gain statistics (while avoiding an increase of the background level). Because of the exponential nature of the muon-decay process, already small changes of the lower $e^-_{delayed}$-window bound have a large impact on the number of ($\mathbf{X}$+$\mathbf{e^-_{delayed}}$)-events. It has to be mentioned that the plots in Fig. B.16 represent mainly the background behaviour of the prompt events: the prompt μp-atoms still have a significant kinetic energy causing them to drift into the target walls. The decay constant of $\sim 0.6\,\mu$s of the exponential decay at early times in Fig. B.16(a) agrees with the time the μp atoms need to drift into the target walls. Here, the muons are transferred to atoms with higher Z-values (undergoing electron-free decay processes), and do not show up as signals at late time differences. However, the ($\mathbf{X}$+$\mathbf{e^-_{delayed}}$)-events at laser time were slowed down substantially and will, therefore, not be quenched by mentioned effects. Instead, the lifetime should be similar to the free muon lifetime of $\tau_\mu = 2.2\,\mu$s resulting in a much less pronounced contribution to the present background.

Class	LAAPDs	Mean FWHM [keV]	Energy Cut [keV] lower	upper
1	A0	0.57	1.4	2.4
2	A6,A7,B4,B5,B6	0.67	1.5	2.5
3	A2,A3,A4,A5,B2,B3	0.73	1.2	2.6
4	A8,B0,B8	0.91	1.1	2.7
5	A1,A9,B1,B7,B9	1.23	1.0	2.8

Table B.2: LAAPD Classification. *The LAAPDs are grouped into 5 different classes according to their energy resolution. The FWHM is extracted by fitting the 1.9 keV peak in the LAAPDs' energy spectra with a simple Gaussian. LAAPD A0 has its own class because of its outstanding energy resolution. The upper and lower bounds of the energy cut are extracted with the help of Fig. B.18.*

B.9 Energy Cut

To stay well below the tolerable background level of 3×10^{-4}, the energy resolution of the 20 LAAPDs is considered as well. The prominent 1.9 keV peak in the energy spectra (e.g. Fig. B.7) has a median FWHM of 0.7 keV (with 0.6 keV for the best LAAPD A0 and 1.3 keV for the worst). In order to extract only the 1.9 keV X-rays together with their delayed electron from the ($\mathbf{X}$+$\mathbf{e}^-_{delayed}$)-class, cuts on the X-ray energy are chosen for all LAAPDs individually. For this, the LAAPDs are grouped into five classes according to their energy resolution (see Table B.2).

Figure B.18 clarifies the influence of the X-ray energy cut and background amplitude and the number of recorded (prompt) events. The plot in Fig. B.18(a) shows the background level obtained for different widths of the X-ray energy window. It reveals that for almost all slices of the X-ray energy the background amplitude will stay below 3×10^{-4}. From this point of view, the energy window could be chosen to be rather wide. Nevertheless, Figure B.18(b) has to be considered, as well. It shows how many more (prompt) events are recorded (i.e. gain in recorded prompt events) when the width of the energy window is increased in steps of 0.2 keV. The plot exposes how wide the energy window can be chosen in a meaningfull manner before the gain in statistics starts to level out and stops outweighing the increase of background (from Fig. B.18(a)).

The effect of the energy resolutions of the different classes is visible in this plot as well: with good LAAPDs (like A0), most of the events are concentrated within a narrow energy window with a width of $\sim$ 1.0 keV. In this case, increasing the width from 1.0 keV up to 1.8 keV would be of no use and would only increase the background amplitude from 2.0×10^{-4} to 3.5×10^{-4} (as can be seen in Fig. B.18(a)). The resulting

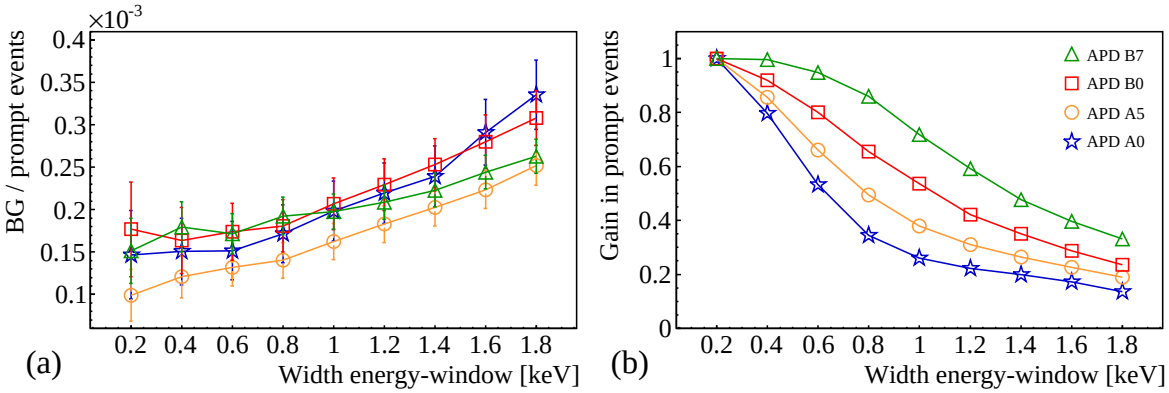

Figure B.18: Influence of the X-Ray Energy Cut. ***(a)*** *The background level (normalized to the number of prompt events) is plotted versus the window width of allowed X-ray energies centered around 1.9 keV. The four representatives shown each belong to a different LAAPD class. The background level remains below the tolerable* 3×10^{-4} *for most of the LAAPDs.* ***(b)*** *This plot shows the increase in statistics when the energy window is widened to the next value. The data is normalized to the first value. For LAAPD A0, opening the window-width above 1 keV increases the gain only marginally. LAAPDs from class 5 (like B7 depicted here), on the other hand, show a much slower variation of the gain because of the worse energy resolution.*

lower and upper bounds of the energy window for the individual LAAPD-classes are mentioned in Table B.2.

B.10 Second Muon Cut

With a non-negligible probability of $\sim$ 3 % a further muon can enter the target at random times after the first muon has opened a time window in which muon events are recorded. Such a muon (termed *second muon*) will also slow down and form a μp atom. A 2 keV X-ray will be emitted causing an accidental, evenly distributed background event at random times in the time spectra such as in Figure B.14. In the case this X-ray is emitted in the LTW, it would fake a laser-induced signal stemming from the first muon. As shown in Eq. (2.10), the effectiveness to detect a second muon is $\epsilon_{2nd} = 94\,\%$. A second muon is claimed if either of the two muon detectors S_1 or S_2 trigger (Sect. 2.4.1). The transition from the blue to the red time spectrum in Figure B.14 demonstrates nicely the effectiveness of the second muon cut. The late region with $t > 7\,\mu$s shows that rejecting detected second muons reduces the flat background by a factor $\sim$ 20.

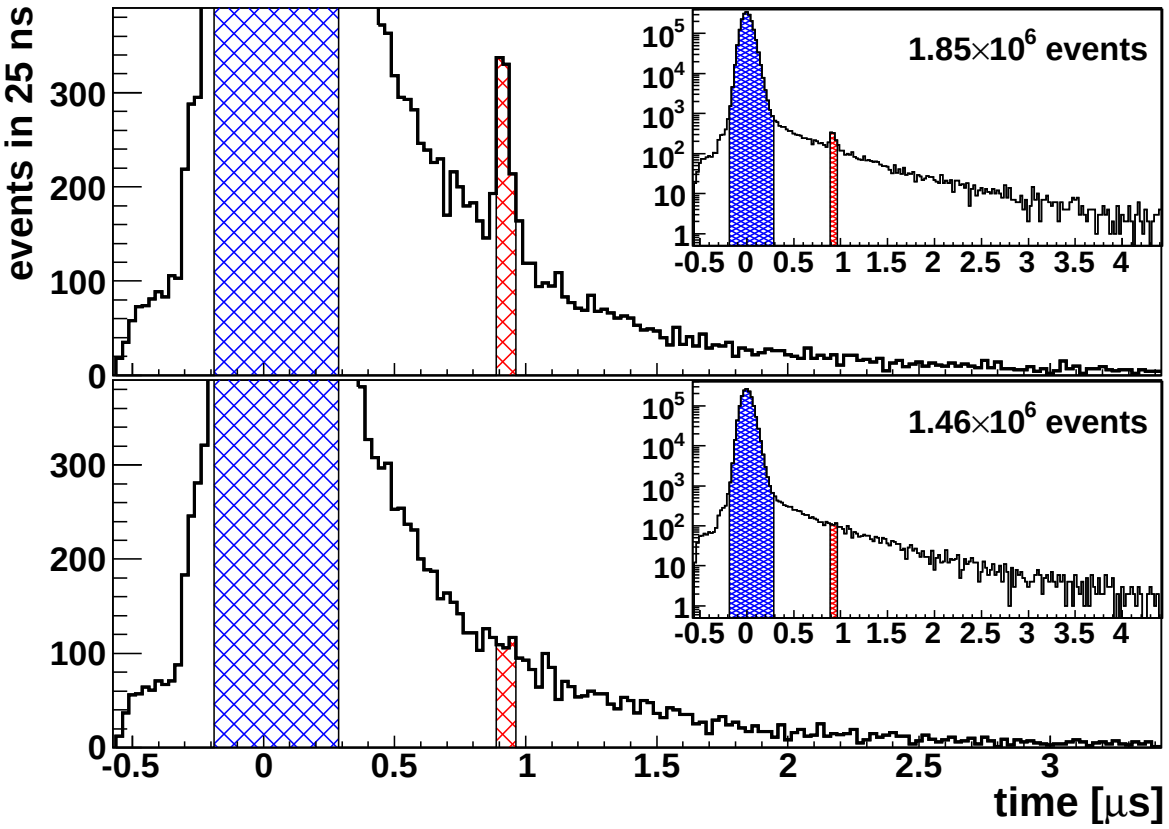

Figure B.19: Accumulated Time Spectra on and off Resonance. *Summed X-ray time spectra recorded on resonance (top, FP #282884 – 28906) and off resonance (bottom) shown in linear and logarithmic scale. The LTW $t \in [0.887, 0.962]\,\mu$s in which the muonic atoms in the target are illuminated by the laser is indicated in red. The contribution of the prompt X-rays is marked in blue.*

B.11 Fruits of the Analysis: the Resonance

Finally, the analyzed data can be assembled to deliver the $2S_{1/2}^{F=1} - 2P_{3/2}^{F=2}$ resonance line in muonic hydrogen. For this, the time information of the 2 keV X-rays with a delayed electron but without second muons present (i.e. class 110 events with 2 keV and 2^{nd} muon cuts), are summed up into time specta, one for every laser frequency. Since the laser is locked to a reference Fabry-Pérot (FP) cavity with a free spectral range FSR = 1.5 GHz (cf. Section 4.2.1), the resonance treated here is given against the FP-fringe number. After a proper laser frequency calibration in Section 4.2, the final resonance is presented in Section 4.4. The data analysis that has been introduced in this appendix is optimized such that the statistics and the position determination of the resonance line is maximized (which is accompanied by a degradation of the signal-to-background ratio). For a more detailed explanation refer to Section 4.4.

Figure B.19 shows the time spectra of the mentioned X-ray class united into two groups, one on-resonance and one off-resonance (see below). In the plots, the prompt

peak caused by the muonic cascade during μp formation is indicated in blue. For each laser frequency, it serves to normalize the data to the number of formed μp atoms. The 75 ns wide laser time window (LTW) $t \in [0.887, 0.962]\,\mu$s, in which the laser light illuminates the muonic atoms in the target and laser induced K_α X-rays are expected is marked in red. It coincides nicely with the LTW decuded in Section B.5.2. Note the clear excess of events in the LTW of the on-resonance time spectrum.

The $2S - 2P$ resonance line is plotted in Figure B.20. It is obtained by plotting the number of $K_\alpha$events recorded in the LTW, normalized to the number of prompt events, as a function of the FP-fringe number (equivalent to the laser frequency). The fit to the data is a simple Lorentzian profile on top of a flat background. In total we have measured 900 events in the resonance where 404 background events are expected. Three of the four parameters, namely the position of the Lorentzian, its amplitude, and its width are varied freely. Only the background amplitude is fixed to the value obtained from a fit to data recorded without laser (empty circles in Fig. B.20). It agrees well with the extrapolated background amplitude in the LTW in the Laser_{on} data.

A centroid position of 895.33 ± 0.45 FP-fringes and a width of 11.40 ± 1.34 FP-fringes are extracted. The uncertainties quoted are of statistical nature. The width is a bit smaller than the 13.7 FP-fringes expected from the laser-bandwidth and Doppler- and power-broadening of the natural line-width of 12.4 FP-fringes or 18.6 GHz (cf. Section 4.3). A value of $\chi^2 = 32.2$ for 28 degrees of freedom (dof) or $\chi^2/dof = 1.15$ is associated with the fit. A fit of a flat line, assuming no resonance, would result in $\chi^2 = 251.9$ for 31 dof ($\chi^2/dof = 8.13$), making this line $15\,\sigma$ significant. The measurement time has varied between 3 and 13 hours per laser frequency. The data has been recorded at a rate of 8 events per hour in the LTW when on resonance. The background of $\sim$ 2 event/hour originates mainly from falsely identified muon-decay electrons and from effects related to delayed muon transfer to the target walls. The on-resonance time spectrum in Fig. B.19 is produced from events recorded between FP-fringe 282884–282906. Events from outside this range contribute to the time spectrum of the off-resonance data.

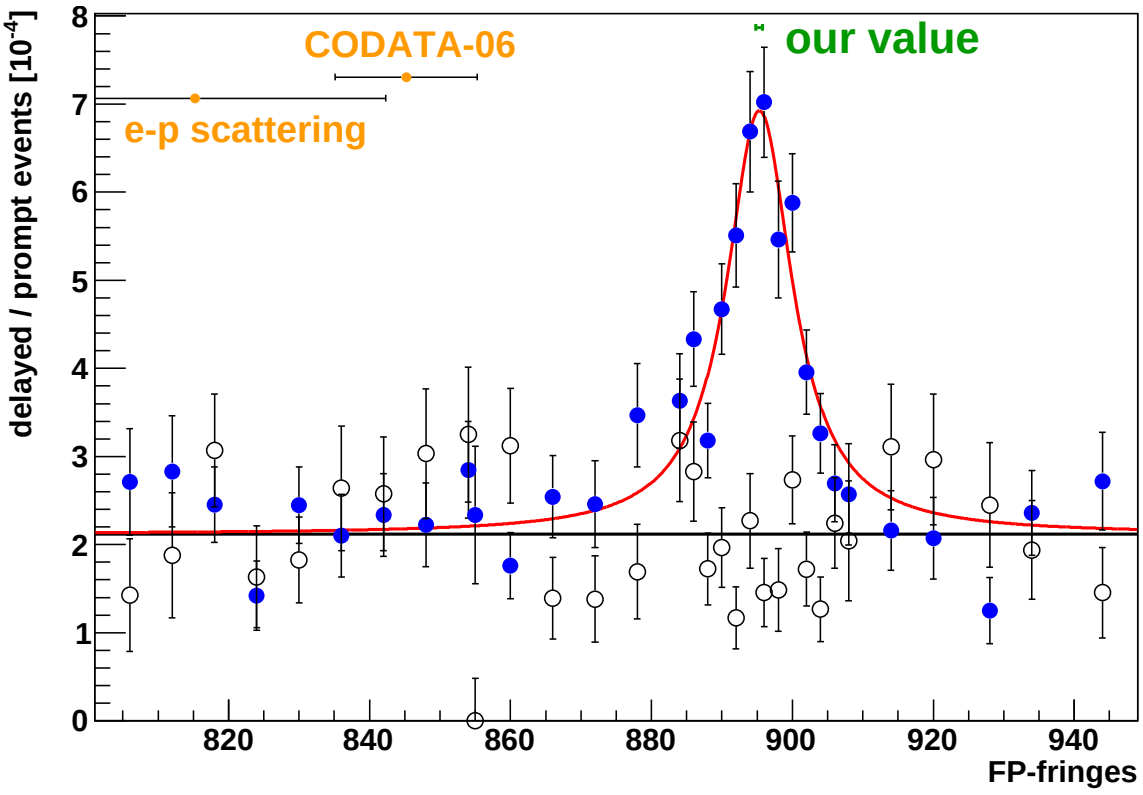

Figure B.20: The Resonance as Obtained from this Data Analysis. *The signature of the* $2S^{F=1}_{1/2} - 2P^{F=2}_{3/2}$ *transition in μp is plotted versus the laser frequency (FP-fringes) (solid blue circles) obtained using the wide parameter cuts introduced in this chapter. The number of events in the LTW is normalized to the number of prompt events. The fit is a Lorentzian profile on top of a flat fixed background. The empty circles represent data that have been recorded simultaneously under the same conditions. The only difference is that the correctly tuned laser has not been ready and could therefore not be fired. As expected, this data set does not show any indication of laser induced events. The predictions for the line position using the proton charge radius from CODATA [76] and from electron scattering [11, 111] are indicated. To obtain the absolute FP-fringe numbers, 282800 has to be added to the value on the x-axis. For a final resonance including laser frequency calibration and systematics refer to Figure 4.15.*

Appendix C

Ringdown Measurements for the Reflectivity of the Target Mirrors

Extensive research has gone into the development of a non-radioactive HR coating for the target cavity (Section 2.3.4) during the preparation of the 2007 and 2009 runs. In 2003, a dielectric coating containing ThF_4/ZnSe was employed with a reflectivity at $6\,\mu$m as high as $R_{ThF_4} = 99.97\,\%$. However, the ThF_4 layers are radioactive and emit alpha particles which hit the X-ray detectors and destroy them. Hence, an alternative had to be found, and as candidates, coatings containing Ge/ZnSe stacks and Ge/ZnS stacks have been considered. Several samples of different companies have been examined and their reflectivities have been measured in a cavity ringdown setup. Using our pulsed laser system at $6\,\mu$m, cavity transmission signals containing a ringdown signature have been recorded in a setup shown in Figure C.1. The cavity ringdown time, i.e. the time an injected pulse needs to decay, has been recorded using a fast infra-red photo detector. The cavity is set up inside a vacuum chamber to avoid losses stemming from water absorption.

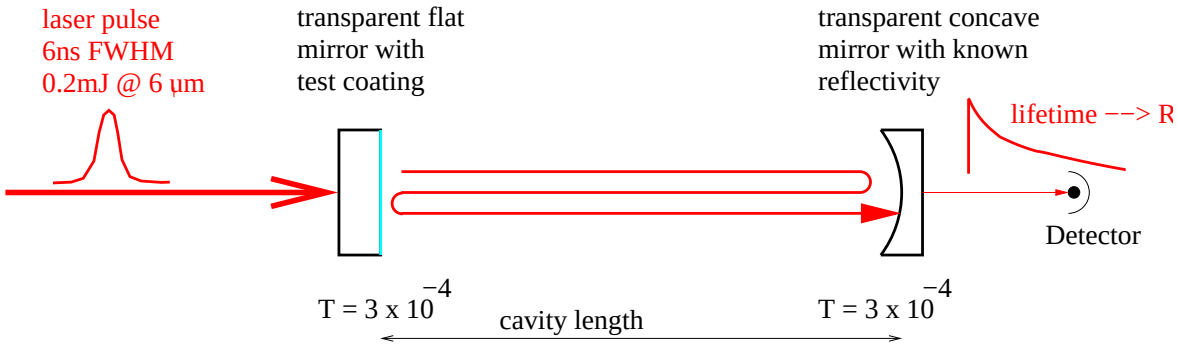

Figure C.1: Cavity Ringdown Setup. *Inside a vacuum chamber, a flat-concave cavity of a test mirror and a ThF_4 reference mirror of known reflectivity are set up to measure the cavity ringdown time. Both mirror substrates have to be transparent for $6\,\mu$m radiation, therefore their material is chosen to be either ZnSe or CaF_2.*

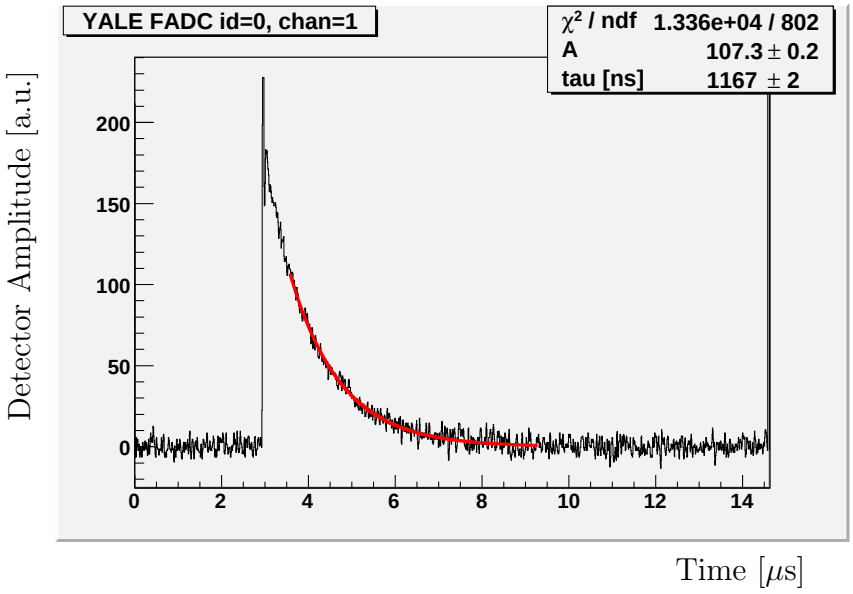

Figure C.2: Sample Ringdown Trace. *A cavity ringdown trace of the best Ge/ZnS test coating together with the ThF_4 reference coating is shown. The exponential fit shows a decay constant of $\tau = 1167\,(2)$ ns.*

The exponential decay has been fitted to extract the decay time τ of the ringdown signal. A most typical trace obtained for a Ge/ZnS coating is shown in Figure C.2 and has a fitted decay time $\tau = 1167\,(2)$ ns. The time needed by the laser pulse to travel the lenght of the cavity $L = 194.6$ mm is 0.6491 ns. From this, the number of reflections can be deduced to be $n = 1798$. With half the reflections occuring on the sample mirror and the other half on the reference mirror, one obtains

$$(R_{\mathrm{ZnS}})^{n/2} \cdot (R_{\mathrm{ThF_4}})^{n/2} = e^{-1}. \tag{C.1}$$

Using $R_{\mathrm{ThF_4}} = 99.97\,\%$, this leads to

$$R_{\mathrm{ZnS}} = \frac{e^{-2/n}}{R_{\mathrm{ThF_4}}} = 99.92\,(1)\,\%. \tag{C.2}$$

Several test coatings have been received from Umicore[1] and from QIoptIQ[2]. Table C.1 gives a compilation of all measured samples. Umicore # 2 and # 3 have been purchased at the same time. According to the log-books of the company, Umicore # 2 (a Ge/ZnS coating) was coated in a freshly cleaned depositioning chamber while for Umicore # 3 (Ge/ZnSe), a "dirty" chamber was used. Because of the assumption that a Ge/ZnSe coating deposited in a freshly cleaned chamber would outrange the reflectivity of Umicore # 2, the target cavity mirror substrates have been coated with such a Ge/ZnSe coating (Umicore # 4). Unfortunately, this strategy did not improve the reflectivity which ended up being $R_{\mathrm{Umi\#4}} = 99.89\,(1)\,\%$.

[1] Umicore Coating Services, UK, `http://eom.umicore.com`
[2] QIoptIQ Ltd., UK, `http://www.qioptiq.com`

Company	Sample	Stack Type	Reflectivity
QIoptIQ	# 1	Ge/ZnSe	99.0
QIoptIQ	# 2	Ge/ZnSe	99.28
QIoptIQ	# 3	Ge/ZnSe	99.95
QIoptIQ	# 4	Ge/ZnSe	99.80(2)
Umicore	# 1	Ge/ZnS	99.85(2)
Umicore	# 2	Ge/ZnS	99.92(1)
Umicore	# 3	Ge/ZnSe	99.89(1)
Umicore	# 4	Ge/ZnSe	99.89(1)

Table C.1: Reflectivities of Target Cavity Coatings. *The reflectivities of the different samples obtained by cavity ringdown measurements. The best one is Umicore # 2, a Ge/ZnS coating produced in a clean depositioning chamber. The target cavity substrates have been coated with Umicore # 4.*

Finally, the transmission scan of Umicore # 2 provided by the company is opposed to the one of ThF_4 in Figure C.3. It shows a slightly worse and much narrower HR-band compared to ThF_4.

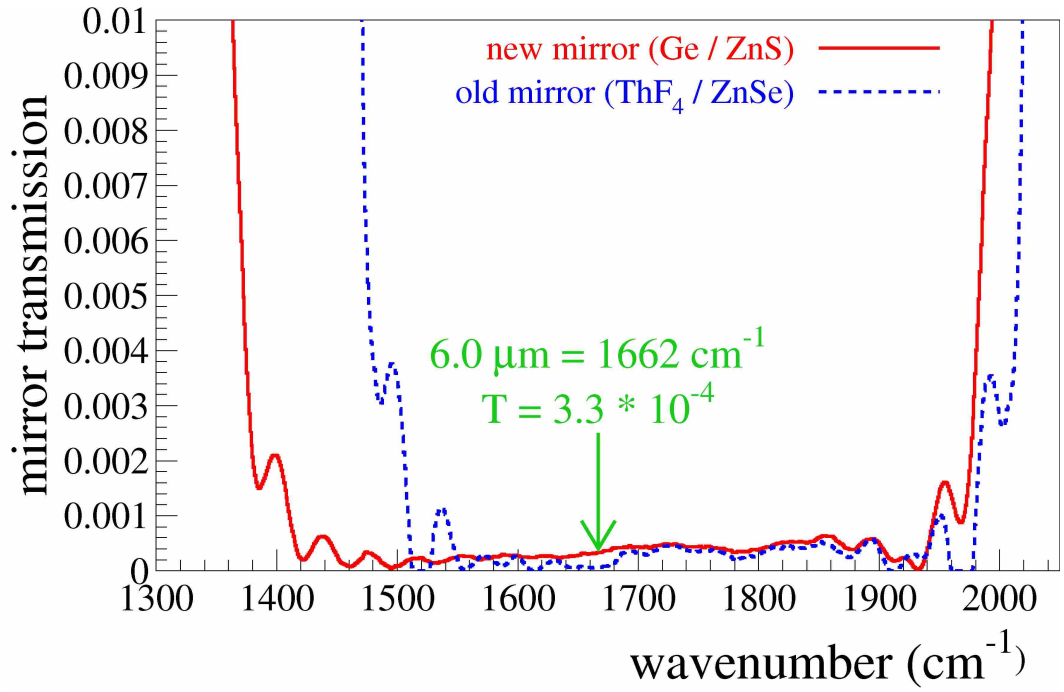

Figure C.3: Cavity Coating Transmission Signal. *The transmission spectra of the Ge/ZnS coating Umicore # 2 and of the ThF_4/ZnSe coating are shown. In our wavelentgh region the transmission of Umicore # 2 goes down to $T = 3.3 \times 10^{-4}$.*

Appendix D

Muon Drift-Time

The LAAPDs are arranged above and below the target in two rows of ten devices along the muon beam axis. LAAPDs at the entrance window (AB0) see the muons earlier than the LAAPDs AB9 at the downstream end of the target. By looking at the prominent prompt 1.9 keV peak in the time-spectra of the individual LAAPDs, a stop-time distribution for the muons can be extracted. From this, one can evaluate a mean velocity and a mean kinetic energy.
In a first step, all data stemming from the first resonance in μp are summarized for all LAAPDs individually. For every LAAPD, a time-spectrum of all detector hits is produced. The usual prominent prompt peak (stemming from muons cascading to the $1S$ ground state of muonic hydrogen immediately after muon-capture) is fitted with a Gaussian function $f(x) = 1/\left(\sigma\sqrt{2\pi}\right) \cdot exp\left[-\frac{(x-b)^2}{2\sigma^2}\right]$ within a very narrow interval around the expected peak. Since the model function does not reproduce the real peak perfectly, the error in the resulting fit-parameters (i.e. the position b and the width σ of the Gaussian) is multiplied by the square root of the reduced χ^2 to account for the introduced offset.
By plotting the resulting positions of the prompt peak versus the APD-number and fitting with a polynomial of first degree $p(x) = p_0 + p_1 \cdot x$, the mean axial velocity (parallel to the beam axis) of the muons can be extracted, as can be seen in Figure D.1; since the inter-LAAPD spacing is constant at 16.5 mm (except between AB4 and AB5, where it is 19.5 mm), this results in a plot of time vs distance with a linear fit (black) of $p(x) = 830\,\text{ns} + 0.394\,\text{ns/mm} \cdot x$. The slope is the inverse of the muons' velocity $p_1 = 0.394 \pm 0.003\,ns/mm$. This is equivalent to an axial muon velocity of $v_a = 2.54 \pm 0.02 \cdot 10^6\,m/s$. The axial velocity spread (i.e. the width of the fitted Gaussian σ) does not change throughout the target-length and stays constant within the errors of a linear fit.

An non-relativistic estimate of the muons' mean kinetic energy is calculated using $E^a_{kin} = \frac{1}{2} m_\mu v_a^2$ and results in $E^a_{kin} = 3.8\,\text{keV}$. This is consistent with estimation for the energy-budget of a muon being guided through the beam line.

It has to be emphasized that this consideration is rather crude: neither the muons'

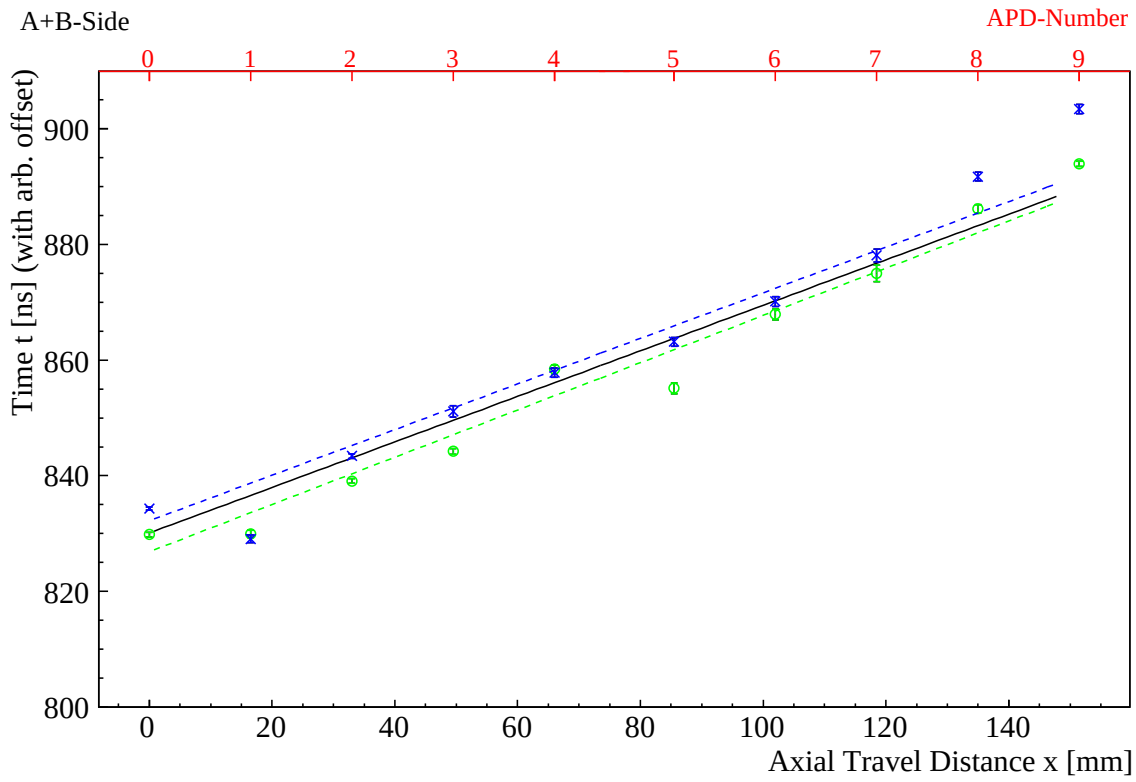

Figure D.1: The Axial Muon Drift. *The plot shows the mean detection times for prompt muonic hydrogen cascading into the 1S ground state immediately after muon-capture, extracted from accumulated time-spectra recorded for each LAAPD. Versus distance (and equivalently versus LAAPD-number), the mean stopping time is plotted for the two opponent sets of LAAPDs. The open green circles (blue crosses) represent the LAAPDs from the A-side (B-side). Since the muon stopping in the hydrogen gas is succeeded by the* prompt *cascade within a constant offset in time, this plot can be utilized to determine the time needed for a muon to drift from one APD to the next (cf. text). The black fit is a linear regression of the complete set of data. The dashed green line below (blue line above) the main fit is a fit of the A-side (B-side) subset of data and has a slope of* $p_1 = 0.409 \pm 0.005\,ns/mm$ *(*$p_1 = 0.394 \pm 0.004\,ns/mm$*). The result of the common linear regression of both the A-side and the B-side is mentioned in the text.*

energy-distribution nor the stopping power of molecular hydrogen on the muons was taken into account. Furthermore, the axial (parallel to the muon-beam) and the radial (from the spiral of the muon in the 5 Tesla magnetic field) velocity components are not independent from each other; faster muons pass the magnetic field on a spiral with larger diameter leading to a larger travelled distance they have to cover before reaching the next LAAPD.

Appendix E

Abbreviations and Expressions

Some terms and expressions are frequently used throughout this thesis. This appendix is supposed to give brief explanations of their abbreviations.

Analyzer *THE Analyzer.* The computer program processing the recorded data to produce a multitude of histograms during the offline analysis is referred to as the "Analyzer".

ADC *Analog-to-digital converter.* An electronic device recording the amplitude of a signal and converting it into digital, numerically processable information.

AR *Anti reflection.* An AR coating is applied to optical surfaces to reduce reflection.

ASE *Amplified spontaneous emission.* Spontaneous emission that is amplified by stimulated processes in a gain medium.

BBO *Beta barium borate.* Beta barium borate (β-BaB_2O_4) is a crystal used for nonlinear optics. It is birefringent and exhibits the electro-optical Pockels effect in which electrically induced birefringence is produced. See also PC.

BG *Background.* In contrast to the 1.9 keV X-rays, the BG contributes to the unwanted part of the signal. It originates from electro magnetic or acoustic noise, falsely identified particles and X-rays, and many other sources.

BN *Beat note.* Beating two sinusoidal electromagnetic waves with each other results in a beat note as the difference of their frequencies.

CODATA *Committee on Data for Science and Technology.* Established in 1966 as an interdisciplinary committee of the International Council of Science (ICSU), it seeks to strengthen science by promoting improved data management and use. The CODATA Task Group on Fundamental Constants provides a globally accepted set of values

of the fundamental physical constants. This set is updated on a regular basis.

cw *Continous wave.* Lasers of constant amplitude and frequency are referred to as cw lasers.

DAQ *Data aquisition.* A term used to describe the hardware needed for the data-taking. Also used as a synonym for data-taking.

dof *Degrees of freedom.* In a fitting procedure, the number of dof is the number of parameters that are free to vary minus the number of independent scores. Theχ^2-value of a fit is usually stated in conjunction with the number of dof.

event *An event.* The signals recorded by the various detectors when a muon has been detected are collected by the DAQ system and form an event. An event can contain single or multiple hits in the LAAPDs and the electron detectors.

FP *Fabry-Pèrot.* A high-finesse optical cavity whose transmission fringes are used as a frequency marker for the calibration of the laser's frequency.

FSR *Free spectral range.* The frequency separation between two adjacent transmission peaks of an optical cavity. In the case of our FP cavity, the FSR $\simeq 1497\,\mathrm{MHz}$.

FWHM *Full width at half maximum.* Describes the width of a resonance line at half the maximum amplitude of the line.

HFS *Hyperfine splitting.* Splitting in the atomic energy levels caused by spin-spin interactions between the orbiting particle and the nucleus.

HR *High reflection.* HR coatings are used for cavity mirrors when a high finesse wants to be achieved

HV *High voltage.*

HWHM *Half width at half maximum.* A value for half the width at half of the peak's maximum amplitude. Half of the FWHM.

LAAPD *Large area avalanche photo diode.* Silicon based photo diodes with a large square surface area to detect X-rays. They are described in Section 2.4.2.

LTW *Laser time window.* The time window in which the laser pulse illuminates the target cavity volume. During the LTW, the laser induced K_αX-rays are expected.

MOPA *Master oscillator power amplifier.* Pulsed laser system consisting of an oscillator producing a laser pulse and an amplifier which amlpli-

fies the power of the pulse (often in a multi-pass arangement).

μd *Muonic deuterium.* An deuteron (consisting of a proton and a neutron) orbited by a negatively charged muon.

μp *Muonic hydrogen.* A proton orbited by a negatively charged muon.

NR *Non relativistic.*

OC *Output coupler.* The mirror through which usually the laser light exits an optical cavity. It usually has a transmission of some percent.

PC *Pockels cell.* Is used to rotate the polarization of a laser beam. Makes use of the Pockels effect which causes birefringence in a nonlinear crystal induced by a strong electric field.

PM *Photo multiplier.* Extremly sensitive photon detectors making use of the photoelectric effect and amplifying the photo current in a series of dynodes. They are sometimes referred to as PMTs (photo multiplier tubes).

PTDC *Pipeline time-to-digital converter.* Compared to a TDC (see below), a PTDC is able to record multiple hits and process their timing information.

pulse *LAAPD-pulse.* The hits in the LAAPDs recorded by the WFDs are called pulses. An event can consist of pulses from more than one LAAPD.

PZT *Lead zirconate titanate.* PZT is a ceramic perovskite material that exhibits the piezoelectrical effect. It is frequently used as a electromechanical component of a feedback loop.

QED *Quantum electrodynamics.* The relativistic quantum field theory of electrodynamics.

RC *Raman cell.* Hydrogen-filled multipass cell to convert visible to infra-red light.

rms *Root mean square.* Quadratic Mean. A statistical measure of the magnitude of a varying quantity. For the proton radius, it is $\langle r_p^2 \rangle = \int dr\, r^2 \rho(\mathrm{r})$.

RWA *Rotating wave approximation.* The RWA is an approximation employed in quantum mechanics of atom optics and magnetic resonances. It neglects rapidly oscillating terms in the Hamiltonian. This is a valid approximation when the applied laser is of low intensity and its frequency is close to the atomic resonance.

SHG *Second harmonic generation.* Another term for frequency doubling.

In this process, the frequency of a laser beam can be doubled by converting photons in a non-linear crystal.

TDC *Time-to-digital converter.* An electronic device recording the timing information of a falling (or rising) edge of a signal and converting it into digital, numerically processable information. An ordinary TDC can usually only handle the first pulse of a series of events and, therefore, omits the following ones (in contrast to a PTDC).

TEM *Transverse electromagnetic.* A particular electromagnetic field pattern meassured in the plane perpendicular (i.e. transverse) to the propagation direction of the wave.

TFP *Thin film polarizer.* Made from a transmissive substrate with a special coating applied that act like a polarizing beam splitter.

Ti:Sapph *Titanium sapphire.* Ti:Sapph lasers use titanium-doped sapphires (Ti:Al_2O_3) as laser active material.

VP *Vacuum polarization.* The creation and annihilation of an electron positron pair as an insertion to the photon propagator.

WFD *Wave form digitizer.* Used to digitize an analog signal and make the entire wave form processable numerically.

Yb:YAG *Ytterbium doped Yttrium aluminium garnet.* Yb:$Y_3Al_5O_{12}$ is a ytterbium doped synthetic crystal used as laser gain medium.

Coauthored Publications

1. The Size of the Proton

R. Pohl, A. Antognini, F. Nez, F.D. Amaro, F. Biraben, J.M.R. Cardoso, D.S. Covita, A. Dax, S. Dhawan L.M.P. Fernandes, A. Giesen, T. Graf, T.W. Hänsch, P. Indelicato, L. Julien, C.-Y. Kao, P. Knowles, J.A.M. Lopes, E. Le Bigot, Y.-W. Liu, L. Ludhova, C.M.B. Monteiro, F. Mulhauser, T. Nebel, P. Rabinowitz, J.M.F. dos Santos, L.A. Schaller, K. Schuhmann, C. Schwob, D. Taqqu, J.F.C.A Veloso & F. Kottmann
Nature **466**(7303), pp. 213–216 (2010)

2. Thin-Disk Yb:YAG Oscillator-Amplifier Laser, ASE, and Effective Yb:YAG Lifetime

A. Antognini, K. Schuhmann, F. D. Amaro, F. Biraben, A. Dax, A. Giesen, T. Graf, T. W. Hänsch, P. Indelicato, L. Julien, C.-Y. Kao, P. E. Knowles, F. Kottmann, E. Le Bigot, Yi-Wei Liu, L. Ludhova, N. Moschüring, F. Mulhauser, T. Nebel, F. Nez, P. Rabinowitz, C. Schwob, D. Taqqu & R. Pohl
IEEE Journal of Quantum Electronics **45**, pp. 993–1005 (2009)

3. Status of the muonic hydrogen Lamb-shift experiment

T. Nebel, F.D. Amaro, A. Antognini, F. Biraben, J.M.R. Cardoso, C.A.N. Conde, A. Dax, S. Dhawan, L.M.P. Fernandes, A. Giesen, T.W. Hänsch, P. Indelicato, L. Julien, P.E. Knowles, F. Kottmann, E. Le Bigot, Y.-W. Liu, J.A.M. Lopes, L. Ludhova, C.M.B. Monteiro, F. Mulhauser, F. Nez, R. Pohl, P. Rabinowitz, J.M.P. dos Santos, L.A. Schaller, K. Schuhmann, C. Schwob, D. Taqqu & J.F.C.A. Veloso
Canadian Journal of Physics **85**, pp. 469–478 (2007)

Bibliography

[1] R. Pohl, A. Antognini, F. Nez, F. Amaro, F. Biraben, J. Cardoso, D. Covita, A. Dax, S. Dhawan, L. Fernandes, A. Giesen, T. Graf, T. Hänsch, P. Indelicato, L. Julien, C.-Y. Kao, P. Knowles, J. Lopes, E.-O. Le Bigot, Y.-W. Liu, L. Ludhova, C. Monteiro, F. Mulhauser, T. Nebel, P. Rabinowitz, J. dos Santos, L. Schaller, K. Schuhmann, C. Schwob, D. Taqqu, J. Veloso, and F. Kottmann. "The size of the proton". *Nature* **466**(7303), (2010) pp. 213–216.

[2] W. Heisenberg. "Über die quantentheoretische Umdeutung kinematischer und mechanischer Beziehungen." *Z. Phys. A* **33**(1), (1925) pp. 879–893.

[3] W. E. Lamb and R. C. Retherford. "Fine structure of the hydrogen atom by a microwave method". *Phys. Rev.* **72**(3), (1947) pp. 241–243.

[4] W. Liu, M. G. Boshier, S. Dhawan, O. van Dyck, P. Egan, X. Fei, M. Grosse Perdekamp, V. W. Hughes, M. Janousch, K. Jungmann, D. Kawall, F. G. Mariam, C. Pillai, R. Prigl, G. zu Putlitz, I. Reinhard, W. Schwarz, P. A. Thompson, and K. A. Woodle. "High precision measurements of the ground state hyperfine structure interval of muonium and of the muon magnetic moment". *Phys. Rev. Lett.* **82**(4), (1999) pp. 711–714.

[5] M. W. Ritter, P. O. Egan, V. W. Hughes, and K. A. Woodle. "Precision determination of the hyperfine-structure interval in the ground state of positronium." *Phys. Rev. A* **30**(3), (1984) pp. 1331–1338.

[6] J. Verdú, S. Djekić, S. Stahl, T. Valenzuela, M. Vogel, G. Werth, T. Beier, H.-J. Kluge, and W. Quint. "Electronic g factor of hydrogenlike oxygen $^{16}O^{7+}$". *Phys. Rev. Lett.* **92**(9), (2004) p. 093002.

[7] H. Häffner, T. Beier, N. Hermanspahn, H.-J. Kluge, W. Quint, S. Stahl, J. Verdú, and G. Werth. "High-accuracy measurement of the magnetic moment anomaly of the electron bound in hydrogenlike carbon". *Phys. Rev. Lett.* **85**(25), (2000) pp. 5308–5311.

[8] M. Niering, R. Holzwarth, J. Reichert, P. Pokasov, T. Udem, M. Weitz, T. W. Hänsch, P. Lemonde, G. Santarelli, M. Abgrall,

P. Laurent, C. Salomon, and A. Clairon. "Measurement of the hydrogen $1S - 2S$ transition frequency by phase coherent comparison with a microwave cesium fountain clock". *Phys. Rev. Lett.* **84**(24), (2000) pp. 5496–5499.

[9] B. de Beauvoir, C. Schwob, O. Acef, L. Jozefowski, L. Hilico, F. Nez, L. Julien, A. Clairon, and F. Biraben. "Metrology of the hydrogen and deuterium atoms: Determination of the Rydberg constant and Lamb shifts". *Eur. Phys. J. D* **12**, (2000) pp. 61–93.

[10] M. Fischer, N. Kolachevsky, M. Zimmermann, R. Holzwarth, T. Udem, T. W. Hänsch, M. Abgrall, J. Grünert, I. Maksimovic, S. Bize, H. Marion, F. Pereira Dos Santos, P. Lemonde, G. Santarelli, P. Laurent, A. Clairon, C. Salomon, M. Haas, U. D. Jentschura, and C. H. Keitel. "New limits on the drift of fundamental constants from laboratory measurements". *Phys. Rev. Lett.* **92**(23), (2004) p. 230802.

[11] I. Sick. "On the rms–radius of the proton". *Phys. Lett. B* **576**(1–2), (2003) pp. 62–67.

[12] P. Kusch and H. M. Foley. "The magnetic moment of the electron". *Phys. Rev.* **74**(3), (1948) pp. 250–263.

[13] F. Kottmann. Private communication (2010).

[14] A. Di Giacomo. "A sensitive test of quantum electrodynamics. The 2S-2P energy difference of muonic hydrogen". *Nucl. Phys. B* **11**(2), (1969) pp. 411–427.

[15] R. Pohl. *Investigations of the long-lived metastable* $2S$ *state in muonic hydrogen.* Ph.D. thesis, ETH Zürich (2001). `http://e-collection.ethbib.ethz.ch/view/eth:23936`.

[16] R. Pohl, H. Daniel, F. J. Hartmann, P. Hauser, F. Kottmann, V. E. Markushin, M. Muhlbauer, C. Petitjean, W. Schott, D. Taqqu, and P. Wojciechowski-Grosshauser. "Observation of Long-Lived Muonic Hydrogen in the $2S$ State". *Phys. Rev. Lett.* **97**(19), (2006) p. 193402.

[17] C. Cohen-Tannoudji. *Quantum Mechanics* (John Wiley and Sons, Inc., New York, 1977).

[18] J. Bjorken and S. Drell. *Relativistic Quantum Mechanics* (Plenum, New York, 1977).

[19] M. I. Eides, H. Grotch, and V. A. Shelyuto. *Theory of light hydrogenic bound states*, vol. 222 of *Springer tracts in modern physics* (Springer, Berlin Heidelberg, 2007).

[20] J. Sapirstein and D. Yennie. *Quantum Electrodynamics*, vol. 7, chap. Theory of hydrogenic bound states, pp. 560–672 (World Scientific, Singapore, 1990).

[21] E. Salpeter and H. Bethe. "A relativistic equation for bound-state problems". *Phys. Rev.* **84**, (1951) pp. 1232–1242.

[22] H. Grotch and D. R. Yennie. "Effective potential model for calculating nuclear corrections to the energy levels of hydrogen". *Rev. Mod. Phys.* **41**(2), (1969) pp. 350–374.

[23] E. V. Cherednikova, R. N. Faustov, and A. P. Martynenko. "Proton polarizability contribution to the hyperfine splitting in muonic hydrogen". *Nucl. Phys. A* **703**(1–2), (2002) pp. 365–377.

[24] J. Arrington, W. Melnitchouk, and J. A. Tjon. "Global analysis of proton elastic form factor data with two-photon exchange corrections". *Phys. Rev. C* **76**(3), (2007) p. 035205.

[25] A. V. Volotka, V. M. Shabaev, G. Plunien, and G. Soff. "Zemach and magnetic radius of the proton from the hyperfine splitting in hydrogen". *Eur. Phys. J. D* **33**(1), (2005) pp. 23–27.

[26] S. J. Brodsky, C. E. Carlson, J. R. Hiller, and D. S. Hwang. "Constraints on Proton Structure from Precision Atomic-Physics Measurements". *Phys. Rev. Lett.* **94**(2), (2005) pp. 022001–4.

[27] A. Dupays, A. Beswick, B. Lepetit, C. Rizzo, and D. Bakalov. "Proton Zemach radius from measurements of the hyperfine splitting of hydrogen and muonic hydrogen". *Phys. Rev. A* **68**(5), (2003) p. 052503 (5).

[28] M. A. Belushkin, H. W. Hammer, and U.-G. Meissner. "Dispersion analysis of the nucleon form factors including meson continua". *Phys. Rev. C* **75**(3), (2007) p. 035202.

[29] J. L. Friar and I. Sick. "Zemach moments for hydrogen and deuterium". *Phys. Lett. B* **579**(3–4), (2004) pp. 285–289.

[30] P. Indelicato. Private communication (2010).

[31] K. Pachucki. "Theory of the Lamb shift in muonic hydrogen". *Phys. Rev. A* **53**(4), (1996) pp. 2092–2100.

[32] K. Pachucki. "Proton structure effects in muonic hydrogen". *Phys. Rev. A* **60**(5), (1999) pp. 3593–3598.

[33] A. Veitia and K. Pachucki. "Nuclear recoil effects in antiprotonic and muonic atoms". *Phys. Rev. A* **69**(4), (2004) pp. 042501–4.

[34] E. Borie. "Lamb shift in muonic hydrogen". *Phys. Rev. A* **71**(3), (2005) pp. 032508–8.

[35] T. Kinoshita and M. Nio. "Sixth-Order Vacuum-Polarization Contribution to the Lamb Shift of Muonic Hydrogen". *Phys. Rev. Lett.* **82**(16), (1999) pp. 3240–3243.

[36] V. G. Ivanov, E. Y. Korzinin, and S. G. Karshenboim. "Second-order corrections to the wave function at the origin in muonic hydrogen and pionium". *Phys. Rev. D* **80**(2), (2009) p. 027702.

[37] G. A. Rinker. "Nuclear polarization in muonic helium". *Phys. Rev. A* **14**(1), (1976) p. 18.

[38] E. Borie and G. A. Rinker. "Improved calculation of the muonic-helium Lamb shift". *Phys. Rev. A* **18**(2), (1978) p. 324.

[39] M. I. Eides, H. Grotch, and V. A. Shelyuto. "Theory of light hydrogenlike atoms". *Phys. Rep.* **342**(2–3), (2001) pp. 63–261.

[40] R. Barbieri, M. Caffo, and E. Remiddi. "Fourth-order charge radius of the muon and its contribution to the lamb shift". *Lettere al Nuovo Cimento* **7**(60).

[41] H. Suura and E. H. Wichmann. "Magnetic Moment of the Mu Meson". *Phys. Rev.* **105**(6), (1957) p. 1930.

[42] A. Petermann. "Magnetic Moment of the mu Meson". *Phys. Rev.* **105**(6), (1957) p. 1931.

[43] E. Borie. *Helvetica Physica Acta* **48**, (1975) p. 671.

[44] J. L. Friar, J. Martorell, and D. W. L. Sprung. "Hadronic vacuum polarization and the Lamb shift". *Phys. Rev. A* **59**(5), (1999) pp. 4061–4063.

[45] A. Martynenko and R. Faustov. "Proton polarizability and Lamb shift in the muonic hydrogen atom". *Physics of Atomic Nuclei* **63**(5), (2000) pp. 845–849.

[46] A. Martynenko and R. Faustov. "Effects of vacuum polarization and of proton polarizability in the Lamb shift of muonic hydrogen". *Physics of Atomic Nuclei* **64**(7), (2001) pp. 1282–1287.

[47] W. A. Barker and F. N. Glover. "Reduction of Relativistic Two-Particle Wave Equations to Approximate Forms. III". *Phys. Rev.* **99**(1), (1955) pp. 317–324.

[48] R. Rosenfelder. "Proton polarization shifts in electronic and muonic hydrogen". *Phys. Lett. B* **463**(2–4), (1999) pp. 317–322.

[49] J. L. Friar. "Nuclear finite-size effects in light muonic atoms". *Annals of Physics* **122**(1), (1979) pp. 151–196.

[50] L. A. Borisoglebsky and E. E. Trofimenko. "The nuclear size correction to the energy levels of the light hydrogen-like and muonic atoms". *Phys. Lett. B* **81**(2), (1979) pp. 175–177.

[51] J. L. Friar. "Approximate normalized wave functions for the finite-size Coulomb problem". *Z. Phys. A* **292**(1), (1979) pp. 1–6.

[52] J. L. Friar. "Approximate normalized wave functions for the finite-size Coulomb problem". *Z. Phys. A* **303**(1), (1981) pp. 84–84.

[53] P. Abbon and others (COMPASS collaboration). "The COMPASS experiment at CERN". *Nucl. Inst. Meth. A* **577**(3), (2007) pp. 455–518.

[54] S. Aid et al. "A measurement and QCD analysis of the proton structure function f-2(x,q(2)) at HERA". *Nucl. Phys. B* **470**(1–2), (1996) pp. 3–38.

[55] E. AKER and others (Crystal Barrel Collaboration). "The crystal barrel spectrometer at lear". *Nucl. Inst. Meth. A* **321**(1–2), (1992) pp. 69–108.

[56] M. Hori, J. Eades, R. S. Hayano, T. Ishikawa, J. Sakaguchi, E. Widmann, H. Yamaguchi, H. A. Torii, B. Juhasz, D. Horvath, and T. Yamazaki. "Sub-ppm laser spectroscopy of antiprotonic helium and a CPT-violation limit on the antiprotonic charge and mass". *Phys. Rev. Lett.* **87**(9).

[57] S. G. Karshenboim and V. G. Ivanov. "The g factor of the proton". *Phys. Lett. B* **566**(1–2), (2003) pp. 27–34.

[58] G. FRICKE, C. BERNHARDT, K. HEILIG, L. A. SCHALLER, L. SCHELLENBERG, E. B. SHERA, and C. W. DEJAGER. "Nuclear Ground-state Charge Radii From Electromagnetic-interactions". *Atomic Data and Nuclear Data Tables* **60**(2), (1995) pp. 177–285.

[59] D. B. Leinweber, T. Draper, and R. M. Woloshyn. "Decuplet baryon structure from lattice QCD". *Phys. Rev. D* **46**(7), (1992) pp. 3067–3085.

[60] J. L. Friar, J. Martorell, and D. W. L. Sprung. "Nuclear sizes and the isotope shift". *Phys. Rev. A* **56**(6), (1997) pp. 4579–4586.

[61] D. R. Yennie, M. M. Lévy, and D. G. Ravenhall. "Electromagnetic structure of nucleons". *Rev. Mod. Phys.* **29**(1), (1957) pp. 144–157.

[62] R. G. Sachs. "High-energy behavior of nucleon electromagnetic form factors". *Phys. Rev.* **126**(6), (1962) pp. 2256–2260.

[63] G. Simon, C. Schmitt, F. Borkowski, and V. Walther. "Absolute electron-proton cross sections at low momentum transfer measured with a high pressure gas target system". *Nucl. Phys. A* **333**(3), (1980) pp. 381–391.

[64] P. Lehmann, R. Taylor, and R. Wilson. "Electron-proton scattering at low momentum transfers". *Phys. Rev.* **126**(3), (1962) pp. 1183–1188.

[65] L. N. Hand, D. G. Miller, and R. Wilson. "Electric and magnetic form factors of the nucleon". *Rev. Mod. Phys.* **35**(2), (1963) pp. 335–349.

[66] J. J. Murphy, Y. M. Shin, and D. M. Skopik. "Proton form factor from 0.15 to 0.79 fm^{-2}". *Phys. Rev. C* **9**(6), (1974) pp. 2125–2129.

[67] C. Wong. "Deuteron radius and nuclear forces in free space". *Int. J. Mod. Phys.* **3**(3), (1994) pp. 821–907.

[68] P. Mergell, U.-G. Meissner, and D. Drechsel. "Dispersion-theoretical analysis of the nucleon electromagnetic form factors". *Nucl. Phys. A* **596**(3–4), (1996) pp. 367–396.

[69] R. Rosenfelder. "Coulomb corrections to elastic electron-proton scattering and the proton charge radius". *Phys. Lett. B* **479**(4), (2000) pp. 381–386.

[70] S. Bourzeix, B. de Beauvoir, F. Nez, M. D. Plimmer, F. de Tomasi, L. Julien, F. Biraben, and D. N. Stacey. "High Resolution Spectroscopy of the Hydrogen Atom: Determination of the $1S$ Lamb Shift". *Phys. Rev. Lett.* **76**(3), (1996) pp. 384–387.

[71] T. Udem, A. Huber, B. Gross, J. Reichert, M. Prevedelli, M. Weitz, and T. W. Hänsch. "Phase-Coherent Measurement of the Hydrogen $1S - 2S$ Transition Frequency with an Optical Frequency Interval Divider Chain". *Phys. Rev. Lett.* **79**(14), (1997) pp. 2646–2649.

[72] C. Schwob, L. Jozefowski, B. de Beauvoir, L. Hilico, F. Nez, L. Julien, F. Biraben, O. Acef, J.-J. Zondy, and A. Clairon. "Optical frequency measurement of the $2S - 12D$ transitions in hydrogen and deuterium: Rydberg constant and Lamb shift determinations". *Phys. Rev. Lett.* **82**(25), (1999) pp. 4960–4963.

[73] K. Pachucki. "Logarithmic two-loop corrections to the Lamb shift in hydrogen". *Phys. Rev. A* **63**(4), (2001) p. 042503.

[74] K. Pachucki and U. D. Jentschura. "Two-Loop Bethe-Logarithm Correction in Hydrogenlike Atoms". *Phys. Rev. Lett.* **91**(11), (2003) p. 113005.

[75] S. G. Karshenboim. "What do we actually know about the proton radius". *Can. J. Phys.* **77**, (1999) pp. 241–266.

[76] P. J. Mohr, B. N. Taylor, and D. B. Newell. "CODATA recommended values of the fundamental physical constants: 2006". *Rev. Mod. Phys.* **80**(2), (2008) pp. 633–730.

[77] F. Biraben. "Spectroscopy of atomic hydrogen: How is the Rydberg constant determined?" *Eur. Phys. J. Special Topics* **172**(1), (2009) pp. 109–119.

[78] T. Nebel, F. D. Amaro, A. Antognini, F. Biraben, J. M. R. Cardoso, C. A. N. Conde, A. Dax, S. Dhawan, L. M. P. Fernandes, A. Giesen, T. W. Hänsch, P. Indelicato, L. Julien, P. E. Knowles, F. Kottmann, E. Le Bigot, Y.-W. Liu, J. A. M. Lopes, L. Ludhova, C. M. B. Monteiro, F. Mulhauser, F. Nez, R. Pohl, P. Rabinowitz, J. M. P. dos Santos, L. A. Schaller, K. Schuhmann, C. Schwob, D. Taqqu, and J. F. C. A. Veloso. "Status of the muonic hydrogen Lamb-shift experiment". *Can. J. Phys.* **85**(5), (2007) pp. 469–478.

[79] "Muon and Pion Beams at Paul Scherrer Institute". `http://ltp.web.psi.ch/accelerator_and_beams/pion_muon_beams.htm`.

[80] T. S. Jensen and V. E. Markushin. "Collisional deexcitation of exotic hydrogen atoms in highly excited states". *Eur. Phys. J. D* **21**, (2002) pp. 261–270.

[81] E. Fermi, E. Teller, and V. Weisskopf. "The Decay of Negative Mesotrons in Matter". *Phys. Rev.* **71**(5), (1947) pp. 314–315.

[82] M. Leon and H. A. Bethe. "Negative meson absorption in liquid hydrogen". *Phys. Rev.* **127**(2), (1962) pp. 636–647.

[83] V. E. Markushin. "Atomic cascade in muonic hydrogen and the problem of kinetic-energy distribution in the ground state". *Phys. Rev. A* **50**(2), (1994) pp. 1137–1143.

[84] L. Ludhova, F. D. Amaro, A. Antognini, F. Biraben, J. M. R. Cardoso, C. A. N. Conde, A. Dax, S. Dhawan, L. M. P. Fernandes, T. W. Hänsch, V. W. Hughes, P. Indelicato, L. Julien, P. E. Knowles, F. Kottmann, Y.-W. Liu, J. A. M. Lopes, C. M. B. Monteiro, F. Mulhauser, F. Nez, R. Pohl, P. Rabinowitz, J. dos Santos, L. A. Schaller, C. Schwob, D. Taqqu, and J. F. C. A. Veloso. "Muonic hydrogen cascade time and lifetime of the short-lived $2S$ state". *Phys. Rev. A* **75**(4), (2007) p. 040501.

[85] H. Anderhub, H. Hofer, F. Kottmann, P. LeCoultre, D. Makowiecki, O. Pitzurra, B. Sapp, P. G. Seiler, M. Wälchli, D. Taqqu, P. Truttmann, A. Zehnder, and C. Tschalär. "Search for the metastable $2S$ state in muonic hydrogen". *Phys. Lett. B* **71**(2), (1977) pp. 443–445.

[86] H. Anderhub, H. P. von Arb, J. Böcklin, F. Dittus, R. Ferreira Marques, H. Hoper, F. Kottmann, D. Taqqu, and J. Unternährer. "Measurement of the K-line intensity ratios in muonic hydrogen between 0.25 and 150 Torr gas pressures". *Phys. Lett. B* **143**(1–3), (1984) pp. 65–68.

[87] P. O. Egan, S. Dhawan, V. W. Hughes, D. C. Lu, F. G. Mariam, P. A. Souder, J. Vetter, G. z. Putlitz, P. A. Thompson, and A. B. Denison. "Search for long-lived $2S$ muonic hydrogen in H_2 gas". *Phys. Rev. A* **23**(3), (1981) pp. 1152–1163.

[88] A. Antognini. *The Lamb Shift Experiment in Muonic Hydroden.* Ph.D. thesis, University of Munich (Nov. 2005). `http://edoc.ub.uni-muenchen.de/5044/`.

[89] J. Shapiro and G. Breit. "Metastability of $2S$ states of hydrogenic atoms". *Phys. Rev.* **113**(1), (1959) pp. 179–181.

[90] J. S. Cohen and J. N. Bardsley. "Radiative collisional quenching of metastable muonic hydrogen $p\mu - (2S)$ and the metastable muonic helium ion $\alpha\mu - (2S)$". *Phys. Rev. A* **23**(1), (1981) pp. 46–51.

[91] J. Wallenius, S. Jonsell, Y. Kino, and P. Froelich. "Muonic atom deexcitation via formation of metastable molecular states, in light of experimental verification". *Hyp. Interact.* **138**(1–4), (2001) pp. 285–288.

[92] E. Lindroth, J. Wallenius, and S. Jonsell. "Decay rates of excited muonic molecular ions". *Phys. Rev. A* **68**(3), (2003) p. 032502. and Erratum *Phys. Rev. A* **69**(5), (2004) p. 059903(E).

[93] R. Pohl, H. Daniel, F. J. Hartmann, P. Hauser, Y. W. Liu, F. Kottmann, C. Maierl, V. E. Markushin, M. Mühlbauer, C. Petitjean, W. Schott, and D. Taqqu. "Observation of the molecular quenching of μp(2S) atoms". *Hyp. Interact.* **138**(1–4), (2001) pp. 35–40.

[94] V. Popov and V. Pomerantsev. "Long-lived $2S$ state of muonic hydrogen: population and lifetime" (Sep. 2008). arXiv:0809.0742v1[nucl-th].

[95] F.Kottmann et al. In P. Kienle, J. Marton, and J. Zmeskal, (Editors) *Proceedings of the International Workshop on Exotic Atoms (EXA02)*, p. 159 (Austrian Academy of Sciences, Vienna, 2003).

[96] L. Simons. "Recent results on antiprotonic atoms using a cyclotron trap at LEAR". *Phys. Scripta* **T22**, (1988) pp. 90–95.

[97] L. Simons. "Die Zyklotronfalle". *Phys. Bl.* **48**, (1992) p. 261.

[98] P. DeCecco, P. Hauser, D. Horváth, F. Kottmann, L. M. Simons, and D. Taqqu. "A new method to produce a negative muon beam of keV energies". *Nucl. Inst. Meth. A* **394**(3), (1997) pp. 287–294.

[99] M. Mühlbauer, H. Daniel, F. Hartmann, P. Hauser, F. Kottmann, C. Petitjean, W. Schott, D. Taqqu, and P. Wojciechowski. "Frictional cooling: Experimental results". *Hyp. Interact.* **119**(1–4), (1999) pp. 305–310.

[100] A. Antognini, F. Amaro, F. Biraben, J. Cardoso, C. Conde, D. Covita, A. Dax, S. Dhawan, L. Fernandes, T. Hänsch, V. Hughes, O. Huot, P. Indelicato, L. Julien, P. Knowles, F. Kottmann, Y.-W. Liu, J. Lopes, L. Ludhova, C. Monteiro, F. Mulhauser, F. Nez, B. Perry, R. Pohl, P. Rabinowitz, J. dos Santos, L. Schaller, C. Schwob, D. Taqqu, and J. Veloso. "Powerful fast triggerable 6 μm laser for the muonic hydrogen $2S$-Lamb shift experiment". *Optics Communications* **253**(4-6), (2005) pp. 362–374.

[101] P. Rabinowitz, B. Perry, and N. Levinos. "A continuously tunable sequential Stokes Raman laser". *IEEE J. Quant. Electr.* **22**(6), (1986) pp. 797–802.

[102] A. Giesen, H. Hügel, A. Voss, K. Wittig, U. Brauch, and H. Opower. "Scalable concept for diode-pumped high-power solid-state lasers". *Appl. Phys. B* **58**(5), (1994) pp. 365–372.

[103] C. Stewen, K. Contag, M. Larionov, A. Giesen, and H. Hügel. "A 1-kW CW thin disc laser". *IEEE J. Sel. Top. Quant. Electron.* **6**(4), (2000) pp. 650 – 657.

[104] A. Giesen and J. Speiser. "Fifteen years of work on thin-disk lasers: Results and scaling laws". *IEEE J. Sel. Top. Quant. Electron.* **13**(3), (2007) pp. 598 –609.

[105] A. Antognini, K. Schuhmann, F. Amaro, F. Biraben, A. Dax, A. Giesen, T. Graf, T. Hänsch, P. Indelicato, L. Julien, K. Cheng-Yang, P. Knowles, F. Kottmann, E. Le Bigot, Y.-W. Liu, L. Ludhova, N. Moschüring, F. Mulhauser, T. Nebel, F. Nez, P. Rabinowitz, C. Schwob, D. Taqqu, and R. Pohl. "Thin-disk Yb:YAG oscillator-amplifier laser, ASE, and effective Yb:YAG lifetime". *IEEE J. Quant. Electr.* **45**(8), (2009) pp. 993–1005.

[106] J. Dong, M. Bass, Y. Mao, P. Deng, and F. Gan. "Dependence of the Yb3+ emission cross section and lifetime on temperature and concentration in yttrium aluminum garnet". *J. Opt. Soc. Am. B* **20**(9), (2003) pp. 1975–1979.

[107] L. Ludhova, F. Amaro, A. Antognini, F. Biraben, J. Cardoso, C. Conde, D. Covita, A. Dax, S. Dhawan, L. Fernandes, T. Hänsch, V.-W. Hughes, O. Huot, P. Indelicato, L. Julien, P. Knowles, F. Kottmann, J. Lopes, Y.-W. Liu, C. Monteiro, F. Mulhauser, F. Nez, R. Pohl, P. Rabinowitz, J. dos Santos, L. Schaller, D. Taqqu, and J. Veloso. "Planar LAAPDs: temperature dependence, performance, and application in low-energy x-ray spectroscopy". *Nucl. Inst. Meth. A* **540**(1), (2005) pp. 169–179.

[108] L. M. P. Fernandes, F. D. Amaro, A. Antognini, J. M. R. Cardoso, C. A. N. Conde, O. Huot, P. E. Knowles, F. Kottmann, J. A. M. Lopes, L. Ludhova, C. M. B. Monteiro, F. Mulhauser, R. Pohl, J. M. F. dos Santos, L. A. Schaller, D. Taqqu, and J. F. C. A. Veloso. "Characterization of large area avalanche photodiodes in X-ray and VUV-light detection". *Journal of Instrumentation* **2**(08), (2007) p. P08005.

[109] L. M. P. Fernandes, J. A. M. Lopes, and J. M. F. dos Santos. "Excess noise factor in large area avalanche photodiodes for different temperatures". *Nucl. Inst. Meth. A* **531**(3), (2004) pp. 566–568.

[110] L. M. P. Fernandes, A. Antognini, M. Boucher, C. A. N. Conde, O. Huot, P. Knowles, F. Kottmann, L. Ludhova, F. Mulhauser, R. Pohl, L. A. Schaller, J. M. F. dos Santos, D. Taqqu, and J. F. C. A. Veloso. "Behaviour of large-area avalanche photodiodes under intense magnetic fields for vuv- visible- and x-ray photon detection". *Nucl. Inst. Meth. A* **498**(1-3), (2003) pp. 362–368.

[111] P. G. Blunden and I. Sick. "Proton radii and two-photon exchange". *Phys. Rev. C* **72**(5), (2005) p. 057601.

[112] R. Pohl. "6 μm energy calibração and a 'line shape model'" (Mar. 2010). Internal report (unpublished).

[113] F. Nez and F. Biraben. "Calibration of the Fabry-Perot" (Oct. 2009). Internal report (unpublished).

[114] S. Gerstenkorn and P. Luc. "Atlas du spectre d'absorption de la molecule de l'iode entre 14000–15000 cm^{-1}". Edition CNRS II, 91405 Orsay, France (1978).

[115] H. Knöckel, B. Bodermann, and E. Tiemann. "High precision description of the rovibronic structure of the I_2 B-X spectrum". *Eur. Phys. J. D* **28**(2), (2004) pp. 199–209.

[116] K.-H. Weber and C. J. Sansonetti. "Accurate energies of nS, nP, nD, nF, and nG levels of neutral cesium". *Phys. Rev. A* **35**(11), (1987) pp. 4650–4660.

[117] L. Rothman, I. Gordon, A. Barbe, D. Benner, P. Bernath, M. Birk, V. Boudon, L. Brown, A. Campargue, J.-P. Champion, K. Chance, L. Coudert, V. Dana, V. Devi, S. Fally, J.-M. Flaud, R. Gamache, A. Goldman, D. Jacquemart, I. Kleiner, N. Lacome, W. Lafferty, J.-Y. Mandin, S. Massie, S. Mikhailenko, C. Miller, N. Moazzen-Ahmadi, O. Naumenko, A. Nikitin, J. Orphal, V. Perevalov, A. Perrin, A. Predoi-Cross, C. Rinsland, M. Rotger, M. Šimečková, M. Smith, K. Sung, S. Tashkun, J. Tennyson, R. Toth, A. Vandaele, and J. V. Auwera. "The hitran 2008 molecular spectroscopic database". *J. Quant. Spect. Rad. Trans.* **110**(9–10), (2009) pp. 533–572. HITRAN-Database: `http://www.cfa.harvard.edu/HITRAN/`.

[118] A. Antognini and F. Nez. "Laser Wavelength Calibration with Water Lines at 6 μm" (Feb. 2010). Internal report (unpublished).

[119] R. A. Toth. "Water Vapor Measurements between 590 and 2582 cm^{-1}: Line Positions and Strengths". *J. Molec. Spectr.* **190**(2), (1998) pp. 379–396.

[120] G. Guelachvili. "Experimental Doppler-limited spectra of the v_2 bands of $H_2^{16}O$, $H_2^{17}O$, $H_2^{18}O$, and HDO by Fourier-transform spectroscopy: secondary wave-number standards between 1066 and 2296 cm^{-1}". *J. Opt. Soc. Am.* **73**(2), (1983) pp. 137–150.

[121] H. Metcalf and P. van der Straten. *Laser Cooling and Trapping*. Graduate Texts in Contemporary Physics (Springer New York, 2002).

[122] B. W. Shore. *The Theory of Coherent Atomic Excitation*, vol. 1. Simple Atoms and Fields (John Wiley and Sons, Inc., New York, 1990).

[123] P. Indelicato. Private communication (2009).

[124] D. Taqqu. Private communication.

[125] W. Demtröder. *Laserspektroskopie: Grundlagen und Techniken* (Springer Verlag, Berlin, 2000), 4 ed.

[126] S. Kilic, J.-P. Karr, and L. Hilico. "Coulombic and radiative decay rates of the resonances of the exotic molecular ions $pp\mu$, $pp\pi$, $dd\mu$, $dd\pi$, and $dt\mu$". *Phys. Rev. A* **70**(4), (2004) p. 042506.

[127] J. Olivero and R. Longbothum. "Empirical fits to the voigt line width: A brief review". *J. Quant. Spect. Rad. Trans.* **17**(2), (1977) pp. 233–236.

[128] S. R. Lundeen and F. M. Pipkin. "Measurement of the Lamb Shift in Hydrogen, $n = 2$". *Phys. Rev. Lett.* **46**(4), (1981) pp. 232–235.

[129] D. Hanneke, S. Fogwell, and G. Gabrielse. "New measurement of the electron magnetic moment and the fine structure constant". *Phys. Rev. Lett.* **100**(12), (2008) p. 120801.

[130] A. P. Martynenko. "Fine and hyperfine structure of P-wave levels in muonic hydrogen". *Physics of Atomic Nuclei* **71**(1), (2008) pp. 125–135.

[131] A. C. Zemach. "Proton Structure and the Hyperfine Shift in Hydrogen". *Phys. Rev.* **104**(6), (1956) pp. 1771–81.

[132] E. Borie. "Lamb shift of muonic deuterium". *Phys. Rev. A* **72**(5), (2005) p. 052511.

[133] W. Leidemann and R. Rosenfelder. "Deuteron nuclear polarization shifts with realistic potentials". *Phys. Rev. C* **51**(1), (1995) pp. 427–430.

[134] Y. Lu and R. Rosenfelder. "Nuclear polarization corrections for the S-levels of electronic and muonic deuterium". *Phys. Lett. B* **319**(1–3), (1993) pp. 7–12.

[135] A. Huber, T. Udem, B. Gross, J. Reichert, M. Kourogi, K. Pachucki, M. Weitz, and T. W. Hänsch. "Hydrogen-deuterium $1S - 2S$ isotope shift and the structure of the deuteron". *Phys. Rev. Lett.* **80**(3), (1998) pp. 468–471.

[136] C. G. Parthey, A. Matveev, J. Alnis, R. Pohl, T. Udem, U. D. Jentschura, N. Kolachevsky, and T. W. Hänsch. "Precision Measurement of the Hydrogen-Deuterium $1S - 2S$ Isotope Shift". *Phys. Rev. Lett.* **104**, (2010) p. 233001.

[137] M. Herrmann, M. Haas, U. D. Jentschura, F. Kottmann, D. Leibfried, G. Saathoff, C. Gohle, A. Ozawa, V. Batteiger, S. Knünz, N. Kolachevsky, H. A. Schüssler, T. W. Hänsch, and T. Udem. "Feasibility of coherent xuv spectroscopy on the $1S - 2S$ transition in singly ionized helium". *Phys. Rev. A* **79**(5), (2009) p. 052505.

[138] E. Borie. "Hyperfine structure of light exotic atoms". *Z. Phys. A* **278**(2), (1976) pp. 127–131.

[139] A. P. Martynenko. "$2S$ Hyperfine splitting of muonic hydrogen". *Phys. Rev. A* **71**(2), (2005) pp. 022506–11.

[140] R. Pohl. "The data aquisition software of the $\mu p(2S - 2P)$ experiment" (Apr. 2006). Internal report (unpublished).

Dankeschön

How could such a project be led to success without the help, the passion, the patience, and the endurance of many, who wouldn't technically have to lift a finger but still did big time? Let me tell you something: Thank you all! I am deeply grateful and humbled by your support!

Foremost, I would like to thank **Prof. Hänsch** for the warm welcome in his group. We are blessed with such a stimulating working environment enabling us to concentrate on unraveling the secrects of Physics. Thank you for believing in an exotic bunch of people measuring the μp Lamb shift even in the barren moments of *maybe not so successful* beamtimes.

Prof. Faessler's contribution to this thesis needs to be emphasized because he agreed to prepare a report of this thesis and be one of my examiners in a time where everything had to happen very quickly and I was under *slight* pressure. Thank you very much!

Randolf Pohl (*On-sight Randy, Co-spokesman, and 3-star programmer*) had to endure a lot of questions from a sometimes very puzzled student ("Du, Scheff..."). Thank you for sharing the night shifts and the appartments during the beamtimes, and of course, for your friendship. It is you who convinced me to spend 5 years of my life on muonic atoms and who made sure that I got to know a great crowd of people and that I thoroughly enjoyed every single moment!

Mr. Lamb-shift-in-μp **Franz Kottmann** is an inexhaustible well of insight and calmness. Even in moments during the runs when the whole experiment seemed to go down in flames, the Captain would still remain on the bridge. Thank you for keeping up the morale and for mentoring me during all these years! And then there is **Aldo** *Ciaociao* **Antognini**, the guy who gave me a hard time finding aspects of this experiment which were not yet covered by the most extensive μp-thesis ever... I will always remember the parties at your place during beamtime. Your benevolence will always be an ideal for me to strive for!

Every individual member of the μp-Collaboraçaõ made this experiment possible in the first place. Without mentioning the long list of all your names I would like to thank every single one of you! A big Thank you has to go to **François Nez**, the tamer of the Ti:Sapph laser. He tought me a lot about his baby and how to treat it well.

The entire Hänsch-group at MPQ and at LMU made sure working here was great fun! Thank you all for all the moments beside work like hiking, climbing, and, recently, slack-lining or for shared lunch-times and cups of tea. **Christian Parthey** went through the draft of this thesis like oatmeal through a pre-buttered weasel (as a colleague put it). Together with him, Randolf, **Max Herrmann**, **Katharina Predehl**, **Thomas Udem**, and **Tobias Wilken**, I enjoyed dynamic moments in a quite stinky climbing-gym sometimes even early in

the morning where normal people were still sleeping. Christian and Max made it all the way to Switzerland to give us more than just a hand during the setup of the 2009-experiment.

Without the administrative talent and sedulous support of **Rosemarie Lechner** (who passed away before I could thank her in person), **Gabriele Gschwendtner**, and **Ingrid Hermann** and also of **Ksenija vom Malm**, the administrative hurdles would have created an annoying aftertaste. With all of you, however, these challenges were *Mostly Harmless*...

Wolfgang Simon and **Charly Linner** are an astonishing team of experts in putting the mechanical and technical aspects of your experiment into reality ("Naa, des machma gscheid!"). The same holds, of course, for the electronical side and **Helmut Brückner** without whom the LAAPDs in 2009 would have just been shiny blocks of semiconductors. Die Weisswürste zum Frühstück mit Euch und zusammen mit **Peter Fendel** und Randolf sind legendär!

In diesem Zusammenhang möchte ich auch die **MPQ-Werkstatt** und den **Einkauf** erwähnen, die zu jedem Zeitpunkt Geduld mit den Wissenschaftlern hatten und so manchen dringenden Auftrag in Überlichtgeschwindigkeit ausgeführt haben. Danke! At PSI, the help of all people and support groups was also amazing! If you asked any one of them for a favour they said "I'll do it in the afternoon." and it was done before lunch!

Finally, I cannot express how grateful I am to my entire **family** for their love and for everything they taught me. **Isaak**, **Elias**, and my wife **Nathalie** helped me to find my place in life, thank you! I hope I can still be a good father to our kids despite having been rather unavailable during beamtimes and during the last weeks of writing. I love you.